Summary

Author Statement

No other animal species, except for consentient human beings, were involved in the research for what concerns blood and tissue samples. Immortalized cells have been obtained by cloning the original lines, already existing, and then bought from certified structures. In any case, no animal species have been harmed, nor threated, while the whole study was carried on.

Being the topic of the work a study for the development of devices for the oncological screening, aimed to improve the life quality and health monitoring for the human kind, this last one species has been the rightful subject of the studies involved.

Not for immutable ethics, nor for imposed morals, but because for this individual conscience it was the right thing to do.

Introduction

Medical screening protocols allow national health systems to detect pathologies before their degeneration into harmful, or even terminal, stages. This preventive approach shows two great advantages compared to medical intervention on already developed diseases: greater chances for the patients to heal without repercussions nor relapses of the original pathology, and lower expenses for health systems to cure and treat the patients. For this reason, screening devices and tests development is heavily promoted in the scientific community, with various fields involved (medicine, surgery, physics, chemistry, biology, informatics, electronics and so forth) in order to perfect the ones already existing, or even creating new ones for pathologies previously not early-detectable.

In particular, oncological field gains great benefit from this kind of approach, being neoplasms hardly removable once that they reach the malignant stage and the consequential metastatization. For what concerns tumors, early-screening while on benignant stages means often to save patient lives, allowing physicians and surgeons to operate on them with minor risks and high successful rates. One way to early detect neoplasms is using devices able to recognize the variety of tumor markers emanated from them: molecules of different nature (often called in literature volatile organic compounds – VOCs), that due to tumor activity are released in the hosting body, and from the last expelled in breath, feces, sweat and other means.

In this thesis, volatile chemicals of oncological interest (particularly but not exclusively, produced from colorectal and gastric cancers) have been detected by using nanostructured chemoresistive sensors: chemical sensors capable to change their conductance/resistance due to a dynamic reaction happening thanks to the oxidation/reduction of their surface once the markers go in contact with it. They are called nanostructured because the dimensions of the grains, tubes, beads, wires and spheres composing them spans the tenth of nanometers; the reason behind the choice to prepare sensors with this geometrical property lays in the fact that it widely increases the surface of reaction, and thus the output signal.

Tests with these sensors have been carried on three different kind of specimens:

- first, in order to verify the capability of the sensing units to actually respond to markers from a biological source, cell cultures breed in laboratory were tested. Primary, immortalized and tumoral lines have been plated at different times, to detect possible differences in their exhalations. After testing them with their breeding ground, cells have been washed to test their responses without breeding round hosting them, and also the recovered breeding ground itself was tested alone. This last approach led to the idealization of the second kind of test, descripted below;
- then, tests on human blood samples were carried on donors affected from colorectal and gastric cancers, in different stages of degeneration, while comparing them to healthy donors. The aim of this part of the study was to verify if and how much malignant tumor could pollute the blood stream with markers useful for tumor detection, in a perspective of after-surgery/treatment, fast responding post-screening;
- finally, tumor tissues and healthy tissues of human origin have been compared, in order to verify the capability of the sensors to detect markers from dissected biological material and their reliability of response, in a perspective of fest-responding histological analysis.

The experiments were carried on and data were acquired in the lapse of time including the ending months of the author Master's Degree thesis, "Detection of tumor markers and cell metabolites on feces and cells with nanostructured sensors", the following year, and the

three years of doctorate. This thesis itself is the extension and continuation of the previously mentioned Master's Degree graduation work.

It is important to notice that, since research on human biological material was involved, it has been necessary to obtain an ethical authorization from the bodies responsible. The trial protocol and the informed consent form for this research were presented, accepted and retrospectively registered from the to the Ethical Committee of the District of Ferrara, with trial number 170484, on 13 July 2017.

The research was carried on together with the support brought and the fundings provided by SCENT S.r.l., a startup constituted on 21 April 2015 and aimed to the development of devices for the medical screening.

Given the great results obtained during the initial tests, the startup decided to secure the intellectual property of the prototype on 2 October 2015 by depositing the license request, and has been successfully patented in Italy with the patent number 102015000057717 on 8 March 2018.

Chapter 1 – Chemoresistive sensors

Chemoresistive solid state sensors are devices able to convert chemical or physical quantities (like gases concentration or light wavelength) into an electric signal, occurring due to the reactions happening in the material due to the measured phenomenon, which changes the electrical properties (resistance/conductance) of the sensing material. The most important solids that display semiconductor properties are: Silicon (Si), Germanium (Ge) and compounds of Gallium, followed by MOX (metal oxides, like Tin Oxide, Titanium Oxide, Zinc Oxide, Indium Oxide, and their doped versions) and non-MOX materials (like Cadmium Sulfide, Tin Sulfide, and so on), which are widely used in electronic devices, nanostructures, integrated circuits, lasers and so on. In the following subchapters, a swift description of the sensors properties used in this work is given for the reader, to understand the physics behind their functioning.

1.1 – Semiconductors Properties and Band Structure

Chemoresistive solid state sensors operating principle is based on two different phenomena:

- Change in the surface conductance
- Variation of the bulk (the internal volume of the sensitive material constituting the sensor) conductance

The text discusses now a panoramic on the most relevant properties of semiconductors, which has been exploited for the realization of sensors.

1.1.1 – Conduction and Valence Bands

Semiconductors, as all the crystalline solids, being ordered structure of atoms linked each other with small mutual distance (of order of few Angstroms), have an internal **band energy structure**. The origin of the solid band energy structure (i.e. allowed electron energies) is because atoms, closed together with small mutual distance, undergo to overlapping of **outer atomic orbitals** (i.e. atomic energy levels allowed, to accommodate electrons) which “melt together” in bands. **Inner atomic orbitals** are not involved in the

formation of bands because they are tightly bound to the atomic nucleus not performing overlap with orbitals of nearest atoms. The energy bands can be calculated using different methods. It depends by the approach that is chosen:

- **Tight Binding Method** [1], if the starting point are the energy levels of single atom
- **Nearly Free Electron Model** [2] if the target is to solve the Schrödinger equation where is inserted the periodic potential of the lattice

The result of these methods is the energy band diagram $E(k)$. It can count a great number of bands, but for the targets of this thesis the bands of interest are two: **Conduction Band (CB)** and **Valence Band (VB)** [2,3]. The bands with minor energy of VB are all totally filled by electrons and, consequently, VB is the highest energy band containing electrons. Figure 1.1 shows schematically the band structure of a solid. Electrons in VB are responsible for metallic or covalent bond among atoms. The size of the energy gap depends by the type of considered solid: Metal, Semiconductor or Insulator [4]. In a semiconductor, if **T=0K**, VB is filled by electrons and CB is completely empty. When **T>0K** electrons in VB acquire thermal energy. When thermal energy is enough, they can jump from VB to CB where they can move as free electrons into the solid. The energy gap ($Egap$=Ec−Ev), in a semiconductor, is smaller of 2 eV (Examples: $Egap$ (Silicon)=1.12eV, $Egap$ (Germanium)=0.67eV) and obviously greater than 0 eV. When **T>0K** electrons in VB acquire thermal energy, and when the thermal energy is enough, they jump on CB where they can move as free electrons into the solid. In a semiconductor at **room temperature**, the thermal energy acquired by electrons in VB is enough to populate the CB [3,5].

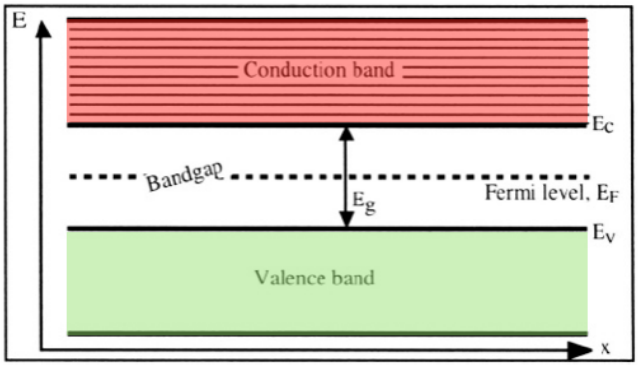

Figure 1.1: schematic band structure of a solid. The red band is the conduction band, the green band is the valence band and the white band among them is the band gap of forbidden energies. The energy of CB is higher than that of VB.

1.1.2 – Fermi Level, Direct and Indirect Transitions

Before discussing the properties of sensors, it is necessary to introduce the notion Fermi energy and Fermi level (E_F). Considering a typical metal, the highest energy band (i.e. the CB) is partially filled. The CB is effectively continuous, so thermal energy can excite electrons within this band leaving holes lower in the band. At absolute zero there is no thermal energy, so electrons fill the band starting from the bottom and there is a sharp cutoff at the highest occupied energy level. This energy defines the **Fermi energy**. At finite temperatures there is no sharply defined most energetic electron because thermal energy is continuously exciting electrons within the band. It is possible so only to define the energy level with a 50% probability of occupation, the **Fermi level**. Levels above E_F are completely empty, while levels below E_F are totally filled, by other electrons [6]. In a semiconductor, being the VB full of electrons and the CB empty at $T = 0K$, E_F resides in the band gap among VB and CB (Figure 1.1), spanning between $0.5eV$ and $2eV$. Figure 1.2A represents the energy band behavior of a semiconductor. When electrons are excited by thermal energy, they can jump from VB to CB, where E_{gap} is the smallest. In other words, among the maximum energy value for the VB, (E_{max}^{V}), and the minimum energy value for CB, (E_{min}^{C}), less thermal energy is required for the jump to happen. As shown in Figure 1.2B, the transition takes place on the boundaries of the first Brillouin zone, where E_{gap} is smaller than everywhere else. At this point, the parabolic approximation must be introduced to define the shape of the bands [7]. This approximation considers that bands have parabolic shape at the first Brillouin zone boundaries, with opposite concavity (as can be seen in Figure 1.2B).

$$E^{c}(k) = E_{min}^{c} + A(k - k_{min})^2 \quad (1.1a)$$

$$E^{v}(k) = E_{max}^{v} - B(k - k_{max})^2 \quad (1.1b)$$

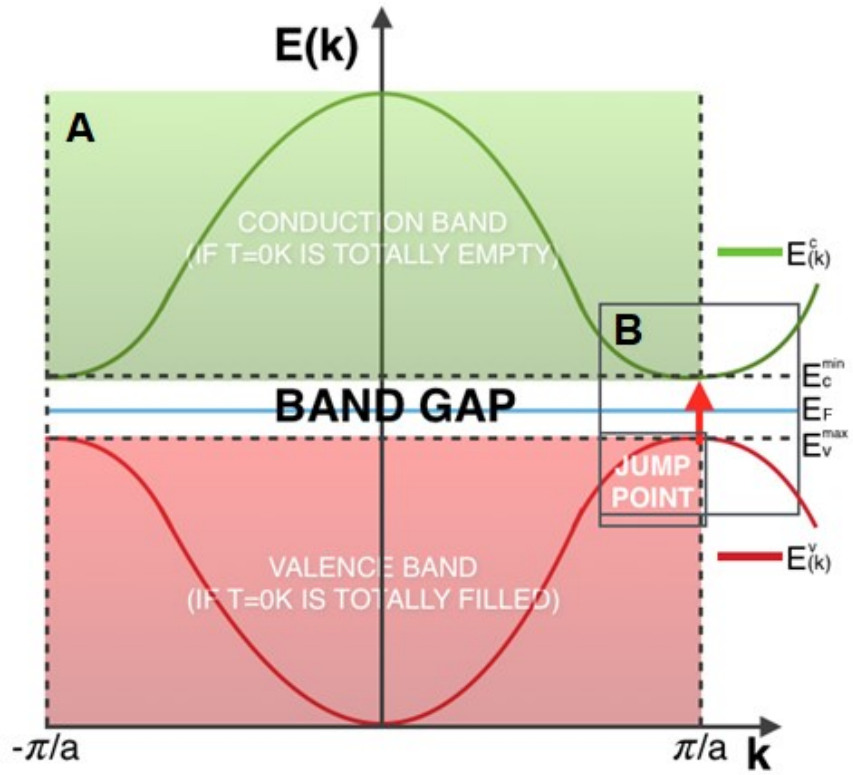

Figure 1.2: A) Semiconductor band scheme with general features. B) Inset of the zone where electrons can jump from VB to CB due to thermal energy. The bands at the boundaries are approximated with parabolic shape.

- If E^c_{min} and E^v_{max} have the **same wave vector** $\boldsymbol{k}$, the electron jump can occur **directly**, thanks to an energy amount equal to E_{gap}, which anyway conserves the crystalline momentum
- If E^c_{min} and E^v_{max} **have different wave vectors**, the electron jump can occur through an **indirect** transition, which requires also the contribution of a thermal phonon of energy $E_{ph} = \hbar\Omega$ [7]

These two cases are shown in Figure 1.3.

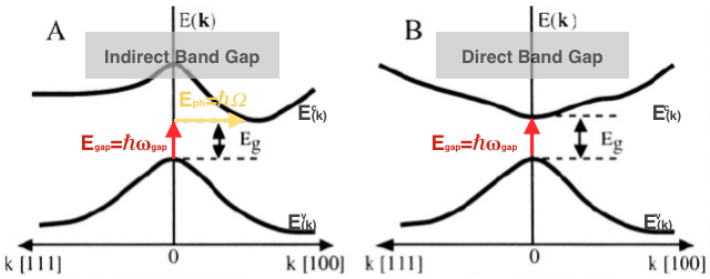

Figure 1.3: A) Indirect transition. B) Direct transition.

1.1.3 – Hole Concept and Effective Mass

As discussed in the previous paragraph, if an electron acquires thermal energy enough, it can jump from VB to CB, resulting in a vacant orbital in VB. The electron absence is called **hole [8]**. Holes behave like electrons under the application of electric or magnetic field, but with positive charge. Additionally, they show the following properties:

- The energy of a hole has opposite sign compared to the energy of the absent electron: $E_h = -E_e$
- The velocity of a hole is the same of an absent electron: $v_h = v_e$, as shown in Figure 1.4
- The hole effective mass has opposite sign compared to the electron effective mass: $m_e^* = -m_h^*$. Near the top of the VB, m_e^* is negative and m_h^* is positive
- Holes and of positively charged particles share the same equation of motion

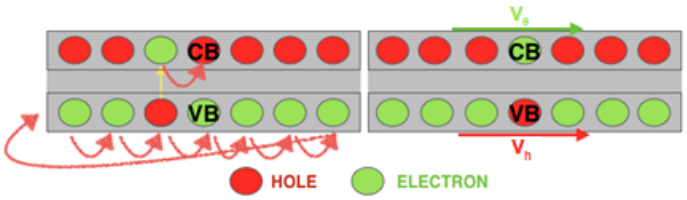

Figure 1.4: the motion of electrons and holes under the influence of an external field.

The electrons moving in a periodic crystal lattice have a different mass compared to the mass of a free electron in vacuum. It is necessary to introduce the **Effective Mass [9]**:

$$m^*(k) = \frac{\hbar}{\frac{d^2E}{dk^2}} \qquad (1.2)$$

m^* (Equation 1.2) is not constant in the periodic lattice, but varies with k:

- If the electron is in the upper half of an energy band, its effective mass is negative
- If the electron is in the lower half of an energy band, its effective mass is positive
- If the electron is near the middle of an energy band, its effective mass tends to infinity
- Effective mass of a hole is merely minus sign the effective mass of the electron
- If a 3D crystal is considered, the effective mass is a tensor 3x3 (matrix). This is due to a possible electron acceleration anisotropy in the different directions of the crystal

1.1.4 – Bulk, Fermi-Dirac Distribution and Density of Electrons/Holes

n(k) is defined as the density of the allowed states per unit of volume in a 3D crystal:

$$n(k) = \frac{1}{8\pi^3} \quad (1.3)$$

f(k) is defined as the probability that these states are occupied. Being electrons and holes fermions, f(k) follows the Fermi-Dirac distribution as shown in Figure 1.5:

$$f(k) = \frac{1}{1 + e^{(E_n(k) - E_F)/K_b T}} \quad (1.4a)$$

$$f(E) = \frac{1}{1 + e^{(E - E_F)/K_b T}} \quad (1.4b)$$

where E_F is the Fermi level energy, K_b is the Boltzmann constant, T is the temperature in Kelvin, $E_n(k)$ or E is the energy of an electron permitted level (k) in a certain band.

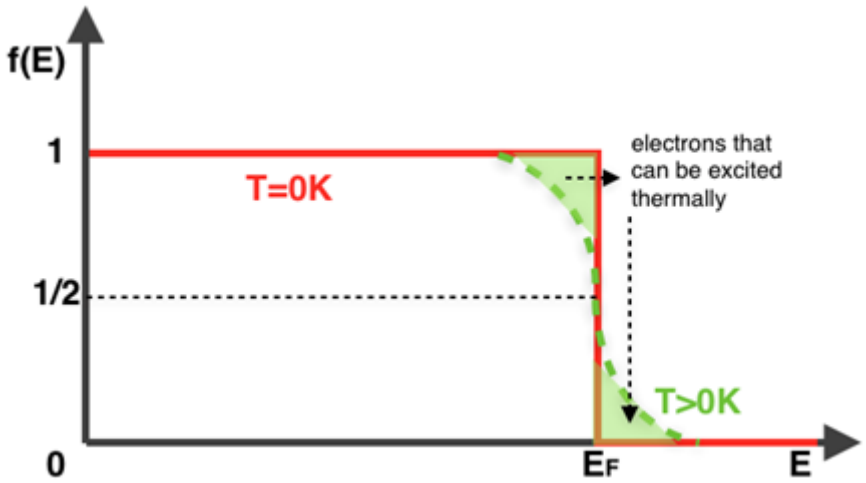

Figure 1.5: Behavior of Fermi Dirac distribution at T=0K (red line) and T>0K (green dashed line). The green areas represent excited electrons.

Thus, electron (n) and hole densities (p) are:

$$n = \int_{BZ}^{BZ} n(E) f(E) dE \quad (1.5a)$$

$$p = \int_{BZ}^{BZ} p(E)[1 - f(E)] dE \quad (1.5b)$$

To solve these integrals, it is useful to introduce some simplifications:

1. Electrons of interest in this calculation are those in CB with energy E very close to the CB bottom (between E_{min}^{c} and $E_{min}^{c} + dE$). Therefore, the number of electron states in dE interval is:

$$n(E)dE = \frac{1}{2\pi^2\hbar^3}(2m_e^*)^{3/2}(E - E_c)^{1/2}dE \qquad (1.6a)$$

2. Likewise, holes of interest are those in VB with energy E very close to the VB top (between E_{max}^{v} and $E_{max}^{v} + dE$). Therefore, the number of hole levels in dE interval is:

$$p(E)dE = \frac{1}{2\pi^2\hbar^3}(2m_h^*)^{3/2}(E_v - E)^{1/2}dE \qquad (1.6b)$$

3. In semiconductors, E_F lies in the deep Band Gap and then the condition: $\boldsymbol{E - E_F \gg K_B T}$ is usually satisfied at T=300K. Therefore, Fermi Dirac distribution (1.4) degenerates into Maxwell-Boltzmann distribution as follows:

$$f(E) = Ae^{-(E-E_F)/K_B T} \quad (1.7)$$

Then, by using these simplifications, it is possible to calculate the integrals 1.4a and 1.4b, obtaining the total number of electrons in CB (n) and the total number of holes in VB (p) [10]:

$$n = N_c e^{-\frac{E_c - E_F}{K_B T}} \quad (1.8a) \quad and \quad p = N_v e^{-\frac{E_F - E_v}{K_B T}} \quad (1.8b)$$

where n is the electron density for the conduction band (CB), p is the hole density for the valence band (VB), N_v is the effective density of states for the valence band (number of states with energy E_v for holes), N_c is the effective density of states for the conduction band (number of states with energy E_c for electrons), E_c is the energy of the conduction band, E_v is the energy for the valence band, E_F is the Fermi level, T is the temperature in kelvin, K_B is the Boltzmann constant.

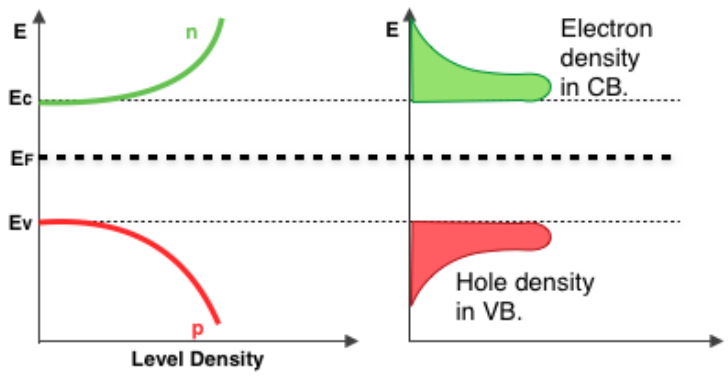

Figure 1.6: Left – density of permitted electron levels in CB and permitted hole levels in VB. Right – electron density (n) in CB and hole density (p) in VB.

1.1.5 – Intrinsic and Extrinsic Semiconductors, Fermi Level Alignment

Semiconductors can be of two types, depending on the position of the E_F with respect to the forbidden energy band of the crystal. If E_F is located very close to the center of the gap, there will be the same number of carriers in the **VB** and in the **CB**; in this case, it is called **intrinsic semiconductor** [11]. On the other hand, if some impurities are added or if the crystal has structural imperfections, the E_F can be shifted from the middle of the gap, and the semiconductor is now called **extrinsic** and the number of holes and electrons is different. Sometimes the crystal can be so much doped that the Fermi level can enter in the conduction or in the valence band. In this case the semiconductor is **degenerate** and the Fermi level has almost the same meaning of the Fermi level for metals, because it well separates the empty zones from the filled ones and the semiconductor behaves like a metal. Considering the extrinsic, non-degenerate case, it is possible to observe:

- ***n*-type semiconductors** if the number of holes in the valence band is less than the number of electrons in the conduction band and the Fermi level is shifted above the middle of the gap;
- ***p*-type semiconductors** if the number of holes in the valence band is bigger than the number of electrons in the conduction band and the Fermi level is moved below the middle of the gap.

The creation of extrinsic semiconductors can take place via the **doping** technique, a method that consists in the introduction of foreign atoms which replace those proper of the material. If they provide electrons to the material, they are called **donors**. An example of

donor is P, which has a valence electron more than Si. It creates a defect in the periodical structure of the silicon crystal, placing an electron next to the conduction band. It is sufficient a little thermal excitation (and so a small energy) to send the electron towards the **CB** ionizing the donor, which assumes a positive charge; on the other hand, if the foreign atoms introduced via the doping provide holes to the material they are called **acceptors**. An example of acceptor is Boron which has only three valence electrons. In a silicon crystal, it creates a defect slightly above the **VB** and with a little thermal excitation an electron can jump from the valence band to the acceptor, conferring it a negative charge. In a typical lattice, the number density of atoms is of the order of $10^{23} cm^{-3}$, while the density in volume of donors (or acceptors) is $N_d \sim 10^{16 \div 18} cm^{-3}$. To know the density of electrons in the conduction band, and the density of holes in the valence band, it is necessary to use, as stated above, the Maxwell-Boltzmann distribution. In fact:

- Assuming $E_C - E_F > 3k_bT$, then $n = N_C e^{-\frac{E_C - E_F}{k_bT}}$, where E_C is the energy of the edge of the conduction band and N_C is the effective density of states in a neighborhood of the **CB** bottom
- Assuming $E_F - E_V > 3k_bT$, then $p = N_V e^{-\frac{E_F - E_V}{k_bT}}$, where E_V is the energy of the edge of the valence band and N_V is the effective density of states in a neighborhood of the **VB** top

Hereinafter in this paragraph, the two types of semiconductors are going to be discussed from a mathematical point of view. Multiplying n and p for a semiconductor under conditions of thermodynamic equilibrium results into:

$$pn = N_c e^{-\frac{E_c - E_F}{K_B T}} N_v e^{-\frac{E_F - E_v}{K_B T}} = N_c N_v e^{-\frac{E_{gap}}{K_B T}} = 32 \left(\frac{\pi^2 k^2 m_e^* m_h^*}{h^4} \right)^{\frac{3}{2}} T^3 e^{-\frac{E_{gap}}{K_B T}} \equiv n_i^2 \quad (1.9)$$

$$n_i \equiv \sqrt{32 \left(\frac{\pi^2 k^2 m_e^* m_h^*}{h^4} \right)^{\frac{3}{2}} T^3 e^{-\frac{E_{gap}}{K_B T}}} \quad (1.10)$$

where n_i is the intrinsic carrier concentration, and is function of the temperature T, as shown in Figure 1.7, and of the material through E_{gap}. Physically n_i is the number of electrons that, thanks to thermal energy, can jump in CB. These are the electrons free to

move in the semiconductor, giving contribution to electrical current and thus to the conductivity (for example: in silicon $n_i = 1.45 \bullet 10^{10} cm^{-3}\ at\ \ T = 300K$). For the case of intrinsic semiconductors, when an electron receives thermal energy enough to jump from VB to CB, it leaves a hole in VB, thus every hole in VB corresponds to an electron in CB.

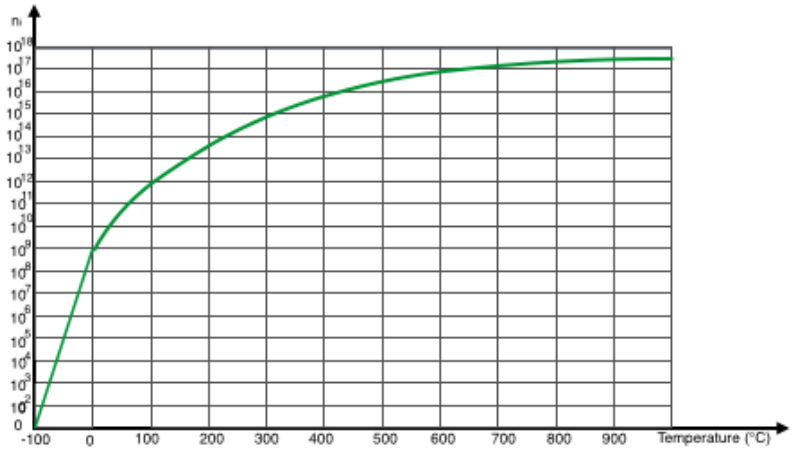

Figure 1.7: Free carrier concentrations as function of temperature. The number of carriers in CB is zero for $T = 0K$ but it increases with temperature, because electrons acquire thermal energy enough to jump in CB and leave the semiconductor atoms.

The number of conduction electrons is the same of the valence holes: $p = n = n_i$, and the Fermi level is calculated matching n and p. The result for E_F is:

$$E_F = \frac{E_c + E_v}{2} + \frac{3}{4} K_b T\ ln\left(\frac{m_h^*}{m_e^*}\right) \equiv E_i \quad (1.11)$$

If $\frac{m_h^*}{m_e^*} = 1$ (simplifying approximation): $E_i = \frac{E_c + E_v}{2}$, where E_i is called the **intrinsic energy level**. Physically, this is the Fermi level in an intrinsic semiconductor. This does not stand for the **extrinsic semiconductors**, where impurities are added. Impurities are atoms of different elements that, combined to a semiconductor, modify significantly its electrical and optical properties. If atoms of the V column of the periodic table (like phosphorus or arsenic) are added to a silicon crystal semiconductor, in place of some silicon atoms, they form four covalent bonds each one with the nearest four silicon atoms of the material, but one electron remains weakly bonded to the impurity atom. At room temperature, these weakly bond electrons own enough thermal energy to break the bound and became free electrons in CB. This kind of impurities are called **donors**, because they are atoms that donate one electron in the crystal CB, as shown in Figure 1.8. Likewise, if atoms of the III column of the periodic table are added to the semiconductor (like boron) in place of some

silicon atoms, they generate free holes in VB. This happens because one boron atom, having valence three, takes an electron from a silicon atom, generating a hole in VB. These impurities are called **acceptors**, because they accept an electron from a silicon atom and free a hole in VB. Impurity atoms are called **dopants** of the semiconductor. **n-type semiconductors** are doped with donor atoms, and most of the free carriers have negative charge (electrons); **p-type semiconductors** are doped with acceptor atoms, and most of the free carriers have positive charge (holes) [12].

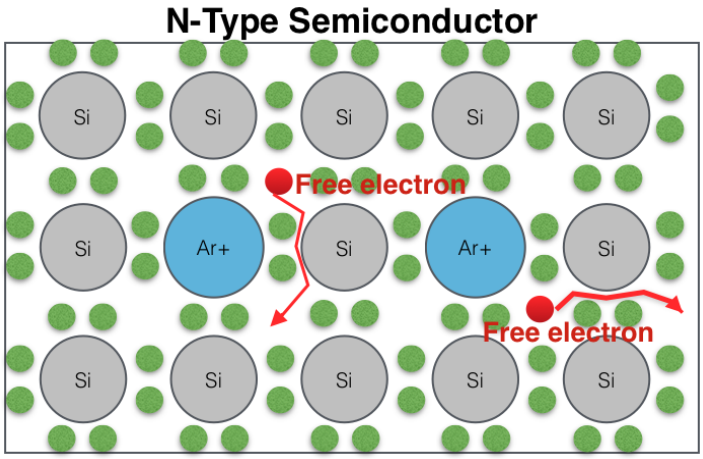

Figure 1.8: n-type doped semiconductor. Green points are the electrons making covalent bonds. Red points are electrons that, at room temperature, leave the impurity atom and become free. It is shown that the impurity atoms (in this case Arsenic), after the electron loss, become positive.

The introduction in silicon of donor atoms, such as phosphorus (P) or arsenic (As), gives rise to a **permitted energy level in the bandgap** called E_d. This level is located a few meV below the bottom of the conduction band and, at very low temperature, it contains the electrons which can be given to the crystal by the impurity atoms. At room temperature, electrons on the level with energy E_d possess enough thermal energy (equal to $\frac{K_b T}{q} = 25.6\, meV$) to break free from the impurity atoms and move freely in the crystal. In other words, they can "jump" from the energy level introduced by the impurity (E_d) into the CB as it is shown in Figure 1.9. When an electron moves away from a donor atom, such as arsenic, this atom becomes ionized and carries a positive charge, $+q$, as already discussed. Similarly, the introduction of an acceptor atom such as boron (B) in Silicon gives rise to a permitted energy level in the bandgap. This level is located a few meV above the top of the VB. At room temperature electrons in the top of the VB possess enough thermal energy to "jump" into the energy levels created by the impurity atoms E_a.

This way, holes in the VB are generated as it is shown in Figure 1.9. Holes are free to move in the crystal, and when an electron is captured by an acceptor atom, a hole is thus released in the crystal, and the acceptor atom (boron) becomes ionized carrying a negative charge, $-q$. It is important to notice that the total crystal must have the total charge equal to zero for neutrality. Additionally, for doped semiconductors is rationale to suppose that all impurity atoms are ionized at room temperature.

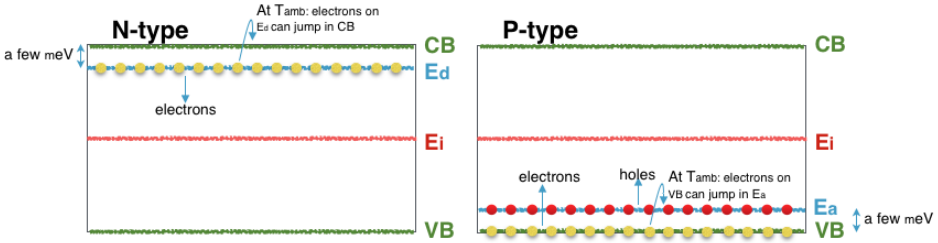

Figure 1.9: Difference in the band structures between p-type and n-type semiconductors.

This approximation is called **Depletion Approximation (DA) [12]**. Charge neutrality is explained from the following equation, for a semiconductor containing both n-type and p-type impurities:

$$n + N_a^- = p + N_d^+ \quad (1.12)$$

where n is the electron density in CB, p is the hole density in VB, N_a^- is the ionized acceptor density, and N_d^+ is the ionized donor density. Since all impurities are ionized, as it is supposed in DA, it is possible to impose $N_a^- = N_a$ and $N_d^+ = N_d$. Through further calculations, n and p can be defined as:

$$n = \frac{1}{2}\left[(N_d - N_a) + [(N_d - N_a)^2 + 4n_i^2]^{\frac{1}{2}}\right] \quad (1.13a)$$

$$p = \frac{1}{2}\left[(N_a - N_d) + [(N_d - N_a)^2 + 4n_i^2]^{\frac{1}{2}}\right] \quad (1.13b)$$

For an n-type semiconductor $(N_d \gg N_a)$ and $(N_d \gg N_i)$, the electron/hole concentrations are:

$$n \cong N_d \quad and \quad p \cong \frac{n_i^2}{N_d} \quad (1.14a)$$

For a p-type semiconductor $(N_d \ll N_a)$ and $(N_a \gg N_i)$, the electron/hole concentrations are:

$$p \cong N_a \quad and \quad n \cong \frac{n_i^2}{N_a} \qquad (1.14b)$$

Furthermore, it is possible to define the equations linking the concentration of electrons (n) or holes (p) as a function of Fermi level E_F for doped semiconductors, where E_F is different with respect to E_i of intrinsic semiconductor:

$$n = N_d = n_i e^{-\left[\frac{E_F - E_i}{K_b T}\right]} \qquad (1.15)$$

Therefore, if the electronic concentration n is known, it is easy to define E_F:

$$E_F = E_i + K_b T \ln\left(\frac{N_d}{n_i}\right) \qquad (1.16)$$

In an n-type semiconductor the Fermi level is placed in the upper half of the bandgap, above the intrinsic energy level E_i. E_F increases logarithmically with the donor atom concentration N_d. It is now possible to introduce a new variable, called Fermi potential ϕ_F, defined as it follows:

$$-q\phi_F = E_F - E_i \qquad (1.17)$$

and then the previous two equations can be written as:

$$n = n_i e^{-\left[\frac{q\phi_F}{K_b T}\right]} \quad (1.18) \quad and \quad \phi_F = -\frac{K_b T}{q} \ln\left(\frac{n}{n_i}\right) \quad (1.19)$$

Likewise, for the holes:

$$p = N_a = n_i e^{-\left[\frac{E_i - E_F}{K_b T}\right]} \quad (1.20) \quad and \quad E_F = E_i - K_b \, \mathrm{T} \ln\left(\frac{N_a}{n_i}\right) \qquad (1.21)$$

In a p-type semiconductor the Fermi level is placed in the lower half of the bandgap, below the intrinsic energy level. The Fermi level decreases as acceptor atom concentration increases, with the Fermi potential becoming:

$$p = n_i e^{\left[\frac{q\phi_F}{K_b T}\right]} \quad (1.22) \quad and \quad \phi_F = \frac{K_b T}{q} \ln\left(\frac{p}{n_i}\right) \quad (1.23)$$

Note that ϕ_F is positive in a p-type semiconductor and negative in an n-type semiconductor [12].

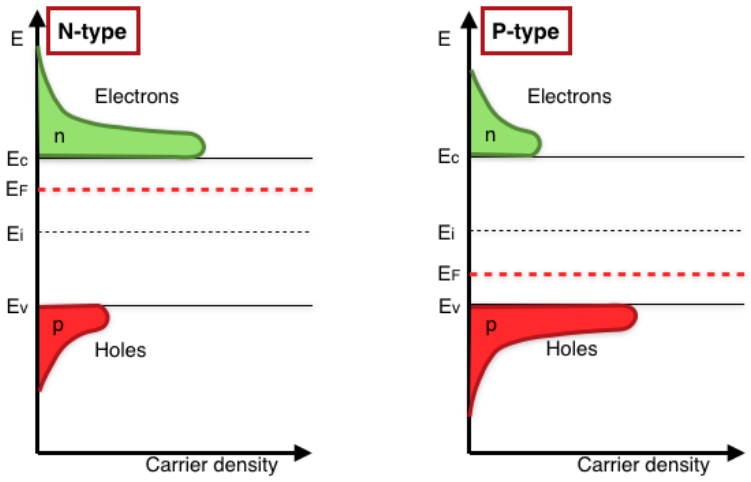

Figure 1.10: electron and hole densities in a p-type (right) and n-type (left) semiconductor. The n-type doping leads to a surplus of electrons in CB, instead the p-type doping leads to a surplus of holes in VB.

An n-type semiconductor carriers concentration is not constant in the whole material. It is variable along x $(N_d(x))$, such that $N_d(right) > N_d(left)$ and consequently $E_F(right) > E_F(left)$. An important property of the Fermi level is that, at thermodynamic equilibrium, E_F must be **unique** and **constant** through all crystal sample. This property is valid not only for non-homogeneous doped semiconductors, but also for metal-semiconductor junction and for two different semiconductors junction. Thus, being the Fermi level unique, CB, VB and intrinsic level are linked to each other through a curvature around the junction as is showed in Figure 1.11. Under **thermodynamic equilibrium** conditions, electrons are transferred from the electron-rich right part of the sample (where the Fermi level is higher) to the electron-poor left part of the sample (where the Fermi level is lower). This happens through a **diffusion process** that will be analyzed later. However, E_c, E_v and E_i remain parallel to one other, because the bandgap energy (E_{gap}) is a constant of the material.

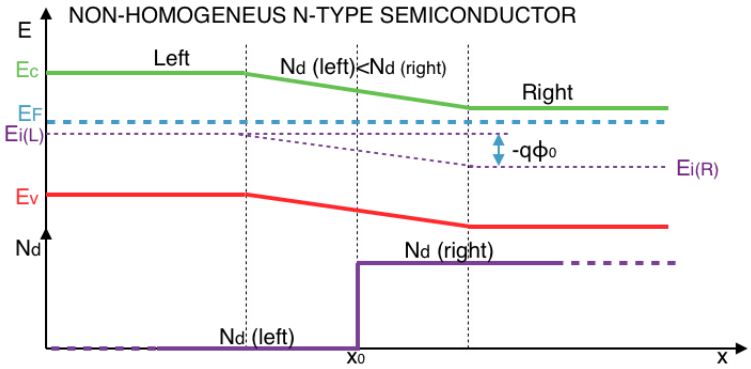

Figure 1.11: Fermi level alignment in a non-homogeneous n-type semiconductor, with consequent band bending of CB, VB and E_i (intrinsic Fermi level). The graphic below (violet) represents the concentration of donors.

The magnitude of this energy level bending reflects the presence of an internal potential (**built-in potential**) $\phi_0(x)$. If it is multiplied by $-q$, it is equal to the variation of bended energy levels. At the same time, an **electric field** is generated due to the charge imbalance into the semiconductor. Thus, in the zone near the sudden change of donor concentration, the band energies depend on x, and consequently also the carrier concentration depends on x:

$$n(x) = n_i e^{\frac{E_F - E_i(x)}{K_b T}} \qquad (1.24)$$

and taking the left side as reference:

$$n(x) = n_i e^{\frac{E_F - E_i(L) + q\phi_0(x)}{K_b T}} = n_0 e^{\frac{q\phi_0(x)}{K_b T}} \qquad (1.25a)$$

where n_0 is the electron concentration and $E_i(L)$ is the intrinsic Fermi level of the left side of the sample taken as reference. Likewise, for the holes:

$$p(x) = n_i e^{-\frac{E_F - E_i(L) + q\phi_0(x)}{K_b T}} = p_0 e^{\frac{-q\phi_0(x)}{K_b T}} \qquad (1.25b)$$

These relations are the **Boltzmann Relationships** (for electrons and holes respectively) [13].

1.1.6 – Electrons Drift, Drift and Diffusion Currents

Electrons inside a real crystal own a certain amount of thermal energy and, during their random motion, they collide with crystal defects and phonons. These elastic collisions change the electrons motion direction. If an external electric field is not applied, the average velocity of electrons (carriers in an n-type semiconductor) is equal to zero. On the other hand, when an external electric field is applied, a net **drift of electrons** in the opposite direction of the field is observed. In any case, the electrons random thermal velocity is much larger than the velocity produced by imposing an electric field [14]. To obtain a current flow in this process, the average electrons drift velocity, caused by the external electric, field must be calculated. A schematization of the phenomenon is shown in Figure 1.12.

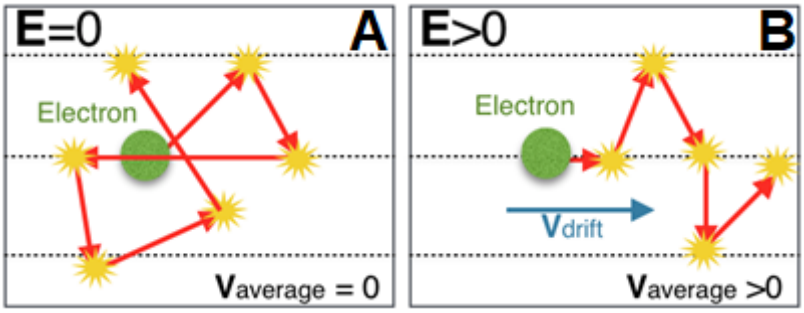

Figure 1.12: Electron velocity: A – if the electric field is equal to zero; B – if the electric field is different from zero.

To describe the motion of electrons in a crystal, two assumptions must be considered:

- Each electron in the CB moves freely in the crystal between a collision and another. The average time between two collisions is called **relaxation time** τ. In a semiconductor at room temperature, the relaxation time is of the order of $\sim 10^{-12} s$, during which the electron can travel around $10nm$.
- The electron direction after a collision is completely randomly directed, and collision events are isotropic.

The resulting number of electrons that does not have a collision from the time instant t_0 to t is:

$$n(t) = n(t_0)e^{\frac{-(t-t_0)}{\tau}} \quad (1.26)$$

Using the equation of motion for an electron with effective mass m_e^*:

$F = ma \rightarrow m_e^* \frac{dv}{dt} = -qE$. The expression of the electron drift velocity becomes the following:

$$v_{drift}(n) = -\frac{q\tau_n}{m_e^*}E = -\mu_n E \quad (1.27a) \quad with \quad \mu_n = \frac{q\tau_n}{m_e^*}, \left(\frac{cm^2}{Vs}\right) \quad (1.28a)$$

where μ_n is the **mobility** of an electron in CB. The mobility is directly proportional to the relaxation time, thus it decreases with τ, and it decreases also with the temperature, because increasing the temperature increases also the phonon amplitude, generating more collisions. Furthermore, mobility depends also from **defects and impurities** if the crystal, because the higher the concentration of defects and impurities, the higher the

probability of collision, and the lower the mobility of the electrons [14]. A similar approach can be used for holes in the VB:

$$v_{drift}(p) = -\frac{q\tau_p}{m_e^*}E = -\mu_p E \quad (1.27b) \quad with \quad \mu_p = \frac{q\tau_p}{m_e^*}, \left(\frac{cm^2}{Vs}\right) \quad (1.28b)$$

If the CB electron density is given by n and the VB hole density is p, the electron and hole **drift current density** is given respectively by:

$$J_n = -qnv_{drift}(n) = q\mu_n nE = \sigma_n E \quad (1.29a)$$

$$J_p = -qpv_{drift}(p) = q\mu_p pE = \sigma_p E \quad (1.29b)$$

where $\sigma_n \; and \; \sigma_p$ are the **conductivity** of an n-type and p-type doped semiconductor respectively. The quantity $\frac{1}{\sigma} = \rho$ is called **resistivity** of the crystal, and it depends strongly on the doping concentration. In a semiconductor, current can be produced by a concentration gradient of carriers. This type of current is called **diffusion current**. Considering a semiconductor in which, for whatever reason, there is an electron concentration gradient; electrons will diffuse from the region where their concentration is highest to the region where is lowest. The flux of electrons, F_n, resulting from the diffusion process, is directly proportional to the electron concentration gradient. It is $\frac{dn}{dx}$ in one dimension. If F_n is multiplied by –q, is equal to the diffusion current density of the electrons:

$$F_n = -D_n\frac{dn}{dx} \;\rightarrow\; J_n = -qF_n = qD_n\frac{dn}{dx} \quad (1.30a)$$

Likewise, the diffusion current for holes is:

$$F_p = -D_p\frac{dp}{dx} \;\rightarrow\; J_p = +qF_p = -qD_p\frac{dp}{dx} \quad (1.30b)$$

where $D_p \; and \; D_n$ are called **diffusion coefficients** for electrons and holes respectively, and represent the ease with which the carriers can move and diffuse in the semiconductor crystal. This situation is represented in Figure 1.13a, where is shown how electron and holes diffuse in the sample when the concentration of doping atoms is not homogeneous along x.

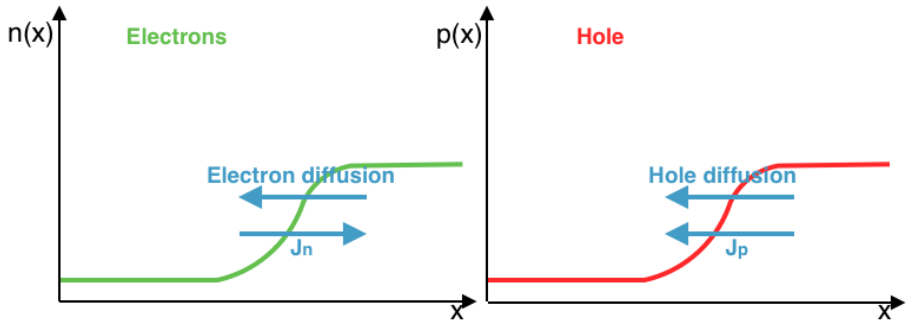

Figure 1.13a: Diffusion diagram of electrons and holes when the concentration of doping atoms $(p(x) and\ n(x))$ is not constant in the sample

The **drift-diffusion equation** in one dimension, considering that the total electron and hole currents ($J_n^{tot}\ and\ J_p^{tot}$) are given by the sum of the drift and the diffusion components, will result as:

$$J_n^{tot} = q\mu_n nE + qD_n \frac{dn}{dx} \quad (1.31a) \quad and \quad J_p^{tot} = q\mu_p pE - qD_p \frac{dp}{dx} \quad (1.31b)$$

The total density of current flowing into the semiconductor ($J_{semicond.}^{tot}$) will be:

$$J_{semicond.}^{tot} = J_n^{tot} + J_p^{tot} \quad (1.32)$$

Equation (1.32) represents the most general case where donors and acceptors impurities are both present in the semiconductor. In a semiconductor, the mobility and diffusion coefficients are related to each other. To demonstrate this, an n-type semiconductor with non-uniform donor concentration $N_d(x)$ and free carriers concentration (electrons) $n(x)$ can be considered. It is supposed that at room temperature all donors are ionized $(N_d(x) = n(x))$ as stated by the depletion approximation. The presence of an electron concentration gradient results in an electron diffusion current, with the fermions diffusing toward the left side, and leaving stationary positively charged donor atoms on the right side. The increasing of the electron concentration on the sample left side and the presence of positive charges in the right side generates a local internal electric field:

$$E_0(x) = -\frac{d\Phi_0}{dx} \quad (1.33)$$

where Φ_0 is, the potential associated to $E_0(x)$ at thermal equilibrium. $E_0(x)$ tends to draw the electrons in their place of origin as shown in Figure 1.13b).

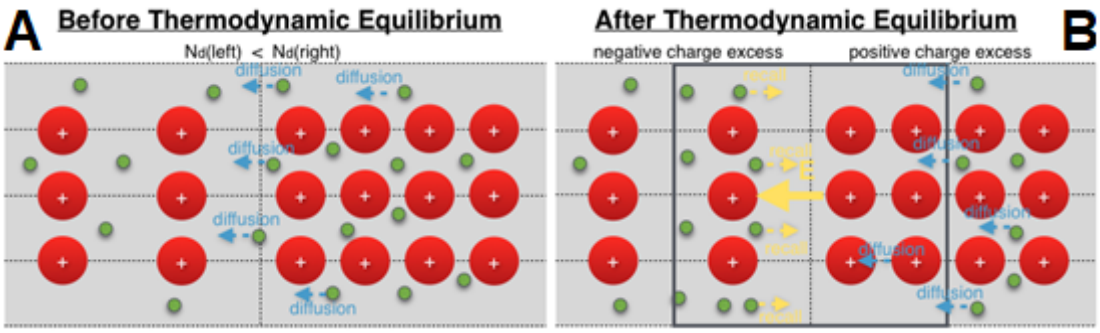

Figure 1.13b: Condition of the sample before (A) and after (B) the thermodynamic equilibrium. In the B case, the compensation between drift and electric force is verified.

With no external bias applied to the sample there is no current flowing, and the force of the internal electric field balances exactly the diffusion force. Using the drift-diffusion equation by imposing it to zero, because the system is in thermodynamic equilibrium, and making some calculations, it will result in the Einstein relationships. These express the connection between the mobility and the diffusion coefficient of electrons and holes:

$$D_n = \frac{K_b T}{q}\mu_n \quad and \quad D_p = \frac{K_b T}{q}\mu_p \qquad (1.34)$$

These two equations allow to tell that the mobility and the diffusion coefficients are practically the same thing aside for a constant [15].

1.1.7 – Quasi Fermi Levels

At thermodynamic equilibrium and in absence of applied external forces, the carrier concentrations is a function of the semiconductor internal potential Φ_0. The carrier concentrations $\left(n(x) and\, p(x)\right)$ are related to the internal potential by the Boltzmann relationships:

$$n(x) = n_i e^{\frac{E_F - E_i(L) + q\phi_0(x)}{K_b T}} \quad and \quad p(x) = n_i e^{-\frac{E_F - E_i(L) + q\phi_0(x)}{K_b T}} \qquad (1.35)$$

Those can be expressed also as:

$$n(x) = n_i e^{\frac{E_F - E_i(L)}{K_b T}} e^{\frac{q\phi_0(x)}{K_b T}} \quad and \quad p(x) = n_i e^{-\left[\frac{E_F - E_i(L)}{K_b T}\right]} e^{\frac{-q\phi_0(x)}{K_b T}} \qquad (1.36)$$

Under thermodynamic equilibrium, as shown previously, the Fermi level is unique for both electrons and holes. This does not stand under **non-equilibrium** conditions (for example

when an external bias is applied to the sample). Boltzmann relationships, however, are still valid if one introduces the notion of **quasi-Fermi levels**. Quasi-Fermi levels are also called **imaginary references (imref)** [16]. From a single Fermi level common to both types of carriers, characterizing a system at the equilibrium, let us define an **electron quasi-Fermi level**, E_{Fn}, and a **hole quasi-Fermi level**, E_{Fp}. Boltzmann relationships, in three dimensions, can be written as:

$$n(x,y,z) = n_i e^{\frac{E_{Fn}(x,y,z)-E_i(L)}{K_bT}} e^{\frac{q\phi_0(x,y,z)}{K_bT}} \quad (1.37a)$$

$$p(x,y,z) = n_i e^{-[\frac{E_{Fp}(x,y,z)-E_i(L)}{K_bT}]} e^{\frac{-q\phi_0(x,y,z)}{K_bT}} \quad (1.37b)$$

and:

$$n(x,y,z)p(x,y,z) = n_i^2 e^{\frac{E_{Fn}(x,y,z)-E_{Fp}(x,y,z)}{K_bT}} \quad (1.38)$$

Being the electron current density: $\boldsymbol{J_n} = q\mu_n n\boldsymbol{E} + qD_n\boldsymbol{\nabla}(n)$, and using the Equation (1.37a) to find $\boldsymbol{\nabla}(n)$:

$$\boldsymbol{\nabla}(n) = n_i e^{\frac{E_{Fn}(x,y,z)-E_i(L)}{K_bT}} e^{\frac{q\phi_0(x,y,z)}{K_bT}} \frac{1}{K_bT}[\boldsymbol{\nabla}(E_{Fn}) + q\nabla(\Phi_0)] =$$

$$= \frac{n}{K_bT}[\boldsymbol{\nabla}(E_{Fn}) + q\boldsymbol{\nabla}(\Phi_0)] \quad (1.39)$$

Now it is possible to define the electronic current density:

$$\boldsymbol{J_n} = q\mu_n n\boldsymbol{E} + qD_n \frac{n}{K_bT}[\boldsymbol{\nabla}(E_{Fn}) + q\boldsymbol{\nabla}(\Phi_0)] \quad (1.40)$$

and using the Einstein relationship, the final form of the current density results as:

$$\boldsymbol{J_n} = n\mu_n[\boldsymbol{\nabla}(E_{Fn})] \quad (1.41a)$$

Using the same approach for holes, the current density results as:

$$\boldsymbol{J_p} = p\mu_p[\boldsymbol{\nabla}(E_{Fp})] \quad (1.41b)$$

From the last two Equations (1.41a) and (1.41b), it is possible to deduce that electron and hole current density depend on quasi-Fermi levels and not from the internal potential Φ_0 [16]. Under thermodynamic equilibrium conditions and without external bias applied, $E_{Fp} = E_{Fn} = E_F = constant$, $n(x,y,z)p(x,y,z) = n_i^2$ and $\boldsymbol{J_n} = \boldsymbol{J_p} = 0$.

1.1.8 – PN, Metal-Semiconductor and Schottky Barrier Junctions

PN junction is formed when a p-type semiconductor is put in contact with an n-type semiconductor [17]. If the two semiconductors are made of the same material (for example silicon-silicon), this junction is called **homojunction**, instead if the two semiconductors are made by different materials (for example silicon-germanium), it will take the name of **heterojunction**. PN junctions are used to build several devices as rectifying elements for current, light-emitting diodes, laser diodes, transistors, bipolar transistors and so on. This kind of junction has the special property of allowing the current flow in a certain direction and forbids it in the other one (**rectify current**). In this paragraph, PN junction is explained in the two possible cases: in absence and in presence of an external bias V_a:

- **NO EXTERNAL BIAS V_a APPLIED**

Initially two pieces of semiconductor are separated: each semiconductor has homogeneous doping and the band structure is shown in Figure 1.14.

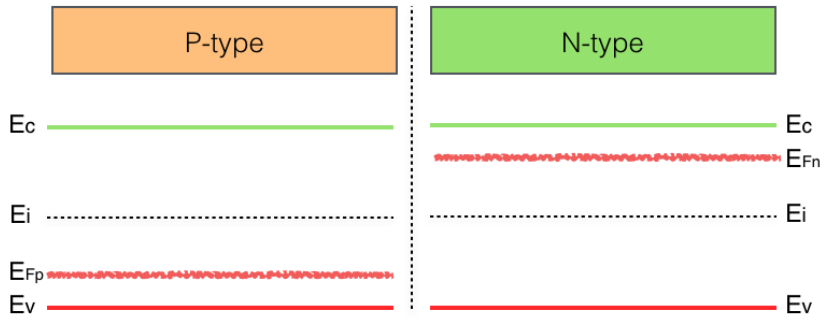

Figure 1.14: p-type and n-type semiconductors band structures. It is clear that the doping concentration is homogeneous in both.

The two semiconductors are then put in contact and a "metallurgical junction" is formed. At this point, it is obvious that the Fermi level must be unique at thermodynamic equilibrium and without applied external bias. Thus, electrons in CB diffuse from the electron rich n-type side toward the electron poor p-type side, and vice versa for holes. Because of the charge displacement, an internal built-in potential is generated (Φ_0) in the region around the junction. If this potential is multiplied by $-q$, bands curvature energy is obtained.

$$E_{Fn} - E_{Fp} = q\,\Phi_0 = K_b T \ln\left(\frac{N_d}{n_i}\right) + K_b T \ln\left(\frac{N_a}{n_i}\right) = K_b T \ln\left(\frac{N_d N_a}{n_i^2}\right) \qquad (1.42)$$

$$\Phi_0 = \frac{K_b T}{q} \ln\left(\frac{N_d N_a}{n_i^2}\right) \quad (1.43)$$

Donors, occupying substitutional sites, are fixed into the lattice, and, having lost an electron, are positively charged.

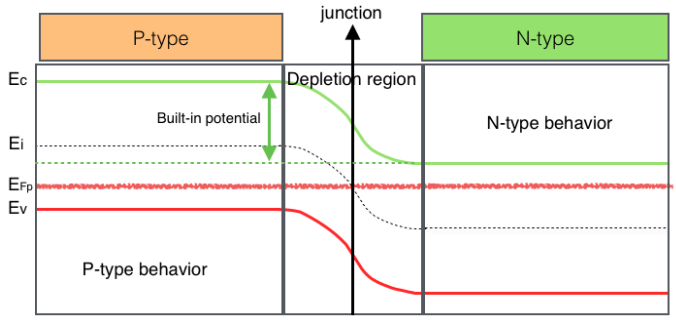

Figure 1.15a: PN junction when the thermodynamic equilibrium is reached. The central part is the depletion region and, being that the Fermi level must be unique, it is verified the band bending. Far from the junction the semiconductors behave as the junction would not be present.

This **charge unbalance** gives raise to the built-in potential, and consequently to an electric field that tries to draw diffused electrons as shown in Figures 1.15a and 1.16. The region where these positive charges are located, constitutes a space charge region called **depletion region**, because there are no moving charges as it is shown in Figure 1.15b. At the equilibrium, the force of diffusion pushing electrons into the p-type region is exactly balanced by the force of the built-in electric field that draws the electrons back into the n-type region. Similarly, the diffusion of holes from the p-type into the n-type region gives rise to a **depletion region** in the p-type material.

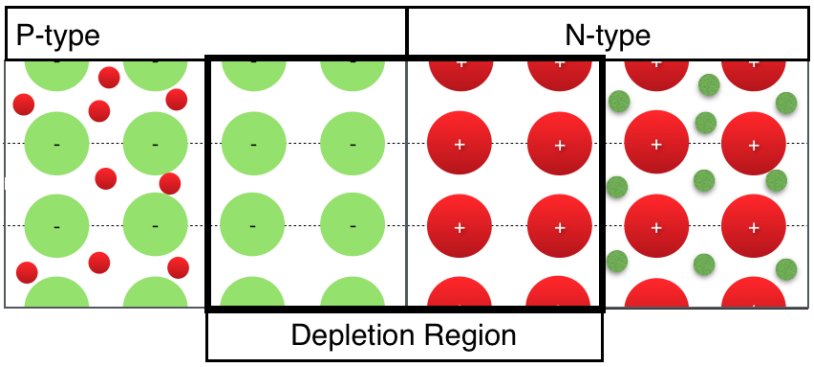

Figure 1.15b: depletion region extending around the PN junction. Moving charges are not present in this region.

This region is depleted of holes and is negatively charged, due to the presence of negatively charged acceptor ionized atoms. Depletion region is formed because, near the

junction, electrons and holes annihilate themselves leaving no moving charge in this region.

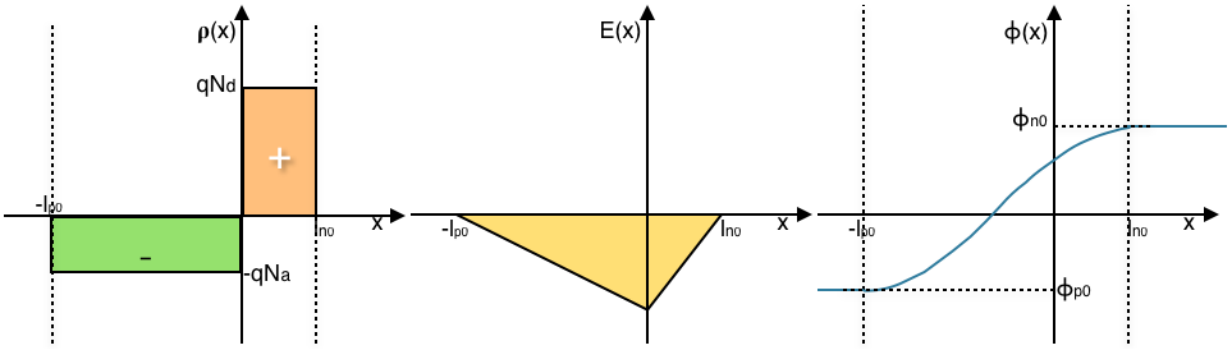

Figure 1.16: LEFT – Charge density distribution of a PN junction in thermodynamic equilibrium (in Depletion Approximation). MIDDLE – Electric field E(x) generated by the unbalance of charge density. RIGHT – Potential Φ_0 around the junction. l_{p0} is the size of depletion region for p-type semiconductors, likewise l_{n0} for n-type semiconductors.

The electric field and the potential variation in **depletion region**, shown in Figure 1.15b and 1.16, can be calculated using **Poisson equation**. For a one-dimensional junction, the problem is very simplified:

$$\frac{d^2\Phi(x)}{dx^2} = -\frac{q}{\varepsilon}(p - n + N_d^+ - N_a^-) \quad (1.44a)$$

Using Boltzmann Relationships (1.25a) and (1.25b):

$$\frac{d^2\Phi(x)}{dx^2} = -\frac{q}{\varepsilon}\left[p_0 e^{\frac{-q\Phi(x)}{K_b T}} - n_0 e^{\frac{q\Phi(x)}{K_b T}} + N_d^+ - N_a^-\right] \quad (1.44b)$$

where $N_d^+ \cong N_d$ and $N_a^+ \cong N_a$. Equation (1.44b) cannot be solved analytically, so it must be simplified by using the depletion approximation (DA), assuming that the space charge is composed only by ionized doping impurities, and the contribution of free carriers to the local charge is negligible. In other words, in DA there are not free electrons in the depletion region on the n-type side and there are not free holes in depletion region on the p-type side. As result, the charge densities in the depletion regions are equal to qN_d in the n-type material, and $-qN_a$ in the p-type material. The depletion regions extend to a distance l_{n0} on the n-type side and $-l_{p0}$ on the p-type side where the metallurgical junction is taken as the origin, as shown in Figure 1.16. After have solved the Poisson equation, the **junction potential**, the **maximum electric field** and the **width of depletion region** can be calculated. The junction potential is:

$$\Phi_0 = \Phi_{n0} - \Phi_{p0} = \frac{qN_a}{2\varepsilon} l_{p0}^2 + \frac{qN_d}{2\varepsilon} l_{n0}^2 = \frac{K_b}{q} \ln\left(\frac{N_d N_a}{n_i^2}\right) \quad (1.45).$$

The junction electric field is:

$$E_{max} = -\frac{qN_a}{\varepsilon} l_{p0} = -\frac{qN_d}{\varepsilon} l_{n0} \quad (1.46)$$

Using the relations (1.45) and (1.46), the length of depletion regions are (p-type and n-type):

$$l_{p0} = \left(\frac{2\varepsilon}{q} \frac{\Phi_0 N_d}{N_a(N_a + N_d)}\right)^{\frac{1}{2}} \quad (1.47a)$$

$$l_{n0} = \left(\frac{2\varepsilon}{q} \frac{\Phi_0 N_a}{N_d(N_a + N_d)}\right)^{\frac{1}{2}} \quad (1.47b)$$

The sum of the two depletion regions is called “transition region”, which contains both ionized acceptor and donor impurities. The width of transition region is:

$$l_{n0} + l_{p0} = \left(\frac{2\varepsilon}{q} \frac{\Phi_0 (N_a + N_d)}{(N_a N_d)}\right)^{\frac{1}{2}} \quad (1.48)$$

Actual PN junctions are strongly asymmetrical, which means that one side is doped much more heavily than the other. Consider for example $N_a \ll N_d$; in this case, it is obtained:

$$l_{p0} = \left(\frac{2\varepsilon}{q} \frac{\Phi_0}{(N_a)}\right)^{\frac{1}{2}} \gg l_{n0} = \left(\frac{2\varepsilon}{q} \frac{\Phi_0 N_a}{(N_d^2)}\right)^{\frac{1}{2}} \quad (1.49)$$

and therefore:

$$l_{n0} + l_{p0} \cong l_{p0} \quad (1.50)$$

The equations (1.49) and (1.50) state that if a junction is strongly asymmetrical, the width of the transition region is virtually equal to the width of the depletion region with the lowest doping concentration. It is important to notice that the built-in potential $\Phi(x)$ acts as a barrier, preventing the diffusion of electrons into the p-type region and holes into n-type region when thermodynamic equilibrium has been established. Φ_0 is practically the potential barrier that carriers must overcome.

- **AN EXTERNAL BIAS V_a IS APPLIED TO THE PN JUNCTION**

Now the internal potential becomes:

$$\Phi = \Phi_n - \Phi_p = \Phi_0 - \mathrm{V}_a \quad (1.51)$$

If the Poisson equation is solved by substituting l_{n0}, l_{p0} and Φ_0 with l_n, l_p and $\Phi_0 - \mathrm{V}_a$ respectively, the result is:

$$l_p = \left(\frac{2\varepsilon}{q}\frac{(\Phi_0 - \mathrm{V}_a)N_d}{N_a(N_a + N_d)}\right)^{\frac{1}{2}} \quad (1.52a)$$

$$l_n = \left(\frac{2\varepsilon}{q}\frac{(\Phi_0 - \mathrm{V}_a)N_a}{N_d(N_a + N_d)}\right)^{\frac{1}{2}} \quad (1.52b)$$

and thus:

$$l_n + l_p = \left(\frac{2\varepsilon}{q}\frac{(\Phi_0 - V_a)(N_a + N_d)}{(N_a N_d)}\right)^{\frac{1}{2}} \quad (1.53)$$

This is the transition region width, which increases when a **reverse bias** is applied $(V_a < 0)$. In this case, also the potential around the junction increases. Transition region width and potential decrease, instead, when a **forward bias** is applied $(V_a > 0)$, as shown in Figure 1.17. Thus, only when a forward bias is applied the current flows. This is the reason why the built-in potential Φ_0 decrease thanks to V_a. The **total potential** acting at the junction in forward bias is $\Phi_0 - V_a$. With the consequent decrease of the potential barrier, the carriers can overcome it and carry current [17]. The behavior of the PN junction under forward bias is represented in Figure 1.17.

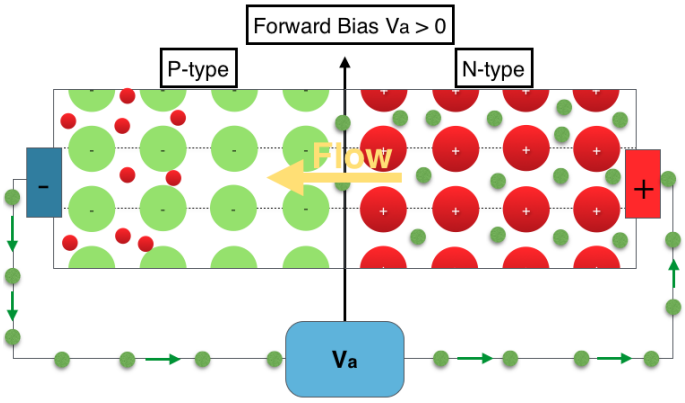

Figure 1.17: PN Junction scheme under forward bias. The electrons are forced to enter in the n-type semiconductor (from right) and then the potential barrier decreases and the current can flow from n-type to p-type.

Consider an n-type **semiconductor** crystal and a **metal** initially separated: thanks to the **photoelectric effect**, it is known that electrons can be extracted from a metal in vacuum when light with a proper wavelength is shone onto the metal. To observe this effect, the wavelength of the incident light must have a higher energy than a given critical value. In other words, the photons must carry enough energy to extract electrons from the metal, ejecting them into the vacuum. This energy $E_{ex} = h\nu$ must be at least equal to the **work function** $q\Phi_m$ of the metal. The work function is therefore defined as the energy that must be added to the electron energy (the metal Fermi level E_{Fm}) to eject the fermion from the metal in the vacuum. Similarly, the work function of the semiconductor is the energy required to extract an electron located at its Fermi level, E_{Fsc}. The energy band diagrams of these two materials are shown in Figure 1.18.

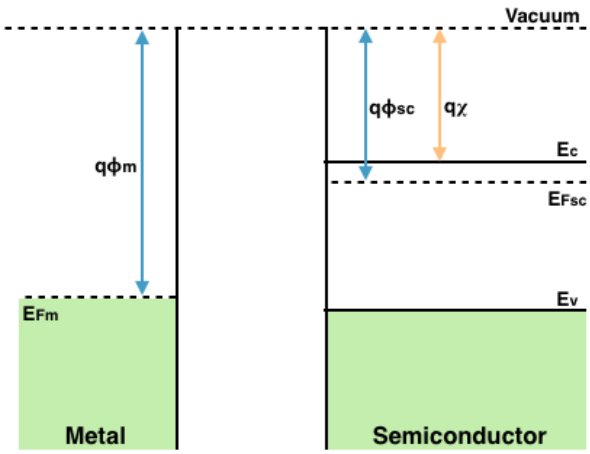

Figure 1.18: energy band diagram of a metal, on the left, and an n-type semiconductor, on the right, separated between them. $q\Phi_m$ is the work function of the metal, $q\Phi_{sc}$ is the work function of the semiconductor and $q\chi$ is the semiconductor electron affinity.

Electron affinity $q\chi$ is the energy required to extract an electron from the CB of the semiconductor to the vacuum. To introduce it, the case in which the metal Fermi level E_{Fm} is lower than that of an n-type semiconductor E_{Fsc} is treated: $E_{Fm} < E_{Fsc}$. When the metal is put in contact with the semiconductor, the Fermi levels align and thermodynamic equilibrium is established through the transfer of electrons from the semiconductor conduction band into the metal. The phenomenon happens because it is energetically convenient ($E_c > E_{Fm}$). Transferred electrons leave positively charged donor impurity atoms in the semiconductor. Consequentially, a **space-charged region,** corresponding to the zone depleted of electrons, is formed in the semiconductor side, near the interface with the metal. The width of this depletion region is called W_0. A negative charge, equal in magnitude to the depletion donor charge, appears on the metal side, at the metal-semiconductor interface. For all practical purposes, this charge can be considered infinitely thin. Such charge distribution is often called a **charge layer**. Because of the alignment of the Fermi levels and the presence of a depletion region, the **semiconductor band curvature** is equal to:

$$qV_i = q(\Phi_m - \Phi_{sc}) \quad (1.54)$$

This curvature is substantially a potential barrier V_i, which, at the thermodynamic equilibrium, prevents further electron migrations into the metal. On the other hand, electrons in the metal see a **potential barrier** of amplitude Φ_b:

$$q\Phi_b = q(\Phi_m - \chi) = qV_i + (E_c - E_F) \quad (1.55)$$

as it sees in Figure 1.19.

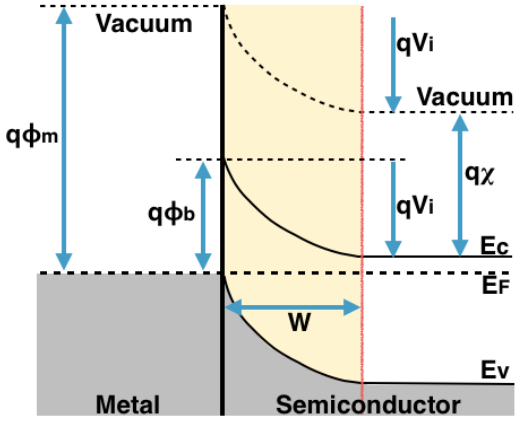

Figure 1.19: Energy band diagram for a metal-semiconductor junction when the thermodynamic equilibrium is reached.

Figure 1.19 shows that, since E_F must be unique at thermodynamic equilibrium, the energy bands of the n-type semiconductor are bended downward, and qV_i is the built-in potential generated by the unbalance of charge due to the junction. W is the width of the depletion zone in the semiconductor. At room temperature, this potential barrier Φ_b is significantly larger than $\frac{K_b T}{q}$ and only a few electrons possess sufficient energy to overcome it. The current, resulting from migrating electrons from the semiconductor to the metal, overcoming the barrier, is $I_{m\to s}$. The notation used is this one because electrons carry a negative charge. At thermodynamic equilibrium, and in absence of an external bias applied, the current $I_{m\to s}$ is exactly balanced by the electron current flowing from the metal into the semiconductor, called $I_{s\to m}$. Thus, at the equilibrium, it will result:

$$I_{s\to m} = -I_{m\to s} \quad (1.56)$$

If a forward bias $(V_a > 0)$ is applied (+ on the metal side and – on the semiconductor side) the potential barrier in the semiconductor side is decreased from V_i to $V_i - V_a$ as it is shown in Figure 1.20A. Thus, a great number of electrons can now flow from the semiconductor into the metal. On the other hand, the flow of electrons from the metal into the semiconductor, $I_{s\to m}$, remains constant because the potential barrier seen from the metal side, Φ_b, is unchanged. Thus, a net flow of electrons is observed from the semiconductor to the metal. If a reverse bias $(V_a < 0)$ is applied to the system (+ on the semiconductor side, and – on the metal side), the potential barrier in the semiconductor is increased from V_i to $V_i - V_a$, as it is shown in Figure 1.20B. The result is that the electron flow from the semiconductor into the metal $I_{m\to s}$ is reduced, while $I_{s\to m}$ remains unchanged. So, only a **small reverse electron current** (from the metal into the semiconductor) is observed [18].

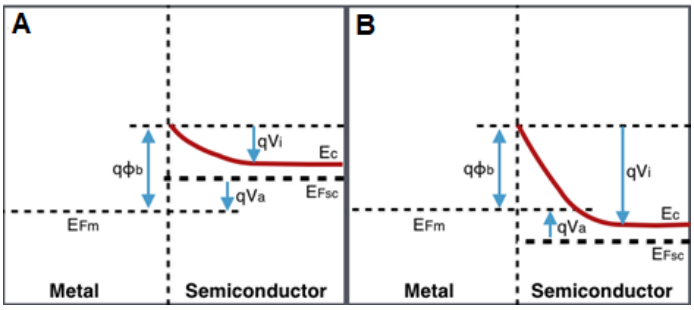

Figure 1.20: Metal-semiconductor junction band diagrams under an external bias: A – Forward bias case; B – Reverse bias case.

The potential generated around the bias is called **Schottky Barrier**.

1.1.9 – Current-Voltage Characteristics

Electrons overcome the potential barrier between the metal and the semiconductor through a quantum-mechanical process called **thermionic emission**. This process is activated by the thermal energy of the electrons. Although the potential barrier is clearly larger than K_bT/q at room temperature, a non-zero probability that some electrons pick up energy enough to overcome the barrier exists. There is also another effect that allows electrons to overcome the barrier, called **tunnel effect or tunneling**. Tunneling is a purely quantum effect, where an electron, hitting against a potential barrier with energy E minor of the barrier energy, has a small non-zero probability to transmit itself over the barrier. Tunneling gives a non-negligible contribution to the current, but this topic will be discussed later in paragraph 1.1.16. When a forward bias V_a is applied to the system, the potential barrier that the electrons must overcame to transit from the semiconductor to the metal is equal to $\Phi_b - V_a$. The resulting **thermionic emission** current is given by:

$$I_{m\to s} = AR^*T^2e^{-\frac{q(\Phi_b - V_a)}{K_bT}} \quad (1.57)$$

where R^* is called the **Richardson constant** and is equal to $\frac{4\pi m_e q k^2}{h^3}$, and A is the **junction area**. Using the fact that, if $V_a = 0$, $I_{m\to s} = -I_{s\to m}$ and $I_{s\to m}$ is constant and independent from the applied voltage:

$$I_{s\to m} = -AR^*T^2e^{-\frac{q(\Phi_b)}{K_bT}} \quad (1.58)$$

Since the net current in the junction is equal to $I_{m\to s} + I_{s\to m}$, the expression of the current as function of the applied voltage is:

$$I = AR^*T^2e^{-\frac{q(\Phi_b)}{K_bT}}\left(e^{\frac{qV_a}{K_bT}} - 1\right) \quad (1.59)$$

The Equation (1.59) shows that the current, flowing through the junction, depends on both the temperature and the height of the potential barrier between metal and semiconductor [19]. A mathematical derivation of the Equation (1.59) is performed in the Paragraph 1.1.15

1.1.10 – Surface states

At the external surface of a real crystal, there is a sudden interruption of the regular reticular structure. This gives birth to mechanisms of rearrangement in the crystal structure, which produces an increasing reactivity of superficial atoms or ions with respect to those of the **bulk.** There is essentially a perturbation that acts on the periodicity of the lattice on the surface; this perturbation is strong enough to create new localized electronic energy states, named **intrinsic**. Most of the metal oxide semiconductors are ionic compounds. Superficial ions are not coupled to the corresponding ion of opposite charge: metallic cations attract electrons acting as acceptors, while oxygen anions give up electrons acting as donors. The unpaired electron represents an orbital, partially extended outside the surface of the semiconductor.

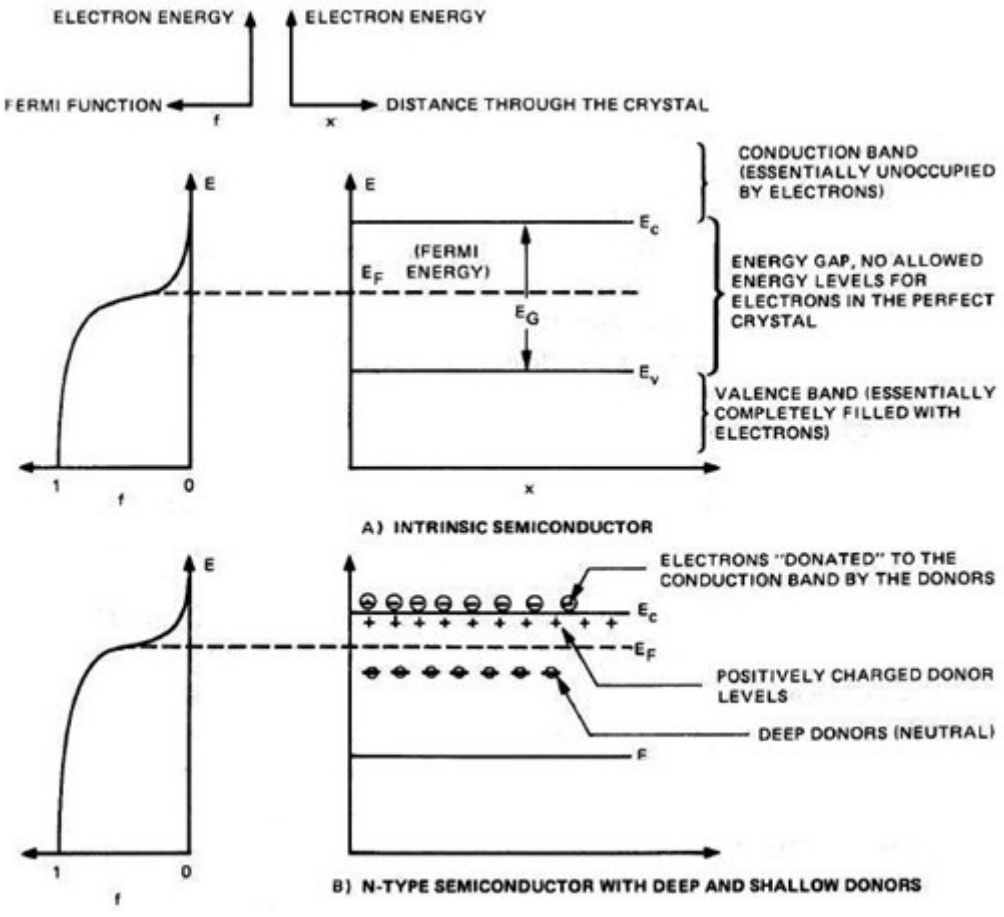

Figure 1.21: Fermi function and band diagram for an intrinsic (A) and an extrinsic (B) semiconductor [163].

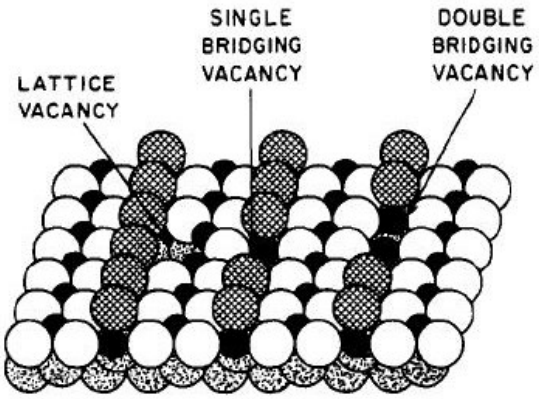

Figure 1.22: Example of surface defects for a surface of TiO_2 [163].

In a similar situation, the unpaired electron can capture another electron in order to form a pair, or it can enter the **bulk** of the crystal freeing a surface state. At this point it is easy to understand why at the surface there are both acceptors that donors, as shown in the band model of surface states in Figure 1.23 (for simplicity here is illustrated the case of "flat band").

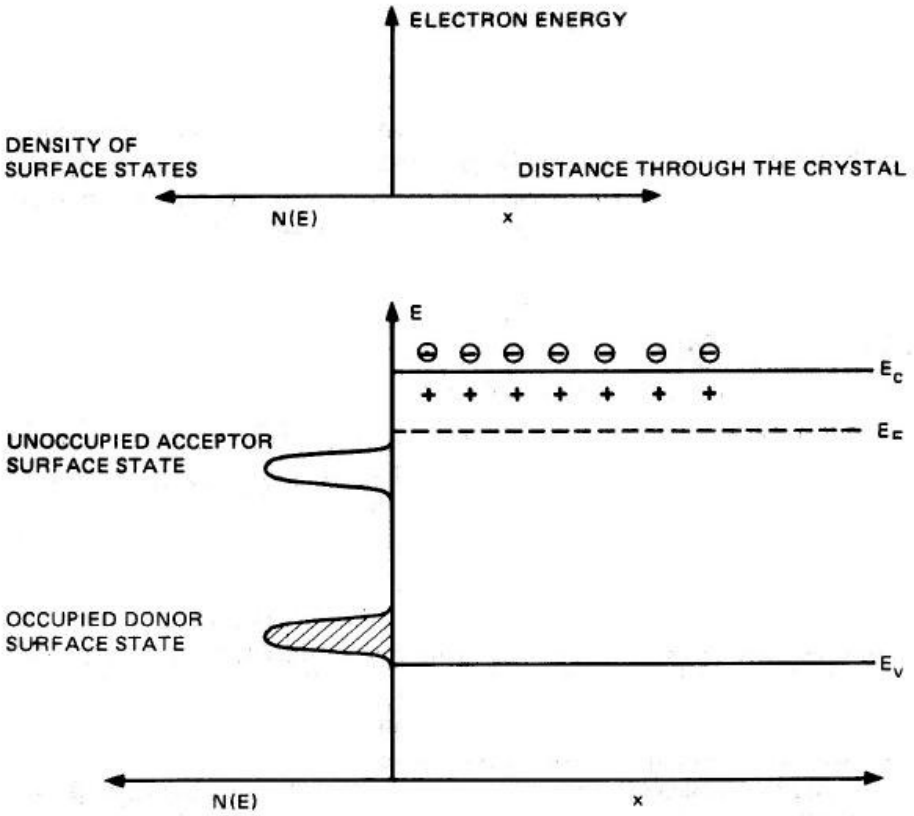

Figure 1.23: Neutral surface states in an n-type semiconductor: donors are occupied while acceptors are not. In the schematic representation, energy bands are represented for simplicity as a single level [163].

1.1.11 – Double layer

It is easily guessable that the "flat band" configuration is far from equilibrium. Electrons in the **CB** are characterized by a higher energy level than that of superficial acceptors (Figure 1.23). When acceptor states are totally empty, while donors totally filled, the E_F should necessary be in an intermediate position. As a consequence, the electrochemical potential of electrons inside surface states is smaller than the electrochemical potential which characterizes the **CB**, and electrons here tend to migrate towards surfaces states, in order to minimize the energy of the system. This phenomenon leads to the formation of an accumulation layer of surface charge, balanced by the charge of donor ions located inside the **bulk**.

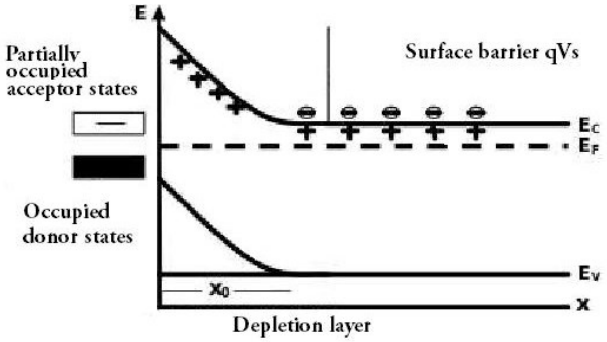

Figure 1.24: Double layer. Electrons in the conduction band are captured from surface states, creating a negative surface which contrasts the presence of positive charged donors just below it [163].

Figure 1.24 represents schematically the charge migration of donor ions towards an n-type semiconductor. There is the formation of the so called "double layer", consisting of positively charged donor ions which acts as a spatial charge, located at one side and, on the other side, of negatively charged states displaced on a plane. So the relative electric field arises in the external region. Now it can be introduced the concept of **depletion layer**, a region in which the only uncompensated charges present are donors, with a density $N_i = N_d - N_a$ (where N_d and N_a are respectively the density of donors and acceptors). All mobile carriers inside the depletion layer are inevitably led to migrate towards the surface. Figure 1.25 represents intuitively the effects of absorption of oxidizing chemical species on the surface of the semiconductor grain: the contribution to the formation of a superficial charged layer is responsible for the creation of an intergranular potential barrier that electrons must overcome to cross multiple grains.

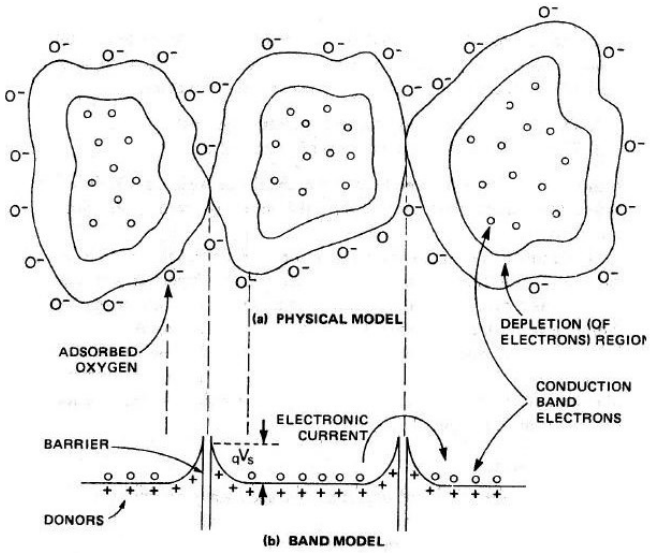

Figure 1.25: Potential barrier between grains [163].

1.1.12 – Limits of Planar Geometry, 3D Geometry Approach

In the previous sections the "Schottky Barrier" was discussed, but it is generally contextualized in the field of DA in planar geometry. In the case in which the average radius of the semiconductor grain is comparable to the width of the **depletion layer**, curvature effects start to be relevant. In order to describe curvature effects, the Poisson equation in spherical coordinates can be written as:

$$\frac{1}{r}\frac{d^2}{dr^2}[r\phi(r)] = -\frac{qN_d}{\epsilon} \quad (1.60)$$

where N_d is the density of donors (supposed to be totally ionized at the working temperature) and ϵ is the absolute permittivity of the material.

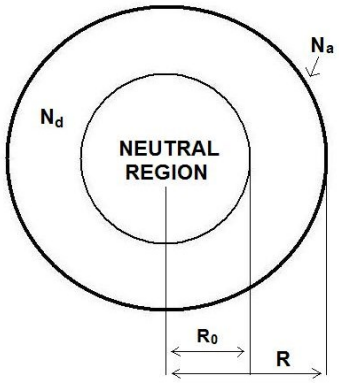

Figure 1.26: Semiconductor grain. N_a is the acceptor density on the surface and N_d donor density in the depletion layer [163].

Referring to the Figure 1.26, R is the grain radius and R_0 is the radius of the internal neutral region. For the DA, the density of charge is qN_d in the region of thickness $R - R_0$ and zero otherwise. Then, the potential $\Phi(r)$ is zero at $r = R_0$ and if $r \leq R_0$ also the electric field is zero. It follows that the width $R - R_0$ represents both the thickness of the *depletion region* and the extinction length of the potential. The difference between the value of the potential at the center of the grain and the value of the potential at the surface is named **built-in-potential (V)**, while the right boundary conditions to impose at the Poisson Equation in spherical geometry 1.60 are:

$$[\phi(r)]_{R_0} = 0 \quad (1.61)$$

$$\nabla\phi(r)|_{R_0} = 0 \quad (1.62)$$

The analytical solution for the electric potential is:

$$\phi(r) = -\frac{qN_d}{6\epsilon}r^2 - \frac{qN_d}{3\epsilon}\frac{R_0^3}{r} + \frac{qN_d}{2\epsilon}R_0^2 \quad (1.63)$$

for $R_0 \leq r \leq R$ and zero otherwise. The passage to the spherical geometry generates in the Equation 1.63, an hyperbolic term of coulomb nature. This term becomes relevant in the limit $R_0 \to 0$. In fact, in the DA for planar geometry, the expression for the potential shows only the parabolic term but not the hyperbolic one. If the grain is globally neutral, the density of surface charge qN_a exactly compensates the spatial charge in the depletion region and the following relation becomes valid:

$$N_a = N_d\left(\frac{R}{3} - \frac{R_0^3}{3R^2}\right) \quad (1.64)$$

Although the model described is of spherical nature it is still based on the DA. However, when the dimension of the grain becomes lower than a limit value, this approximation gets inadequate. In this case, the expression which correctly express the density of charge of an n-type semiconductor is:

$$\rho(r) = qN_d\left(1 - e^{\frac{q\phi(r)}{k_bT}}\right) \quad (1.65)$$

where the exponential term represents the contribution given by mobile charge carriers at a temperature higher than the absolute zero. In particular the charge density qN_d, calculated in the hypothesis of DA, is obtainable from the expression 1.65, considering the energy (and so the potential) to be zero at the value E_{CBB} (**Conduction Band Bottom**) of the bulk. In the case of nanostructured powder, the E_{CBB} level is reachable only in the case in which the grain is sufficiently big, whereas using the DA it is implicitly assumed that the potential has to be zero independently from the dimensions of the grain. In the case of non-applicability of the DA, the Poisson equation in spherical geometry becomes:

$$\frac{1}{r}\frac{d^2}{dr^2}[r\phi(r)] = \frac{qN_d}{\epsilon}\left(e^{\frac{q\phi(r)}{k_bT}} - 1\right) \quad (1.66)$$

In this case, the boundary conditions are different from the constraints (Equations 1.61 and 1.62) implied in the DA. In fact, the spherical symmetry requires that, at the center of the grain, the electric field is zero, whereas the potential $\phi(r)$ is zero at the CBB only if the grain is sufficiently large. It is also necessary to modify the Equation 1.65 of the charge density ρ. The potential at surface $\phi(R)$, if referred to that of CBB, assumes a value independent on R and uniquely determined by working conditions (the type of semiconductor, the type of doping, the temperature and environmental conditions). Being the surface potential, Vs, easily measurable, the boundary condition to be used for the Equation 1.66 is:

$$\phi(R) = -V_s \quad (1.67)$$

Analogously to what happened in the regime of the DA it is necessary to impose the neutrality of the grain: the integral of the density of charge extended to the total volume of the grain must be equal to the integral of the density of surface states N_a, assumed to be uniform over the entire surface:

$$4\pi\int_0^R \left[qN_d\left(1 - e^{\frac{q\phi(r)}{k_bT}}\right)\right] r^2 dr = 4\pi R^2 qN_a \quad (1.68)$$

Hence, the system of equations that defines the model based on the correct density of charge $\rho(r)$ is:

$$\frac{1}{r}\frac{d^2}{dr^2}[r\phi(r)] = \frac{qN_d}{\epsilon}\left(e^{\frac{q\phi(r)}{k_bT}} - 1\right) \quad (1.69)$$

$$-\frac{d\phi(r)}{dr}\Big|_{r=0} = 0 \quad (1.70)$$

$$\phi(r)|_{r=R} = -V_s \quad (1.71)$$

$$-\frac{d\phi(r)}{dr}\Big|_{r=R} = \frac{qN_a}{\epsilon} \quad (1.72)$$

where the Equation 1.72 follows from the neutrality condition 1.68. The model presents the unknown function $\phi(r)$ as dependent on six parameters $(T, \epsilon, V_s, N_d, N_a, R)$. N_d and ϵ are characteristic and measurable values of the semiconductor, while the temperature T is known. Therefore, after setting these three parameters, the value of V_s is influenced only by the working atmosphere of the sensor, and it can therefore be determined through a particular procedure of measurement of the conductance, named *Arrhenius plot*. This measure must be performed in conjunction with a slow variation of the working temperature of the sensor itself. Once established the type of semiconductor material and known the surrounding atmosphere, it becomes possible to calculate the potential $\phi(r)$ and the density of surface states N_a as functions of the grain radius R only. For example the experimental data relative to SnO_2 in air can be considered ($T = 400°C, \epsilon = 10^{-10}\frac{F}{m}, N_d = 5 \cdot 10^{18} cm^{-3}, V_s = 0.68V$), and it is so possible to numerically solve the Equation 1.69. If generally $R > \Lambda$, the potential $\phi(r)$ becomes zero at a distance $\Lambda \simeq 8\lambda_D \simeq 22nm$ from the surface (with $\lambda_D = 2.7nm$ *Debye length*). In the Figure 1.29 are shown the two numerical solutions of the equation 1.69 for $R = 100nm$ and $R = 30nm$. In the first case $R \gg \Lambda \gg \lambda_d$ and the DA in planar geometry is sufficient to well describe the situation; in the second case $R \simeq \Lambda \gg \lambda_d$ and the planar approach is no longer valid even if the DA is still useful.

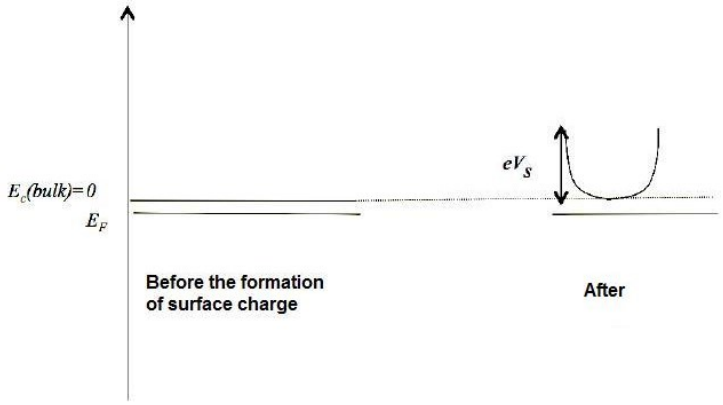

Figure 1.27: Representation of the band bending for the case in which $R > \Lambda$.

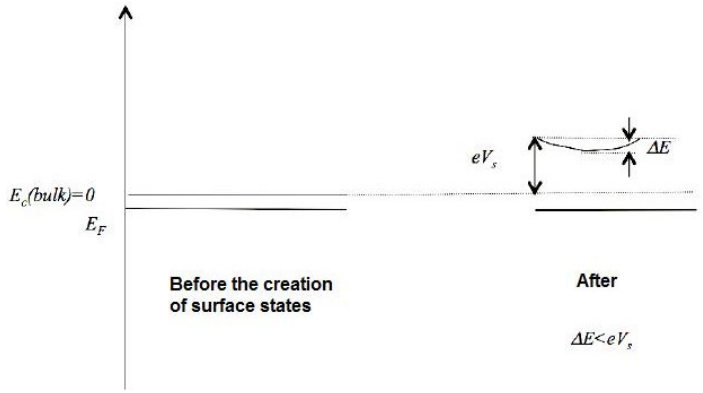

Figure 1.28: Representation of the band bending for the case in which $R < \Lambda$. It is possible to note from the figure that, after the formation of the surface charge N_s, follows a substantial flattening of the band bending between the surface and the center of the grain, smaller than the barrier eV_S [163].

However, as soon as R became less then Λ, the potential would non to be able to cancel, even at the center of the grain: in this case the DA would no longer be valid. Here, the model based on the complete charge density $\rho(r)$ is preferable because it has not intrinsic limitations and it can be used for a wide range of values for the grain radius. In Figure 1.30 it is shown the limiting case for which $R = 10nm$ and the potential cannot extinguish.

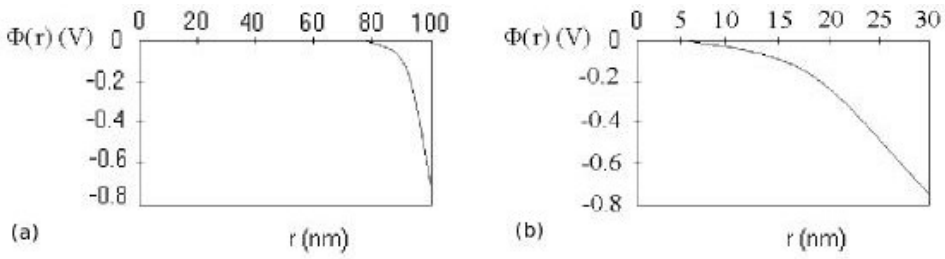

Figure 1.29: Functional form of the potential $\phi(r)$ for $R = 100nm$ (a) and $R = 30nm$ (b). In both the situations the potential becomes zero at a distance $\Lambda = 22\text{nm}$ from the surface [163].

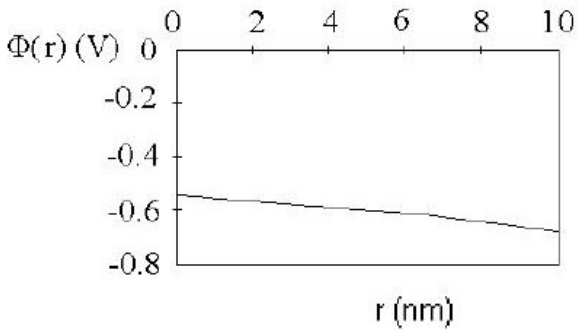

Figure 1.30: Functional form of the potential $\phi(r)$ for $R = 10nm$. The potential does not vanish even in the center of the grain and the behavior is quite constant, differing from that predicted by DA [163].

Sensors used in this work consist in **films** made of semiconductor **nanograins** (n-type or p-type). At this point, it is required to switch from a planar to 3D spherical geometry, suitable to describe grains, considering the semiconductor **spherical grains** having radius R (es. n-type) in contact with each other. It is assumed that the depletion approximation (DA) still stands for this approach. When the grain radius becomes comparable with the size of the depletion region, curvature effects begin to be relevant and new considerations must be taken into account. For symmetry reasons is better to face the problem in **spherical coordinates [20]**, because the grains shape, that usually is rather irregular, is defined approximatively spherical. The Figure 1.31 shows two grains in contact, and the quantities of interest, used in the following discussion.

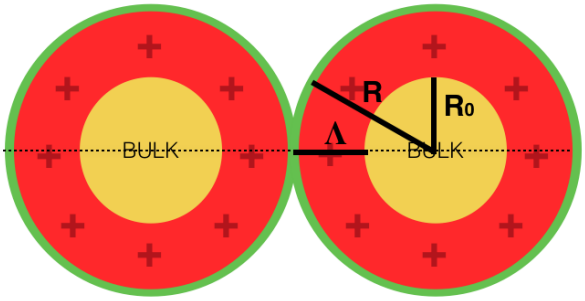

Figure 1.31: Two grains in contact, with R_0 = bulk radius, R = grain radius, $\Lambda = R - R_0$ = depletion region width, In the region $r \leq R_0$, the electric field E and the electric potential ϕ are equal to 0.

Considering first the case with $\Lambda < R$ ($bulk\ is\ present$ ($no\ charge\ density$): $r \leq R_0$):

Converting the Poisson equation in polar coordinates, it results:

$$\frac{1}{r}\frac{d^2[r\phi(r)]}{dr^2} = \frac{-qN_d}{\varepsilon} \qquad (1.73)$$

where N_d is the concentration of donor atoms (it recalls that in DA they are totally ionized) and ε is the absolute dielectric constant of the material. The potential $\phi(r)$ and the electric field E are equal to 0 for $r \leq R_0$, and the difference of potential between the grain center and the surface is a **built-in potential** (i.e. a potential raised by an internal unbalance of charge). The Boundary conditions to find a unique solution for the Poisson equation are:

$$A)\ \frac{d\phi}{dr}|_{r=R_0} = 0 \quad and \quad B)\ \phi|_{r=R_0} = 0 \quad (1.74)$$

The Poisson equation (1.73), discussed previously, must be integrated one time to find the electric field, resulting in:

$$\frac{d[r\phi(r)]}{dr} = \frac{-qN_d}{2\varepsilon} r^2 + A \quad (1.75)$$

If the Poisson equation is integrated a second time, the potential becomes a function of r, the radius of the spherical grain, starting from the center:

$$\phi(r) = \frac{-qN_d}{6\varepsilon} r^2 + A + \frac{B}{r} \quad (1.76)$$

This relation for the potential contains two undefined constants A and B originated from the integrations. To define them, the two boundary conditions (1.74) must be imposed. Thus, a univocal expression for the potential is found. After these calculations, the final expression of the potential as function of r is the relation written as follows:

$$\phi(r) = \frac{-qN_d}{6\varepsilon} r^2 + \frac{qN_d R_0^2}{2\varepsilon} - \frac{qN_d R_0^3}{3\varepsilon r} \quad (1.77)$$

The final equation for the potential (1.77) is built by three terms (as it sees on the right hand): the first term is parabolic and has the same form of the planar case, where only a parabolic term was present. The second term is a constant and has no physical meaning. The third term has hyperbolic shape and is the real news of the spherical 3D model with respect to the planar one. At this point, the grain charge neutrality condition must be introduced:

$$N_d V_{dep} = N_s A_{surface} \quad (1.78)$$

where N_d is the density of donor atoms in the depletion region, V_{dep} is the volume of the depletion region, N_s is the density of surface states, $A_{surface}$ is the surface of the grain. The extended neutrality condition applied to the 3D symmetry is:

$$qN_d\left(\frac{4}{3}\pi R^3 - \frac{4}{3}\pi R_0^3\right) = qN_s(4\pi R^2) \quad (1.79)$$

Now, the potential at the grain surface can be calculated:

$$\phi(r)|_{r=R} = \phi(R) = -V_s \quad (1.80)$$

Finally, two quantities are found:

$$V_s = -\phi(R) = \frac{qN_d}{2\varepsilon}\Lambda^2\left(1 - \frac{2\Lambda}{3R}\right) \quad (1.81)$$

$$N_s = \Lambda N_d\left(1 - \frac{\Lambda}{R} + \frac{\Lambda^2}{3R^2}\right) \quad (1.82)$$

where V_s is the potential at the surface ($r = R$), N_s is the density of surface states, Λ is the width of the depletion region, N_d is the concentration of donor atoms, ε is the dielectric constant of the material, R is the grain radius. At this point, it is possible to draw some important conclusions contained in equations (1.81) and (1.82), allowing to understand deeper some dynamics of the system [20]:

a) **If $\boldsymbol{\Lambda << R}$** (**there is a clear distinction between bulk and depletion zone**), the result obtained is comparable with the result from the Schottky model of planar junction.

b) **If $\boldsymbol{\Lambda \rightarrow R}$ (no bulk case), $\boldsymbol{V_s}$ and $\boldsymbol{N_s}$ are $\boldsymbol{\frac{1}{3}}$ of the value that they had in the planar case.** It results $N_s(grain) = \frac{1}{3}\Lambda N_d$. This means that, in the 3D spherical case, to neutralize the depletion region charge only $\frac{1}{3}$ of the N_s states necessary for the planar case are needed.

Thus, assuming $\boldsymbol{\Lambda \equiv R}$, smaller is the size of the grain Λ, smaller is N_s, smaller is V_s, and greater is the current that generates response.

1.1.13 – Conductivity and Sensor Response

Previously, the density of electrons in CB was calculated:

$$n(x) = N_c e^{\frac{E_F - E_c}{K_b T}} = N_d e^{\frac{q\phi(x)}{K_b T}} \quad (1.83)$$

Now, a new quantity $\boldsymbol{n_{surf}}$ is introduced**,** which represents the **fraction of electrons in CB that manages to reach the grain surface** and crosses the potential barrier V_s:

$$n_{surf} = N_d e^{\frac{-qV_s}{K_b T}} \quad (1.84)$$

If the system is not perturbed from an external bias, the Fermi Level E_F is flat and no current flows. If the system instead is perturbed by an external bias, Fermi Level E_F become a **Quasi-Fermi Level** E_{Fn}, and a current can flow. An electric field $E = \frac{1}{q}\frac{\partial E_{Fn}}{\partial x}$ is generated in one dimension, because the Quasi-Fermi Level is curved, and varies with respect to x. The current and the conductivity will become:

$$\boldsymbol{J}_n = n\mu_n \frac{\partial E_{Fn}}{\partial x} = n_{surf}\mu_n q\boldsymbol{E} = N_d e^{\frac{-qV_s}{K_b T}}\mu_n q\boldsymbol{E} = \sigma\boldsymbol{E} \quad (1.85\text{A})$$

$$\sigma = N_d e^{\frac{-qV_s}{K_b T}}\mu_n q \quad (1.85B)$$

where σ is the **conductivity of the material**, and μ_n is the **mobility of electrons** in an n-type semiconductor. At this point, if the conductivity is multiplied by the **junction geometry** (length and size of the contacts), the **conductance G** is obtained:

$$G = G_0 e^{\frac{-qV_s}{K_b T}} \quad (1.86)$$

Conductance (1.86) depends from temperature and potential barrier height (greater is the temperature, greater is the conductance; smaller is V_s, greater is the flowing current).

The **response R(t)** of a sensor is the variation of G in percentage:

$$R(t) = \frac{G_{gas} - G_{air}}{G_{air}} = \frac{G_{gas}}{G_{air}} - 1 \propto e^{\frac{-q(V_{gas} - V_{air})}{K_b T}} \quad (1.87)$$

Where G_{gas} is the conductance of the sensor in presence of a certain gas and G_{air} is the conductance of the sensor in air (synthetic, or pumped from the environment; in both

cases, it plays the role of carrier and background of the mixture analyzed). Qualitatively, the response is proportional to the exponential of the difference between the barrier height while the material is exposed to the gas and in clean air. A graphic representation of the conductance and response is shown below, in Figure 1.32. Zone 1 represents the situation in which the reaction with gas produces an increase of the flowing current and consequentially of the response, while zone 2 represents the plateau (stabilization) of the response.

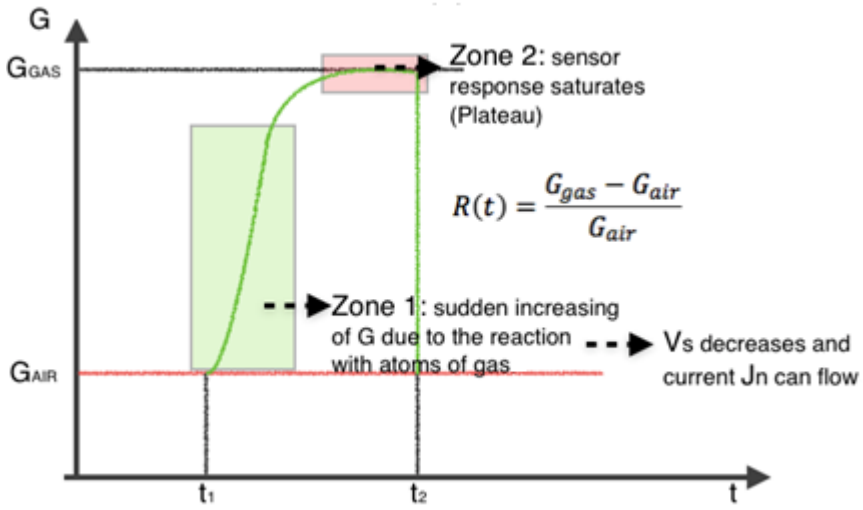

Figure 1.32: Variation curve of the conductance G when a sensor, previously left in air, detects a certain reducing gas. This curve can lead to the response through the formula expressing $R(t)$.

Now lets consider a grain of semiconductor:

- **If** $\boldsymbol{\Lambda \equiv R}$, the bulk disappears; only a negative charge distribution remains, generated by the electrons on the surface of the grain and the positive charge density, due to the donors inside the grain. This situation is shown below in Figure 1.33.
- **If the size of the grain** $(\boldsymbol{\Lambda \to 0})$ **is reduced further,** a new effect is observed, the **flattening of the band bending.** In this limit, the depletion approximation fails because the potential does not reach the zero value at the grain center [21].

1.1.14 – Failure of the Depletion Approximation

The **flattening of the band bending** consists in the flattening upward of the conduction band between grains, as shown in Figure 1.33. As consequence, the variation of energy

$\Delta E_c = E^c_{max} - E^c_{min}$ decreases, where E^c_{max} is the maximum energy of the CB, coinciding with the surface energy, and E^c_{min} is the minimum energy of the CB. If the grain is big enough to contain a bulk region, E^c_{min} is the bulk CB energy; if the gain size decreases enough, the bulk disappear, flattening of the band bending occurs, and E^c_{min} will be greater than before. In the small grain, showed on the right of the Figure 1.33, the potential in the middle does not manage to reach the value zero as it would have happened if the bulk existed.

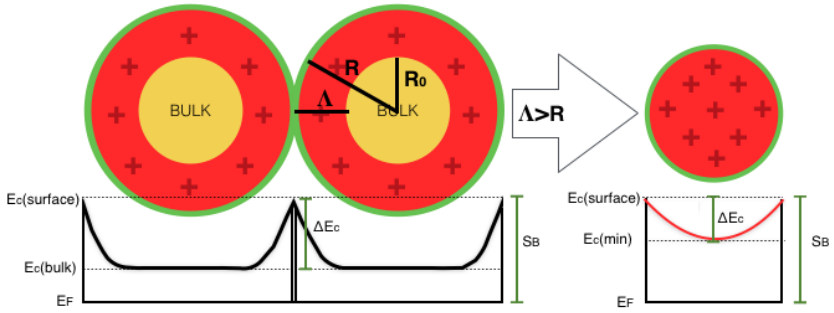

Figure 1.33: Changing of ΔE_c due to the flattening of the band bending effect. The grains on the left have a bulk region $(\Lambda < R)$, while the grain on the right does not $(\Lambda > R)$.

In the small grain, showed on the right of the Figure 1.33, the potential in the center does not vanish as it would happen if the bulk exists, because the grain is not large enough to allow the complete extinction of the potential. Thus, if grains are small enough:

$$\Delta E_c = E_{c\,surface} - E_{c\,center} \ll qV_s. \quad (1.88)$$

With these boundaries, $\Lambda \equiv R \; and \; \Lambda \to 0$, **the failure of the depletion approximation** is observed. In these conditions, it is correct to consider the real charge density without approximations. Thus, the 3D spherical Poisson equation became:

$$\frac{1}{r}\frac{d^2[r\phi(r)]}{dr^2} = \frac{\rho}{\varepsilon} = -\frac{qN_d}{\varepsilon} + \frac{qN_d}{\varepsilon}e^{\frac{q\phi}{K_bT}} \quad (1.89A)$$

In the Equation (1.89A), charge density appears in the following expression:

$$\rho = -qN_d + qN_d e^{\frac{q\phi}{K_bT}} \quad (1.89B)$$

To solve uniquely the differential Equation (1.89A), **three boundary conditions are required**. The first two are the following:

$$1)\; \phi(r)|_{r=R} = \phi(R) = -V_s \quad (1.90A)$$

$$2) -\frac{d\phi}{dr}|_{r=0} = 0 \qquad (1.90B)$$

The first boundary condition states that on the surface potential is equal to V_s. The second one states that, in the grain center, the tangent to the conduction energy band is parallel to the x axes (as deducible from the Figure 1.33). The boundary condition used to solve the Poisson equation in depletion approximation, $\phi|_{r=0} = 0$ is no more available, because the potential does not vanish at the grain center. Furthermore, the grain neutralization relation is different with respect to DA, and defines the third boundary condition to solve uniquely (1.89A):

$$\int_V \rho d^3r = \int_l \left(\frac{qN_d}{\varepsilon} - \frac{qN_d e^{\frac{q\phi}{K_b T}}}{\varepsilon}\right) 4\pi r^2 dr = \int_{surf} \frac{q}{\varepsilon} N_s d^2r = \frac{q}{\varepsilon} N_s 4\pi R^2 \quad (1.91)$$

In Equation (1.91), the exact expression for the charge density is used. After some calculations, the relation representing the third boundary condition is obtained:

$$-\frac{d\phi}{dr}|_{r=R} = \frac{q}{\varepsilon} N_s \quad (1.92)$$

This model reflects that the unknown potential $\phi(r)$ is function of six parameters:

- T, usually known
- N_d and ε, that are measurable properties of the material
- N_s and R.
- V_s, that after have set N_d, N_s and R, is influenced only from the working environment of the sensor.

Therefore, V_s can be determined through a procedure of measurements of the conductance, called Arrhenius Plot. This procedure is made in conjunction with a slow variation of the sensor working temperature, and knowing the type of semiconductor material and the surrounding atmosphere, it is possible to determine the potential $\phi(r)$ and the density of surface states N_s as functions of the grain radius R [20].

EXAMPLE SnO_2 in air:

SnO_2 metal-oxide in air; $T = 400°C$; $\varepsilon = 10^{-10}\ \frac{F}{m}$; $N_d = 5 \cdot 10^{18} cm^{-3}$ and $V_s = 0.68\,V$. With these values, it is possible to solve numerically Poisson equation. If $R \gg \Lambda$, the potential

$\phi(r)$ becomes zero at a distance $\Lambda \approx 8\lambda_d \approx 22nm$ from the surface, where $\lambda_d = 2.7nm$ is the **Debye Length.** In Figure 1.33 are shown two numerical solutions of the Poisson equation:

1. $R \gg \Lambda \gg \lambda_d$; the DA in planar geometry is sufficient to well describe the system
2. $R \cong \Lambda \gg \lambda_d$; the planar approach is no longer valid even if the DA is still useful

where in the first case the bulk is wide and occupies almost the total volume of the grain, while on the second the bulk begins to disappear and the potential is zero only in the grain center. This case represents the system close to its critical size [20].

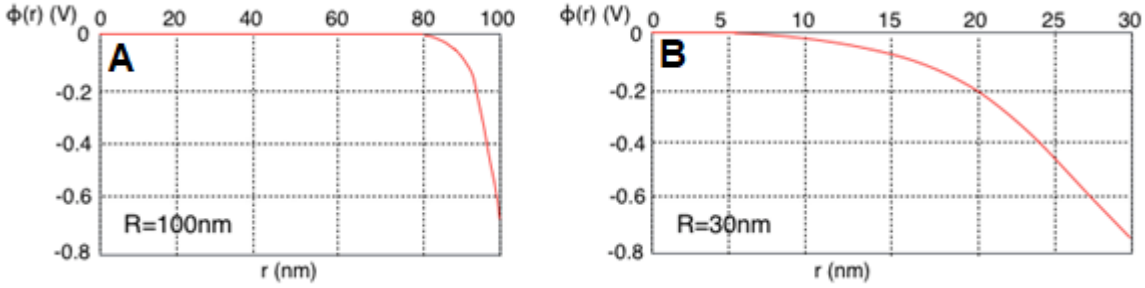

Figure 1.34: Behavior of the potential $\phi(r)$ as function of the grain radius R. A – $\mathrm{R} \gg \Lambda \gg \lambda_\mathrm{d}$ case (grain with $R = 100nm$); the potential is equal to zero about at $22nm$ from the surface of the grain. B – $\mathrm{R} \cong \Lambda \gg \lambda_\mathrm{d}$ case (grain with $R = 30nm$); the potential is equal to zero practically at the center of the grain.

Figure 1.35 shows the behavior of the potential in a grain of $R = 10\ nm$. Here the potential is almost constant in all grain volume and never vanishes at the center of the grain.

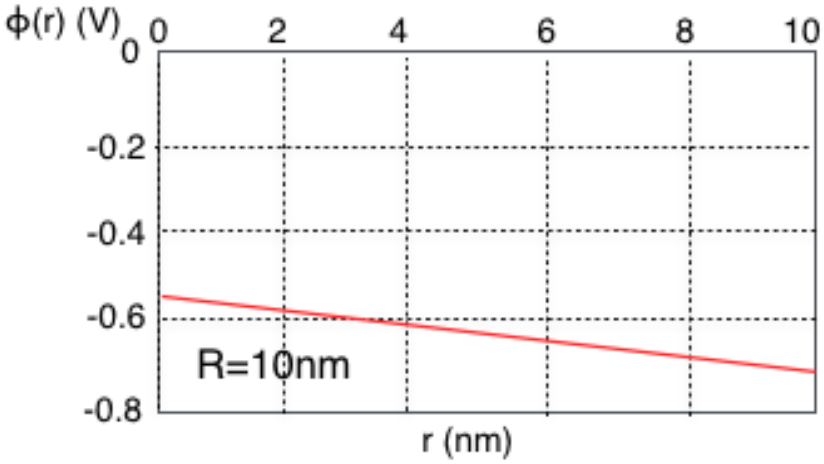

Figure 1.35: behavior of the potential $\phi(\mathrm{r})$ in a grain with radius $R = 10nm$. The potential does not manage to vanish in the center of the grain and remains different from zero.

1.1.15 – Tunneling Effect Contribution and Thermionic Current

Classically, when a particle is thrown toward a potential barrier, if its energy (E_p) is higher than the max energy of the potential (qV), the particle passes certainly over the potential barrier with probability 1, while if the particle has an energy smaller than that of the potential barrier, it bounces back and cannot cross the barrier. In quantum mechanics, if a particle is thrown against a potential barrier with energy smaller than that of the potential barrier itself ($E_p < qV$), there is a small yet different from zero probability that the particle could be transmitted over the barrier as shown in Figure 1.36 in a very simplified way. This is called tunnel effect or tunneling, a purely quantum mechanical effect [22].

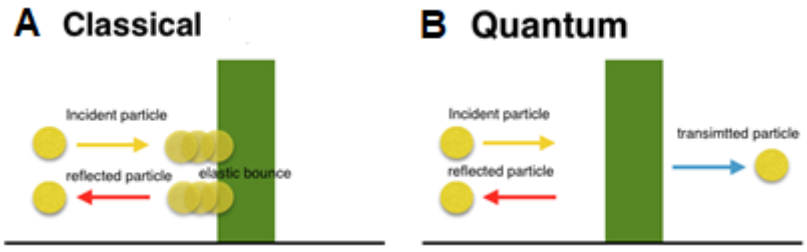

Figure 1.36: Difference between probabilities of particle transmission over a potential barrier: A – Classical approach. B – Quantum physics approach.

This effect takes place because a particle, in quantum mechanics, is seen as a propagating wave packet (simplified as a plain wave) and not as a small solid particle. Consistently with what was said before, an electron is supposed to be represented by a plain wave:

$$\psi(x) = Ae^{ikx} \quad (1.93)$$

In this case, the potential barrier is the double **Schottky Barrier** generated by two adjacent grains, as discussed in Paragraph 1.1.14, and represented in Figure 1.37.

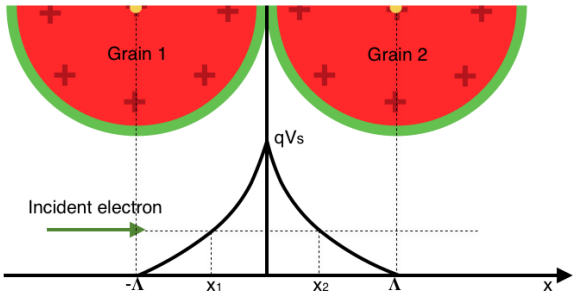

Figure 1.37: Double Schottky Barrier generated in correspondence of the junction between two grains. The electron that hits the barrier in x_1 can overcome it, thanks to the tunneling effect.

$$qV(x) = \begin{cases} \frac{qV_s}{\Lambda^2}(x+\Lambda)^2 & x \leq 0 \\ \frac{qV_s}{\Lambda^2}(x-\Lambda)^2 & x \geq 0 \end{cases} \quad (1.94)$$

and:

$$V_s = \frac{qN_d}{2\varepsilon}\Lambda^2 \quad (1.95)$$

An electron with energy $E < qV_s$ with respect to CB impinges the barrier in x_1 and, tunneling the barrier, exits in x_2. If $E < qV_s$, k (**wave vector** of the plain wave representing the electron) must be imaginary ($k = i\beta$), where β is a real number such that:

$$\beta = \sqrt{\frac{2m}{h^2}(qV(x) - E)} \quad (1.96)$$

$$\psi(x) \propto e^{-\beta x} \quad (1.97)$$

Through some calculations, it is possible to find the **transmission coefficient** T of the wave over the barrier, defined substantially as the probability possessed by the particle to pass through the potential barrier [23].

In WKB approximation (semiclassical approximation):

$$T(E) = e^{-2\int_{x_1}^{x_2}\beta(x)dx} = e^{-2\int_{x_1}^{x_2}\sqrt{\frac{2m}{h^2}(qV(x)-E)}dx} \quad (1.98)$$

Now, using the conditions shown in the System of Equations (1.94), the integral is divided in two parts Equation (1.99):

$$T(E) = \mathrm{e}^{\left\{-2\left(\frac{2m}{h^2}\right)^{\frac{1}{2}}\left[\int_{x_1}^{0}\left(\frac{qV_s}{\Lambda^2}(x+\Lambda)^2-E\right)^{\frac{1}{2}}dx+\int_{0}^{x_2}\left(\frac{qV_s}{\Lambda^2}(x-\Lambda)^2-E\right)^{\frac{1}{2}}dx\right]\right\}} \quad (1.99)$$

Furthermore, they are inserted in the integration extremes as functions of Λ *and* E:

$$V(x_1) = E = \frac{qV_s}{\Lambda^2}(x_1+\Lambda)^2 \quad (1.100A)$$

$$V(x_2) = E = \frac{qV_s}{\Lambda^2}(x_2-\Lambda)^2 \quad (1.100B)$$

and then:

$$x_1 = -\Lambda\left[1-\left(\frac{E}{qV_s}\right)^{\frac{1}{2}}\right] \quad (1.101A)$$

$$x_2 = \Lambda\left[1-\left(\frac{E}{qV_s}\right)^{\frac{1}{2}}\right] \quad (1.101B)$$

Now the problem is reduced to solve two integrals, S_1 and S_2, such that:

$$S_1 = \int_{-\Lambda\left[1-\left(\frac{E}{qV_s}\right)^{\frac{1}{2}}\right]}^{0}\left(\frac{qV_s}{\Lambda^2}(x+\Lambda)^2 - E\right)^{\frac{1}{2}}dx \quad (1.102A)$$

$$S_2 = \int_{0}^{\Lambda\left[1-\left(\frac{E}{qV_s}\right)^{\frac{1}{2}}\right]}\left(\frac{qV_s}{\Lambda^2}(x-\Lambda)^2 - E\right)^{\frac{1}{2}}dx \quad (1.102B)$$

Then, when $S_1\ and\ S_2$ are solved, it is clear that $S_1 = S_2$, and by performing $S_1 + S_2$, it results:

$$S_1 + S_2 = 2\frac{\sqrt{qV_s}}{\Lambda}\int_{\Lambda\left(\frac{E}{qV_s}\right)^{\frac{1}{2}}}^{\Lambda}\left(\mu^2 - \frac{E}{qV_s}\Lambda^2\right)^{\frac{1}{2}}d\mu \quad (1.103)$$

where $\mu = \Lambda - x$. This integral can be transformed using the following relation:

$$\int (x^2-a^2)^{1/2}dx = \frac{x}{2}(x^2-a^2)^{1/2} - \frac{a^2}{2}\ln\left[x + (x^2-a^2)^{\frac{1}{2}}\right] \quad (1.104)$$

and then:

$$S_1 + S_2 = \Lambda\sqrt{qV_s}\left\{\left(1-\frac{E}{qV_s}\right)^{\frac{1}{2}} - \frac{E}{qV_s}\ln\left[\frac{1+\left(1-\frac{E}{qV_s}\right)^{\frac{1}{2}}}{\left(\frac{E}{qV_s}\right)^{\frac{1}{2}}}\right]\right\} \quad (1.105)$$

Thereby, $T(E)$ is:

$$T(E) = e^{-2\left(\frac{2m}{h^2}\right)^{\frac{1}{2}}(S_1+S_2)} \quad (1.106)$$

At this point, it is defined:

$$\alpha = \frac{E}{qV_s} \quad (1.107A) \quad and \quad E_{00} = \frac{qh}{2}\left(\frac{N_d}{m\varepsilon}\right)^{\frac{1}{2}} \quad (1.107B)$$

and remembering from Equation 1.95 that:

$$\Lambda = \sqrt{\frac{2\varepsilon V_s}{qN_d}} \quad (1.108)$$

$T(E)$ can be rewritten as follows:

$$T(E) = e^{-2\frac{qV_s}{E_{00}}y(a)} \quad (1.109)$$

where:

$$y(a) = (1-\alpha)^{\frac{1}{2}} - \alpha \ln\left[\frac{1+(1-\alpha)^{\frac{1}{2}}}{(\alpha)^{\frac{1}{2}}}\right] \quad (1.110)$$

At the end of this calculation, the electron probability of tunneling, with respect to the CB bottom with energy E_{00}, is found. The flat band density of current (if no barrier must be overcome) is:

$$J_m = R^* T^2 e^{-\frac{(E_c-E_F)}{K_d T}} \quad (1.111)$$

where R^* is the Richardson constant. Thermionic current density was already derived previously. The total current density (the sum of the currents in the two cases: if the energy of the particle is smaller than the potential barrier, and if it is higher than the energy of the potential barrier) is given by the integration of the tunneling probability with the distribution of electrons at a certain energy:

$$J_{tot} = \frac{R^* T}{K_b}\int_0^{\infty} T(E)\, e^{-\frac{(E+E_c-E_F)}{K_d T}} dE \quad (1.112)$$

Normalizing J_{tot} with respect to the flat band current density, J_a, a dimensionless quantity is obtained. J_a represents a "background current", generated without barrier. Then J_{tot}/J_a represents uniquely the contribution of the barrier to the current. Two contributions are expected into J_{tot}/J_a: one from the tunneling phenomenon (for $0 < E(particle) < qV_s$) and one from the thermionic current (for $qV_s < E(particle) < \infty$).

It then results that:

$$\frac{J_{tot}}{J_a} = \frac{1}{K_b T}\int_0^{\infty} T(E)\, e^{-\frac{(E)}{K_d T}} dE = \frac{1}{K_b T}\int_0^{qV_s} T(E)\, e^{-\frac{(E)}{K_d T}} dE + \frac{1}{K_b T}\int_{qV_s}^{\infty} e^{-\frac{(E)}{K_d T}} dE \quad (1.113)$$

In the second integral $T(E) = 1$, because for $qV_s < E(particle) < \infty$ the particle has probability 1 to overcome the potential barrier. Equation (1.113) is formed by two pieces: The first, I_1, is the tunneling contribution, and the second, I_2, is the thermionic contribution (as already discussed, I_2 corresponds to the case where $E(particle) > qV_s$, and consequently $T(E) = 1$) such that:

$$I_1 = \frac{1}{K_b T}\int_0^{qV_s} e^{-2\frac{qV_s}{E_{00}} y(a)}\, e^{-\frac{(E)}{K_d T}} dE \quad (1.114A)$$

$$I_2 = \frac{1}{K_b T}\int_{qV_s}^{\infty} e^{-\frac{(E)}{K_d T}} dE = e^{-\frac{qV_s}{K_d T}} \quad (1.114B)$$

Integral 1 can be rearranged recalling equation (1.107A). It is possible to perform a variable substitution ($dE = qV_s d\alpha$) and after the integration it becomes:

$$I_1 = \frac{qV_s}{K_b T}\int_0^{1} e^{-\frac{qV_s}{K_d T}\left[\frac{2K_d T y(\alpha)}{E_{00}} + \alpha\right]} d\alpha \quad (1.115)$$

Inserting experimental values in the equations (1.115), it turns out that the tunneling contribution has the same order of magnitude of the thermionic one, in the cases with working temperatures of interest.

$$n_s = N_d e^{\frac{E_F - E_0 + E_0 - E_c}{K_b T}} = n_0 e^{-\frac{\Delta E}{K_b T}} \quad (1.116)$$

where $n_0 = N_c e^{\frac{E_F - E_0}{K_b T}}$.

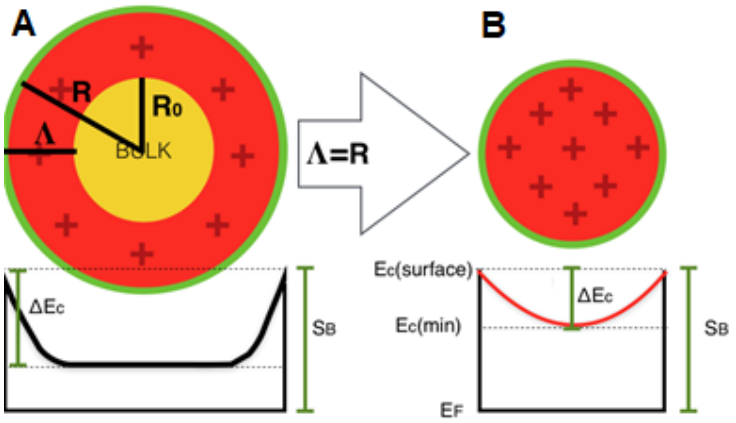

Figure 1.38: Flattening of the band bending resulting from the decrease of the radius in the case $R = \Lambda$. In this scheme is clear that the ΔE decreases with the decrease of the radius of the grain, while the Schottky Barrier remains the same.

The thermionic contribution is independent from R because:

A. $\Delta E = qV_s$ and $n_0 = N_d$
B. $\Delta E \ll qV_s$ and $n_0 \ll N_d$

so, n_s remains the same if the Schottky Barrier is constant.

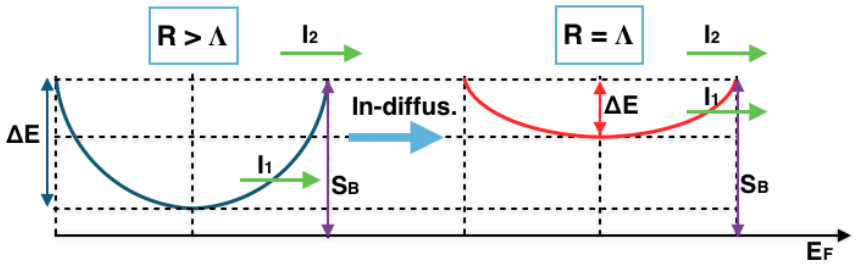

Figure 1.39: Contributions of I_1 and I_2 to the total current in the two cases: 1) $R > \Lambda$; 2) $R = \Lambda$.

Thus, the **thermionic contribution** to the total current is unvaried, because the Schottky Barrier does not change with the decrease of the radius of the grain, and so the thermionic contribution is not dependent on the radius R of the grain. The **tunneling contribution**, instead, is reduced with the decrease of the grain radius R. This happens because the barrier ΔE becomes smaller and smaller with the decrease of grain radius, as shown in Figure 1.39. This last observation justifies the slow increment in resistance after the surface equilibrium is reached [23]. The first current rectifying device is made by a semiconductor and a metal put in contact. Rectifying properties are due to a potential barrier, called Schottky Barrier, that exists at the contact zone. First, it must be considered that the boundaries between an n-type semiconductor and the vacuum. This way it is possible to understand very easily why the potential barrier appears. The electric potential

of the electrons is smaller in the crystal than in the vacuum, because the electrons are attracted by the positive donor ions of the crystal lattice. The energy difference $E_c - E_{vacuum}$ between the bottom of CB and the vacuum energy is called electron affinity (X_{so}); so, if an electron has an energy equal or major than $E_c + X_{so}$, it can leave the crystal. Now, the flux of electrons leaving the crystal can be calculated, supposing that electrons, into the crystal, have a Maxwell-Boltzmann energy distribution:

$$f(E_n) = e^{\frac{E_F - E_n}{KT}} \quad (1.117)$$

where E_n is the energy of the electron and E_F is the Fermi energy. From Equation 1.117, the velocity distribution for electrons in the crystal $(f(v_n))$ can be calculated.

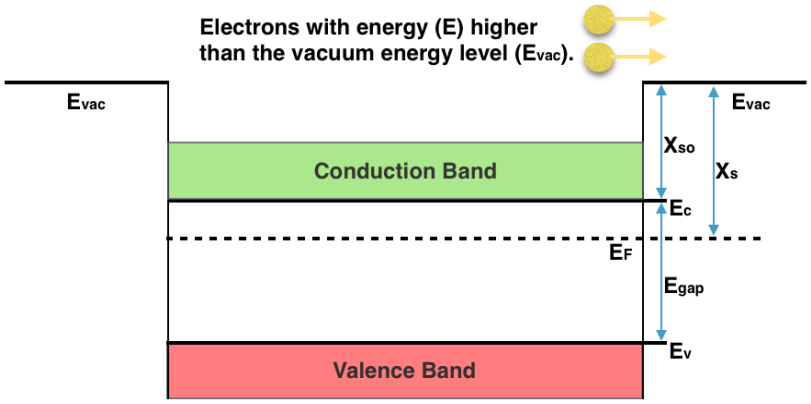

Figure 1.40: Electrons band diagram on a semiconductor. If an electron has energy higher than X_s, it can leave the crystal and propagate in the vacuum.

It is chosen, for simplicity, $E_c = 0$, so that $E = \frac{m(v_x^2+v_y^2+v_z^2)}{2}$, and then:

$$f(v_n) = A_v e^{-\frac{m(v_x^2+v_y^2+v_z^2)}{2K_bT}} \quad (1.118)$$

where $A_v = \left[\frac{m}{2\pi K_b T}\right]^{\frac{3}{2}}$ is a normalization constant:, obtained by solving the following triple integral:

$$\int_{-\infty}^{+\infty}\int_{-\infty}^{+\infty}\int_{-\infty}^{+\infty} f(v_n)\, dv_x dv_y dv_z = 1. \quad (1.119)$$

Then the velocity distribution becomes:

$$f(v_n) = \left[\frac{m}{2\pi K_b T}\right]^{\frac{3}{2}} e^{-\frac{m\left(v_x^2+v_y^2+v_z^2\right)}{2K_b T}} \quad (1.120A)$$

This last equation can be written in another, more general, way:

$$f(v_n) = f(v_x)f\left(v_y\right)f(v_z) \quad (1.120B)$$

Where $f(v_x), f\left(v_y\right)$ and $f(v_z)$ are the distribution functions for velocity components x, y and z respectively:

$$f(v_x) = \left[\frac{m}{2\pi KT}\right]^{\frac{1}{2}} e^{-\frac{m\left(v_x^2\right)}{2KT}} \quad (1.121A)$$

$$f\left(v_y\right) = \left[\frac{m}{2\pi KT}\right]^{\frac{1}{2}} e^{-\frac{m\left(v_y^2\right)}{2KT}} \quad (1.121B)$$

$$f(v_z) = \left[\frac{m}{2\pi KT}\right]^{\frac{1}{2}} e^{-\frac{m\left(v_z^2\right)}{2KT}} \quad (1.121C)$$

Now, it is possible to find the average velocity along x (direction perpendicular to the interface), that is the direction of the current:

$$< v_x >= \int_0^{\infty} v_x f(v_x) dv_x \quad (1.122)$$

After inserting the Equation (1.121C) in the Equation (1.122), and after performing the integral, it is found the average electron thermal velocity:

$$< v >= \left[\frac{8KT}{\pi m}\right]^{\frac{1}{2}} \quad (1.123)$$

then the electron current density, corresponding to the flux of electrons out of the crystal in the positive direction x, can be calculated as it follows:

$$J_s = q\int_{vacuum}^{\infty} v_x \left(\frac{dn}{dE}\right) dE \quad (1.124)$$

where:

$$\frac{dn}{dE} = \left[\frac{4\pi(2m)^{\frac{3}{2}}}{h^3}\right](E - E_c)^{\frac{1}{2}} e^{\frac{E_F - E}{KT}} \quad (1.125)$$

$$E - E_c = \frac{m\left(v_x^2 + v_y^2 + v_z^2\right)}{2} = \frac{mv^2}{2} \quad (1.126)$$

$$dE = mv\, dv \quad (1.127)$$

$$4\pi dv = dv_x\, dv_y\, dv_z \quad (1.128)$$

where E_{vacuum} is the vacuum level and $\frac{dn}{dE}$ is the density of electrons in the bottom of CB, with energies between E and $E + dE$. Now, these four relations (1.125), (1.126), (1.127), (1.128) can be inserted into (1.124) Equation, and it possible to integrate:

- In y from minus infinity to plus infinity
- In z from minus infinity to plus infinity
- In x from $v_{min} = \left(\frac{2X_{so}}{m}\right)^{\frac{1}{2}}$ to plus infinity, where v_{min} is the minimum value required of v_x so that an electron could escape from the crystal;

Consequentially from the last statement, the kinetic energy will be expressed as: $E_k = \frac{1}{2}mv_{min}^2$. It is also necessary to introduce the notion of work function, X_s, which is the energy required from an electron to jump from the Fermi energy level to the vacuum:

$$X_s = E_{vacuum} - E_F \quad (1.129)$$

After resolving the triple integral, the expression for the current density J_s of the electrons leaving the sample is finally obtained:

$$J_s = R^* T^2 e^{-\frac{X_s}{KT}} \quad (1.130)$$

and:

$$R^* = \frac{qmK^2}{2\pi^2\hbar^3} \quad (1.131)$$

where R^* is called Richardson constant, T is the temperature in Kelvin and X_s is the Schottky Barrier. This effect of electrons escaping from a crystal is called **thermionic emission** [24]. The escaped electrons leave an unbalanced positive charge into the

crystal. The positive charge tends to attract back the electrons, establishing the thermodynamic equilibrium. The resulting electric field leads to the **band bending near the surface**. If the previous notation is used, X_s is simply the Schottky Barrier: $E_c^{surf} - E_F$.

1.1.16 – From Grains to Sensors

In the previous paragraphs, the semiconductor physics applied to semiconductor grains of radius R and the decrease of the consequences from the bulk size on the grains band structure were explained. Indeed, **sensors** considered in this thesis and used in laboratory for gas detection, are substantially a **film of sensing nanogranular material**. The **powder** formed by semiconductor nanograins is used, together with some organic additives, to become a **paste** which, printed on a **substrate** and put in contact with two **electrodes**, as it is shown in Figure 1.40. The **substrate** has two function:

- **Supporting** the sensing active material, allowing the connection of the sensor to the electronics of the testing setup/device
- Hosting the **heater** that can be used to modify the sensor working temperature

In Paragraph 1.3 the production of sensors is discussed deeper [25]. Now, it is important focus us on 3 sensors properties:

- Sensors work at a certain working temperature, which can be modified ad hoc through their heater
- The sensing material is in form of a cooked thick-film, spread previously on the substrate, in contact with two electrodes of conducting material
- The thick-film is composed by semiconductor nanograins, put in contact with each other

Electrons in grains CB must have enough energy to overcome the grain-grain potential barrier to generate current. As it will be seen in the following part of the paragraph, the grain-grain potential barrier height changes during the gases detection and, consequently, also the current generated changes. Sensors of interest in this work, also called **chemoresistors**, transduce the presence in the atmosphere of a given chemical compound through a variation of their electrical **resistance/conductance**, translating the chemicals concentration into an **electric signal**. They are composed of **semiconductor**

active material (which can be either **metal-oxides**, like tin oxide, or not, like cadmium sulfide), and the overall phenomenon can be seen as a **dynamic reduction/oxidation interaction of the sensing material surface** with adsorption of the gaseous molecules. In particular, in the environmental air, some different molecules and ions can be found, such as: $\boldsymbol{O^-}$, $\boldsymbol{O_2^-}$, $\boldsymbol{O^{2-}}$. These are **adsorbed** on the grains surfaces and cover them. The rate of adsorption depends by some variables such as sensor temperature, atmospheric composition and so on. In the typical **temperature range** of chemoresistors (between 200 and $500°C$), O_2^- ions are the most abundant at low temperatures (below $300-350°C$), while for high temperature, O^- are the most abundant ions, because the high temperature favors the dissociation of molecular oxygen. When oxygen ions reach the grains surface and are adsorbed, they generate some acceptor surface states. Thanks to their **electron affinity**, they attract and bond electrons from conduction band of the grains bulk. This results in bounds between bulk-grain CB electrons and oxygen atoms on the grain surface, and a consequently decrease of the current detected by sensor. This way, the grain **resistivity** is increased with consequent band bending at the grain surfaces, as shown in Figure 1.41. After a certain time, the **coverage** of the grains performed by the oxygen reaches an **equilibrium point**, where grains are covered by a constant average number of ions. This situation gives the **background response in air** (R_{air}).

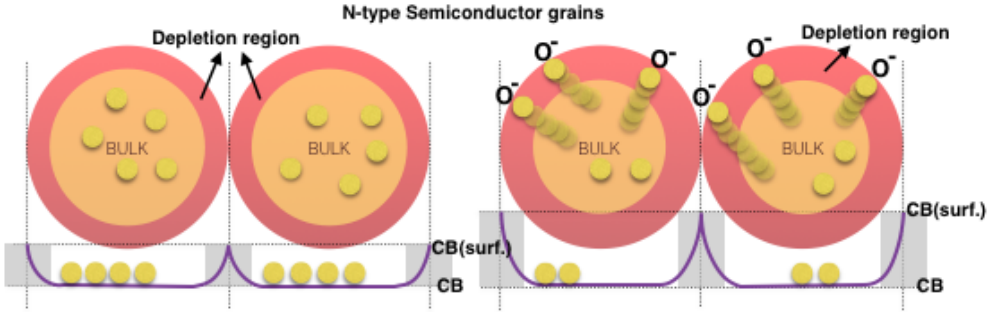

Figure 1.41: Capture of conducting electrons due to the oxygen ions on the surface.

Thus, in an n-type semiconductor, such as SnO_2, WO_3, ZnO, the band bending will lead to a conductance decrease. If the active material grains have further interactions with certain gaseous molecules, the number of oxygen ions over the semiconductor surface changes. Thus, also the electrical properties of the material change, and so the response. For example, if a **reducing gas** (like CO) is introduced, it oxidizes with oxygen ions. Thus, the number of oxygen ions over the surface decreases, and consequentially the conductance of the sensing material is increased, because the electrons previously bonded to the

oxygen ions are freed from the oxygen bounds, and return in the bulk-grain CB, being able again to carry current [26]. Vice versa, **Oxidizing gases** (like NO_2 or O_3) are reduced by the interaction with the semiconductor surface and, consequently, the number of oxygen ions on the surface increases like the material resistivity (for n-type semiconductors). Generally, high performance semiconductor sensors are divided into **two subcategories**: **thin-film sensors** and **thick-film sensors**. Sensors of both categories have optimized and well performing sensing layers, but both have pros and cons. The **thin-film approach** takes advantage of a compact layer with thickness as close as possible to the space charge layer width (W_0). In the abrupt approximation, the macroscopic conductance of this structure is described by a non-conducting layer of thickness W_0, located at the outermost surface, and a conducting layer below it, having thickness $z_0 - W$. A schematic representation is shown in Figure 1.42.

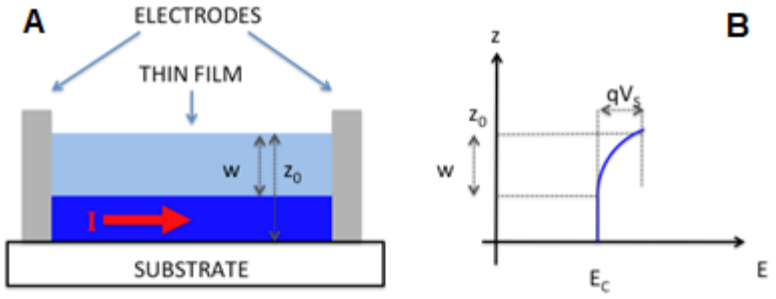

Figure 1.42: Structure of a thin-film sensor. A – The blue zone is the space charge layer and the dark blue zone is the bulk where the current can flow. B – Shows the potential barrier that forms at the surface.

A great advantage of this kind of sensors is the **reproducibility**, because the electrons can move only along the same path (as shows the red arrow in Figure 1.42) into the bulk, parallel to the surface. Thin-film sensors have a very **simple geometry**, but possess a limited surface area, eventually enhanced by a relatively small factor depending on the **surface roughness**. This fact limits the **sensitivity** of the device because the interaction with the gas to investigate is only on the film plain surface. The **thick-film approach** exploits the **granular and porous structure** of the sensing layer. This allows gases diffusion within the layer, so that the inner portion is also exposed to gaseous molecules, as shown in Figure 1.43A. The thick-film approach gives an enhancement to **sensitivity**, because the gas can penetrate between grains in the sensing material porous layer. The result is a wider reacting surface if compared to thin-film sensors and, generally, the **response** of a thick-film sensor is greater. The main **downside** of this approach is the

more complicated conduction mechanism with respect to thin-film, because electrons pass through the grain interfaces, as red dashed line underlines in Figure 1.43, and the paths threaded can be very different.

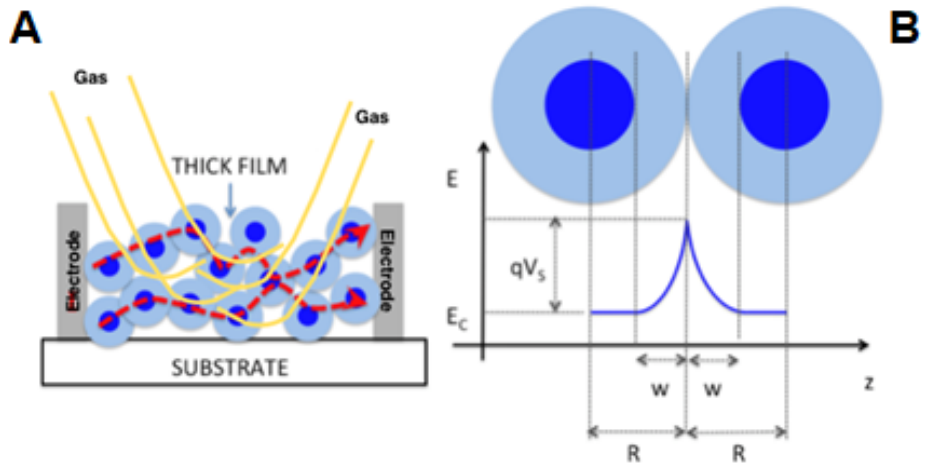

Figure 1.43: A – Thick-film sensor. Gases can interact with all grains of the film. B – Double potential barrier generated between two grains.

Grain size is another feature that affects electronic current in thick-film sensors, because the conductance changes with the grain size (in fact, by decreasing the grain size the conductance increases, because the potential barrier decreases as shown in the paragraphs 1.1.9 and 1.1.10). Thus, when the metal-oxide material is prepared, it is important that all grains are about the same critical size. If this condition is not satisfied, the **repeatability** is compromised and tests on the same sample can give results dramatically different. It is worth noting that this sensing mechanism is highly sensitive to a wide range of chemical substances and it is weakly **selective** (which means that a sensor would detect in the same way the presence of several different gases in a mixture of them). To solve this problem, different strategies have been adopted to give more selectivity to semiconductor chemoresistors [27]. Some of the preferred solutions are:

- The use of sensors arrays
- Making blends between different semiconductor materials (ex. SnO_2 and TiO_2 can be merged to produce the wide ST sensor family, used in the tests presented)
- Making blends between a semiconductor material and other elements, such as a noble metal (palladium, gold, silver, platinum, copper and so on)

The measures that will be discussed in this thesis are obtained using thick-film semiconductor sensors. The complete description of the sensors used in the measures is in the Paragraphs 1.2.8.1–6 and 1.2.9.

1.1.17 – Thick-Film Sensors Functioning and Surface Reactions

As aforementioned, **thick-film sensors** are composed by a powder of nanometric grains semiconductor material. After mixing it with some additives, the resulting paste is spread on a substrate between and over two electrodes. The active material is spread in form of a porous layer, where the grains are connected to each other as shown in Figure 1.44A. After heating the sensor through the heater inserted in the substrate (the features of the sensors construction are discussed deeply in Paragraphs 1.3), the sensor is placed in air where the oxygen ions and other gaseous molecules "bound" to the surface of each inner and outer grains of the layer. Electrons in the grain-bulk conduction band are attracted to the surface from the adsorbed oxygen ions, which act as acceptor surface states, as shown in Figure 1.44B, consequentially reducing the conductivity of the grains (because electrons are removed from the CB and brought to the surface). This phenomenon is called "**ionosorption**" [26]. When the system is in **equilibrium** (adsorption layer does not change), the **conductivity-in-air as ground measure** (G_{air}) is obtained. During the oxygen adsorption on the grain surface, the "depleted shell" thickness at the grain surface is increased, together with the band bending. The "depleted shell" at the grain surface is more resistive than the grain bulk and then, macroscopically, the metal-oxide layer resistivity is increased as shown in Figure 1.44B. The mean reactions of the oxygen adsorption on the grain surface are

$$O_2(gas) + e^- \leftrightarrow O_2^-(ads) \quad (1.132)$$

$$O_2^-(ads) + e^- \leftrightarrow O_2^{2-}(ads) \leftrightarrow 2O^-(ads) \quad (1.133)$$

If the grains are large enough to have a bulk, the electrons in CB must overcome a not negligible potential barrier (of energy qV_s) to move from a grain to another.

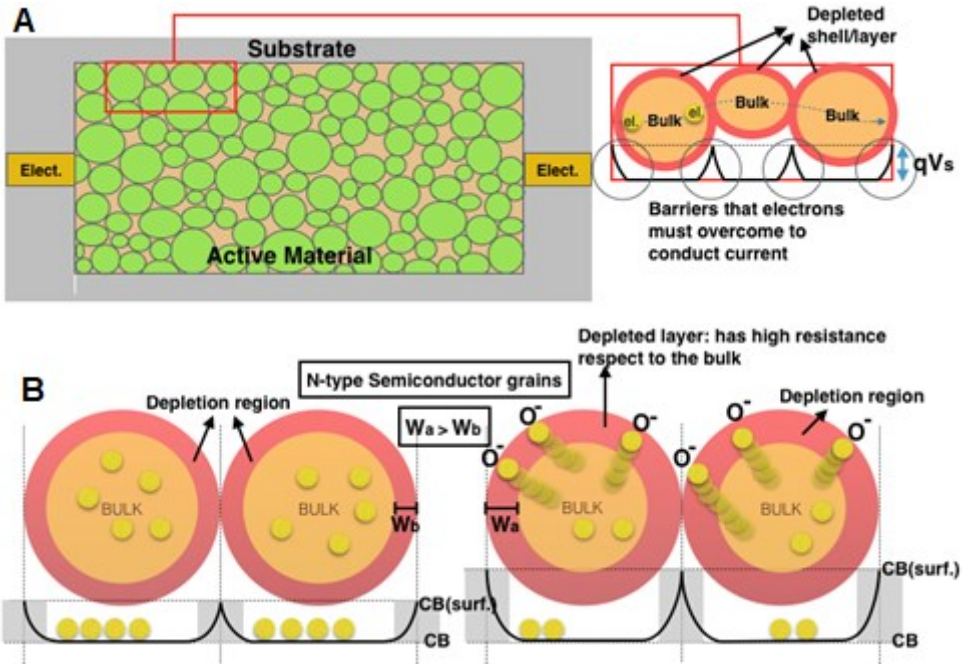

Figure 1.44: A – Grain-grain interface and the potential that electrons must overcome to conduct current. B – Action of the oxygen ions interacting with the grains, consequentially decreasing their conductance.

This means that the electric flow is limited by the density of electrons with energy at least equal to (for n-type semiconductor):

$$n_s = N_C e^{-\frac{qV_S + E_C - E_F}{K_b T}} = N_d e^{-\frac{qV_S}{K_b T}} \quad (1.134)$$

where N_C is the effective density of states close to the bottom of the CB, and N_d is the number of donor ions. When reducing gases, such as CO, approach to the sensor surface, they react with the absorbed oxygen ions and release electrons in CB. The final effect is a decrease in the resistance and thus the increase of sensor conductivity (see Figure 1.45).

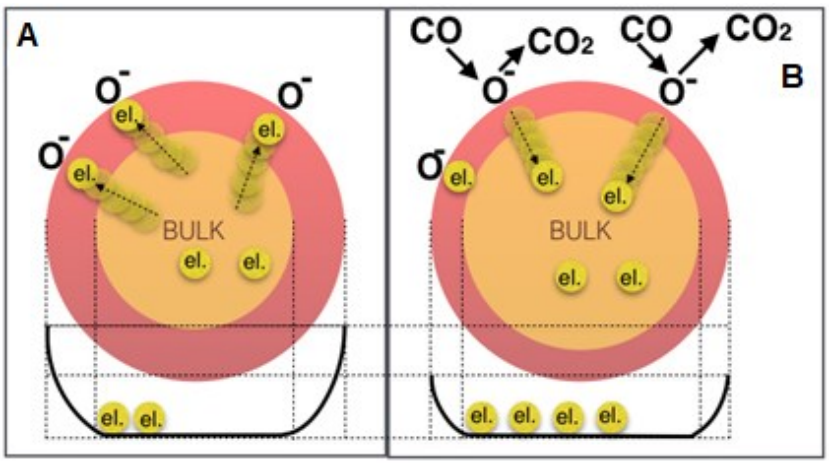

Figure 1.45: A – Electrons are trapped by oxygen ions on the surface. B – Reaction of adsorbed oxygen with a reducing gas (in this case CO). CO_2 forms and electrons are free to return in the CB.

Thus, having increased the sensor conductivity, the electrons must overcome a smaller barrier than before and the current exiting from by sensor electrodes and detected by the electronic circuit is higher. In this situation, after waiting the stabilization of the system, it is possible find the conductivity in presence of a reducing gas (for oxidizing gases is simply the contrary) G_{gas} [26]. It is possible to finally recall the concept of response, as a function of time $R(t)$, already defined in the paragraph 1.13:

$$R(t) = \frac{G_{gas} - G_{air}}{G_{air}} \quad (1.135)$$

1.1.18 – Intragrain Oxygen Diffusion

Before discussing the production of the final sensing devices, an important concept must be taken into account. Even if the usual process sees the oxygen ions binding to the surface of the grains, it might happen that these ions could migrated inside the bulk of the grain, changing the electrical properties of the material. The phenomenon is known as i**ntragrain oxygen diffusion** or **in/out oxygen diffusion** [28,29].

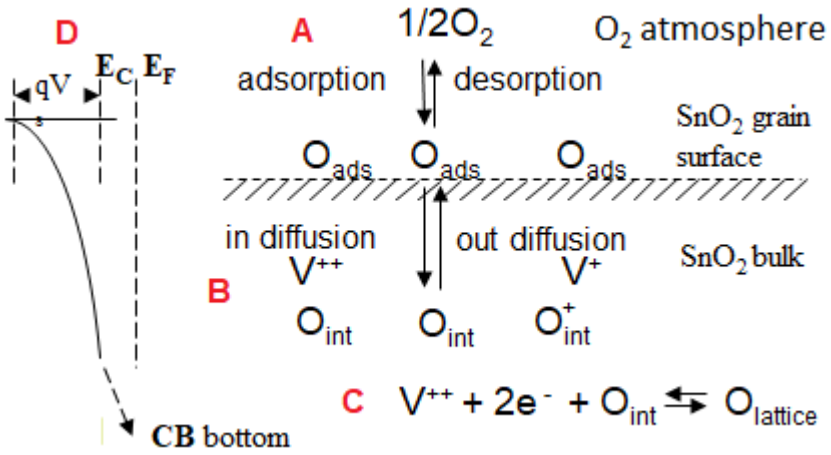

Figure 1.46: A – Oxygen exchange equilibrium between the atmosphere and the grain surface. B – Diffusion of oxygen in and out of the grain. C – Interstitial-vacancy creation and recombination. D – Energy band diagram.

Oxygen ions reaction with the vacancies is mediated from the following equation:

$$O_0 \leftrightarrow V^{++} + 2e^- + \frac{1}{2}O_2 \quad (1.136)$$

resulting in the Law of Mass Action:

$$K = [V^{++}]n^2 p(O_2)^{1/2} \quad (1.137)$$

First of all, it is possible to notice that:

1. K is constant as definition of the Law of Mass Action
2. The partial pressure of oxygen $p(O_2)^{1/2}$ could be constant, too

In case the condition 2 stands, also $[V^{++}]n^2$ must be constant, with the two components $[V^{++}]$ and n^2 increasing and decreasing coherently. Investigating deeper in the steps that lead to the previous equation, it can be observed that:

- $O_0 + S \leftrightarrow V + O_S^0$; an oxygen atom is taken from a lattice site inside the crystal and landed at the surface of the grain, and the concentrations of vacancies, superficial oxygen ions and surface sits follow this equation: $\frac{[V]\cdot[O_S^0]}{[S]} \propto exp^{(-E_{sur}/kT)}$
- $O_S^0 \leftrightarrow \frac{1}{2}O_2 + S$; adsorption process at surface, S is a surface site; the concentrations follow this equation: $\frac{p(O_2)^{1/2}\cdot[S]}{[O_S^0]} \propto exp^{(-E_{ads}/kT)}$

but the second observation actually falsifies condition 2, being the $p(O_2)^{1/2}$ variable due to the adsorption. Now, from the previous two observations, the following equation can be obtained to define the concentration of vacancies in the crystal lattice:

$$[V] \propto p(O_2)^{-1/2} \cdot exp^{\{[-(E_{sur}+E_{ads})]/kT\}} \quad (1.138)$$

The numerator at the exponential can be written as $E_{tot} = E_{sur} + E_{ads}$, with E_{tot} total energy required to take an atom from a lattice site inside the crystal to the vapor phase, and thus the Equation (1.138) becomes:

$$[V] \propto p(O_2)^{-1/2} \cdot exp^{(-E_{tot}/kT)} \quad (1.139)$$

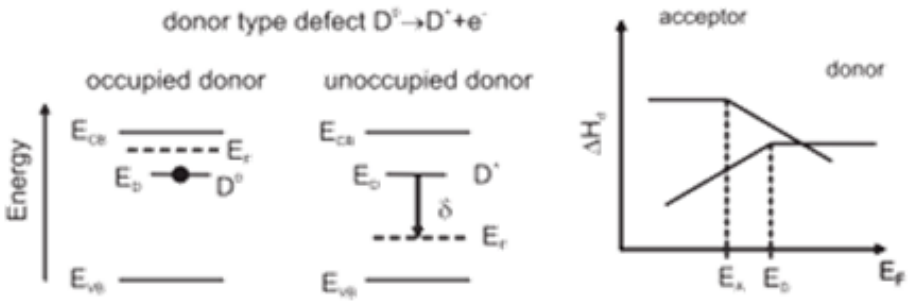

Figure 1.47: Dependence of the defect formation enthalpy ΔH_d on the Fermi Energy [164].

From Figure 1.47 it can be observed that:

- $E_F > E_D$ → electrically neutral, ΔH_d not dependent from E_F
- $E_F < E_D$ → positively charged, electrons expelled are transferred to the electron reservoir ($\boldsymbol{E_v}$), leading to an energy gain $\boldsymbol{\delta}$, lowering the ΔH_d

with E_D energy level of a donor. To obtain $[V^{++}]$, electrons relaxed to the Fermi level lead to an energy gain: $E_{d_1} - E_F + E_{d_2} - E_F$. It is time to define $E_0 = E_{tot} + 2E_{cs} - E_{d_1} - E_{d_2}$, so that the Equation (1.139) can be rewritten as:

$$[V] \propto p(O_2)^{-1/2} \cdot exp^{\{-[E_0 - 2(E_{cs} - E_F)]/kT\}} \quad (1.140)$$

which shows clearly that, at a fixed oxygen partial pressure and in equilibrium, the (ionized) oxygen vacancies density increases exponentially as E_F goes down in band gap, which results in the impossibility to have a uniform doping level along the whole space charge region. Now, considering the density of vacancies in the bulk N_d:

$$N_d \propto p(O_2)^{-1/2} \cdot exp^{\{-[E_0 - 2(E_{cb} - E_F)]/kT\}} \quad (1.141)$$

it is possible to calculate that:

$$[V^{++}] = N_d \cdot exp^{[2(E_{cs}(x) - E_{cb})/kT]} \quad (1.142)$$

This last equation was also obtained from Lantto [30] following drift-diffusion approach.

Since $E_{cs}(x) - E_{cb} = eV(x)$, it is possible to substitute in Equation (1.142):

$$[V^{++}] = N_d \cdot exp^{[2eV(x)/kT]} \quad (1.143)$$

and the Poisson's equation becomes:

$$\frac{d^2V(x)}{dx^2} = \frac{2e}{\varepsilon} N_d \cdot exp^{[2eV(x)/kT]} \quad (1.144)$$

which leads to obtain the potential:

$$V(x) = \frac{kT}{2e} \ln\left[1 + tan^2\left(\frac{x}{\sqrt{2}L_D}\right)\right] \quad (1.145)$$

where $L_D = (\varepsilon kT/4e^2N_d)^{1/2}$ is the Debye length.

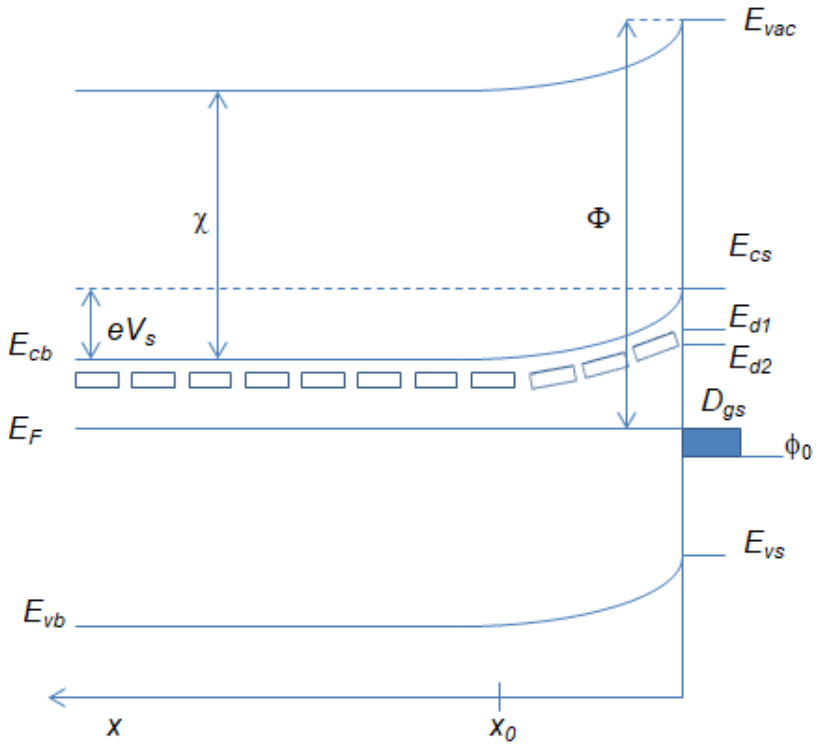

Figure 1.48: Bands at a semiconductor surface illustrating the formation of the space charge region. ϕ is the work function, χ is the electron affinity, eV_s is the band bending, D_{gs} represents surface states, E_{d_1} and E_{d_2} are the donor levels, and ϕ_0 is the neutral level for surface states [29].

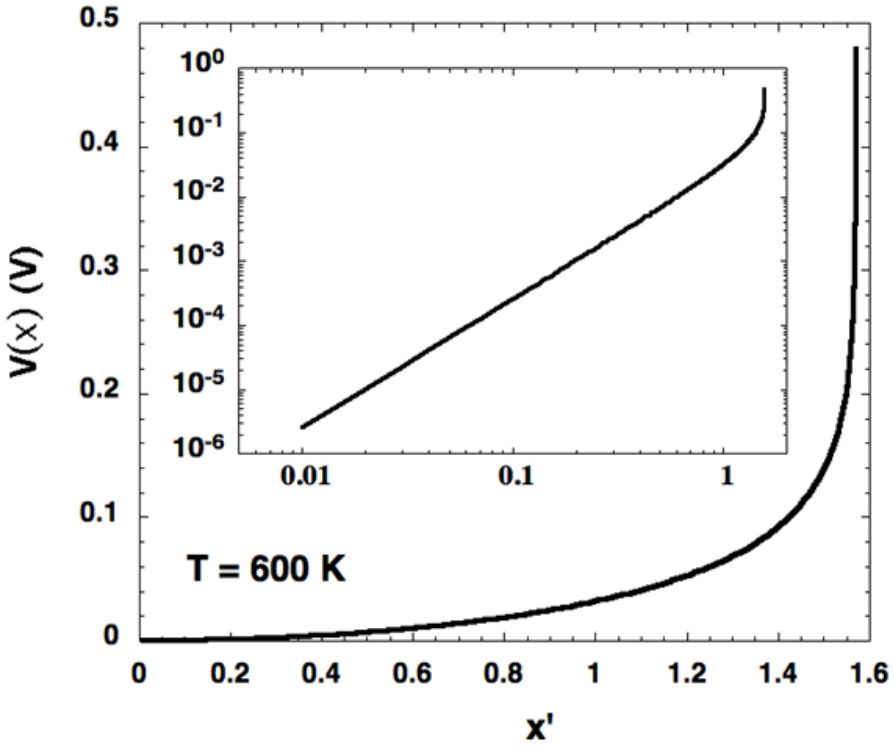

Figure 1.49: Profile of the potential near the surface due to band bending. The variable $x' = x/(2^{1/2}L_D)$, with L_D being the Debye length. The inset shows the same potential in a log-log scale to show the abruptness of the potential [29].

The width of the depletion region can be determined resorting to charge neutrality:

$$x_0 = \sqrt{2}L_D arctan\left(\frac{N_s}{2\sqrt{2}N_d L_D}\right) \quad (1.146)$$

the height of the surface potential energy barrier is finally obtained:

$$V_s = \frac{kT}{2e}\ln\left(1 + \frac{N_s^2}{8N_d^2 L_D^2}\right) \quad (1.147)$$

It is possible now to calculate the equation to determine the doping level and E_F position. From the equilibrium it is possible to observe that:

$$N_d = Cp(O_2)^{-1/2} \cdot exp^{\{-[E_0 - 2(E_{cb} - E_F)]/kT\}} \quad (1.148)$$

where C is a constant. From general solid state physic background, it is known that:

$$n = N_c \cdot exp^{\left(-\frac{E_{cs} - E_F}{kT}\right)} \quad (1.149)$$

where N_c is the **effective** density of states in CB. Under the assumption that at working temperature all donors are doubly ionized, it will be $n = 2N_d$, which leads to:

$$E_{cb} - E_F = \frac{E_0 - kT \cdot ln\left(2Cp(O_2)^{-1/2}/N_c\right)}{3} \quad (1.150)$$

Now, the equation to determine the density of chemisorbed oxygen can be obtained. Oxygen is considered to be adsorbed monoatomically ($working\ temperature > 150°C$): $O_S^0 \leftrightarrow \frac{1}{2}O_2 + S$ Assuming low coverage, $[S]$ can be taken as constant:

$$\frac{p(O_2)^{1/2}}{[O_S^0]} \propto exp^{(-E_{ads}/kT)} \quad (1.151)$$

The ratio between ionized and neutral oxygen atoms at the surface depends on the Fermi level position as:

$$\frac{[O_s^-]}{[O_s^0]} \propto exp^{[-(E_t - E_F)/kT]} \quad (1.152)$$

where E_t is the ionization energy which is the energy of an electron at top of the surface barrier:

$$N_s = Ap(O_2)^{1/2} \cdot exp^{[-(eV_s + E_{cb} - E_F - E_{ads})/kT]} \quad (1.153)$$

From [31] $E_{ads} = 2eV$ and $E_0 = 2.2eV$.

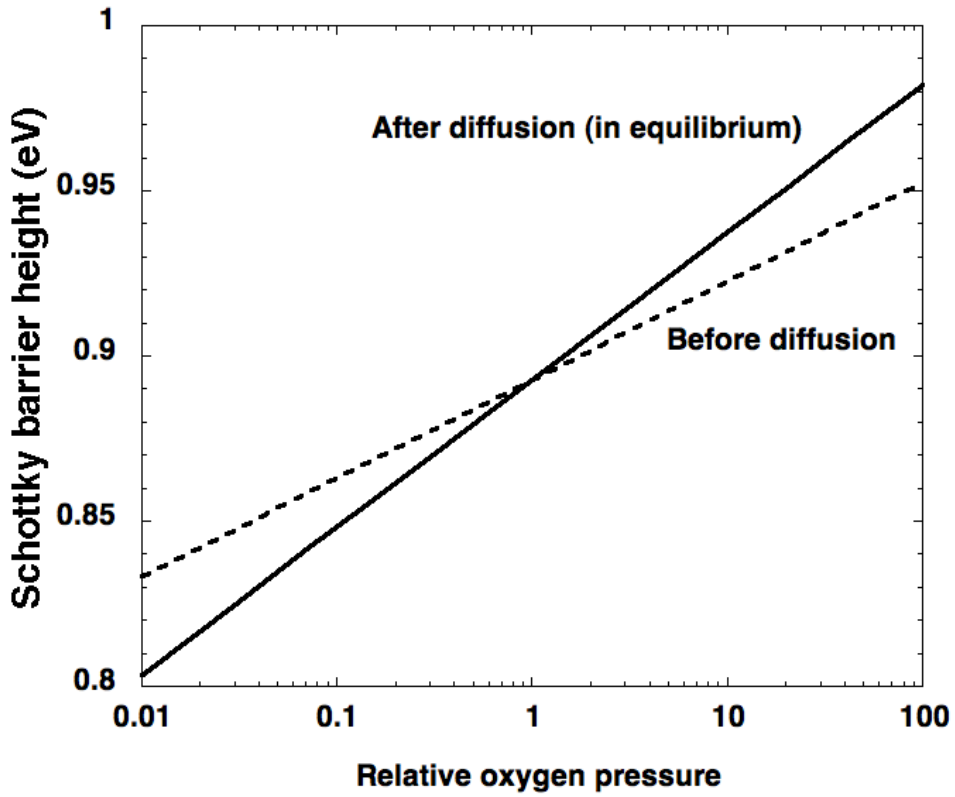

Figure 1.50: Schottky barrier height as a function of the relative oxygen pressure [29].

In figure 1.50, the filled line corresponds to the equilibrium doping of the sensor, considering intragrain oxygen diffusion. The dashed line is the Schottky barrier height keeping the doping constant and equal to that of the reference pressure. Experimentally it is observed that the Schottky barrier height resembles the higher values of the continuous line trend, rather than the ones from the dashed line. To work out the equations it was assumed, as an example, that for a given oxygen pressure p_0 at $T = 600K$ → $N_d = 10^{20}/m^3$ and $N_s = 10^{17}/m^2$. These values were chosen because they lead to regularly observed barrier heights. First, assuming that all oxygen vacancies are doubly ionized, with Equation 1.149 the bulk Fermi level position in the gap can be determined. Knowing that $E_{cb} - E_F$, and having a given $p(O_2)^{1/2}$, by using Equation 1.147 for the potential, the constants C and A in the Equations 1.148 and 1.153 can be determined. In Figure 1.50, Schottky barrier heights are plotted as a function of pressure following the model, considering that the system is in equilibrium (filled line). This means that once all involved parameters are determined, it is possible to find as a function of the relative pressure the

Fermi level position with Equation 1.150. Then, the vacancy concentration in the bulk with Equation 1.148, the density of ionized oxygen atoms at the surface with Equation 1.153, and the height of the surface potential energy barrier with Equation 1.147. Finally, the Schottky barrier height results from the sum of $E_{cb} - E_F$ and eV_s Recently, reported results by Barsan et al. [32] show a change in work function of $\approx \mathbf{53}\boldsymbol{meV}$ at 300ºC after a relative **change** in pressure by **a factor of 20**. It is important to note that changes in work function can be considered to directly reflect changes in the Schottky barrier height. A similar change in the relative pressure gives in the model a change in Schottky barrier height of $\mathbf{58}\boldsymbol{meV}$, a result that seems remarkable given all the assumptions and approximations introduced and the complexities of the experiments.

1.2 – Thick-Film Sensors

The use of nanocristalline material, combined with the screen printing technology allows the production of sensitive films of ceramic type, electrically stabilized at high temperature which, however, retain the nanometric grain structure.

1.2.1 – Production Process

To understand the process of preparation of *thick-film* sensors is necessary a synthesis of all crucial aspects of the fabrication process. *Thick-film* technology is a particular form of serigraphy (which is one of the more ancient techniques of reproduction of graphic arts) introduced in the field of technology during '70s in order to construct printed hybrid circuits. It was applied for the construction of electronic components used in various sectors. Thick-film hybrid circuits are famous for their multiple qualities as compactness, robustness, low cost. Thick-film technology is also relevant because it allows to build very precise geometries, so it is useful in the sensor field. In the last years, the serigraphic technique is highly evolved even if the applied procedures have not substantially changed. However, what makes the thick-film technology suitable for the realization of sensors is its low cost combined to the capability to operate also in hostile working conditions. Besides their rapid responses, some of these sensors are very sensitive, being able to detect chemicals in the range of tenth parts per billions (ppb). These sensors have the following advantageous characteristics:

- Good sensitivity even at low gas concentration
- Discrete reliability and repeatability of the measurement
- Low energy consumption
- Small dimensions
- Excellent cost-performance ratio
- Ease of automation

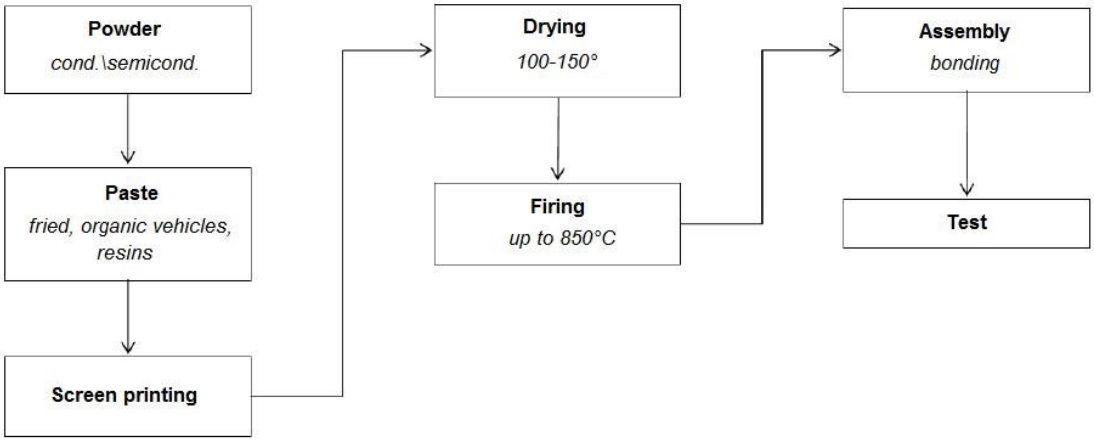

Figure 1.51: Scheme of the entire process to obtain thick-films used as gas sensors [34].

1.2.2 – Substrate

Substrates used for gas sensors have the dual task of mechanical support for the sensitive layer and of electric insulator between the functional part (metal oxide film) and circuit elements. The most used substrate is Al_2O_3 (alumina), because of its good thermal stability and resistance to corrosion and use, its excellent dielectric properties and low cost. Alumina powder is obtained from Bauxite (the principal font of aluminum in nature). It is ground together with other oxides (SiO_2, NaO, MgO) in order to obtain a substrate with the desired chemical-physical characteristics. Grinding is effected in a mill with blades to ensure a good mixing level. Then, the obtained compound undergoes two treatments at different pressures depending on the desired thickness (later or less than 1mm). Then, after imposing a form to the substrate, it is exposed to firing for 12–24 hours; this thermal treatment is composed by two principal steps:

- Pretreatment
- Sintering

The first step is performed at $300-600°C$ and is necessary to eliminate organic additives, used for grinding; the second step, the **sintering**, is done at $1500-1700°C$ and serves to promote the adhesion between powder particles through events named "densification" and "growth of grains". Densification is a process that reduces the porosity of the sample, making it denser; the growth of grains, instead, is a process which increases the average dimension of the particles constituting the material. While densification needs high temperatures, the growth of grains occurs naturally during the process itself. The modulation of temperatures and of total firing times is the key to optimize physical-chemical characteristics of materials.

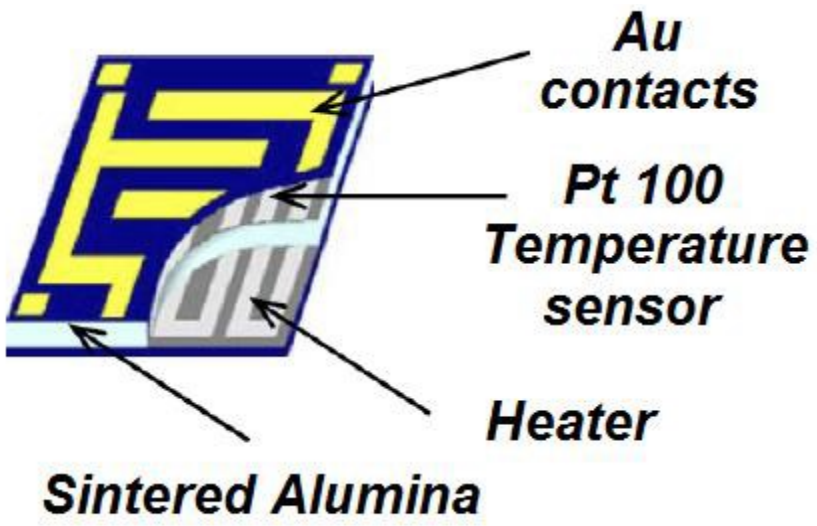

Figure 1.52: Illustration of a support for sensors produced in the Sensor and Semiconductor laboratory of the Department of Physics and Earth Sciences in Ferrara [34].

The substrate should not play an active role in the sensing activity, moreover a certain compatibility between the sensitive layer and the support must subsist, in order not to create tensions as a result of thermal expansion. Then, substrates have to be characterized from a smooth and uniform surface and from the lowest number possible of visible surface defects. Furthermore, the substrate materials must have a chemical and physical compatibility with the materials with which they are in contact.

1.2.3 – Deposition of the Screen Printed Paste

To be interfaced with the control electronics and to be placed on the substrate, the active material of the metal oxide semiconductor must be mixed with other substances; is therefore obtained a paste, whose principal components are:

- The active material (semiconductor oxide)
- The glass frit
- Organic vehicles

The active material consists of a nanometric powder of semiconductor particles with an average diameter smaller than 100 nm, which must be chosen depending on the type of gas to be detected with the sensor. Therefore, the first step consists in the preparation in laboratory of the powder. The second step consists in the preparation of the ink, a powder suspension in one or more organic vehicles suitably dosed. Then to the preparation must be added the glass frit in small percentages in weight depending on the powder used. The fried is a powder formed by a mixture of glassy oxides based of silica (SiO_2) charged with alkaline-earth oxides or with oxides of the IV group, to modify its behavior with temperature. Its function is to fix particles between them and to anchor the paste to the substrate. The first aspect is of fundamental importance in order to form a uniform network of particles and also to obtain intergranular Schottky Barriers; the second aspect is practical and is essential so that the film does not detach from the substrate. Organic vehicles are generally made of organic solvents in which are dissolved resins and surfactants in order to optimize the dispersion of solid particles inside the medium and to regulate the visco-elastic behavior for an ideal printing. The organic vehicle is completely removed in the following thermal processes. The printing of the paste on the substrate is carried out with a screen printing machine (see Figure 1.53).

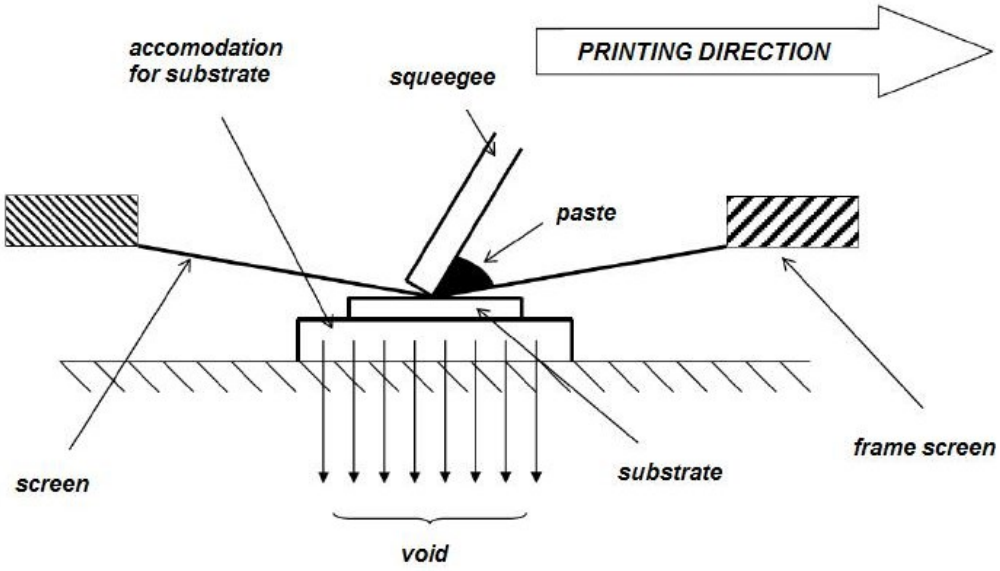

Figure 1.53: Screen printing, lateral simplified section of the machine [34].

The essential components of a screen printing machine are:

- Screen, which shows the geometry of the design to be printed;
- Squeegee, a spatula which, exerting pressure, allows the paste to cross the screen and to settle on the substrate, reproducing the design with high quality.

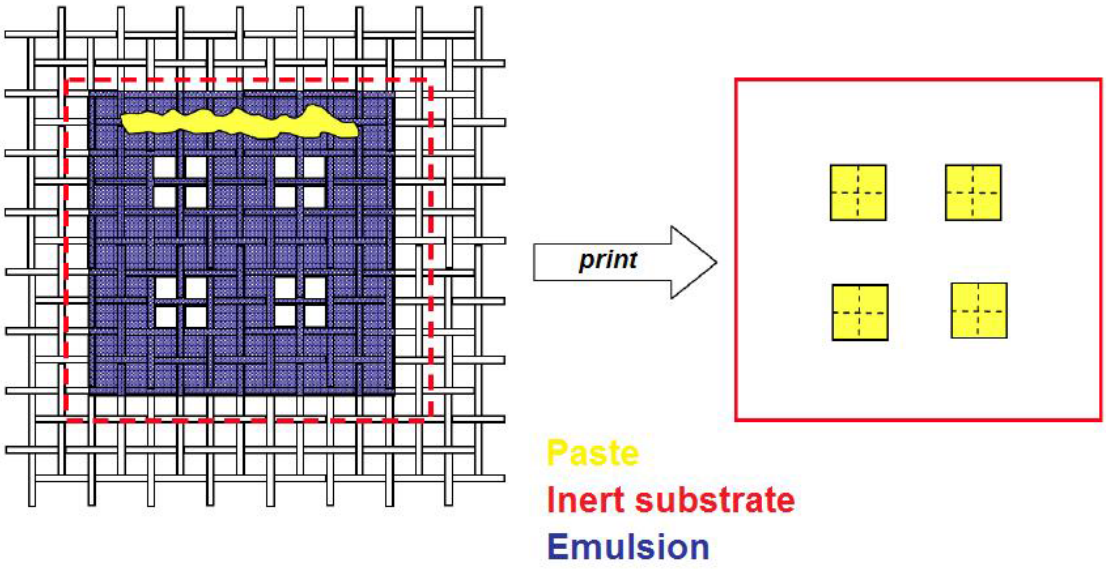

Figure 1.54: Illustration of the squeegee passage on the screen after the application of the photosensitive emulsion and of the paste [34].

A typical screen consists of a network of finely twisted steel wires (of 100μm), stretched over a frame of aluminum. As shown in Figure 1.54, between cables there is an empty space; to characterize a printing screen a specific unit of measure, named mesh should be defined. The mesh number corresponds to the number of wires per linear inch that can be calibrated as a function of the required application. The cables network is covered by an UV-sensitive emulsion, on which is impressed photographically the design to be printed. Moreover, the screen presents some areas in which the emulsion is absent, through which the paste can be printed on the substrate. Therefore, the function of the printing screen is to define the design and to calibrate the quantity of paste. The paste must be a pseudo-plastic fluid, which varies its viscosity as a function of the applied stress. The squeegees must be resistant to solvents involved in the process and present in the paste. They are two: the first one forces the paste through the screen, while the second one works in the opposite direction and brings back the paste in the initial position for a new print.

1.2.4 – Drying and Firing

Once printed, the ink undergoes two different treatments: the *drying* and the *firing*. The *drying* is a low-temperature treatment, around $100-150°C$ that serves to eliminate the most volatile organic solvents and to avoid the draining of the printed ink. It can be done in a common airy hotplate or in an infrared oven. The *firing* is a high-temperature process (up to $850°C$) made in a muffle furnace or in an infrared oven. It serves to eliminate oil organic additive used to obtain the ink and to leave on the substrate only the film composed by the functional material and by the small percentages of fried. During these two processes, the temperature must be rigorously controlled in order to limit the formation of cracks on the handwork, which may prejudice conductive phenomenon through the material.

1.2.5 – Assembly

The sensor must be assembled by means of a technique named *bonding*, which consists in the connection of the sensor to a support, using four pins. These pins are welded, by thermo-compression, to the heater and to the contacts of the plate on which the film is deposited.

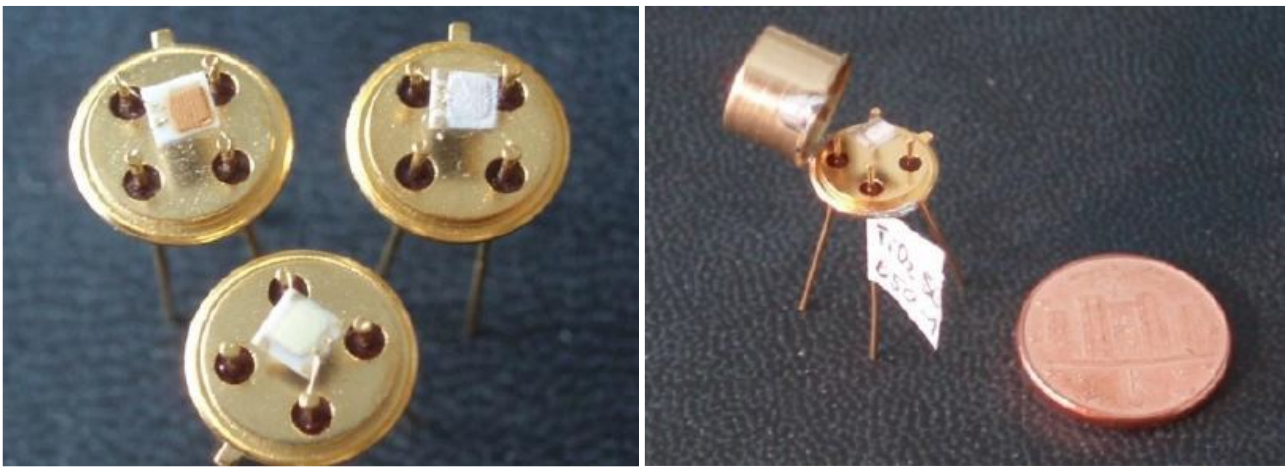

Figure 1.55 – 1.56: Bonded sensors (left) and comparison between a sensor and a 1cent money (right) [34].

This connection, powered by golden wires (99.99%) with a diameter of 0.06mm, is carried out via the apparatus shown in Figure 1.57.

1.2.6 – Powder Synthesis: Sol-Gel Technique

Chemical techniques to obtain in laboratory polycrystalline metal oxides semiconductors, are essentially of two types: the conventional chemical-mechanical techniques as the synthesis for solid state reaction and the more recent techniques called "wet", that occur in solution. With wet-techniques, controlling reaction parameters as temperature, pH and purity of reagents, one can obtain materials with controlled requirements. The mainly used technique at the Sensors and Semiconductors Laboratory consists in the so called sol-gel process. It is a chemical treatment performed in solution, responsible for the synthesis of ceramic or glassy materials. It has, in fact, many advantageous features as versatility, relative simplicity, economy and above all it allows to obtain spherical nanoparticles with a high level of purity, with a single-mode distribution of the grains size.

Figure 1.57: Instrument for the assembly [34].

The fundamental steps of the sol-gel technique are the following:

- A starting reactive (dissolved in water or alcoholic solutions) is converted in a colloidal suspension (*sol*) of the precursor of the final oxide (*gel*) through processes of hydrolysis and condensation
- Removal of the solvent, through evaporation
- Execution of an irreversible thermal oxidation of the precursor from which the final oxide, with a well-defined crystalline structure, is obtained

---

1.2.7 – Humidity

The change in the response of sensors in wet conditions can be interpreted as the negative effect due to the superficial adsorption of OH^- groups that compete with the gas molecules in the reaction mechanism that involves the surface of the film just described before. The result of the interaction between H_2O molecules in the wet ambient and the surface of the film is to deposit a hydrogen atom (H) which, binding to adsorbed oxygen (O^-), produces on the surface the hydroxyl group (OH^-). Consequently, the number of available active surface states decreases. On the other hand, increasing the temperature, an increasing number of OH^- groups leave the reactive sites and the water molecules lesser interferer with the reaction with the gas. As an example, an investigation of the humidity effects was made on SnO_2-based sensors in CO detection [33]. The result is an algorithm for compensating water vapor partial pressure in the detection of the gas.

1.2.8 – Sensor Typologies

The following subchapters expose the characteristics and preparation processes for the different semiconductor materials used for the sensing films. Most of these preparation has been described deeply in a book published as extract from the previous thesis [34]. For sake of completeness, transmission electron microscopy (TEM), scanning electron microscopy (SEM), TEM diffraction scan and energy-dispersive X-ray spectroscopy (EDS) analysis have been performed to characterize most of the semiconductor materials used. From the third analysis, it was possible to calculate the interplanar distance between the

crystalline planes for some of the sensing materials used. This distance, $D_{interplanar} \pm$ S. E. M., is calculated by the equation:

$$D_{interplanar} = \lambda_{e^-} \cdot \frac{L_{camera}}{R_{ring}} \qquad (1.154)$$

on the basis of the diffraction figures shown in Figures 1.158C, 1.162C, 1.163C, 1.164C, 1.166C and 1.167C (from which the ring radii R_{ring} can be estimated); having TEM beam energy$\simeq 100kV$, camera length $L_{camera} \simeq 58cm$, and electron wavelength $\lambda_{e^-} \simeq 0.037$Å.

	INTERPLANAR DISTANCE±ERROR (Å) (Electron-beam energy=100kV; electron wave-length=0.037Å; camera length=58cm)					
	SmFeO3	ST 25 650+Au	CdS	SnO2	ZnO 850	TiTaV
FIRST RING	3.72±0.34	2.99±0.27	2.82±0.26	3.02±0.27	2.82±0.26	2.92±0.27
SECOND RING	2.42±0.22	2.38±0.22	1.58±0.14	2.33±0.21	2.31±0.21	1.94±0.18
THIRD RING	1.74±0.16	2.05±0.19	1.02±0.09	2.07±0.19	1.75±0.16	1.57±0.14
FOURTH RING	1.08±0.10	1.61±0.15		1.56±0.14	1.55±0.14	1.39±0.13
FIFTH RING	0.76±0.07	1.28±0.12		1.28±0.12	1.27±0.12	1.22±0.11
SIXTH RING		0.99±0.09		0.94±0.09	0.94±0.09	1.12±0.10
SEVENTH RING		0.83±0.08		0.84±0.08	0.84±0.08	1.04±0.09
EIGHT RING						0.96±0.09
NINTH RING						0.87±0.08

Table 1.1: Interplanar distance between the crystalline planes of some of the semiconductor materials used.

1.2.8.1 – TiTaV

The most selective sensor to benzene among the ones used in these work is TiTaV [35]. It represents a new material based on titanium dioxide (TiO_2) modified by tantalum and vanadium. When fired between 410 and $850°C$, the doped titania powders are in the anatase phase; further heating up to $1050°C$ is required to obtain the rutile phase. The presence of dopant atoms delays the rate of transformation as compared to pure titanium powders. M. Sacerdoti et al. [36], to better understand the role played by dopant atoms in inhibiting bot the phase to rutile and grain growth, performed X-Ray Absorption Spectroscopy measurements at the $L_{III} - L_I$ absorption edges of Ta and Nb K absorption edge. The results from experiment made by Carotta et al. (2004, 2005) [37,38] showed that Ta addition inhibited the anatase-to-rutile phase transformation and hindered drain growth during heating, keeping TiO_2 grain size in the nanometric range. On the other hand, V addition facilitated the anatase-to-rutile phase transformation. This trend is ultimately determined by the ratio between tantalum and vanadium contents and these sensors showed a good response to tumor markers, especially with greatest content of Ta. In particular, in previous researches, it was shown that TiTaV response to benzene, in a

laboratory setup simulating the intestinal environment, was not influenced at all from the presence of hydrogen, methane, or humidity, showing a rare case of selectivity against these simpler gases for thick-film sensors [35] (see also Figure 1.61).

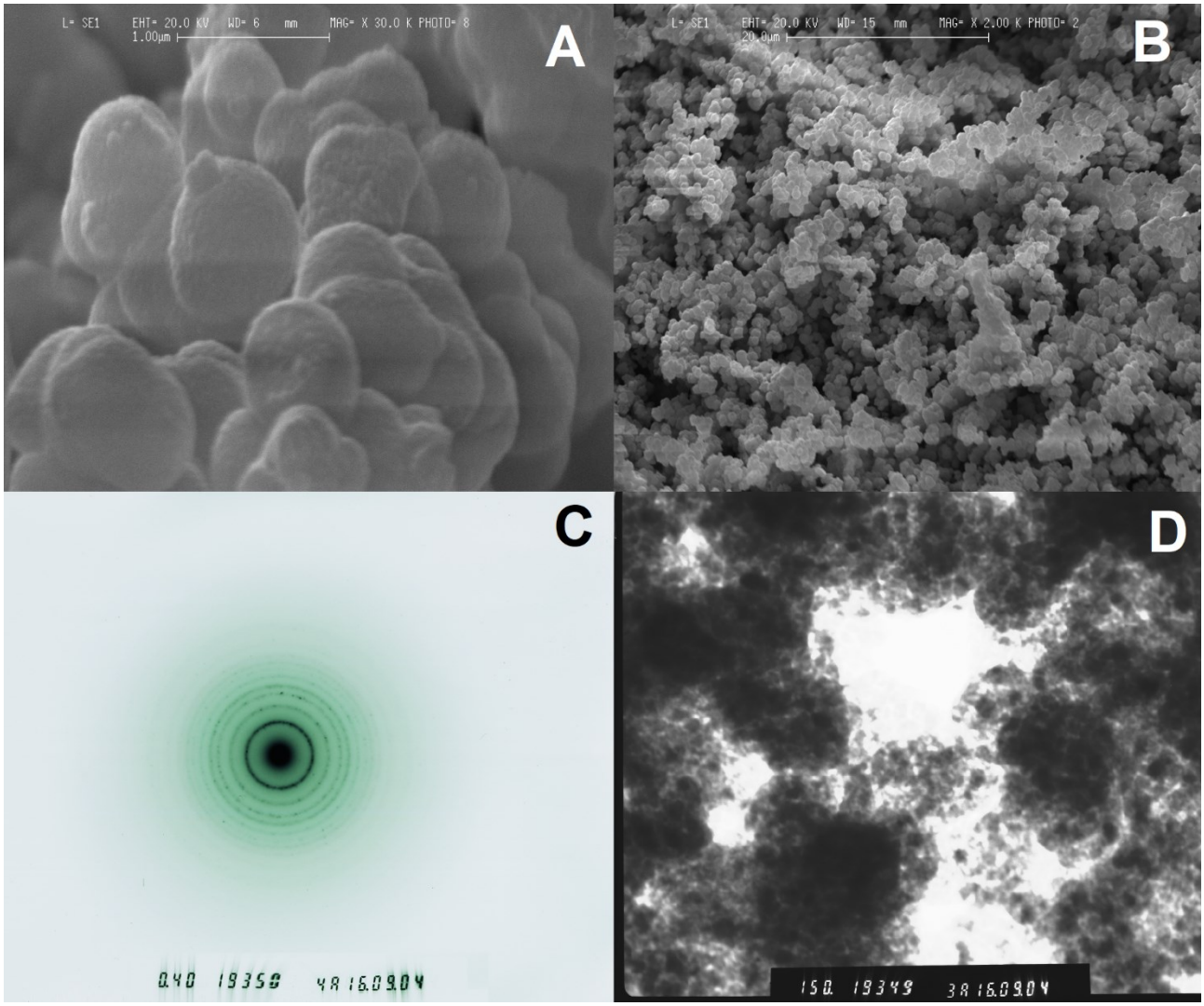

Figure 1.58: A – SEM image of TiTaV nanostructure (scale: $1\mu m$); B – SEM image of TiTaV nanostructure (scale: $20\mu m$); C – TEM diffraction image of TiTaV ($x0.40\ magn.$); D – TEM diffraction image of TiTaV nanostructure ($x150\ magn.$).

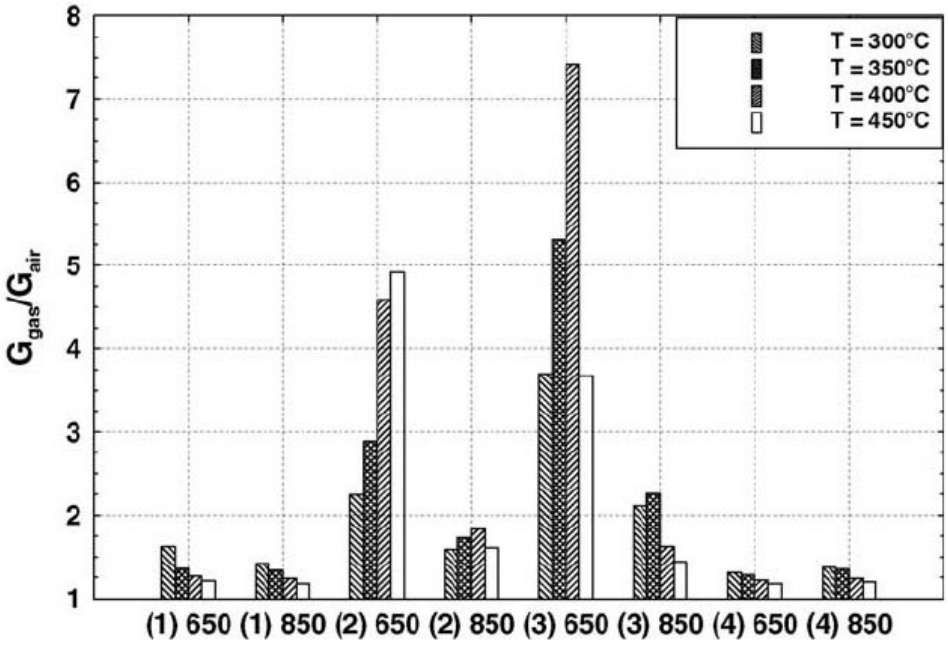

Figure 1.59: Electrical response to benzene ($10ppm$) in dry air for four TiTaV samples: (1) Ti:Ta:V=100:5:5, (2) Ti:Ta:V=100:8:2, (3) Ti:Ta:V=100:15:5 and (4) Ti:Ta:V=100:2:8, measured at 300, 350, 400 and $450°C$ [38].

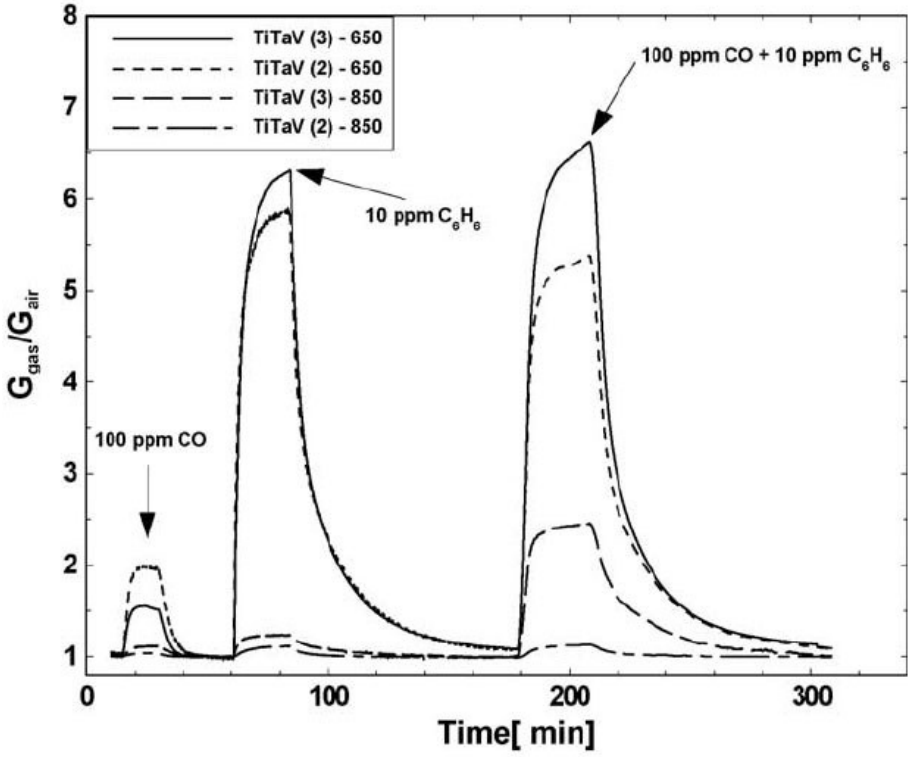

Figure 1.60: Electrical response to $100ppm$ of CO, to benzene ($10ppm$) and to mixtures of the two gases in dry air for TiTaV (2) and TiTaV (3) fired at 650 and $850°C$ at the working temperature of $380°C$ [38].

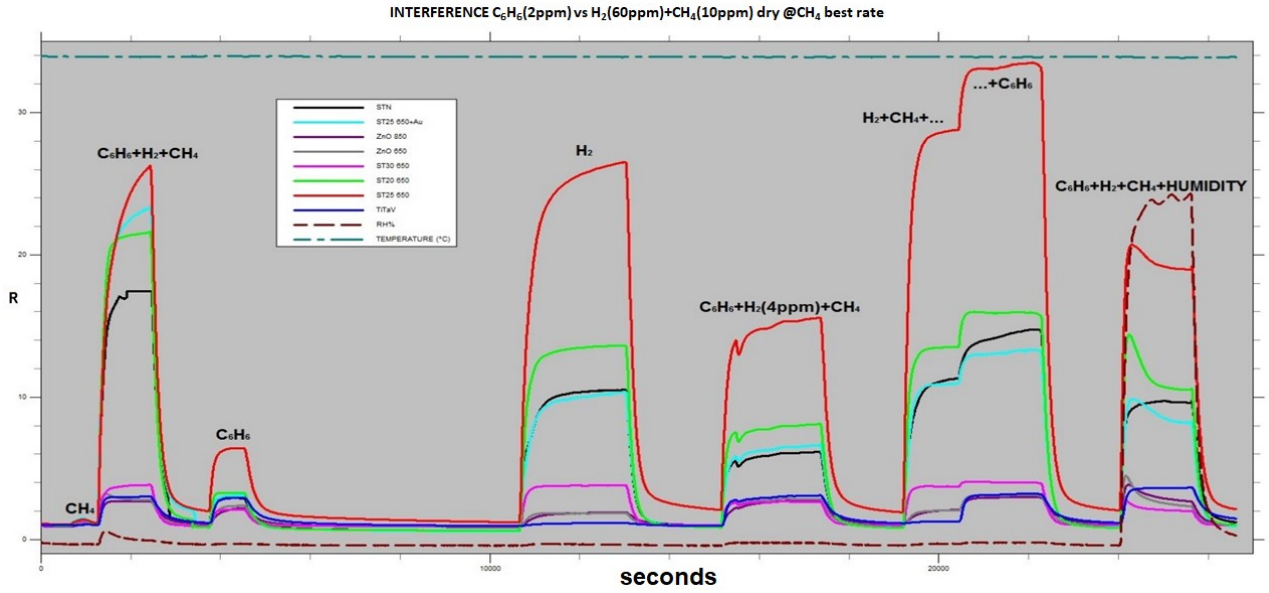

Figure 1.61: Various sensors responding to the gases mixtures written in the graphic. TiTaV shows its selectivity to benzene while mixed with hydrogen and methane, both in dry and moist conditions [35].

1.2.8.2 – ZnO-Based Materials

ZnO has been a pioneering material in gas sensing (Seiyama et al., 1962 [39]). Zinc oxide has a direct wide band-gap ($3.37eV$) semiconductor and exhibits high excitation binding energy ($60meV$), which causes an efficient UV emission ($\sim 380nm$). Among the various oxides, ZnO is particularly suitable to be synthesized in such nano-forms (Schmidt-Mende et al., 2007 [40]; Wand, 2004 [41]. ZnO mainly exhibits very good responses towards oxidizing gases, in particular with ozone. ZnO has been successfully employed also to detect other gases, such as H_2, O_2, H_2S, LPG, HCHO and NH_3. In addition to thermally activated gas sensors, ZnO is particularly suitable to be assisted by UV irradiation. In this operational mode, the sensors work at room temperature overcoming the main technical limitation of the high operating temperature, essential in chemo-resistive gas sensors.

ZnO-based sensor used in this work had $850°C$ as firing temperature, and were used on cell tests and blood samples.

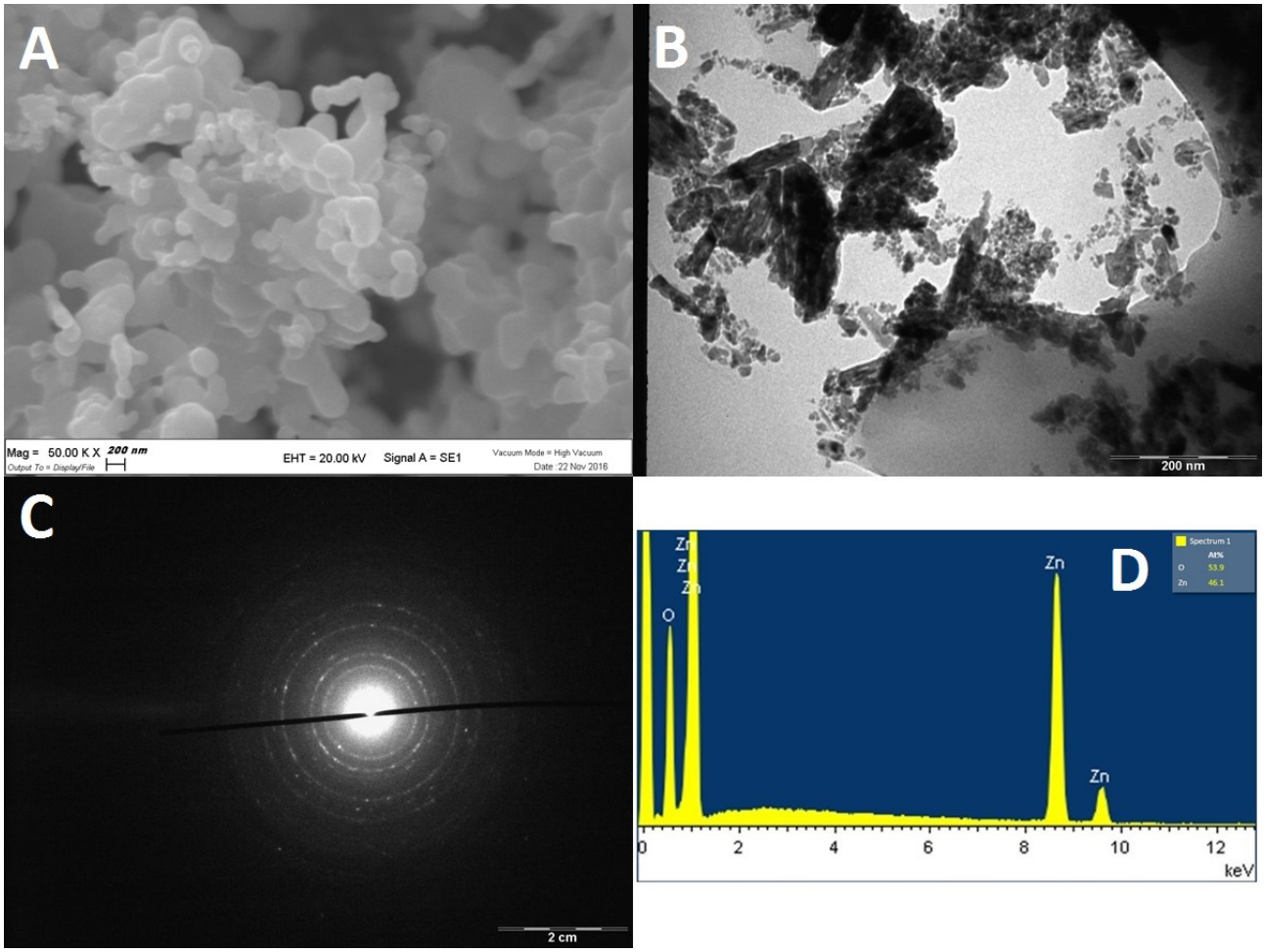

Figure 1.62: A – SEM image of ZnO nanostructure (scale: $200nm$); B – TEM image of ZnO nanostructure (scale: $200nm$); C – TEM diffraction image of ZnO nanostructure (scale: $2cm$); D – EDS analysis ZnO nanostructure [47].

1.2.8.3 – SnO_2-Based Materials

Tin dioxide in the most widely used material for gas sensing. It exhibits *n*-type semiconductor behavior due to lattice defects, in particular oxygen vacancies acting as electronic donor levels. The typical behavior of SnO_2 energy barrier versus temperature exhibits a minimum and maximum corresponding to the increase of the depletion layer depth with temperature attributed to a negative surface charge accumulation, typically O^- ions. As the first material extensively investigated in gas sensing, many studies have been performed to improve the sensing and selectivity properties of SnO_2 above all by adding small amounts of ions to the crystal lattice. Further information on the preparation of hybrid tin/titanium oxides semiconductor materials are reported in literature [42]. In this work are

used both pure SnO_2 films and materials derived from tin and titanium oxides in different percentage, as ST20 650, ST25 650+Au1%, and doped with niobium as STN. In Figures 1.63 and 1.64, pure tin dioxide and ST25 650+Au1% are characterized with TEM, SEM and analyzed with EDS approach.

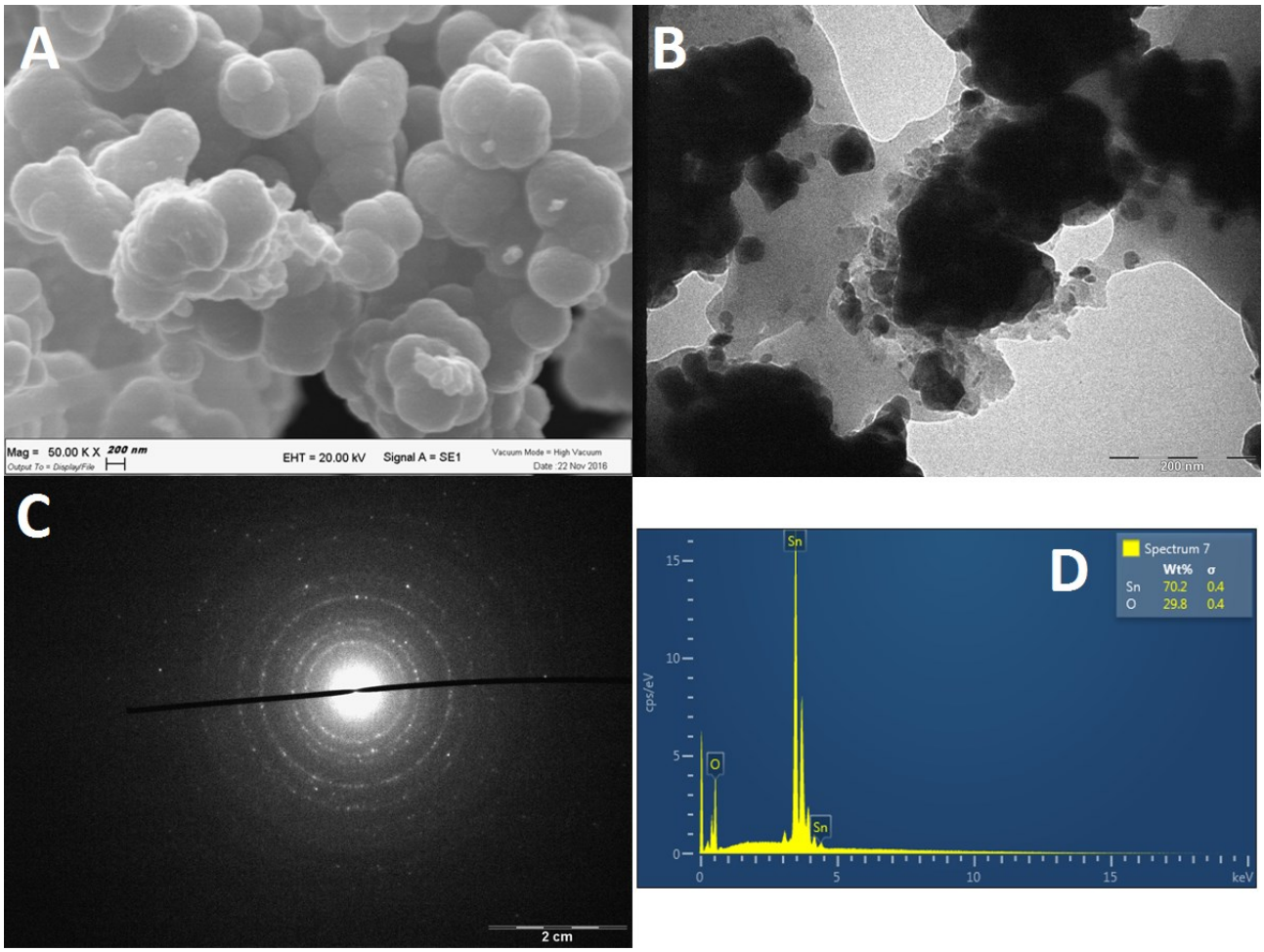

Figure 1.63: A – SEM image of SnO_2 nanostructure (scale: $200nm$); B – TEM image of SnO_2 nanostructure (scale: $200nm$); C – TEM diffraction image of SnO_2 nanostructure (scale: $2cm$); D – EDS analysis SnO_2 nanostructure [47].

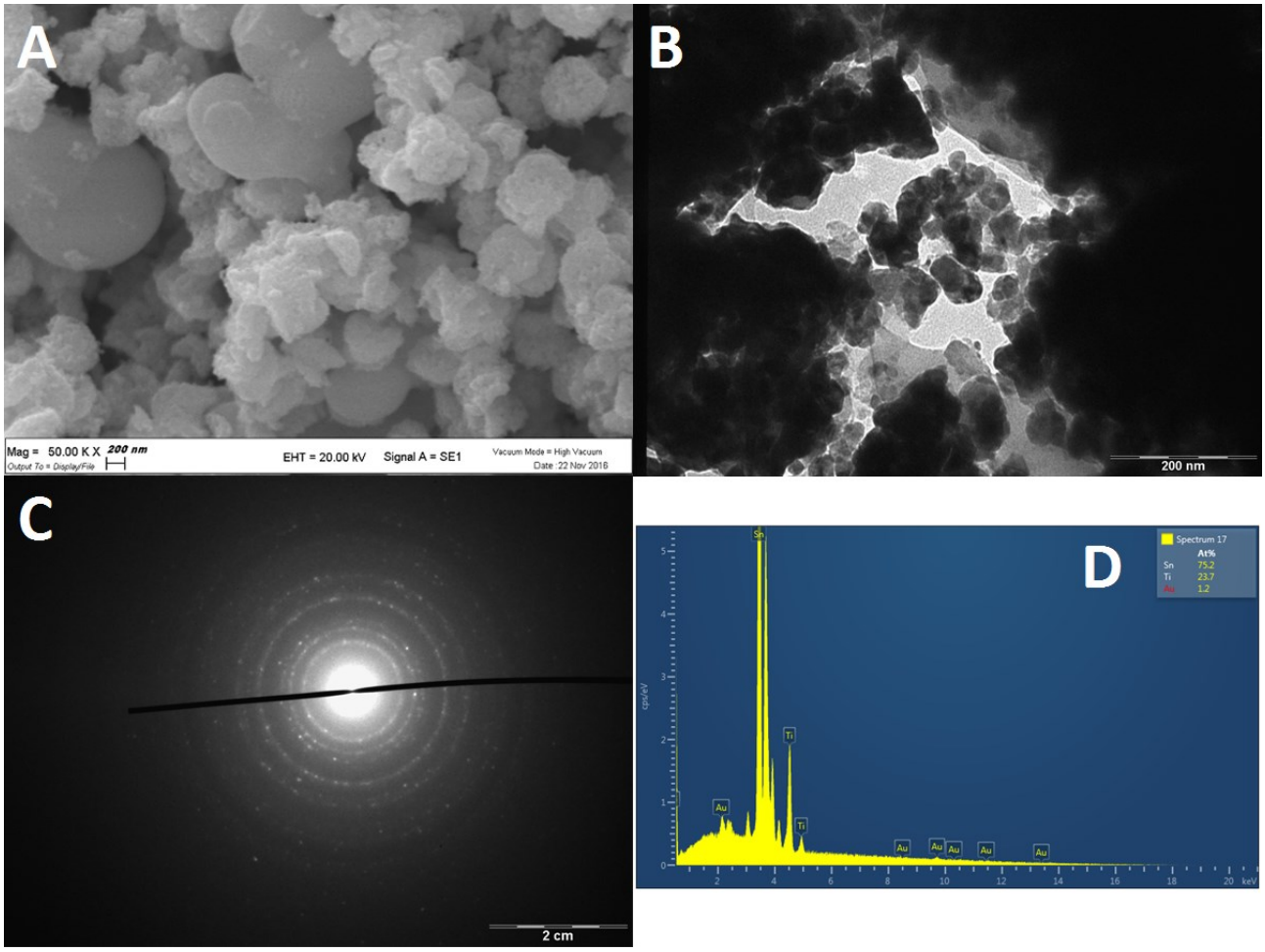

Figure 1.64: A – SEM image of ST25 650+Au nanostructure (scale: $200nm$); B – TEM image of ST25 650+Au nanostructure (scale: $200nm$); C – TEM diffraction image of ST25 650+Au nanostructure (scale: $2cm$); D – EDS analysis ST25 650+Au nanostructure [47].

1.2.8.4 – WO_3-Based Materials

Tungsten trioxide has been investigated mainly because of its wide number of crystalline forms. Like SnO_2 it behaves as an n-type semiconductor because of lattice defects in particular, oxygen vacancies acting as electronic donor levels. However it shows a band gap ranging from 2.5 to $2.8eV$ (Erbs et al., 1984 [43]) and contemporaneously a conductance value, at low temperature, almost three orders of magnitude higher than SnO_2. Both materials present the same trend versus temperature, but a very low value in the case of WO_3 to detect oxidizing gases. Also the preparation of mixed oxides of tungsten and tin tends to exhibit the same behavior in relation to oxidizing gases. Indeed, as shown in Chiorino et al., (2001) [44], adding 1 or 5% of W in SnO_2 progressively

modifies the sensing properties of the sensors from the detection of reducing to the detection of oxidizing gases. In this work only pure WO_3 film (sometimes named W11 for sake of classification).

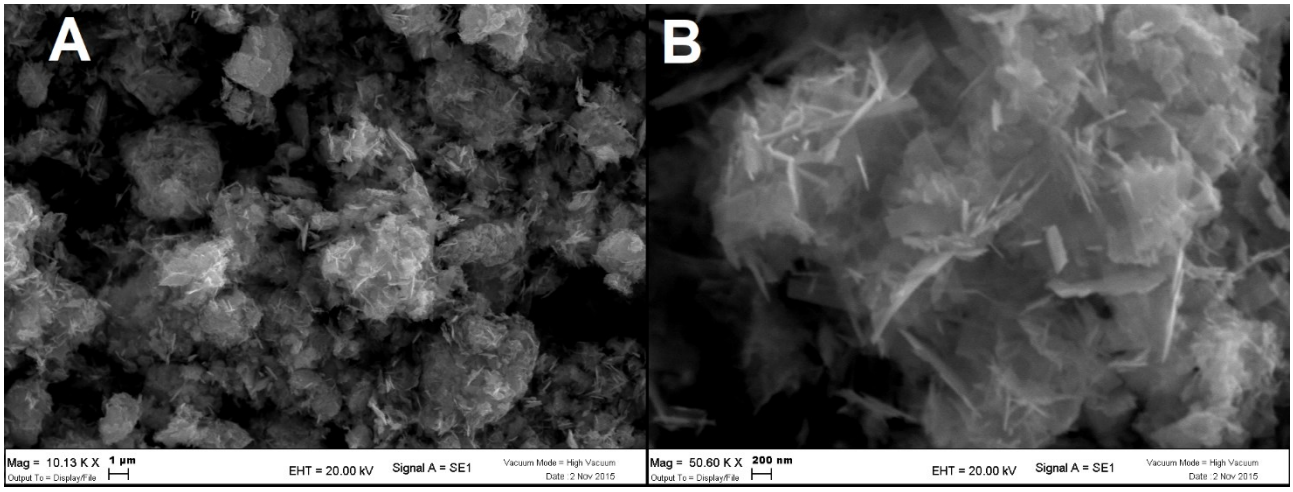

Figure 1.65: A – SEM image of WO_3 nanostructure (scale: $1\mu m$); B – SEM image of WO_3 nanostructure (scale: $200nm$).

1.2.8.5 – S-Based Materials

Cadmium sulfide (CdS) [45] is a wide gap semiconductor ($E_g = 2.40eV$), used in many fields of science and technology due to its interesting chemical and physical properties. In particular, this material shows piezoelectricity, photoconductivity, chemoresistivity and electroluminescence. Owing to these properties, CdS-based devices can be employed as solar cells, photoresistors, piezoelectric transducers and gas sensors CdS nanoparticles were synthesized by an aqueous precipitation route at room temperature and atmospheric pressure. In a typical preparation, $2.66g$ of cadmium acetate hydrate ($10mmol$) ando-diaminobenzene ($2.16g$, $20mmol$) were dissolved in water and stirred for two hours. Then, $20mmol$ of thioacetamide ($1.5g$) were added to the solution and the mixture was stirred again for six hours. A yellow-orange precipitate was formed. It was isolated by vacuum filtration and washed several times with water and methanol. Finally, the product was dried for four hours at $40°C$. The sensing layers were realized by adding a proper amount of organic vehicles to the CdS powder, in order to obtain a screen-printing paste with the right viscosity for the deposition of thick-films onto alumina substrates (resulting thickness $\sim 20-30\mu m$).

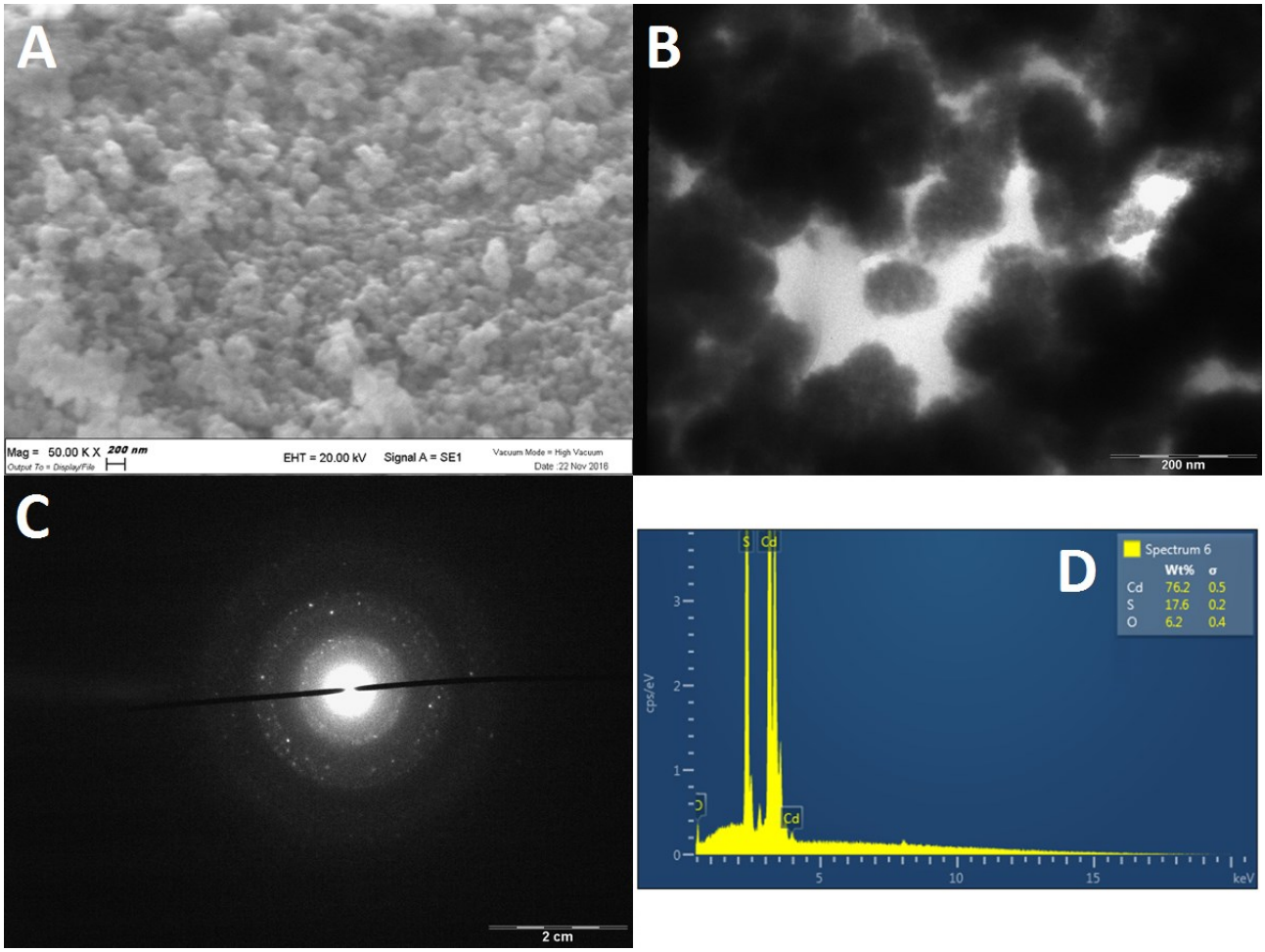

Figure 1.66: A – SEM image of CdS nanostructure (scale: $200nm$); B – TEM image of CdS nanostructure (scale: $200nm$); C – TEM diffraction image of CdS nanostructure (scale: $2cm$); D – EDS analysis CdS nanostructure [47].

1.2.8.6 – Fe-Based Materials

$SmFeO_3$ thick-films instead prepared using oxide powders from the thermal decomposition of the heteronuclear complex, $Sm[Fe(CN)_6]\cdot 4H_2O$. The films were screen-printed on alumina substrates with comb-type Au electrodes. The heteronuclear complex, $Sm[Fe(CN)_6]\cdot 4H_2O$, was synthesized by mixing aqueous solutions of equimolar amounts of $Sm(NO_3)_3\cdot 6H_2O$ and $K_3Fe(CN)_6$ under continuous stirring. The resulting precipitate was washed with water, ethanol and diethyl ether, before drying in air at $50°C$. The $SmFeO_3$ oxide powders were prepared by the thermal decomposition of the complex at $700°C$ for 30 minutes. The lowest temperature was chosen from thermogravimetric analysis, at which the complex is completely decomposed [46]. The thick-films were deposited from pastes prepared by adding to the $SmFeO_3$ powder an organic vehicle containing mainly

ethyl-cellulose and *α*-terpineol and 1 wt.% of a sintering aid for improving the adhesion of the layers to the substrates. In a first set of samples, the paste which was used contained 25 wt.% of *α*-terpineol over the total content of the paste. The pastes were printed on 96% alumina substrates precut in squares of 2.54 by $2.54mm^2$ area, each one provided with an adequate heater element and comb-type gold electrodes for electrical measurements. The films were then fired for one hour at various temperatures in the range of $750-1000°C$, in flowing N_2 or air. The curve behavior of $SmFeO_3$-kind sensors resembles the ones of oxidative responses (p-type).

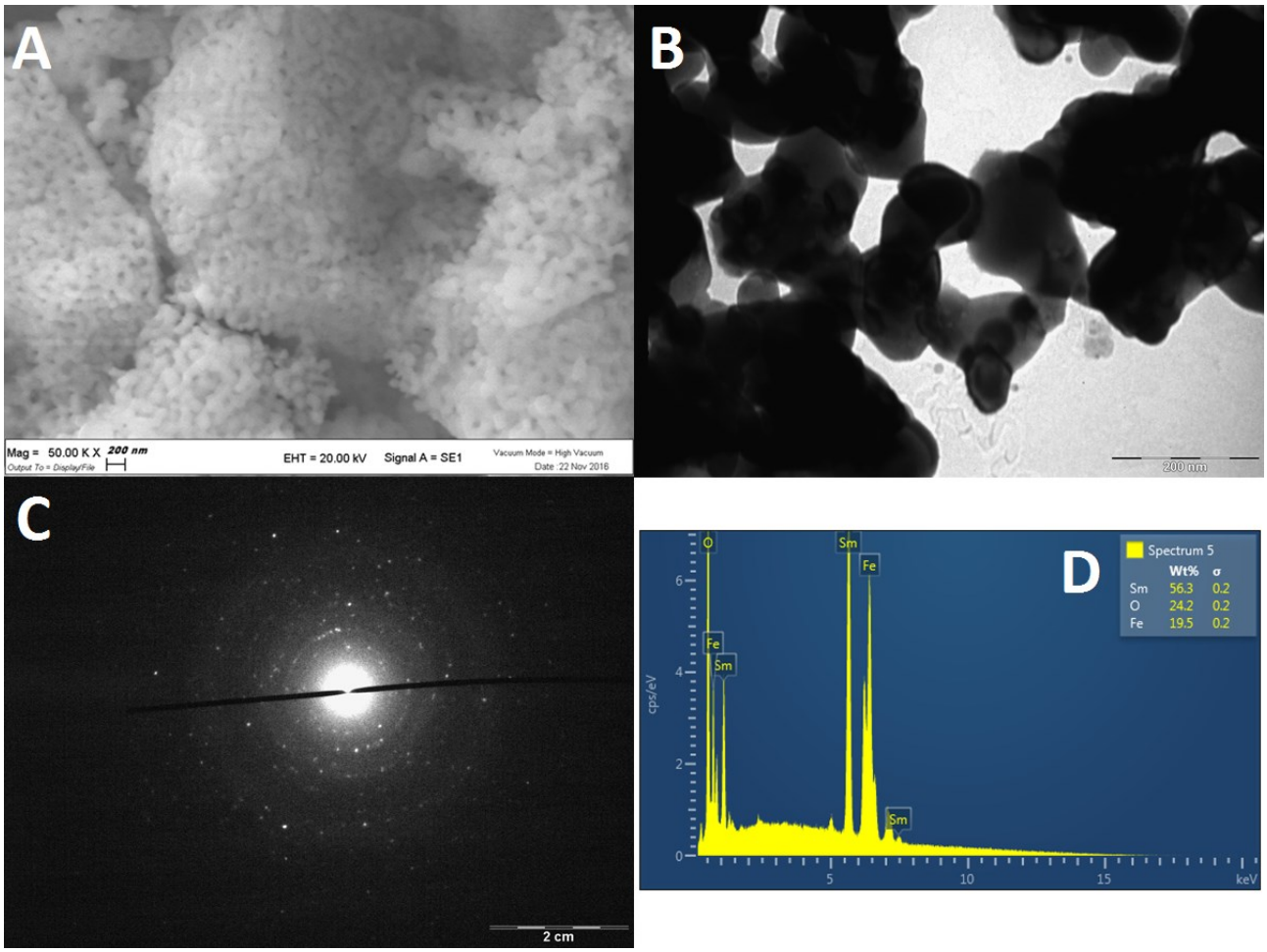

Figure 1.67: A – SEM image of $SmFeO_3$ nanostructure (scale: $200nm$); B – TEM image of $SmFeO_3$ nanostructure (scale: $200nm$); C – TEM diffraction image of $SmFeO_3$ nanostructure (scale: $2cm$); D – EDS analysis $SmFeO_3$ nanostructure [47].

1.2.9 – Sensors Working Temperatures

To let the sensing units perform at their best, identify the best working temperatures for each sensor is mandatory. To do that, an apparatus consisting in a polystyrene box where sensors are connected to a multimeter with a four-tip output (in order to avoid the noise of about $0{,}4\Omega$ introduced by a standard two-tip output) that measures their resistance at ambient temperature. The temperature is measured after some minutes of stabilization by a thermometer put inside the box. By applying Equation 2.5 is possible to obtain the resistance to be set so that the heater could bring the sensing film at a given temperature. Working temperatures data for the sensors used in this work are listed in table 1.2:

CODE	SENSOR	Rh_{amb}	T_{amb}	R0	200	250	300	350	400	450	500	550	600	650
139A/A4	ST20 650	8.896	20.1	8.25	14.43	15.91	17.36	18.77	20.16	21.53	22.86	24.17	25.44	26.69
142C/E11	ZnO 850	9.489	20.1	8.80	15.40	16.97	18.51	20.03	21.51	22.96	24.38	25.78	27.14	28.47
102 A A6	SnO2	9.027	22.8	8.30	14.51	15.99	17.44	18.87	20.27	21.63	22.97	24.29	25.57	26.83
154 A1	SmFeO3	9.934	22.4	9.14	15.99	17.62	19.22	20.79	22.33	23.84	25.32	26.77	28.18	29.56
158A A2	ST25 650+Au	7.970	21.3	7.36	12.88	14.19	15.48	16.75	17.99	19.20	20.39	21.56	22.70	23.81
11	CdS2	9.35	20.8	8.65	15.13	16.68	18.20	19.68	21.14	22.57	23.97	25.34	26.67	27.98
173 A12	ST 25 650+Au B	10.7	23.6	9.81	17.15	18.90	20.62	22.30	23.95	25.57	27.16	28.71	30.22	31.71
129/E8	STN	9.049	24.2	8.28	14.47	15.95	17.40	18.82	20.21	21.58	22.92	24.23	25.51	26.76
86A A8	TiTaV	9.255	23.7	8.48	14.83	16.34	17.83	19.28	20.71	22.11	23.48	24.82	26.13	27.42
97 A	W11	8.890	22.9	8.17	14.28	15.74	17.17	18.58	19.95	21.30	22.62	23.91	25.17	26.41

Table 1.2: Resistances associated to the various working temperatures of the sensors used.

where R is the resistance at ambient temperature, measured in Ω by the multimeter (with an error of 0.001Ω, because the following digits are variable); T is the ambient temperature, indicated in $°C$ (with an error of $0.1°C$); R_0 is the resistance at $0°C$, in Ω, calculated by inverting Equation 2.5 and other values are the resistances to be set to obtain temperatures from 200 to $650°C$, through Equation 2.8. Errors for these last values can be obtained using the formula for error propagation. By reversing Equation 2.5, it is possible to obtain:

$$R_0 = \frac{R_h}{1 + \alpha T + \beta T^2} \qquad (1.155)$$

so, its error should be calculated in the following way:

$$\Delta R_0 = R_0 \left(\frac{\Delta R_h}{R_h} + \frac{\Delta(1 + \alpha T + \beta T^2)}{1 + \alpha T + \beta T^2} \right) = R_0 \left(\frac{\Delta R_h}{R_h} + \frac{\alpha \frac{\Delta T}{T} + 2\beta \frac{\Delta T}{T})}{1 + \alpha T + \beta T^2} \right) \qquad (1.156)$$

$$R_0 \left(\frac{\Delta R_h}{R_h} + \frac{\Delta T}{T} \frac{\alpha + 2\beta)}{1 + \alpha T + \beta T^2} \right) \qquad (1.157)$$

For each measure, considering only three digits, the error is of 0.001Ω. For the resistance to be set to obtain desired temperatures, knowing the relative errors for power packs $\left(\frac{\Delta V_h}{V_h} = \frac{1}{100}, \frac{\Delta i}{i} = \frac{1}{1000}\right)$, are given by the formula $\Delta R_h = \left(\frac{\Delta V_h}{V_h} + \frac{\Delta i}{i}\right) R_h = 0{,}011 R_h$.

This corresponds to a relative error of about 4% on the temperature.

Chapter 2 – SCENT B1 Prototype

In this thesis, all the experiments were conducted on a device developed in collaboration with the startup SCENT S.r.l., and thanks to the fundings supplied from this society. The device, actually patented in Italy, is called SCENT B1 (patent number: 102015000057717 on 8 March 2018). The prototype works like a portable sensor laboratory setup, allowing to combine different sensors into arrays and registering their electronic outputs as responses, so that an operator can monitor the experiments from a common computer (of course, having previously installed the dedicated software). In this prototypal phase, two approaches has been tried: single sensor approach (checking if the amplitude alone of the sensor response could discriminate the presence of the tumor compared to healthy control groups) and combination of the responses of all the sensors to a test into a statistical model (principal component analysis – PCA). It is important to notice that this work does not follow an e-nose approach. No machine learning system nor single tumor marker detection logic have been used. Instead, the experiment investigated with an iterative "trial and error" combination of sensors, called arrays, if a threshold system Healthy/Tumor logic could be viable, with a simpler PCA approach, able to discriminate patterns behind the responses of the sensors arrays. The reason behind this choice lays on the fact that, as widely shown in literature and observed during the medical protocol, tumor have erratic and complex production of numerous, unstable markers, which are often altered by their travel into the human body in both quantity and quality. Training a device to detect one or few molecules, that might not have the same form or concentration once exhaled from the blood sample, looked more like a risk in the optic of a medical screening device, rather than a simpler two-ways logic as explained above. Therefore, single sensor approaches have been carried out to see which kind of semiconductor material looked more reliable for the goal, and then Principal Component Analysis was used to combine all the information obtained from the responses to verify any capability of discrimination from the arrays and the sensors hosted in the device. A part of the preliminary studies on cells were realized on a previous device, as part of a Master's Degree thesis from the same author, called SCENT A1, and patented in Italy, Germany and United Kingdom (patent number: 3210013 on 28 March 2018).

2.1 – Device

The sensors were finally integrated in the testing device, SCENT B1 (patent number: 102015000057717), schematized in Figure 2.1A. Sensors are hosted inside a series of four separate metal chambers, connected one by one by a Teflon tube of $3.5mm$ internal diameter. The choice of the material with which the chambers are made was to allow the best dissipation of heat, generated by the heater included in each substrate inside the chamber. The cylindrical opening in which the sensor is hosted has $8mm$ diameter and $25mm$ depth. Each chamber contains also a SHT11 sensor [159] to monitor continuously both humidity and temperature inside of them. An electric pump kept a constant airflow through a carbon filter in series with a $0.2\mu m$ filter, so that neither foreign chemical specimens nor microorganism interfered with the experiment. Carbon filter is emptied, cleaned and replenished and antibacterial filters are changed every 10 tests, to avoid possible contaminations. After every test, the specimen chamber got cleaned by washing it with hydrogen peroxide 30%, dried and then irradiated with UV sterilizing light. Finally, the specimen chamber was connected to the air circuit again and flushed for 8 hours before usage. The sensor chambers were simply flushed for the same time. Restore of the sensors baseline after a measurement/cleaning cycle is representation that cleaning is effective. This “clean air” flux could be routed directly to the sensors to measure the baseline, or through an air-tight Teflon chamber, in which the vial containing the blood sample was inserted. This flux could be routed also by a valve to an exhaust port or to the sensors. When the flux is routed from the specimen-holding chamber to the sensors chambers, the volatile tumor markers naturally released from the blood sample get carried from one chamber to the other. This allows the sensors to detect the tumor markers in the air surrounding them, changing their voltage output. Two flux regulators were used to carefully control the airflow rate in the two lines. The constant “clean” air flux flowing to the sensors was necessary to avoid abrupt pressure changes when operating the deviator, otherwise this would affect response stability. To verify if the flux in the chambers and tubes is laminar or turbulent, the Reynold number for the flux was obtained. In order to acquire this quantity, dynamic viscosity and density of the air fluxed in the air circuit has been calculated for the conditions measured from the SHT11 sensors hosted in the chambers, that is a temperature of $28°C$ and a relative humidity of 38%. The velocity of the

flux inside the tubes was calculated from the flow rate (known, $0.0033 m/s$) and the diameter of the tubes. It resulted that:

- $\rho = 1.1697\ kg/m^3$
- $\eta = 1.8763 \cdot 10^{-5}\ Pa \cdot s$
- $v = 0.35\ m/s$

Having diameter $d_t = 3.5 \cdot 10^{-3} m$ for the tubes, the Reynold numbers resulted as:

$$Re_t = \frac{\rho v d_t}{\eta} = \frac{1.1697\ kg/m^3 \cdot 0.35 \frac{m}{s} \cdot 3.5 \cdot 10^{-3} m}{1.8763 \cdot 10^{-5} Pa \cdot s} \approx 0.7637 \cdot 10^2 = 76.37 \quad (2.1)$$

Since the number calculated at the working condition of the prototype is much smaller compared to the threshold of transition between laminar and turbulent behaviors for straight tubes with circular section ($Re > 2000$, [160]), it is possible to say that the flux flowing in the tubes remains laminar with good approximation. From previous works, it was possible to observe that heating from the heater enclosed in the substrate give negligible effects to the surrounding environment, not effecting significantly the laminarity of the air-flow [161]. The variations in the sensors output voltage were then acquired by custom made software written in Labview®, which continuously plotted the updated sensor responses (a visualization of the raw data processed by the software is shown in Figure 2.1B; each trace was labelled with a color coding each sensor, in this case from the second sensors array 2). Beside the operative switches, whose functions are obvious (INSTANT. DATA, STOP, OPEN, SHOW CHART, COM PORT and the acquisition start/stop hotkeys on the top of the screen), the most important ones are SETTINGS, which control the working temperature of the sensors, and DATA LOGGER, which returns a set of twelve numbers, updated every 10 seconds (the acquisition rate), which represent the voltage response (mV) of the sensors, and the temperature ($°C$) and the relative humidity ($\%$) measured in each one of the four chambers where are allocated the four sensors. Since chemoresistivity changes the conductance/resistance of the semiconductor material hosted in the circuit, a variation in the output voltage is measurable from the custom electronic. The four labeled (a – d) traces of the screenshot represent the output voltage generated by each one of the four sensors of an array (in this case the second sensors array: a → SnO2, b → ST 25 650+Au, c → SmFeO3, d → CdS) in response to three different blood samples (identified with the number 1, 2, and 3) in function of time.

The x-axis represents the number of points acquired: 1 point corresponds to 10 seconds. The four responses in the example are from a blood test: the ones labeled with 1 are relative to the exhalation from a healthy blood sample, the ones labeled with 2 are from an individual with a small colorectal cancer, and the ones labeled with 3 are from an individual with a large stomach cancer. To have the results independent from the voltage baseline at which each sensor worked, since the condition of work were heavily safe and sterilized for all the sample, the ratio *R* was calculated as average value between the average response amplitude V_{sens} (in the presence of the sample) and the average baseline V_0 (in the sample absence) for three successive tests (named A, B and C) over the same sample, instead of a single test as described from Equations 1.87 and 1.135, according to the formula: $R = \frac{\frac{V_{sensA}}{V_{0A}} + \frac{V_{sensB}}{V_{0B}} + \frac{V_{sensC}}{V_{0C}}}{3}$.

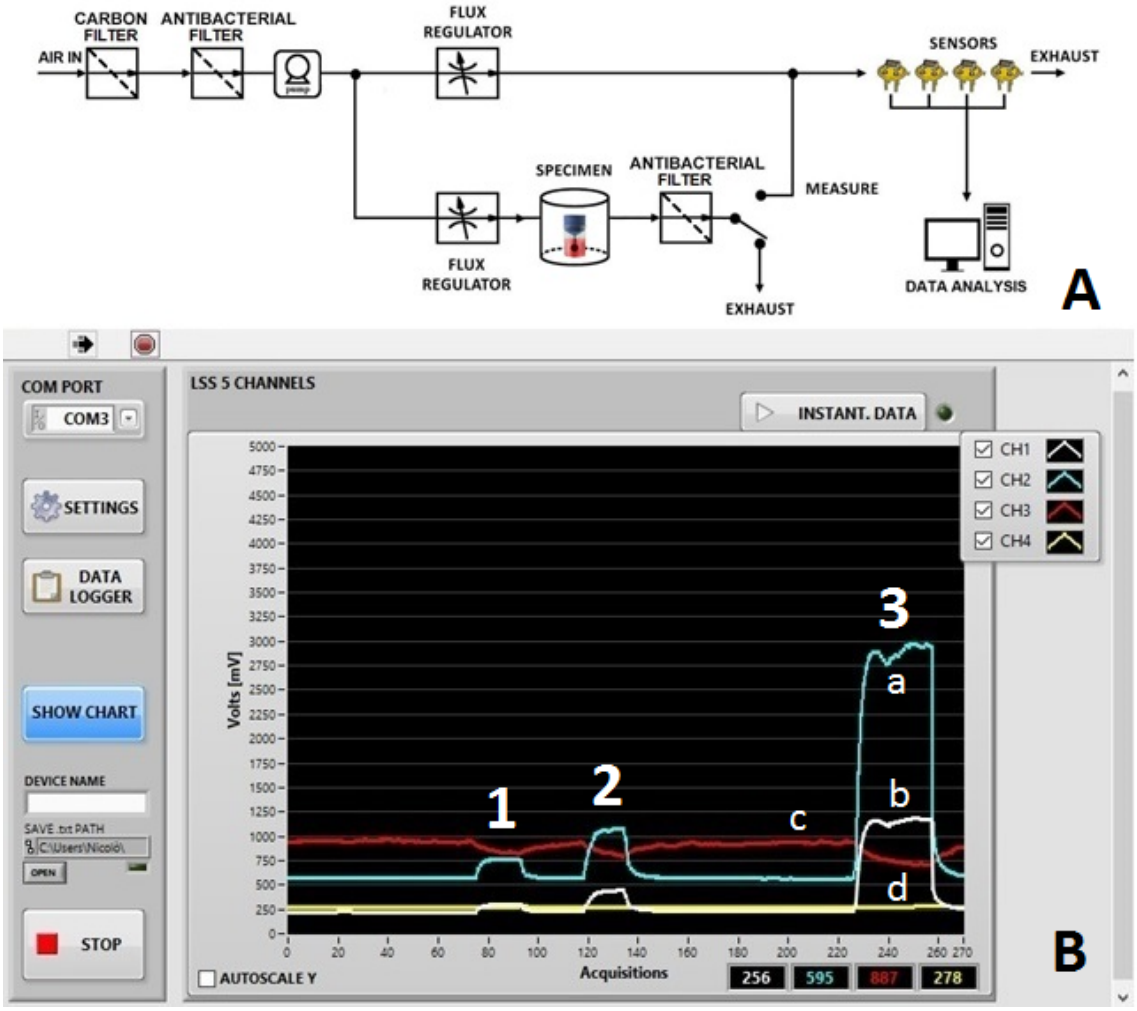

Figure 2.1: A – Schematization of SCENT B1. B – Screenshot of the Labview® acquisition software control panel [47].

2.2 – Electronic Circuit

In order to detect the changes in conductance of the sensor, it is necessary to insert the sensing unit inside a circuit, represented in Figure 2.2:

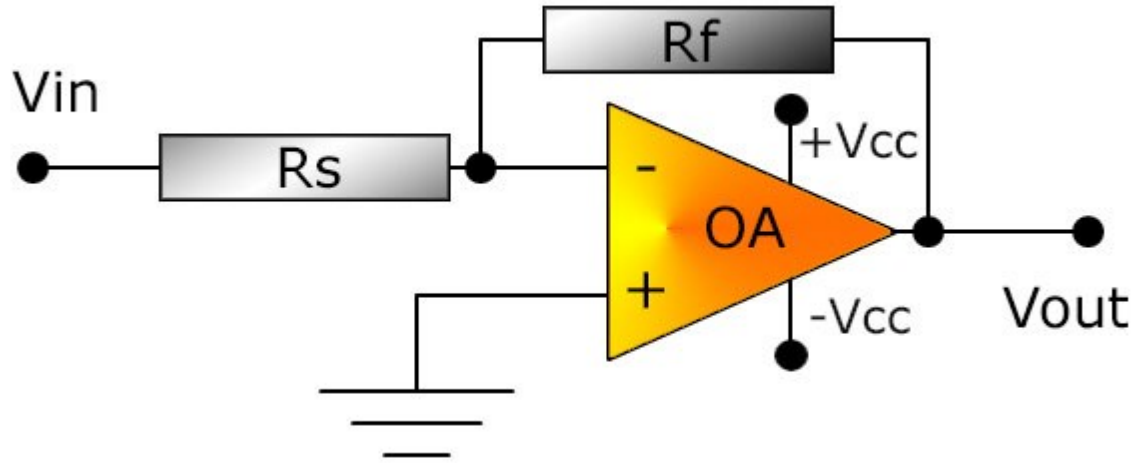

Figure 2.2: Circuit in which the sensor is hosted [34].

This is an inverting operational amplifier (OA), in fact the input signal is connected at the negative entrance of the amplifier, while the positive one is grounded. At the ends of the resistors R_s and R_f there are respectively the voltage values V_{in} and V_{out}, so:

$$\frac{V_{out}}{R_f} = -\frac{V_{in}}{R_s} \quad (2.2)$$

The gain is given by:

$$\frac{V_{out}}{V_{in}} = -\frac{R_f}{R_s} \quad (2.3)$$

Fixing $V_{in} = -5V$, because of the virtual short circuit to the inputs of the OA, the inverting input terminal is at the same potential that the non-inverting input terminal. This way the sensor is subjected to a constant potential difference of $5V$ until the OA works far from saturation. Being the values of V_{in} and R_f known and constant, the output voltage V_{out} is then proportional to the conductance:

$$V_{out} = -R_f \cdot V_{in} \frac{1}{R_s} = -const \cdot G \quad (2.4)$$

Moreover, the expression of for response assumes a really simple shape, independent from the circuit parameters:

$$\frac{G}{G_{air}} = \frac{V_{out}(gas)}{V_{air}(air)} \quad (2.5)$$

where G is the conductance in the presence of the gas and G_{air} the conductance measured without the gas. The wordings gas or air indicate the presence or not of the gas to measure. For what concerns the heater, the circuit is represented in Figure 2.3.

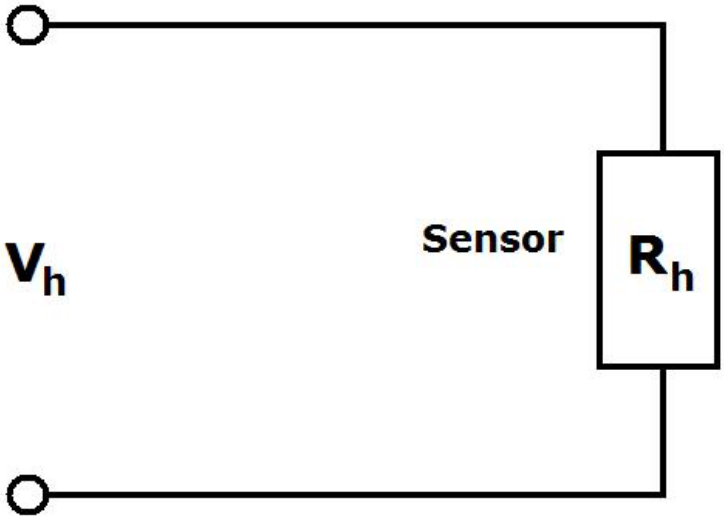

Figure 2.3: Heater circuit [34].

The heater is a thermal sensor and consists of a platinum coil in which resistance increases linearly with temperature. The relation between temperature and resistance is the following:

$$R_h = R_0(1 + \alpha T + \beta T^2) \quad (2.6)$$

in which R_h is the resistance at room temperature, R_0 is the resistance at $0°C$, T is the temperature at which the operator wants to set the sensor, while α and β are two characteristic constants of the material. For the specific case of platinum, they are:

$$\alpha = 0.003263°C^{-1}G \quad (2.7)$$

$$\beta = -6.6668 \cdot 10^{-7}°C^{-2}G \quad (2.8)$$

By measuring the resistance at room temperature and inverting the Equation 2.5 is possible determine R_0. At this point, choosing the working temperature it is possible to find

the corresponding R_h. Applying a voltage V_h to the circuit the current that circulates, according to Ohm Law, will be:

$$R_h = \frac{V_h}{i} \quad (2.9)$$

where V_h is established by the user and the current is measured by the feeder. It is so possible to control and directly modify R_h and so the temperature of sensors (modifying V_h).

2.3 – Safety, Operational and Cleaning Procedures

The device requires a proper relaxation time after every sample removal, to clean the sensors film, the sensor chambers and the teflon box itself from remaining chemicals. In order to avoid contaminations from the external environment, a carbon filter in series with two $0.2\mu m$ antibacterial filters, on the connectors of the sampling box, avoid alterations so that neither foreign chemical specimens nor microorganism can interfere with the experiment, as stated in Paragraph 2.1. Blood and biological tissues samples are both sources of and ideal ground for pathological agents, while cells are really susceptive to any contaminant present in the teflon box in which they are contained. To keep the samples safe, each kind of sample was hosted from a different teflon container, so to not mix and possibly contaminate specimen from the same donor, tested the same day. To sterilize each box after usage, both liquid soap and 30% hydrogen peroxide were used to kill any possible bacteria inside of it. H_2O_2 works particularly well, killing any possible bacteria without the ability to sporulate (leaving them defenseless to that chemical); also, this chemical remains get removed fast enough and does not leave any long lasting compound altering responses (ethanol instead, for example, requires more time to be removed from the sensitive chambers from the flux). After the chemical cleaning, the container meets its final step of sterilization under UV lamps. Cells can be washed from breeding ground and be tested again as well, leaving just a thin film of nutrient fluid and allowing a closer measure to the pure metabolites production per second, as shown in Figure 5.5. This leads also to another possibility, though, studied in the Master's Degree thesis from the same author. Cells require care on the safety of their environment, not only for the possible contaminations but also because the breeding ground too can be tested

alone (see Figure 5.5), once washed away from the cells into another petri dish, and monitored again to detect further exhalations from markers still trapped in the medium and freed later. The positive results from this application led to the idea of testing another nutrition fluid, blood itself, to detect the presence of tumors far from the sampling zone. This has been possible thanks to the fact that the markers expelled from vascularized malignant tumors pollute the cardiovascular system, and are carried around the body from the blood stream. This application actually gave the best results in this work [47]. All biological samples are hazardous and potentially pathological, thus they require extra care and strict measures to avoid contagion during the test and the disposal of the sample. Masks and gloves were mandatory for all measurement operations, as well as for the preparation under sterilized/aseptic and different laboratory fume cupboards, to avoid that microorganism could infect the cells, the human tissues or the blood samples). Multiple tests have been realized for each sample, to verify the repeatability of the screening and the temporal evolution of the emissions.

2.4 – Sensors Arrays

Due to the amplitude of targets, various sensors arrays were tested, depending on the aim of the analysis. The sensors used for this thesis have been already shown in the section regarding the working temperatures (Paragraph 1.2.9, Table 1.2) and are here discussed further (with their identification codes between parenthesis):

- TiTaV (86A A8), a sensor based on titanium, tantalum and vanadium oxides
- ST20 650 (139A A4), a sensor based on tin oxides and titanium (20%) with a firing temperature of 650°C
- STN (129 E8), a sensor based on tin, titanium and niobium oxides with a firing temperature of 650°C
- ST 25 650+Au (158A A2) and ST 25 650+Au B (173 A12), two sensors based on tin oxides and titanium (25%) and gold (1%) with a firing temperature of 650°C
- ZnO 850 (142C/E11), sensors based on zinc oxide with a firing temperature of 850°C
- CdS2 (11), a sensor based on cadmium sulfide with a firing temperature of 180°C

- SnO2 (102 A A6), a sensor based on pure tin oxide with a firing temperature of 650°C
- W11 (97 A), a sensor based on tungsten oxide with a firing temperature of 650°C
- $SmFeO_3$ (154 A1), a sensor based on samarium and iron oxide with a firing temperature of 750°C

The sensors names are internal to the laboratory and do not refer strictly to the chemical names of powders. Those kind of sensors have been chosen due to their capability of recognize tumor markers, defined from previous tests on laboratory setup and other prototypes, carried on standard gas bottles, feces, and cell cultures, during other work of thesis and researches. Overall, five sensors arrays have been hosted inside SCENT B1. In the following tables, the combinations are presented, together with their code and working temperature WT:

FIRST SENSOR ARRAY (ARRAY 1)		
SENSOR	**CODE**	**WT (°C)**
ST 25 650+Au	158 A2	450
ZnO 850	142C E11	450
SmFeO3	154 A1	350
CdS2	11	250
SECOND SENSOR ARRAY (ARRAY 2)		
SENSOR	**CODE**	**WT (°C)**
ST 25 650+Au	158 A2	450
SnO2	102 A A6	450
SmFeO3	154 A1	350
CdS2	11	250
THIRD SENSORS ARRAY (ARRAY 3)		
SENSOR	**CODE**	**WT (°C)**
ST 25 650+Au	158 A2	450
W11	97 A	450
SmFeO3	154 A1	350
ST 25 650+Au B	173 A12	450
FOURTH SENSORS ARRAY (ARRAY 4)		
SENSOR	**CODE**	**WT (°C)**
ST 25 650+Au	158 A2	450
W11	97 A	450
ST20 650	139A A4	450
ST 25 650+Au B	173 A12	450
FIFTH SENSORS ARRAY (ARRAY 5)		
SENSOR	**CODE**	**WT (°C)**
ST 25 650+Au	158 A2	450
W11	97 A	450
STN	129/E8	450
TiTaV	86A A8	450

Table 2.1: Sensor arrays composition.

As it is noticeable, ST 25 650+Au has been kept for all the sensors arrays, and even doubled in the third and fourth array. The reason behind it lays not only for its high sensitivity and fast response (actually, the best between all the sensors tested by now), but also because it gave the best single sensor approach responses. Due to the fact that it was not always possible to obtain samples of every kind for all the arrays used (some sensors did not manage to survive prolonged use during 3 years of researches, and few power surges took their toll on some of them, too), the following list divides the arrays used for which type of specimen:

- **CELL CULTURES TESTS:**
    - First Array
    - Third Array
    - Fourth Array
- **HUMAN BLOOD TESTS:**
    - **First Data Set:**
        - First Array
        - Second Array
    - **Second Data Set:**
        - Fifth Array
- **HUMAN TISSUES TESTS:**
    - Single sensor approach from first, second and fourth sensors arrays (ST25 650+Au)
    - Fifth Array

Chapter 3 – Statistics

In order to process the information acquired by the device, and obtain displayable and easily understandable results, the great amount of data need to undertake some statistical approach. In this case, single sensor approach (organizing the responses for each sensor, highest to lowest, to observe trends merely on the amplitude of their output) often does not suffice to discriminate behavior patterns between the data, since chemoresistive sensors response is modulated by electrons freed to conduce or stolen from the CB by the oxygen ions binding in the lattice vacancies, and not directly from the type of chemical reacting. For this reason, more complex statistic approaches are mandatory to perform a good analysis and draw a recognition model between healthy and tumor affected blood and tissue samples, or even cell samples from different lines. In this thesis, principal component analysis (PCA) was the chosen method to process the data and obtain a visible separation between the different groups of donators. It has been chosen as statistical method, because it allows to plot and visualize patterns (in this case, healthy vs tumor affected individuals) within enormous data sets, even with a great number of dimensions (each sensor giving an output is a dimension, in the experiment). Even if it is a well-known statistical method, applied in a variety of fields, for sake of completeness and help the reader to understand the reasons behind this choice of approach, the next subchapters are dedicated to characterize and swiftly explain the operation needed to process a set of random data with PCA.

3.1 – PCA: Principal Component Analysis

PCA is a statistical method used to identify patterns in data, and expressing the data in such a way as to highlight their similarities and differences. Since these patterns can be hard to find in data of high dimension, where the luxury of graphical representation is not available (in this work, 4 dimensions/sensors, each with an entry for test), PCA is a powerful tool for analyzing data. The other main advantage of PCA is that once these patterns are found, and the data compressed, for example by reducing the number of dimensions, the finally result will be displayed without much loss of information. The data were processed with PCA by first identifying the principal components (PCs) of the data set (the eigenvector of the covariance matrix ordered by eigenvalue, highest to lowest. For

the first data set (see Figures 7.9 and 7.10), 4 PC# (PC1, PC2, PC3, and PC4) were extracted, because each one of the two arrays used for that set of blood samples is composed by four sensors, and the number of dimensions of the new covariance matrix is the same of the data set. Since PC4 was the lesser significant component (for instance, variance weight sum of PC1+PC2+PC3 gave 99.9% of the statistical weight in the second sensors array), it was ignored in the analysis presented in Figures 7.9 and 7.10. For what concerns the second data set on blood samples, three sensors (STN, TiTaV and ST25 650+Au1%) showed promising trends with single sensor approach, while the W11 sensor did not; for this reason, that PCA was conducted only using the first three sensors, and discarding the fourth. The intrinsic positive trends saw in the single sensors approaches (Figure 7.11) are reflected from the 99% of explained variance (see Equation 3.1) between PC1 and PC2 combined (as shown in Figure 7.12), with nearly no overlap between the "Healthy" and "Cancer" areas. The data for all PCAs were organized in two plots, VARIABLES and SAMPLES, as follows:

- VARIABLES (loadings), showing what type of sensor composing each array are influential for the discrimination between healthy and cancer-affected patients, and how the variables are correlated to each other. Closer are two dots (representing two sensors) in this plot, similar is their discriminating power. Farther are the points, more diverse are the behavior of the sensors and better is the chance that an instrument having an array of these sensors is capable to detect differences among the samples. This distance allows also to assess the performance of a particular sensor in respect to another one, that can be, for instance, particularly efficient (as the ST25 650+Au). From a mathematical point of view, variables are the weight by which each original variable (the sensors) should be multiplied to get the component score (which are combined in the SAMPLE dots), correlations between the original variables and the unit-scaled components in the SAMPLES graphic. They are in fact the coefficients of the linear combinations defining the PC.
- SAMPLES (scores), showing the similarity or dissimilarity of the responses (i.e. how they relate to each other), therefore representing a summary of the sensor responses. Farther are two points obtained by two measurements from a sensors array, on two different blood samples, better is the capability of the array to discriminate between the two samples. Each point corresponds to one blood

sample, with all the information carried from the sensors in the array mutually connected by covariance (as PCA is normally developed). Responses are translated from a 3/4-dimensional space with independent variables having the same information weight (33/25% respectively, for each sensor in the array, as will be explained in the subchapter 3.1.1), to a 2-dimensional space with PC# variables depending from the responses of all the sensors in the array, helping to visualize the grouping trends of the sensors behavior to the samples. Scores are, to summarize, the transformed values corresponding to a particular data point, containing contributions from all the previous variables (so, each dot is one measure, containing information about all the 4 sensors responses to that particular blood sample).

In both plots, the percentage values in parentheses, next to the PC axis, shows how much of the total variance is contained in that component. This “percentage of variance” is called **explained variance**, and is the proportion of variance associated to that “i” eigenvector (PC), having λ_i as characteristic eigenvalue. It refers to the statistical quality of the principal component itself, being the variance a track of the matrix of covariance from which the PCA was originally calculated; the higher the value, the more information from the original set is contained in that PC. Equation 3.1 shows how it is calculated.

$$\% = \frac{\lambda_i}{\sum_{i=1}^{n} \lambda_i} * 100\% \qquad (3.1)$$

While using PCA, the different groups of tumor-affected donors were combined into a single “Tumor” or “Cancer” macro-group. The reason behind that choice was to test the efficiency of the device, verifying capability of separation between two populations: healthy and ill individuals. Examples of the full protocol for blood tests are schematized on Figures 7.5 and 7.6. In this final analysis, the team has not pre-processed the R data obtained as stated above. The PCA software provides an automatic pre-processing utility that sets the center of mass of the data at zero. The data shown in Tables C.1–14 were processed accordingly. One final note referred to the substitution of sensors: if an array does not show promising results to recognize separation of the macro-groups with Principal Component Analysis, sensor rejection and its substitution follows this protocol:

1. Average value and standard deviation of healthy and tumor affected macro-groups, for each sensor, are calculated. The intervals of the groups are set to two-sigma

2. The sensor showing the greatest overlap is rejected

After these steps, a new sensing unit is tested with Principal Component Analysis approach. Selection of the new sensors is based on the users' personal experience.

3.1.1 – Method

The data are divided, with the resulting outputs columned under their "dimension"; for the experiments, "dimensions" are the sensors used in the array, which means four for the prototype. In this example (Figure 3.1), the dimensions are two, to give an easier understanding to the mechanics behind this approach. The local average value is then subtracted from each of the data dimensions, across each dimension; all the x values have $\bar{x}$ (the mean value of the x values of all the data points) subtracted, and all the y values have $\bar{y}$ subtracted from them. This produces a data set which mean, and thus its "center of mass", is zero, normalizing it.

	x	y		x	y
	2.5	2.4		0.69	0.49
	0.5	0.7		-1.31	-1.21
	2.2	2.9		0.39	0.99
	1.9	2.2		0.09	0.29
Data	3.1	3.0	**Normalized Data**	1.29	1.09
	2.3	2.7		0.49	0.79
	2	1.6		0.19	-0.31
	1	1.1		-0.81	-0.81
	1.5	1.6		-0.31	-0.31
	1.1	0.9		-0.71	-1.01

Table 3.1: A – Data set used as example. B – Normalized data set.

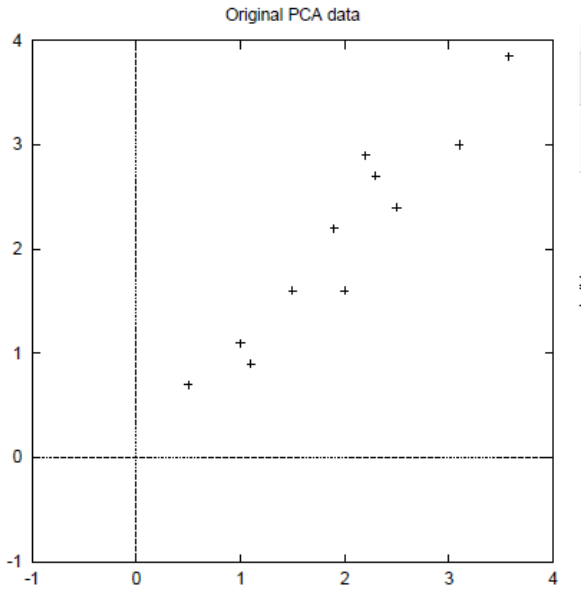

Figure 3.1: Plot of the data from Table 3.1 [165].

The covariance matrix is then calculated from the new normalized data. Since the data set is 2-dimensional, the covariance matrix will be 2 X 2.

$$cov = \begin{pmatrix} 0.6166 & 0.6154 \\ 0.6154 & 0.7166 \end{pmatrix} \quad (3.2)$$

In this case, being the non-diagonal elements in this covariance matrix positive, the two variables x and y will increase together. Since the covariance matrix is square, it is possible to calculate its eigenvectors and eigenvalues. These are rather important, as they bring useful information about the data, like the "weight" of the information contained in the new set of data.

$$eigenvalues = \begin{pmatrix} 0.4908 \\ 1.2840 \end{pmatrix} \quad (3.3)$$

$$eigenvectors = \begin{pmatrix} -0.7352 & -0.6779 \\ 0.6779 & -0.7352 \end{pmatrix} \quad (3.4)$$

It is important to notice that these eigenvectors are both unit eigenvectors (their lengths are both 1). This, because as shown in the plot in Figure 3.2, the two eigenvectors will work as a base of the new set of data, at the end of the PCA. As expected from the covariance matrix, the two variables do indeed increase together. The eigenvectors, more importantly, provide information about the patterns in the data. In fact, one of the two eigenvectors goes through the middle of the points, like drawing a line of best fit, showing how these two data sets are related along that reference. The second eigenvector results in the other, less important, pattern in the data: all the points follow the main eigenvector, but are offside by some amount, defined quantitatively from the eigenvalue correlated to that secondary eigenvector.

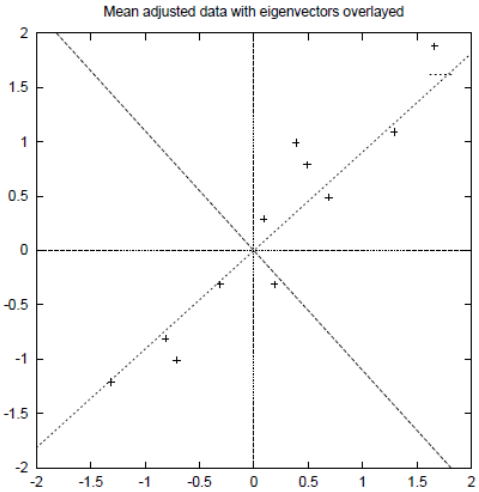

Figure 3.2: Plot of the normalized data (mean subtracted) with the eigenvectors of the covariance matrix overlaid on top [165].

So, by this process of taking the eigenvectors of the covariance matrix, it has been possible to extract components that characterize the data. The rest of the steps involve transforming the set so that it is expressed in terms of the eigenvectors, that will become the new base of reference of the system of data. Here is where the notion of data compression and reduced dimensionality comes in the analysis. Looking at the eigenvectors and eigenvalues from the previous section, it is possible to notice that the eigenvalues are quite different values. In fact, it turns out that the eigenvector with the highest eigenvalue is the principal component 1 (PC1) of the data set. In this example, the eigenvector with the larges eigenvalue was the one that pointed down the middle of the data. It is the most significant relationship between the data dimensions. Once eigenvectors are found from the covariance matrix, the next step is to order them by eigenvalue, highest to lowest. This finally results in the components ordered by significance (in this case, two components, while on the prototype four sensors are hosted). It is important to notice that each component carries information from all the previous dimensions, being the entries of the eigenvectors depending from a covariance matrix. Thus, the new component carries new data including dependence from all the sensors used, and the higher the eigenvalue, the more the “information” from the previous set is contained in the principal component (eigenvector) to which it is referred. This is important, because in a normal set of data acquired from a sensing device, with no pre-processing or weighing between them of the original outputs, each dimension carries a % of information equal to:

$$i\% = \frac{100\%}{n} \quad (3.5)$$

having all the information obtained from the combination of all the sensors equal to 100%, and n the number of dimensions (as expected in this case, having 4 sensors, each brings 25%, of the information compared to the total output given form the device for each test). This is different for the eigenvectors/principal components, because given their weight (eigenvalues), they bring more or less information from the first to the last of the PC# (# = number from 1 to n, since the number of eigenvectors and original dimensions is always the same), as explained in Paragraph 3.1 with Equation 3.1, that is repeated here for sake of completeness:

$$\% = \frac{\lambda_i}{\sum_{i=1}^{n} \lambda_i} * 100\% \quad (3.1)$$

This also means that, while making a graphic between the outputs from two sensors, the total information displayed in 2D will be 50% (total information in the plot = 25%+25% from each of the two sensors), plotting PC1 and PC2 can bring up to even 91,6% or 99% of the total information from the 4 output of the machine, as shown in the Figures 7.10 and 7.12 in the human blood tests section. The fact incredibly increases the capability to observe patterns in a more intuitive, graphical way, that would not be possible with the original set of data, in 4 dimensions. In addition, this means that up to the researcher, it is possible to decide to ignore the components of lesser significance, which bring no interest to the pattern search, and thus lowering the dimensions to 2 or 3, and keep the possibility of plotting the final data. This at the cost of very little % of the original total information (while, with the original set of data, for a 4-D system, it would mean losing 25% of the information for each sensor discarded). To be precise, having originally n dimensions in your data, and thus n eigenvectors and eigenvalues are calculated, if only the first p eigenvectors are chosen to be kept, then the final data set has only p dimensions in the graphic presented (again, as seen in Figures 7.9, 7.10, and 7.12–7.14 in the human blood tests section).

To create the final data set in the number of dimensions desired (to be able to graphic the sensor outputs and visualize the patterns hidden in the data), it is needed to form a feature vector, which is a matrix of vectors. This is constructed by forming a matrix with the eigenvectors kept, having these as columns:

$$FeatureVector = (eig_1 eig_2 eig_3 \dots eig_n) \quad (3.6)$$

Given the set of data in the example, and the fact that in this example there are 2 eigenvectors, two choices are available. It is either possible to form a feature vector with both the eigenvectors:

$$\begin{pmatrix} -0.6779 & -0.7352 \\ -0.7352 & 0.6779 \end{pmatrix} \quad (3.7)$$

or, it is possible to choose to leave out the smaller, less significant component and only have a single column:

$$\begin{pmatrix} -0.6779 \\ -0.7352 \end{pmatrix} \quad (3.8)$$

Once the components (eigenvectors) that will be kept in the data are chosen, and a feature vector is formed, the transpose of the feature vector needs to be multiplied with the original data set, transposed as well:

$$FinalData = RowFeatureVector \times RowDataAdjust \quad (3.9)$$

where $RowFeatureVector$ is the matrix with the eigenvectors in the columns transposed, so that the eigenvectors are now in the rows, with the most significant eigenvector at the top, and $RowDataAdjust$ is the mean-adjusted data transposed, (the data items are in each column), with each row holding a separate dimension. $FinalData$ is the final data set, with data items in columns, and dimensions along rows. This operation results in having the original data expressed solely in terms of the vectors chosen previously. The original data set used as example had two axes, x and y, so these data was in terms of them, but for the experiment data, two principal component where chose every time to play the axis of reference of the system in which the data where added. Usually, the chosen eigenvectors are combined as PC1 vs. PC2 and PC1 vs. PC3, to keep the higher content of information possible from the original set of outputs; in this last case, the new data are only in terms of the vectors kept. In case of keeping both eigenvectors for the transformation, the data and the plot are shown in Figure 3.3. This plot is basically the original data in the example, rotated so that the eigenvectors are the axes. This is understandable since no information were lost in this decomposition. The other transformation possible is by taking only the eigenvector with the largest eigenvalue. The table of data resulting from that is found in Table 3.3. As expected, it only has a single dimension. By comparing this data set with the one resulting from using both eigenvectors, it is noticeable that this data set is exactly the first column of the other. Plotting this data would result in a 1-dimensional system, with the points on a line in sharing the same x positions of the ones in the plot in Figure 3.3. The second axis, which is the other eigenvector, have been effectively removed. The data have been transformed so that they are expressed in terms of the patterns between them, where the patterns are the lines that most closely describe the relationships between the data. Initially, the simple x and y axes did not really give information exactly about how that point relates to the rest of the data. Now, by using the covariance matrix, the values of the data points show exactly what trend the data point have. In the case of the transformation using both eigenvectors, the data have been simply altered so that in terms of those eigenvectors instead of the usual axes.

But the single-eigenvector decomposition has removed the contribution due to the smaller eigenvector, and the data there are only in terms of the remaining component.

Recovering the original data back is obviously of great concern if the PCA transform was used for data compression, or so far as dimensions were subtracted in order to plot the final data, as explained above.

	x	y
Transformed Data	-0.8280	-0.1751
	1.7776	0.1429
	-0.9922	0.3844
	-0.2742	0.1304
	-1.6758	-0.2095
	-0.9129	0.1753
	0.0991	-0.3498
	1.1446	0.0464
	0.4380	0.0178
	1.2238	-0.1627

Table 3.2: Data set transformed on the new reference system.

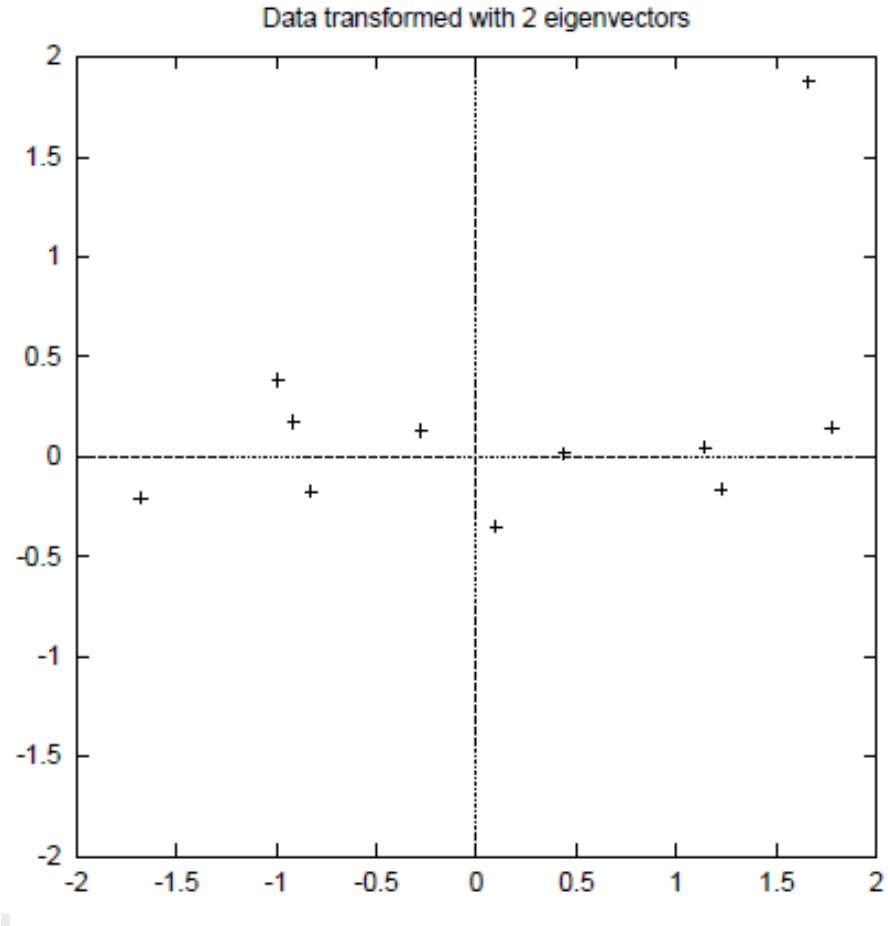

Figure 3.3: The table of data by applying the PCA analysis using both eigenvectors, and a plot of the new data points [165].

Transformed Data (Single eigenvector)
x
-0.8280
1.7776
-0.9922
-0.2742
-1.6758
-0.9129
0.0991
1.1446
0.4380
1.2238

Table 3.3: The data after transforming using only the most significant eigenvector

Before recovering the old data, is important to notice that only all the eigenvectors in this transformation were token, it will be possible to get exactly the original data back. If the number of eigenvectors in the final transformation was reduced, then the retrieved data has lost some information. Recall that the final transform is this:

$$FinalData = RowFeatureVector \times RowDataAdjust \quad (3.10)$$

which can be turned around so that, to get the original data back:

$$RowDataAdjust = RowFeatureVector^{-1} \times FinalData \quad (3.11)$$

where $RowFeatureVector^{-1}$ is the inverse of $RowFeatureVector$. However, when all the eigenvectors in the feature vector are taken, it turns out that the inverse of the feature vector is actually equal to the transpose of the feature vector. This is true only because the elements of the matrix are all the unit eigenvectors of the data set. This makes easier the recover, because the equation becomes:

$$RowDataAdjust = RowFeatureVector^{T} \times FinalData \quad (3.12)$$

but, to get the actual original data back, it is needed to add the mean of that original data (subtracted at the start to normalize the data pool). So, for completeness:

$$RowDataAdjust = (RowFeatureVector^{T} \times FinalData) + OriginalMean (3.13)$$

This formula also applies also when not all the eigenvectors were included in the feature vector. So even when some eigenvectors are left out, the above equation still makes the correct transform.

The result of the data re-creation, using the complete feature vector, is exactly the data used at the beginning of the example. For the reduced feature vector, it is interesting to

calculate the recovered data, to show how information has been lost. Figure 3.4 show this plot.

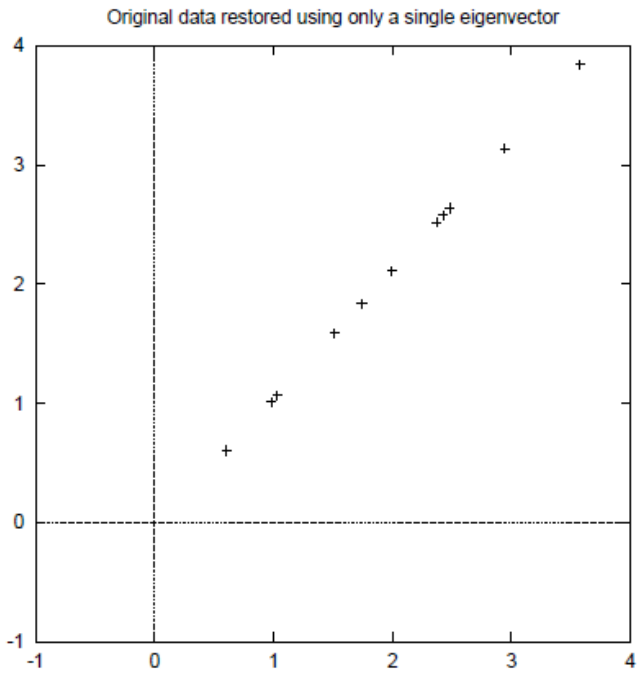

Figure 3.4: The reconstruction from the data that was derived using only a single eigenvector [165].

Comparing it to the original data plot in Figure 3.1 shows how, while the variation along the principle eigenvector (see Figure 3.2 for the eigenvector overlaid on top of the mean-adjusted data) has been kept, the variation along the other component (the other, discarded eigenvector) disappeared. This is expected, since it has been removed on purpose during the buildup of the final data set.

Chapter 4 – Tumors: Overview and Markers

Cells are the basic biological and functional structures of which all the living creature are made of. They are the smallest units able to individually reproduce themselves, thus they can be seen as living building blocks for all the other superior organisms. In this chapter the attention is focused on the negative mutation of these “bricks of life”: tumor cells. Since all the oncological material was brought from colorectal and gastric neoplasms, those two types of neoplasms are described further below.

4.1 – Tumor Cells

Tumor, properly referred to as *neoplasia,* is an abnormal growth of tissue [48] which usually, but not always, forms a mass [49], or biological alterations of the normal behavior of cells (e.g. Leukemia). Neoplasms are clinically categorized into four main groups:

- Benign neoplasms
- In situ neoplasms
- Malignant neoplasms (known also as cancer)
- Neoplasms of uncertain or unknown behavior

To these, also circulating tumor cells (CTC) can be added, since they work as “seeds” for new cancerous formations. Prior to abnormal growth (neoplasia), cells often undergo the stages of metaplasia or dysplasia [50]. Which do not always progress to neoplasia. The growth of neoplastic cells exceeds that of the normal circumstantial tissues and is not coordinated with them. The growth persists in the same excessive manner even after cessation of the stimuli. Mathematics and continuum mechanics have been lately used to simulate tumor development and degeneration. Vascularized tumors are thus looked at as being amalgams of a solid skeleton, formed by sticky cells, and an organic liquid filling the spaces in which cells can grow [51]. Findings from experiments on this model show that the active growth of the tumor is restricted to its external edges, and that the stiffening of the underlying normal tissue inhibits tumor growth as well [52], resembling contact inhibition. Benign masses, which are not associated with an abnormal generation of tissue, can also present themselves as tumors, however lacking of malignant potential. Once encapsulated by some coagulative or calcific response of the body, also hematomas,

necrotic tissue, keloids and granulomas may also be considered tumors, as well as localized enlargements of normal structures (aneurysms and pulmonary inclusions are examples of this last case). Since it can be dangerous to undergo biopsy to those tumor types in which the leakage of contents would potentially be harmful for the organism, various diagnostic tests (ultrasound, CT scan, MRI, angiogram, PET, SPECT) are employed prior to (or during) biopsy, and in some cases surgical exploration is used, in an attempt to avoid such severe complications. Benign neoplasm can turn into malignant one due to a variety of causes, like:

- **DNA damage**, which is the primary cause of cells degeneration into malignant neoplasms [53,54]. The mechanism which allows this progression is illustrated in Figure 4.1. DNA damage is really common, and naturally occurs with an average rate of 60,000 new damages a day per cell [53], mostly caused by cellular metabolism and DNA alterations in water at body temperatures. Other sources of these damages can derive from the exposure to exogenous agents (like tobacco smoke) which are likely to cause lung cancer [55], UV solar radiation, increasing the chance to develop melanomas [56], or Helicobacter pylori infection, which contributes to gastric cancer by producing reactive oxygen species [57]. Finally, bile acids while digesting fats also promote DNA damages and contribute to colon cancer [58]. It has been proved from Katsurano et al. [59] that immune system cells in an inflamed colonic epithelium can be sources of reactive oxygen species, therefore causing the DNA damages that lead to generation of tumors in the colon [59].

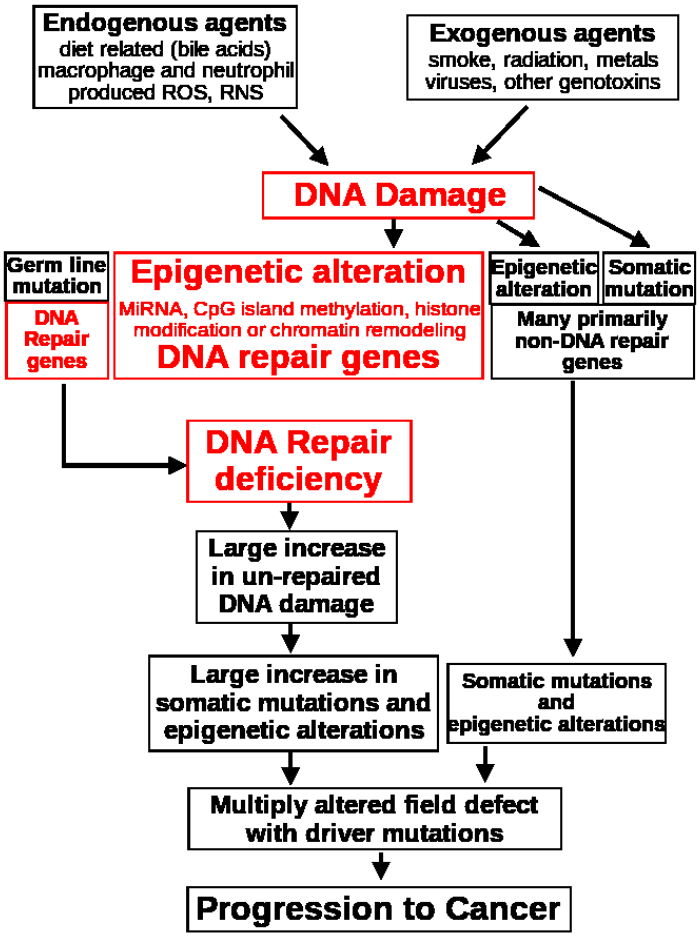

Figure 4.1: The central role of DNA damage and epigenetic defects in DNA repair genes in malignant neoplasms.

- **Field defects** in which promote new cancer progressions [60,61]. For what concerns colon neoplasms, a field defect can be generated because of an epigenetically altered cell. When this cell is located between the stem cells of an intestinal crypt, it may give rise to a patch of abnormal tissue. Figure 4.2 shows a lengthwise-opened segment of the colon with a cancer and four polyps. As explained above, a given mutant stem cell may acquire an advantage compared to other stem cells within the patch, and then may undergo clonal expansion, forming a secondary patch (or sub-clone) within the original patch. Within these new sub-clones, the process may be repeated multiple times, until generating either small polyps or eventually malignant neoplasms. In Figure 4.2, an apparent field defect in this segment of a colon has generated four polyps, together with the cancer itself

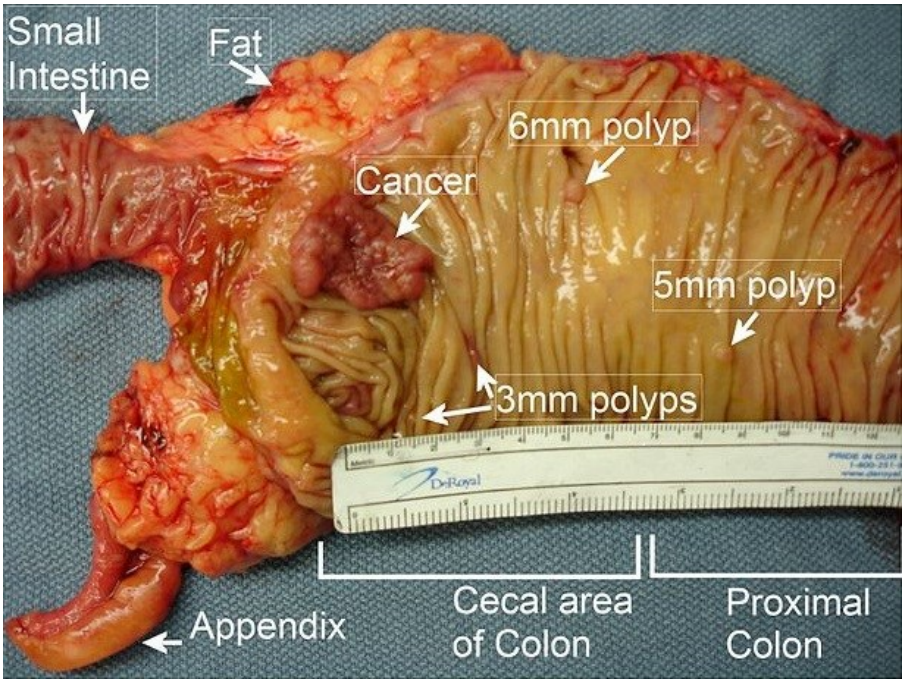

Figure 4.2: Longitudinally opened freshly resected colon segment showing a cancer and four polyps.

- **Genome instability** is often shown in cancers as mutator phenotype [62]. The protein-coding DNA within the nucleus is about 1.5% of the total genomic DNA [63], and thus a colon cancer can have an average of about 70 protein-altering mutations, of which about 4 may be “driver” mutations, while the rest may be “passenger” mutations [64]. Cancers show high frequencies of mutations in the nucleotide sequences, which suggest that, an early alteration in the field defects giving rise to a cancer, may be a deficiency in DNA repair. A Facista et al. work [65] showed that field defects surrounding colon cancers (which are often big, extending for a radius of about $10cm$) have frequently epigenetic defects in 2 or 3 DNA repair proteins, in the entire area of the field defect. As shown in many academic works, deficiencies in DNA repair cause increased mutation rates [66–68], and allow the accumulation of DNA damages; also, faulty repairs of these damages may give rise to epimutations (heritable mutations of gene expression) that, together with normal mutations, may provide a proliferative advantage, generating a field defect. Even if these alterations in DNA repair genes do not confer a selective advantage to the particular cell, they may be carried along as passenger mutations until the cells acquire additional alterations which do provide it

4.1.1 – Benign Neoplasm

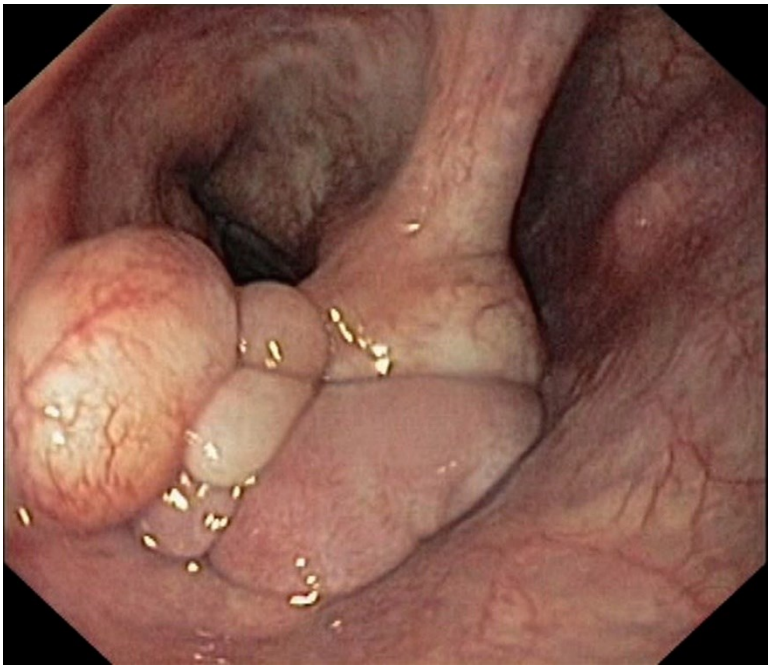

Figure 4.3: Benign laryngeal tumor fibrolipoma, a case of benign tumor [166].

A benign tumor is a mass of cells that lacks the ability to invade neighboring tissues or metastasize (typical of malignant neoplasms) and generally has a slower growth rate than malignant tumors. Furthermore, tumor cells are usually more differentiated than normal ones. [69–71]. Normally benign tumors are surrounded by an outer surface (fibrous sheath of connective tissue) or the epithelium [72] (examples are moles/nevi and uterine fibroids). Even if benign tumors cannot metastasize, some types may still affect negatively the health of an organism, mainly due to the "mass effect". This effect consists in compressing tissues and it may cause nerve damage, ischemia, necrosis and damage to organs; of course, the narrowest the envelopment is (cranium, or even inside bones), the higher is the chance to have damage due to this effect. Overproduction of hormones, especially when the cells are well differentiated, is a negative effect occurring in endocrine tissue tumors (for example thyroid adenomas [69]). Tumor progression [73] is the process that allows benign tumors, which are mostly not life-threatening, to turn into malignant. For this reason and other possible negative health effects, some benign tumors are removed by surgery [74].

4.1.2 – Carcinoma in Situ

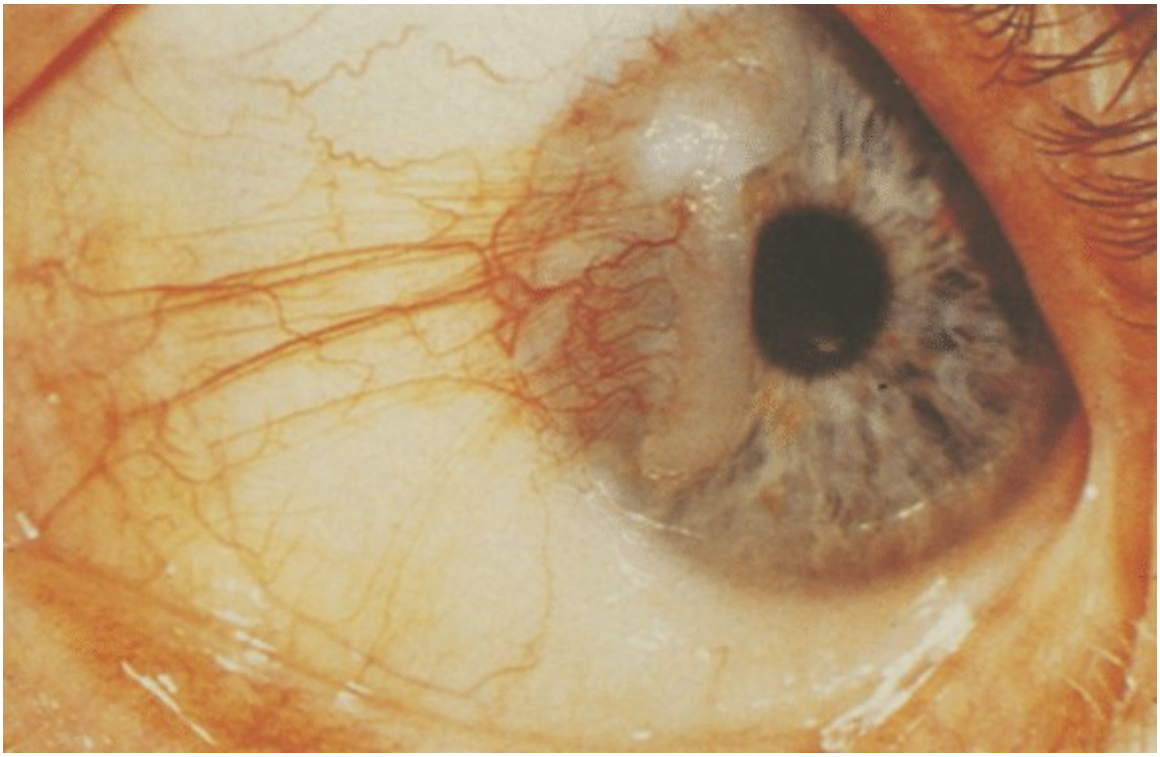

Figure 4.4: Case of ocular surface squamous neoplasia, an example of carcinoma in situ [167].

Carcinoma in situ is known also as “in situ neoplasm”, a group of abnormal cells growing in their original spot [75]. There are neoplasms type whose lesion is flat (an example is the CIS of cervix) or follows the existing architecture of the organ (an example is the CIS of the lung). There are anyway exceptions, like CIS of the colon, of the bladder (pre-invasive papillary cancer), and of the breast. Many forms of CIS can degenerate into malignant neoplasms [76], and therefore the removal may be recommended; in any case, it is proved that degeneration of CIS is highly variable, and some CIS do not become invasive cancers at all.

4.1.3 – Malignant Neoplasm (Cancer)

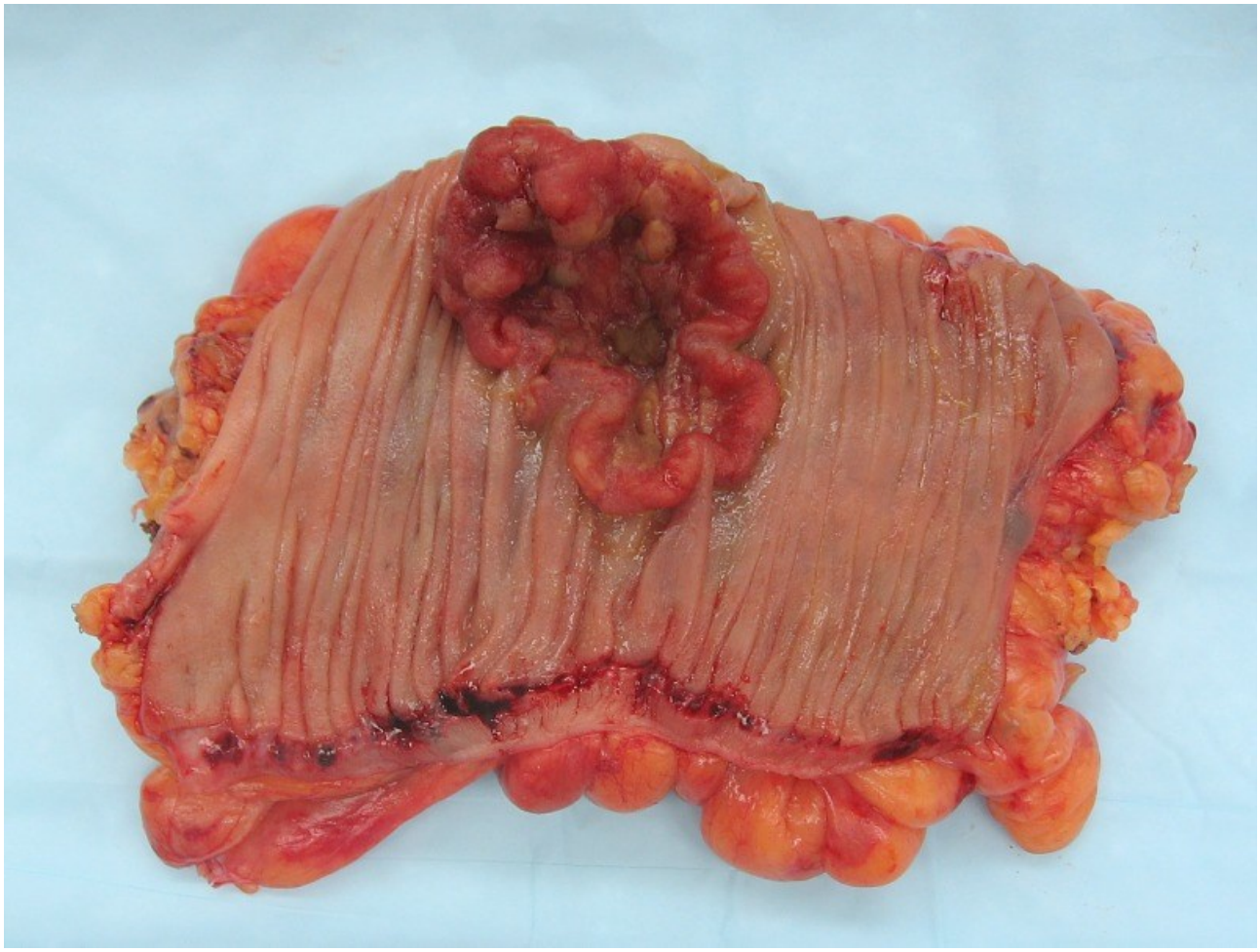

Figure 4.5: Colorectal cancer.

A malignant neoplasm (cancer) is composed of cells which mostly loss their original biological behavior; having these cells higher rate of proliferation and means to invade other tissues or organs, the cancer can potentially metastasize. Cancer types have different denomination, depending on which type of cells they derive from (in case of epithelial cells they are called carcinomas, while those deriving from connective tissue cells are called sarcomas). Malignant brain and immune system neoplasms are special categories with complex nomenclatures. Malignant neoplasms do rapidly increase in size, show less cellular differentiation (or lack of differentiation, called anaplasia), have the tendency to invade surrounding tissues and the ability to invade distant tissues, thanks to the metastasizing process.

4.1.4 – Circulating Tumor Cells

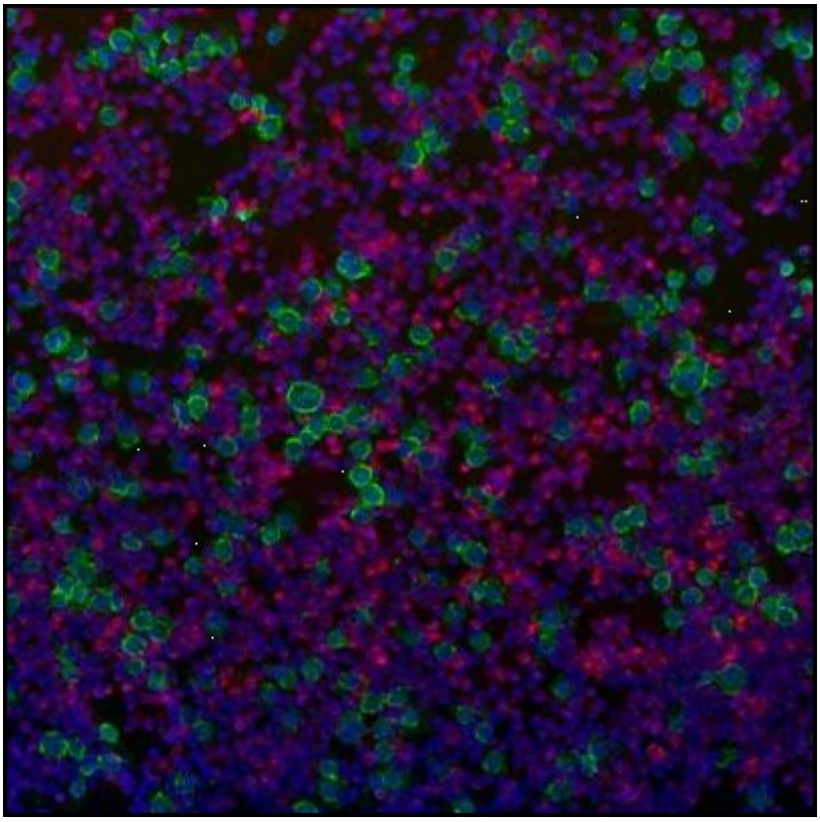

Figure 4.6: Analysis of a blood sample by immunofluorescence, the darkest cells are red blood cells while the cells surrounded by a light grey line are CTC [34].

Circulating tumor cells (CTCs) (Figure 4.6) are cells that, once having reached the bloodstream from a primary tumor, can travel in the circulatory system and spread through the body. They become possible seeds of additional tumors in distant organs, triggering the metastatic process [77]. Various types of CTCs are listed below:

- **Traditional CTCs** are confirmed cancer cells with an intact nucleus, and are often large cells with irregularity shape or morphology [78]
- **Cytokeratin negative (CK-) CTCs** are cancer stem cells or cells undergoing epithelial-mesenchymal transition (EMT). Because of that, CK-CTCs may be the most resistant and most likely to undergo metastasis, having a morphology similar to that of malignant neoplasms cells [79]
- **Apoptotic CTCs** are traditional CTCs that are suffering apoptosis (cell death), which may be caused by nuclear fragmentation or cytoplasmic leak. By monitoring

the ratio between traditional and apoptotic CTCs it is possible to obtain clues about a therapy efficacy in targeting and killing cancer cells [79]

- **Small CTCs** have specific biomarkers that identify them as tumor cells. These cells are involved in progressive disease and differentiation into small cell carcinomas

CTCs can also pack in clusters. The CTCs clusters, which may contain all kinds of CTCs, have cancer-specific biomarkers and are heavily associated with increased metastatic risk and poor prognosis [80].

4.2 – Metastasis Process

Most of mortality (about 90%) associated with cancer is due to metastasis. Metastasis is the process which allows cancer cells to colonize far locations of the organism. To spread through the body, tumor cells must first move through neighboring cells, rearranging their cytoskeleton and attaching to the other cells and the extracellular matrix. Cells can crawl since no blockage too hard to be bypassed is reached (like the layers of proteins which form the basal lamina). In this case, cancer cells secrete digestive enzymes to cross this layer. The enzymes are called matrix metalloproteases, which cut through the proteins of the basal layer and degrade them in the basal lamina, allowing the passage through the blockage. Once the cells have traversed the basal lamina, they can spread through the body via bloodstream or lymphatic stream, floating in the invaded system until they find a suitable location to settle and re-enter the tissues. Here the cells can then restart to proliferate in this new location, forming new neoplasms. Even if this process is heavily inefficient, still most of cancer deaths derive from it, because millions of cells can leave a tumor per day. This means that, even if only a small fraction of CTCs that leave a primary neoplasia are able to survive to form a new tumor, the chance leads to the fact that a distant development of new neoplasms will occur, given enough time. CTC can be neutralized and die in a variety of ways, like anoikis (detachment from the neighborhood of cells and proteins leads to death the separated cell), getting stuck or damaged due to the narrowness of the vessels in which they travel, or simply getting recognized by the immune system and getting destroyed like pathogenies.

4.3 – Colorectal Cancer

[81] In this work one of the goals is the detection of the CRC from human blood and tissue samples. CRC is a major worldwide health problem, due to its high incidence compared to other types of neoplasms, and its mortality rate. In the USA CRC is both the third most commonly diagnosed cancer type (data in 2011 tell that more than 140.000 people have been diagnosed with CRC), and the third leading cause of death between neoplasms for both genders (nearly 50.000 people died in 2011 because of this tumor). In Europe it is estimated that over 40,000 of the adult UK population are diagnosed with CRC every year (with around 15-16.000 deaths), while Italian data speak of about 48.000 cases in 2014, with almost 20.000 deaths. Considering that, if diagnosed early, CRC is one of the most curable types of cancer (rate around 90%), prevention is vital to avoid the degeneration of CRC.

4.3.1 – Symptoms

[82] There are a number of symptoms that may show the presence of CRC, mostly linked to the loss of blood due to the anomalous cellular formation. Anyway, in the preliminary stage of the tumor, generally people attribute their rectal bleeding to hemorrhoids, neglecting early diagnosis because of lack of concern. Rectal bleeding itself may be hidden and show up as an anemia, disguising the true origin of the problem. This factor may be associated with fatigue and pale skin. The main pre-screening to detect CRC is Fecal Occult Blood Test (FOBT), in which samples of feces are submitted to a lab for detection of blood. The problem with this test in the high percentage of false positives and false negatives. The first is due to the use of cardiovascular medicines (cardio-aspirin, warfarin based drugs), together with ulcer and injuries to the gastrointestinal tract. The second is given by the fact that if the tumor is not bleeding or is placed in the initial part of the large intestine (ileum), the FOBT cannot identify it. When the tumor gets large enough, it blocks the colon tract. Symptoms at this point are commonly abdominal distension and pain, unexplained, persistent nausea or vomiting, unexplained weight loss, and change in frequency or character of stool and sensation of incomplete expulsion after the act of defecation.

4.3.2 – Management of the Tumor

[83] The management of CRC has been transformed in the last decade, from a routine activity for general surgeons to a specialist activity, in which the multidisciplinary team (MDT) guides increasingly complex investigations and treatments. Most CRC MDTs stage the disease in three areas:

- Local disease, assessed in the colon by CT scan, which provides information on the presence of invasion through the bowel wall, direct invasion of adjacent structures or extensive lymph node disease; the common pre-operative planning, before resection, consists in the use of MRI (Magnetic Resonance Imaging: MRI scans provide detailed images of soft tissues in the body using radio waves and strong magnets. It is uncomfortable because it takes up to an hour and the patient has to lie inside a narrow tube, which is confining and can upset people with claustrophobia) or transrectal ultrasonography (transrectal ultrasonography is considered to be the most accurate tool for the staging of early rectal cancer, making it important in the selection of cases for local excision. A small, lubricated probe placed into the rectum releases sound waves to create a video image)
- Metastatic disease in the liver and lungs, is assessed routinely and most centers would be expected to perform abdominal and chest CT (Chest Computed Tomography. Before the scan, it may be needed from the patient to drink a contrast solution and/or get an intravenous (IV) injection of a contrast dye that helps better outline abnormal areas in the body. Some people are allergic and get hives or, rarely, more serious reactions like trouble breathing and low blood pressure), PET (Positron Emission Tomography: a form of radioactive sugar, known as F-18 fluorodeoxyglucose or FDG, is injected into the blood. Cancer cells in the body grow rapidly, so they absorb large amounts of the radioactive sugar. After about an hour, the patient will be moved onto a table in the PET scanner, and will be left to lie on the table for about 30 minutes while a special camera creates a picture of areas of radioactivity in the body.) and PET-CT (special machines are able to perform both a PET and CT scan at the same time, this allows the doctor to compare areas of higher radioactivity on the PET with the more detailed appearance of that area on the CT) are important in those patients in whom otherwise occult metastases would

be a contraindication to extensive visceral resection, directed at either primary disease or metastases

- Synchronous disease should be excluded by complete assessment of the remainder of the colon. Synchronous cancers are present in around 2% of patients with a recent diagnosis of CRCs. The optimal investigation is colonoscopy, during which polyps can be removed or the site tattooed, allowing later identification at the time of resection

[84] Together with barium studies or sigmoidoscopy (a procedure used to see inside the sigmoid colon and rectum), these methods of diagnosis of CRC in its three different stages are invasive and unpleasant for patients, some of them present physiologic or psychological contraindications or take a long time. For this reasons, in the last years, the research of non-invasive methods of diagnosis for CRC has become very important. The purpose of this work is to present a new idea to diagnose CRC.

4.4 – Gastric Cancer

Worldwide, stomach cancer is the fifth most-common cancer, with 952,000 cases diagnosed in 2012 [85]. It is more common on males and in developing countries [86,87], and in 2012 it represented 8.5% of cancer cases among men, making it the fourth most-common cancer for that gender [88]. Still in 2012, the number of deaths was 700,000 having decreased slightly from 774,000 in 1990, making it the third-leading cause of cancer-related death (after lung cancer and liver cancer) [89,90]. Less than 5% of stomach cancers occur in people under 40 years of age, with 81.1% of that 5% in the age-group between 30 to 39 years and 18.9% in the age-group from 20 to 29 years old [91]. In 2014, stomach cancer resulted in 0.61% of deaths (13,303 cases) in the U.S. [92]. In China, stomach cancer accounted for 3.56% of all deaths (324,439 cases) [93]. In the United Kingdom, stomach cancer is the fifteenth most-common cancer (around 7,100 people were diagnosed with stomach cancer in 2011), and it is the tenth most-common cause of cancer-related deaths (around 4,800 people died in 2012) [94].

4.4.1 – Symptoms

Stomach cancer is often either asymptomatic, or it may cause only nonspecific symptoms in its early stages. By the time that more serious symptoms occur, the cancer has often reached an advanced stage and may have metastasized, which is one of the main reasons for its relatively poor prognosis [95]. Stomach cancer can cause the following signs and symptoms:

- Early cancers may be associated with indigestion or burning sensations. However, less than 1 in every 50 people referred for endoscopy due to indigestion has cancer [96]. Abdominal discomfort and loss of appetite, especially for meat, can occur
- Gastric cancers that have enlarged and invaded normal tissue can cause weakness, fatigue, bloating of the stomach after meals, abdominal pain in the upper abdomen, nausea and occasional vomiting, diarrhea or constipation. Further enlargement may cause weight loss or bleeding with vomiting blood or having blood in the stool, the latter apparent as black discoloration (melena) and sometimes leading to anemia. Dysphagia suggests a tumor in the cardia or extension of the gastric tumor into the esophagus

The main problem with these symptoms is that they are still aspecific, since other pathologies and problems such as a stomach virus, gastric ulcer, or tropical sprue can cause them.

4.4.2 – Management of the Tumor

Gastric cancer is difficult to cure unless it is detected at an early stage. Unfortunately, because of the problematics related to the symptoms discussed in the previous paragraph, the disease is usually advanced when the diagnosis is made [97]. Treatment for stomach cancer may include surgery [98], chemotherapy [99], and/or radiation therapy [100]. New treatment approaches, such as immunotherapy or gene therapy and improved ways of using current methods, are being studied in clinical trials [101].

- Surgery remains the only curative therapy for stomach cancer [102]. Of the different surgical techniques, endoscopic mucosal resection (EMR) is a treatment for early gastric cancer (tumor only involves the mucosa) that was pioneered in Japan and is

available in the United States at some centers [102]. In this procedure, the tumor, together with the inner lining of stomach (mucosa), is removed from the wall of the stomach using an electrical wire loop through the endoscope. The advantage is that it is a much smaller operation than removing the stomach [102] (partial or total gastrectomy). Endoscopic submucosal dissection (ESD) is a similar technique pioneered in Japan, used to resect a large area of mucosa in one piece [102]. If the pathologic examination of the resected specimen shows incomplete resection or deep invasion by tumor, the patient would need a formal stomach resection [102]. A 2016 Cochrane review found low quality evidence of no difference in short-term mortality between laparoscopic and open gastrectomy (removal of stomach), and that benefits or harms of laparoscopic gastrectomy cannot be ruled out [103]. Post-operatively, up to 70% of people undergoing total gastrectomy develop complications such as dumping syndrome and reflux esophagitis [104]. Construction of a "pouch", which serves as a "stomach substitute", reduced the incidence of dumping syndrome and reflux esophagitis by 73% and 63% respectively, and led to improvements in quality-of-life, nutritional outcomes, and body mass index [104]. Those with metastatic disease at the time of presentation may receive palliative surgery and while it remains controversial, due to the possibility of complications from the surgery itself and the fact that it may delay chemotherapy the data so far is mostly positive, with improved survival rates being seen in those treated with this approach [102,105]

- Chemotherapy treatment for stomach cancer has no firmly established standard of care [99], because unfortunately stomach cancer has not been particularly sensitive to these drugs. Chemotherapy, if used, has usually served to palliatively reduce the size of the tumor, relieve symptoms of the disease and increase survival time [99]. Some drugs used in stomach cancer treatment have included: 5-FU (fluorouracil) or its analog capecitabine, BCNU (carmustine), methyl-CCNU (semustine) and doxorubicin (Adriamycin), as well as mitomycin C, and more recently cisplatin and taxotere, often using drugs in various combinations [99]. The relative benefits of these different drugs, alone and in combination, are unclear [99,106]. Clinical researchers are exploring the benefits of giving chemotherapy before surgery to shrink the tumor, or as adjuvant therapy after surgery to destroy remaining cancer cells [102]

- Recently, treatment with human epidermal growth factor receptor 2 (HER2) inhibitor, trastuzumab, has been demonstrated to increase overall survival in inoperable locally advanced or metastatic gastric carcinoma over-expressing the HER2/neu gene [102]. In particular, HER2 is overexpressed in 13–22% of patients with gastric cancer [101,107]. Of note, HER2 overexpression in gastric neoplasia is heterogeneous and comprises a minority of tumor cells (less than 10% of gastric cancers overexpress HER2 in more than 5% of tumor cells). Hence, this heterogeneous expression should be taken into account for HER2 testing, particularly in small samples such as biopsies, requiring the evaluation of more than one bioptic sample [107]
- Radiation therapy (also called radiotherapy) may be used to treat stomach cancer, often as an adjuvant to chemotherapy and/or surgery [102]

4.5 – Tumor Markers: VOCs

Detecting neoplasms and keeping track of their development is not to always possible before their degeneration into malignant forms without the use of expensive (computed tomography, magnetic resonance imaging, genetic tests) and invasive (colonoscopy, fine-needle aspiration) tests. Likewise, the detection of possible cancer relapses or of its metastasis, previously removed by surgery or by specific therapies, remains the most reliable life-saving opportunity. Both cases, keeping in mind the view to develop cheaper and not invasive screening devices, have been assessed, from the scientific world in the last decades, to follow the detection of chemicals in the body, as markers of malignant neoplasms. These significant substances consist of:

1. Metabolites from cellular breath [108–110]
2. Products of lipid membrane peroxidation, usually known as Volatile Organic Compounds (VOCs) [111–113]
3. Vascular Endothelial Growth Factors (VEGF) [114–117]
4. Wastes from Circulating Tumor Cells (CTC) [118–120]

In this work, nanostructured chemoresistive sensors are used as operative units for a fast response ($10 - 30$ minutes per result) screening device, in order to detect and monitor useful patterns from the volatile chemicals hosted in human blood and human tissues

samples, and thus reach a Healthy/Tumor affected functioning logic. Also, as started from the Master's Degree thesis from the same author, the work of identification of the tumor markers exhaled from cell cultures has been continued, in order to develop a "fingerprint database" of the different kind of tumors. All the four families of chemical markers listed are produced and discharged in the blood stream by cancer cells, and thus can be find as emanations from blood samples. For what concerns instead human tissues, markers of interest are the ones listed with number 1, 2 and with lower concentration from 3, while for cell tests most of the contribution to the signal comes from the chemicals listed as 1, with possible presence due to the action of the first family itself on the phospholipidic membrane, and from further degenerations, of the group 2. Tumor growth is accompanied by gene and/or protein changes that may lead to peroxidation [121] of the cell membrane species and, hence, to the emission of volatile organic compounds (VOCs) which can be considered as biomarkers for the different types of cancers.

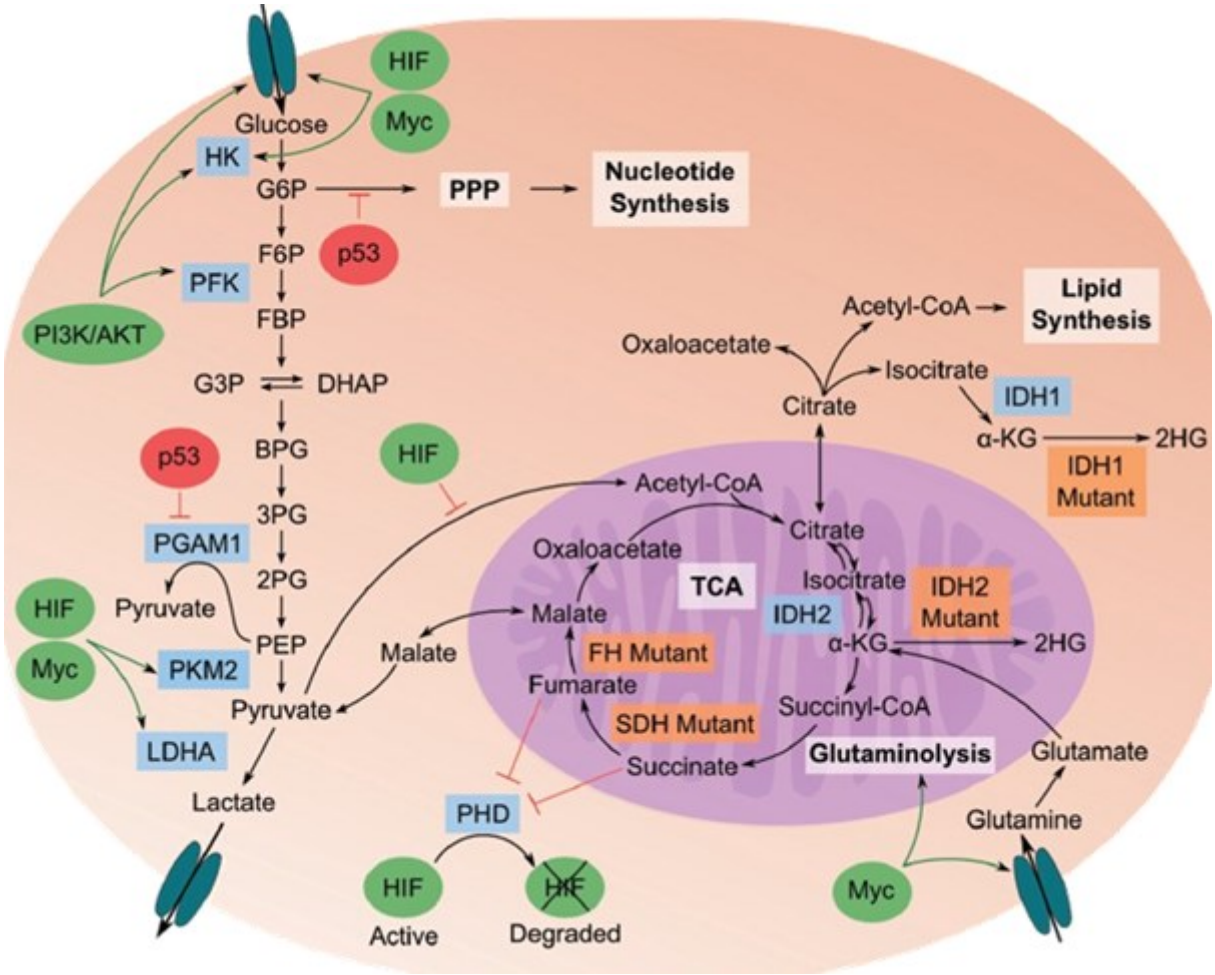

Figure 4.7: Relationships between metabolome, proteome, and genome in cancerous cells [169].

In Figure 4.7, tumor metabolome is schematized. Glycolysis breaks down glucose into pyruvate (and here the Warburg effect enters in account, having higher rate of glycolysis, yet less efficient than Krebs cycle), which is then fermented to lactate. Pyruvate flux through TCA (tricarboxylic acid cycle) cycle is down-regulated in cancer cells. Pathways branching off of glycolysis, such as the pentose phosphate pathway, generate biochemical building blocks to sustain the high proliferative rate of cancer cells. For what concerns the legend of the scheme:

- Blue boxes are enzymes important in transitioning to a cancer metabolic phenotype
- Orange boxes are enzymes that are mutated in cancer cells
- Green ovals are oncogenes that are up-regulated in cancer
- Red ovals are tumor suppressors that are down-regulated in cancer

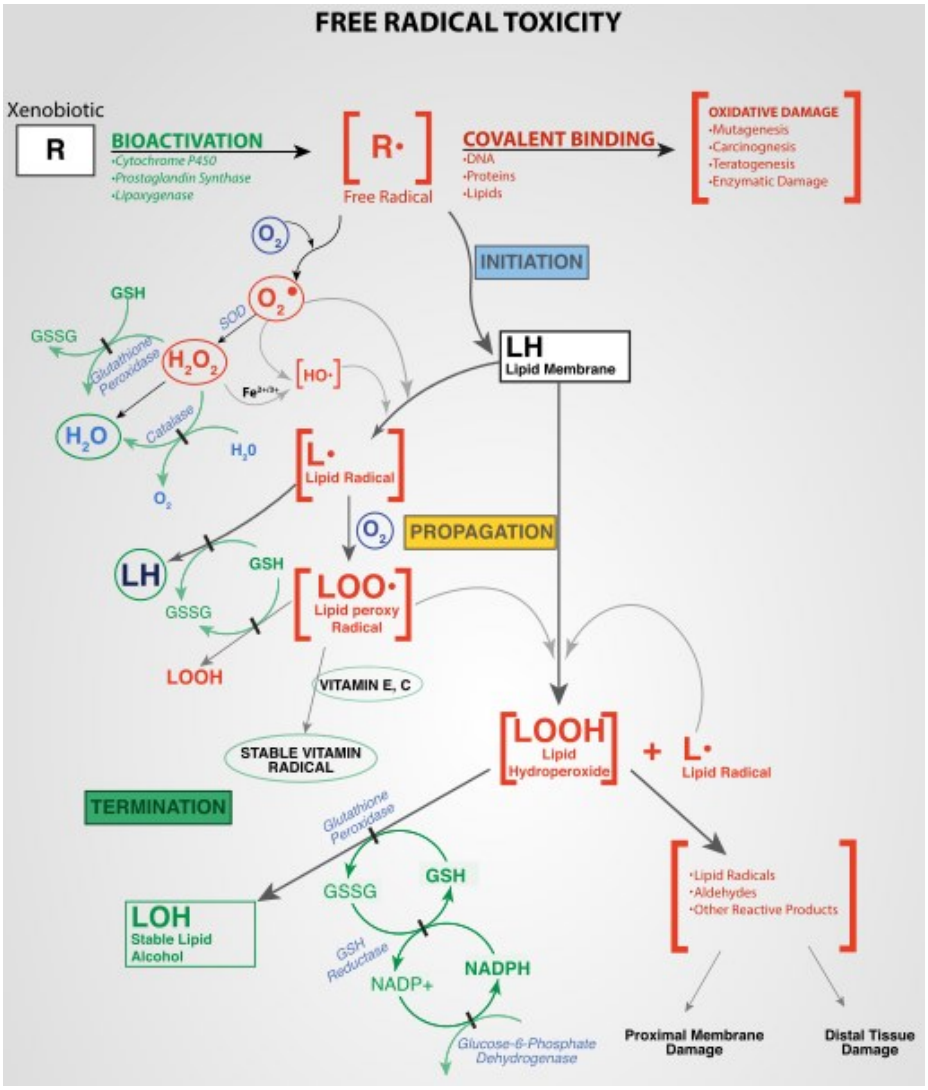

Figure 4.8: Free radical mechanisms in tissue injury. Lipid peroxidation induced by xenobiotics and the subsequent detoxification by cellular enzymes (termination).

When dealing instead with the involvement of reactions with free radicals with normal cells, various effects can occur [122]:

- Protein damage
- Membrane damage
- DNA damage
- Change in membrane permeability
- Mitochondrial damage
- Lipid peroxidation

Lipid peroxidation, which is the one of interest for this work, is the oxidative degradation of lipids, a process in which free radicals "steal" electrons from the lipids in cell membranes, resulting in cell damage caused by a free radical chain reaction mechanism. It most often affects polyunsaturated fatty acids, because they contain multiple double bonds in between which lie methylene bridges (-CH2-) that possess especially reactive hydrogen atoms. As with any radical reaction, the reaction consists of three major steps, schematized in Figure 4.8:

- **INITIATION** – In this step, a fatty acid radical is produced. The most notable initiators in living cells are reactive oxygen species (ROS), such as OH· (hydroxyl radical) and HOO· (perhydroxyl radical), which combines with a hydrogen atom to make water and a fatty acid radical.
- **PROPAGATION** – Fatty acids radical are not very stable molecules, so they reacts readily with molecular oxygen, thereby creating peroxyl-fatty acid radicals. These radicals are also an unstable species that reacts others free fatty acids, producing more different fatty acid radicals and lipid peroxides, or cyclic peroxides if they react with themselves. This cycle continues, as the new fatty acid radicals react in the same way.
- **TERMINATION** – When a radical reacts with a non-radical, it always produces another radical, which is why the process is called a "chain reaction mechanism". The radical reaction stops when two radicals react and produce a non-radical species. This happens only when the concentration of radical species is high enough for there to be a high probability of collision of two radicals. Living organisms have different molecules that speed up termination by neutralizing free radicals and, therefore, protecting the cell membrane. Important antioxidants are

vitamin E and vitamin C. Other anti-oxidants made within the body include the enzymes superoxide dismutase, catalase, and peroxidase.

The chemical products of this oxidation are known as lipid peroxides or lipid oxidation products (LOPs), and since their link to the degeneration of the cell itself into aberrant forms and consequentially to neoplasms, they can be used as tumor markers. The analysis of VOCs that are linked to cancer is a new frontier in medical diagnostics, because it is non-invasive and potentially low cost [123,124]. These VOCs can be detected either directly from the headspace of cancer cells [125–127] or through exhaled breath [123,124,128–131], as cancer-related changes into the blood chemistry lead to measurable changes in the breath by exchanges through the lung [130]. Peng et al (2010) [132] reported that a tailor-made array of cross-reactive sensors based on organically functionalized gold nanoparticles (GNPs) discriminates between breath VOCs of healthy controls and of patients suffering from lung, breast, colorectal, and prostate cancers. They reported also the ability of these GNP sensors to distinguish between the breath patterns of different cancer types in the same pattern analysis, irrespective of age, gender, lifestyle, and other confounding factors. They found also that these results compare favorably with breath testing via a chemical analysis of the constituent compounds by gas chromatography linked with mass spectroscopy (GC-MS). Their study was conducted in three phases. In the first phase exhaled alveolar breath was collected from 177 volunteers aged 20-75 years (lung, colon, breast, and prostate cancer patients and healthy controls) using a method to effectively separate endogenous from exogenous VOCs (endogenous VOCs are those generated by cellular biochemical processes in the body, which provide insight into the body's function [133], whereas exogenous VOCs are adsorbed from the environment [134] in breath, and excluded nasal entrainment. All cancer patients were tested immediately after being diagnosed by conventional clinical means, and before any treatment. In the second phase an array of 14 cross-reactive nanosensors was designed with different organic functionalities and their ability to detect simultaneously primary, lung, colon, breast, and prostate cancers was tested. Signals collected from the 14-sensor-array, after exposure to the breath of the representative subjects, were analyzed using standard PCA (Principal Component Analysis) is an effective method to improve human perception of experimental data by reducing the multidimensional data space to its main components. In the third phase the purposed method of breath testing using a GNP sensors array was compared with breath test analysis using GC-MS combined with

SPME) which identified 300-400 different VOCs for each sample. In Figure 4.9 are shown the characteristic odor prints of the studied cancer types. In this work the focus is on the CRC and gastric cancer, and in the Figure 4.9, the panel (B) shows 6 of the 39 common VOCs for colon cancer compared with healthy subjects. The attention is focused on VOC 6 and VOC 8, respectively **1-1'-(1-butenylidene)bis benzene** ($m/z = 208$, CAS:1726-14-3) and **1-iodo-nonane** ($m/z = 43$; CAS:4282-42-2) which are present in bigger percentage in patients with colon cancer than in healthy subjects and represent possible markers for colon cancer.

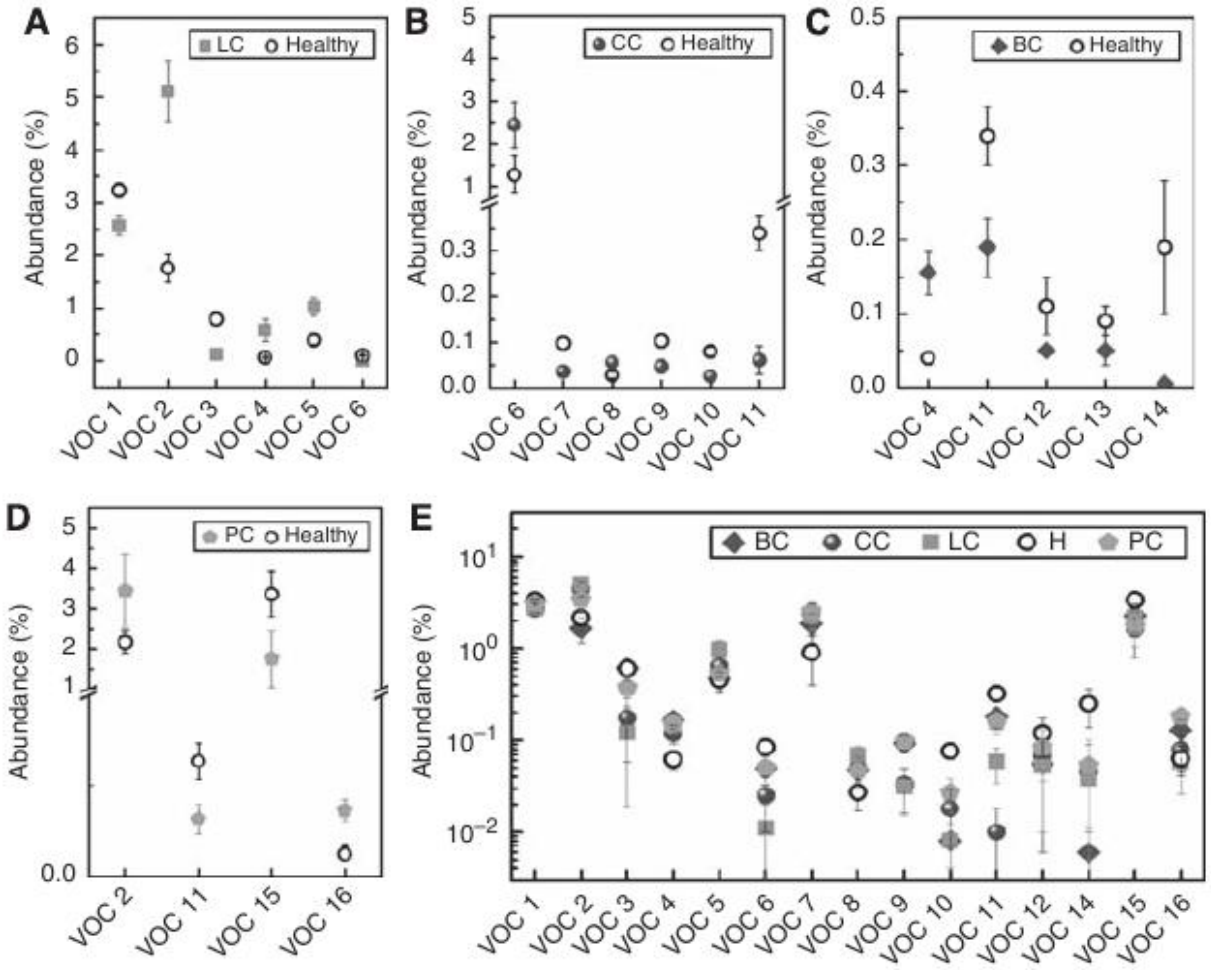

Figure 4.9: Pre selection of the GC-MS input. The most suitable VOCs are selected for distinguishing between healthy subjects and patients suffering from a specific cancer: (A) 6 of 33 common VOCs for lung cancer; (B) 6 of 39 common VOCs for colon cancer; (C) 5 of 54 common VOCs for breast cancer; (D) 4 of 36 common VOCs for prostate cancer; (E) summary of the previous markers [132].

A similar study was conducted by Altomare et al. (2012) [135] at the University of Bari but they was their interest on the colon cancer in particular. The sampling conditions were the

same of that of Peng et al. [132] and volunteers refrained from eating and drinking for 3h before the test. Volunteers were 103: 52 diagnosed with colon cancer (with a mean age of 65 years) and 51 healthy subjects (with a mean age of 60 years). Patients with diabetes or intestinal inflammation were excluded. Patients breathed tidally for 5 min through a mouthpiece connected to a three-way-non-rebreathing valve with an inspiratory VOC filter in order to exclude exogenous VOCs. The analysis of compounds was effectuated through GC-MS and the discrimination between healthy and cancer subjects was made with a probabilistic neural network (PNN), an implementation of a statistical algorithm. The most probable VOCs emerged from this study which can have an high discriminating power are reported in the Table 4.1 (RT is the retention time, the amount of time elapsed from the injection of a sample into the chromatographic system to the recording of the peak (band) maximum of the component in the chromatogram).

Chemical Marker	Recognition Capability (%)
Nonanal	80
4-Methyl-2-pentanone	88
Decanal	92
2-Methylbutane	87
1,2-Pentadiene	95
2-Methylpentane	87
3-Methylpentane	87
Methylcyclopentane	80
Cyclohexane	94
Methylcyclohexane	92
1,3-Dimethylbenzene	96
4-Methyloctane	80
1,4-Dimethylbenzene	80
A (4-methylundecane, RT= 11.3)	59
B (trimethyldecane, RT= 13.2)	72

Table 4.1: Discriminating variable compounds considered in statistical analysis.

Comparing these two works it is possible to observe that the presence of benzene compounds is common to both but it has also bigger values with respect other compounds. For this reason, the first part of this work is the search of materials particularly sensitive on this gas, because it is reasonable to expect that the sensitivity to it is reflected in sensitivity to its compounds and to similar molecules in general. The second part is instead linked to the analysis of two VOCs highlighted in the work of Peng et al. [132] and Altomare et al. [135], the **1-iodo-nonane ($C_9H_{19}I$)** and the **decanal ($C_{10}H_{20}O$)** whose chemical structures are showed in the Figures 4.10 and 4.11. These two aldehydes are, as explained above in this paragraph, highly like to be produced from phospholipidic membrane peroxidation, since their chemical structure results from the hydrophilic “tails” of the phospholipids present in the cellular membrane.

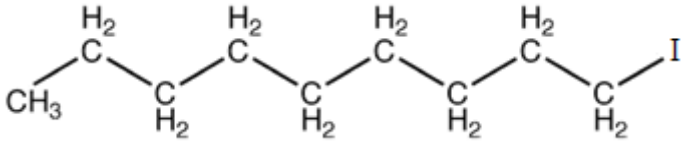

Figure 4.10: 1-iodo-nonane chemical structure [34].

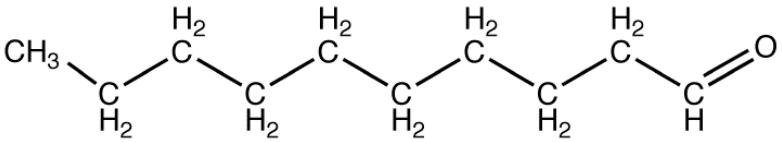

Figure 4.11: Decanal chemical structure [34].

Tumor-marker analysis is already a well-acknowledged test for blood samples, in which different proteins and chemicals are sought in order to verify the presence, and degeneration grade, of neoplastic masses in the human body. Nowadays, the tumor markers mostly searched for neoplasms screening on blood samples (and thus exhaled from tumor cells on both human tissues and cell cultures) are:

Tumor Marker	Cancers Associated With Elevated Results	Non-Cancerous Reasons for Elevated Levels	"Normal" Results
Blood test (blood serum marker), except where noted.	*(**) indicates the most common association, if one exists*		*Different labs may have different high/low values*
AFP Alpha-fetoprotein	Germ cell cancers of ovaries & testes** (Non-seminomatous, particularly embryonal and yolk sac, testicular cancers). Some primary liver cancers (hepatocellular)	Pregnancy (clears after birth), liver disease (hepatitis, cirrhosis, toxic liver injury), inflammatory bowel disease	Low levels present in both men & non-pregnant women (0-15 IU/ml); generally results >400 are caused by cancer (Half-life 4-6 days)
Bence-Jones Proteins (urine test) or **Monoclonal Immunoglobulins** (blood test)	Multiple Myeloma** Waldenstrom's macroglobulinemia, chronic lymphocytic leukemia	Amyloidosis	Generally, a value of 0.03-0.05 mg/ml is significant for early disease
B2M Beta-2-Microglobulin	Multiple myeloma**, chronic lymphocytic leukemia (CLL), and some lymphomas (including Waldenstrom's macroglobulinemia)	Kidney disease, hepatitis	< 2.5 mg/L
BTA Bladder Tumor Antigen (urine test)	Bladder cancer**, cancer of kidney or ureters	Invasive procedure or infection of bladder or urinary tract	None normally detected

Tumor Marker	Cancers Associated With Elevated Results	Non-Cancerous Reasons for Elevated Levels	"Normal" Results
CA 15-3 Cancer Antigen 15-3 or Carbohydrate Antigen 15-3	Breast** (often not elevated in early stages of breast cancer), lung, ovarian, endometrial, bladder, gastrointestinal	Liver disease (cirrhosis, hepatitis), lupus, sarcoid, tuberculosis, non-cancerous breast lesions	< 31 U/ml (30% of patients have an elevated CA 15-3 for 30-90 days after treatment, so wait 2-3 months after starting new treatment to check)
CA 19-9 Cancer Antigen 19-9 or Carbohydrate Antigen 19-9	Pancreas** and colorectal, liver, stomach and biliary tree cancers	Pancreatitis, ulcerative colitis, inflammatory bowel disease, inflammation or blockage of the bile duct, thyroid disease, rheumatic arthritis	< 37 U/ml is normal > 120 U/ml is generally caused by tumor
CA 125 Cancer Antigen 125 or Carbohydrate Antigen 125	Ovarian cancer** breast, colorectal, uterine, cervical, pancreas, liver, lung	Pregnancy, menstruation, endometriosis, ovarian cysts, fibroids, pelvic inflammatory disease, pancreatitis, cirrhosis, hepatitis, peritonitis, pleural effusion, following surgery or paracentesis	0-35 U/ml
CA 27.29 Cancer Antigen 27.29 or Carbohydrate Antigen 27.29	Breast** (best used to detect recurrence or metastasis). Colon, gastric, liver, lung, pancreatic, ovarian, prostate cancers	Ovarian cysts, liver and kidney disorders, non-cancerous (benign) breast problems	< 40 U/ml Generally, levels > 100 U/ml signify cancer (30% of patients have elevated CA 27.29 for 30-90 days after treatment, so wait 2-3 months after starting new treatment to check)
Calcitonin	Medullary thyroid cancer**	Chronic renal insufficiency, Chronic use of Proton-pump inhibitors (medications given to reduce stomach acid)	<8.5 pg/mL for men < 5.0 pg/mL for women
CEA Carcinoembryonic Antigen	Colorectal cancers ** Breast, lung, gastric, pancreatic, bladder, kidney, thyroid, head & neck, cervical, ovarian, liver, lymphoma, melanoma	Cigarette smoking, pancreatitis, hepatitis, inflammatory bowel disease, peptic ulcer disease, hypothyroidism, cirrhosis, COPD, biliary obstruction	<2.5 ng/ml in non-smokers <5 ng/ml in smokers Generally, > 100 signifies metastatic cancer
Chromogranin A	Neuroendocrine Tumors**, carcinoid tumors, neuroblastoma, and small cell lung cancer	Proton-pump inhibitors (medications given to reduce stomach acid)	Normal varies on how tested, but typically < 39 ng/l is normal
Cytokeratin Fragment 21-1 (Blood Test)	Lung, urologic, gastrointestinal, and gynecologic cancers	Lung disease	0.05-2.90 ng/ml
HCG Human Chorionic Gonadotrophin Or Beta-HCG, B-HCG	Germ cell, testicular cancers**, gestational trophoblastic neoplasia	Pregnancy, marijuana use, hypogonadism (testicular failure), cirrhosis, inflammatory bowel disease, duodenal ulcers	In men: < 2.5 U/ml In non-pregnant women: < 5.0 U/ml

Tumor Marker	Cancers Associated With Elevated Results	Non-Cancerous Reasons for Elevated Levels	"Normal" Results
5-HIAA 5-Hydroxy-Indol Acetic Acid (24 hour urine collection)	Carcinoid tumors	Celiac & tropical sprue, Whipple's disease, dietary: walnuts, pecans, bananas, avocados, eggplants, pineapples, plums & tomatoes; medications: acetaminophen, aspirin and guaifenesin	Normal 6-10 mg over 24 hours
LDH Lactic Dehydrogenase	Lymphoma, melanoma, acute leukemia, seminoma (germ cell tumors)	Hepatitis, MI (heart attack), stroke, anemia (pernicious & thalassemia), muscular dystrophy, certain medications (narcotics, aspirin, anesthetics, alcohol), muscle injury	Normal values are 100-333 u/l
NSE Neuron-specific Enolase	Small cell lung cancer**, neuroblastoma	Proton pump inhibitor treatment, hemolytic anemia, hepatic failure, end stage renal failure, brain injury, seizure, stroke	Normal < 9 µg/L
NMP 22 (urine test)	Bladder cancer**	BPH (benign prostatic hypertrophy), prostatitis	Normal < 10 U/ml
PAP Prostatic Acid Phosphatase	Metastatic prostate cancer** Myeloma, lung cancer, osteogenic sarcoma	Prostatitis, Gaucher's disease, osteoporosis, cirrhosis, hyperparathyroidism, prostatic hypertrophy	Normal : 0.5 to 1.9 u/l
PSA Prostate Specific Antigen	Prostate**	BPH (benign prostatic hypertrophy), nodular prostatic hyperplasia, prostatitis, prostate trauma/ inflammation, ejaculation	Normal < 4 ng/ml (half-life 2-3 days)
Tg Thyroglobulin	Thyroid Cancer	Anti-thyroglobulin antibodies	< 33 ng/mL; if entire thyroid removed < 2 ng/mL
Urine Catecholamines: **VMA** Vanillylmandelic Acid (24 hour collection of urine; it is a catecholamine metabolite)	Neuroblastoma** Pheochromocytoma, ganglioneuroma, rhabdomyosarcoma, PNET	Dietary intake (bananas, vanilla, tea, coffee, ice cream, chocolate), medications (tetracyclines, methyldopa, MAOIs)	8 – 35 mmols over 24 hours
HVA Homovanillic Acid (24 hour collection of urine; it is a catecholamine metabolite)	Neuroblastoma**	Same as VMA, in addition: psychosis, major depression, dopamine (a medication)	Up to 40 mmols over 24 hours

Table 4.2: Most common tumor markers used in oncological screening and prevention.

However, many of these substances are unfortunately detected in patients affected by non-oncologic pathologies, making them poorly specific for neoplasm detection. Most notable false-positive cases are from CEA, CA125, and CA15-3 detection, which are measured in high quantities in cirrhotic individuals; CA19-9 is detected in individuals

affected by various inflammatory diseases of the digestive system, and unhealthy behaviors like smoking can alter the presence of CEA as well. For this reason, these substances are mostly searched in case of already suspected tumor presence or either as post-surgery/therapy check, especially to detect possible regeneration of the removed cancer. Also, these compounds are normally detected following immunological reactions with antibodies and other compounds added to the sample [136,137]. However, immunological analysis adulterates the original sample because of the addition of the antibodies against the above antigens, often requiring multiple blood samples, leading to an increase of costs, analysis time, and complexity in the sampling process. Different approaches have been pursued in the years to circumvent these problems, looking for markers univocally connected to the development and spread of tumors, and developing devices minimizing the consumable usage. Different approaches have been applied to detect directly CTC into blood samples [138–140], in order to monitor the metastatization process and the spread of those cells into the human body, and thus as screening for the degeneration of tumors into a malignant state. On the other hand, other devices are targeted to detect new markers or multiple markers (as, for instance, the electrochemical and nanostructured field effect sensors [141–143]). These devices, focused on the early detection of neoplastic pathologies, meet the demand by the health service for pre-screening protocols for tumors, leading to a lower treatment costs and an increase of survival chance. Therefore, some of them are considered in their respective national health system as point-of-care utilities [144]. In particular, nanostructures of various nature [145] and chemoresistive sensors have been successfully applied to detect different kind of tumors, also in whole blood (450 ml) and in test tube (7 ml) blood samples [146,147], detecting a single or a little group of known markers. In this study, instead, the goal was to discriminate between healthy and tumor affected subjects, of known health status, by measuring all the volatile chemicals exhaled by the blood samples, employing nanostructured chemoresistive sensors. This approach gave encouraging results in previous works [35,148–152] by employing these sensors on laboratory-simulated intestinal environment and feces samples, and the part of the work in this thesis on the first data set on blood samples have been already published as well [47], proving the reliability of the device and scientific veracity of the research. The low cost of production of these sensors, allowing to develop more affordable devices compared to the ones mentioned

above, and their fast response to changes in the chemical composition of their environment, make them the ideal sensors to develop a point-of-care medical screening.

4.6 – Immortalized Cells

An immortalized cell line (ICL) is a population of cells from a multicellular organism which would normally not proliferate indefinitely but, due to mutation, have evaded normal cellular senescence and instead can keep undergoing division. The cells can therefore be grown for prolonged periods in vitro. The mutations required for immortality can occur naturally or be intentionally induced for experimental purposes. Immortal cell lines are a very important tool for research into the biochemistry and cell biology of multicellular organisms. Immortalized cell lines have also found uses in biotechnology. ICL share with stem cells the ability to divide indefinitely, but differently from the first, stem cells do that naturally as normal part of the development of a multicellular organism. From a biological point of view, they are not far from a cancerous cell, with the difference that their reproduction happens just on 2D surfaces, and not on 3D masses as cancers. There are various immortal cell lines. Some of them are normal cell lines, e.g. derived from stem cells. Other immortalized cell lines are the in vitro equivalent of cancerous cells. Cancer occurs when a somatic cell which normally cannot divide undergoes mutations which cause de-regulation of the normal cell cycle controls leading to uncontrolled proliferation. Immortalized cell lines have undergone similar mutations allowing a cell type which would normally not be able to divide to be proliferated in vitro. The origins of some immortal cell lines, for example HeLa human cells, are from naturally occurring cancers. ICL are widely used as a simple model for more complex biological systems, for example for the analysis of the biochemistry and cell biology of mammalian (including human) cells. The main advantage of using an immortal cell line for research is its immortality; the cells can be grown indefinitely in culture. This simplifies analysis of the biology of cells which may otherwise have a limited lifetime. ICL can also be cloned giving rise to a clonal population which can, in turn, be propagated indefinitely. This allows an analysis to be repeated many times on genetically identical cells which is desirable for repeatable scientific experiments. The alternative, performing an analysis on primary cells from multiple tissue donors, does not have this advantage. They find use in biotechnology where they are a cost-effective way of growing cells similar to those found in a multicellular organism in vitro. The cells are

used for a wide variety of purposes, from testing toxicity of compounds or drugs to production of eukaryotic proteins. There are several methods for generating immortalized cell lines [153]:

- Isolation from a naturally occurring cancer. This is the original method for generating an immortalized cell line. Major examples include human HeLa cells, obtained from a cervical cancer and mouse Raw 264.7 cells, obtained from a murine leukemia
- Spontaneous or induced random mutagenesis and selection for cells which are able to undergo division
- Introduction of a viral gene that partially deregulates the cell cycle (e.g., the adenovirus E1 gene was used to immortalize the HEK 293 cell line)
- Artificial expression of key proteins required for immortality, for example telomerase which prevents degradation of chromosome ends during DNA replication in eukaryotes
- Hybridoma technology, specifically used for the generation of immortalized antibody-producing B cell lines, where an antibody-producing B cell is fused with a myeloma (B cell cancer) cell

The main common properties of immortalized cells are the following:

- Immortalized with the aid of an adenovirus
- No memory of their former biological form or role
- Uncontrolled reproduction as long as nutrients and surface to bind are available
- Most of them (but not all) reproduce as 2-dimensional tissues, while malignant neoplasms create 3D masses (this is true also for HCT 116, tested as well in this branch of the research)

Most immortalized cell lines are classified by the cell type they originated from, or by the ones that are most similar to them biologically. Below are listed the most common ICL:

- A549 cells, derived from the human lung cancer
- HeLa cells, an extremely widely used human cell line isolated from a cervical cancer, probably derived from epithelial cells

- HEK 293 cells, derived from aborted human fetal cells and a virus
- Jurkat, a human T lymphocyte cell line isolated from a case of leukemia
- 3T3, a mouse fibroblast cell line derived from a spontaneous mutation in cultured mouse embryo tissue
- HCT 116 cells, derived from human colorectal cancer
- Vero cells, a monkey cell line
- F11 Cells, a line of neurons from the dorsal root ganglia of rats
- CHO, Chinese hamster ovary cells

In this thesis, CHO, A549, HCT 116 and HEK 293 immortalized lines were tested for metabolites production analysis using the portable device SCENT B1.

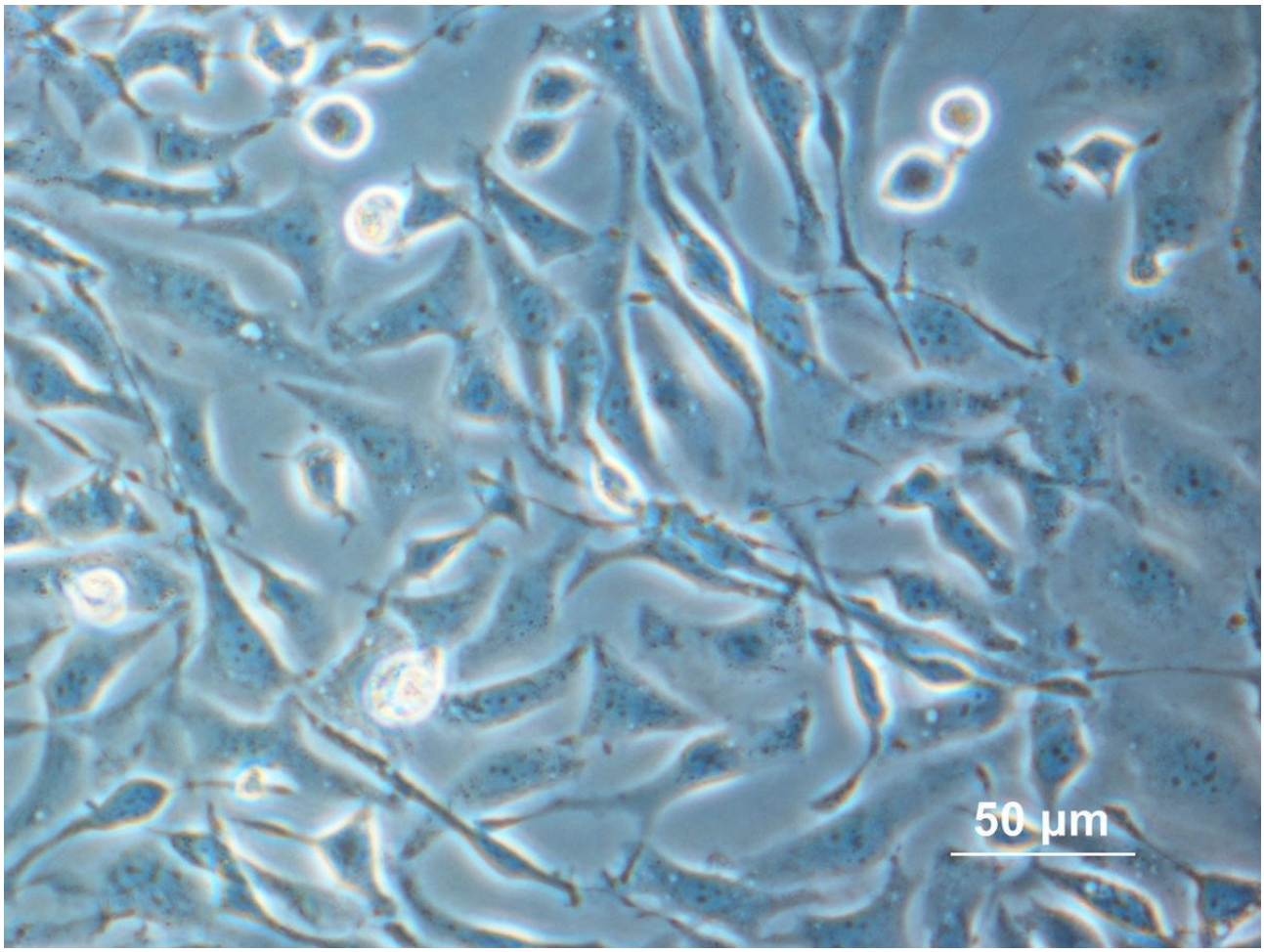

Figure 4.12: Sample of immortalized CHO cells, adherent to their Petri dish.

In Figure 4.13, the cell proliferation with the passing of time is shown. Round shaped cells are dead and in suspension inside the breeding ground, elongated cells are alive and

attached to the bottom of the petri dish, connected to each other while forming a pseudo-tissue. The proliferation has been observed from the variation in the exhalations measured from the sensors also during the experiments, together with the contact inhibition effect as shown in Chapter 6.

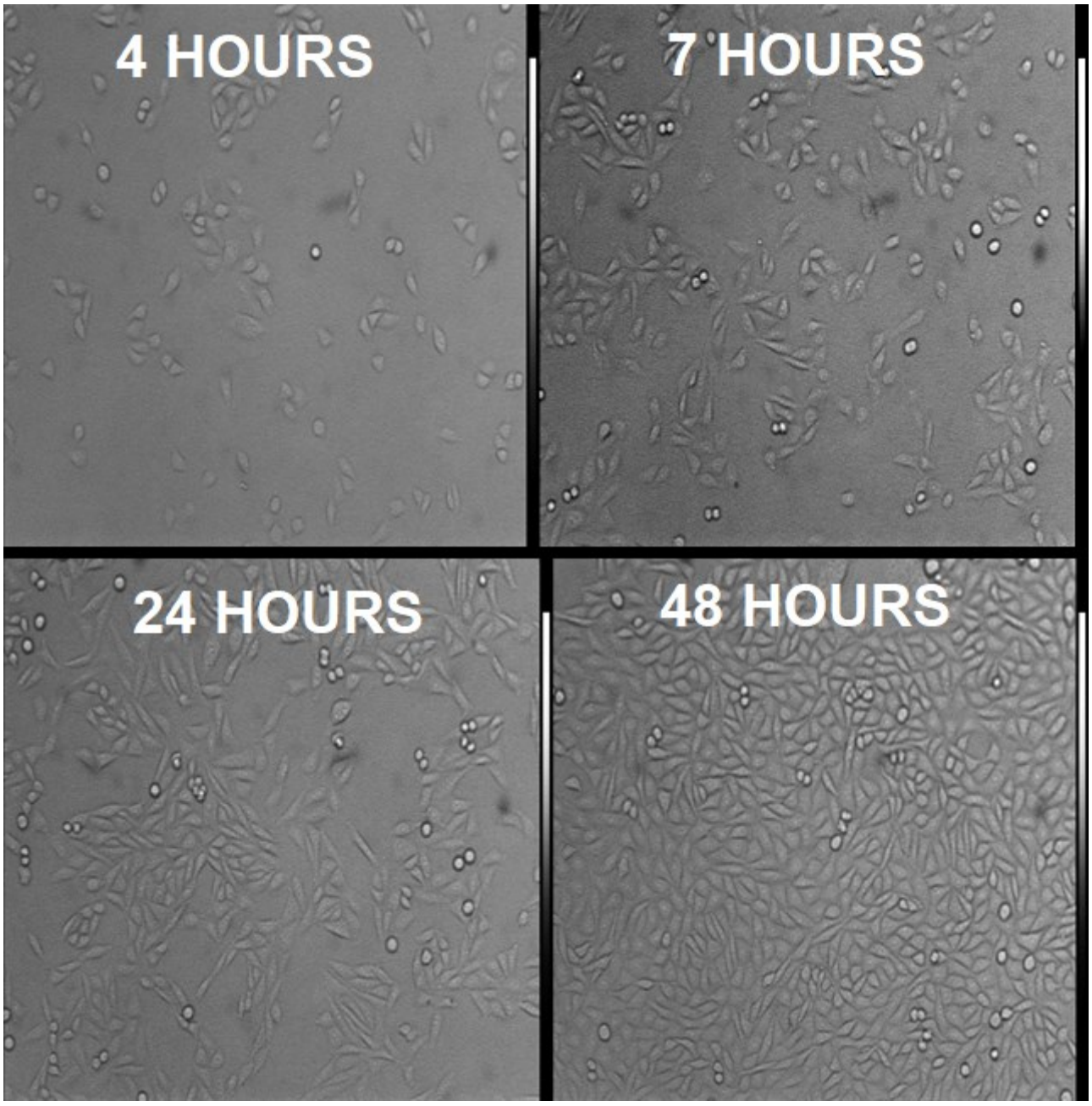

Figure 4.13: Proliferation of CHO cells, from a previous study. The hours indicated are referred to the lapse of time included between the moment in which the cultures have been plated and put into the incubator, and the moment of the test with a SCENT device.

Chapter 5 – SCENT A1: Background Studies

As previously introduced, this thesis is the continuation of part of the work introduced from the Master's Degree thesis "Detection of tumor markers and cell metabolites on feces and cells with nanostructured sensors", where standard laboratory gases, feces and cell cultures have been analyzed to perform studies on tumor markers. Another prototype was used on those researches, which led to multiple publications [35,47,148–152] and reliable and steady results, encouraging the follow-up of the research also on different targets. In particular, the feces studies were conducted with the same approach which is now tried with the new biological samples, starting from single sensor approach and radar diagrams as shown in Figure 5.1 to more complex statistical methods in the next year with PCA, (Figure 5.2), and passing in the recent years to the development of the receiver operating characteristic (ROC, a graphical plot that illustrates the diagnostic ability of a binary classifier system, true positive rate vs true negative rate, as its discrimination threshold is varied) curve, and the correlated confusion matrix, for medical purposes (Figure 5.3A–B).

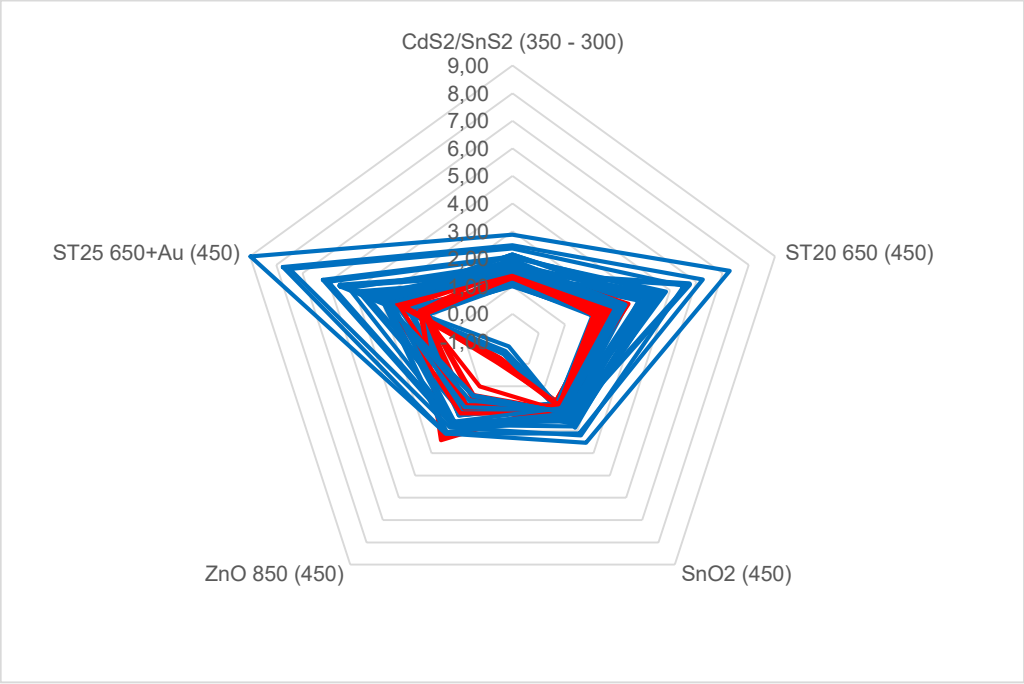

Figure 5.1: Radar diagram from an array of sensors, with each pentagon referring to a different feces sample tested. Blue figures are referred to healthy donors; red ones are from tumor affected donors [34].

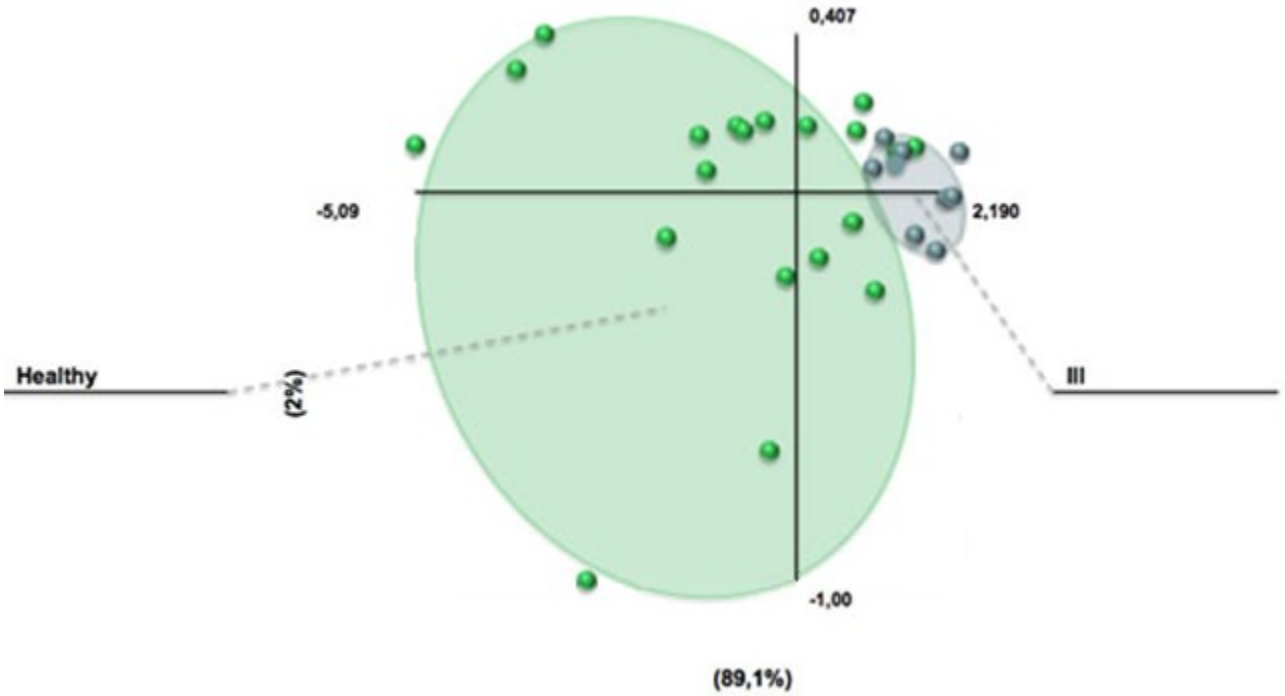

Figure 5.2: PCA from a previous sensors array over feces sample. The discrimination between samples and the small overlap between the areas, with 91,1% explained variance between PC1 and PC2, shows the reliability of the sensors for this application.

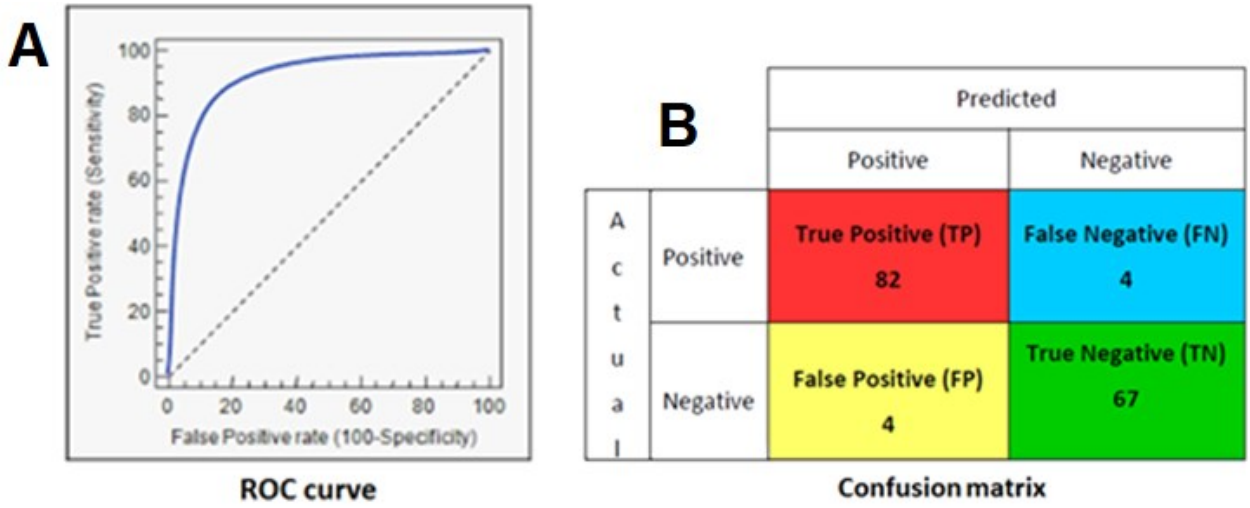

Figure 5.3: ROC curve and confusion matrix on the previous studies on feces.

In particular, from the confusion matrix is possible to extrapolate four important values, as shown from the following Equations: rate of finding true positives and true negatives from the device, and rate of false positives and false negatives (error chances, respectively called fall-out and miss rate) of the device. False positives are also known as Type I error, while false negatives as Type II error.

$$True\ Positive\ Rate/Sensitivity(\boldsymbol{TPR}) = \frac{TP}{TP + FN} \cdot 100\% = \frac{TP}{P} \cdot 100\% = 95.35\% \quad (5.1)$$

$$True\ Negative\ Rate/Specificity\ (\boldsymbol{TNR}) = \frac{TN}{TN + FP} \cdot 100\% = \frac{TN}{N} \cdot 100\% = 94.37\% \quad (5.2)$$

$$False\ Positive\ Rate/Fall\text{-}Out\ (\boldsymbol{FPR}) = \frac{FP}{FP + TN} \cdot 100\% = (1 - TNR) \cdot 100\% = 5.63\% \quad (5.3)$$

$$False\ Negative\ Rate/Miss\ Rate\ (\boldsymbol{FNR}) = \frac{FN}{FN + TP} \cdot 100\% = (1 - TPR) \cdot 100\% = 4.65\% \quad (5.4)$$

After all these preliminary observation, the actual machine learning logic to perform statistical classification and actually pre-screen the presence of tumors was finally adopted. This last method was chosen order to develop the software able to give as output a user-friendly response (Negative / Low Risk / Positive), with a continuous self-training to perfect itself after each test (results shown in the matrix Figure 5.4 are part of the initial training data), while confronting the predicted data obtained in double blind with the golden standard test, colonoscopy.

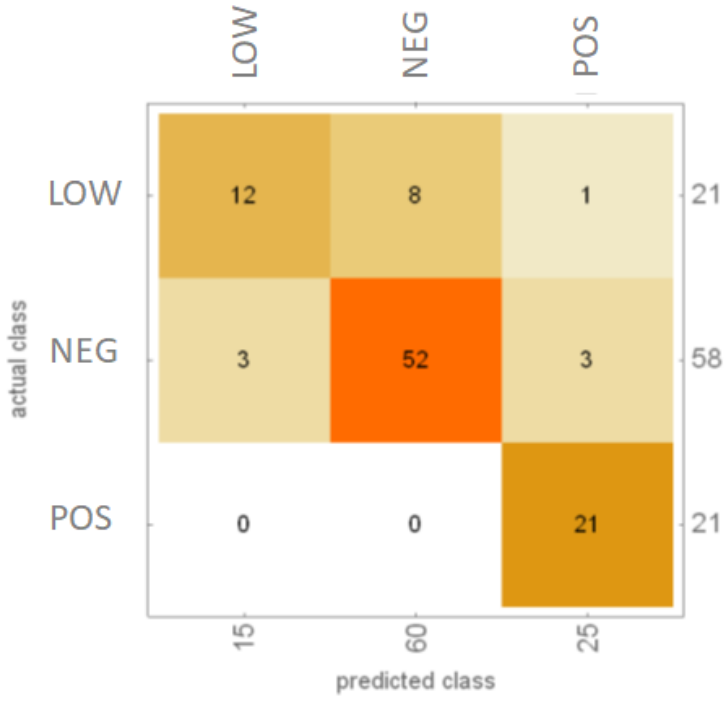

Figure 5.4: Matrix representing the results from the preliminary tests in machine learning. The main diagonal shows the data correctly predicted in double blind against colonoscopy exam, while the remaining squares show the classification error done by the predicting software, between the three different classes.

For what concerns the cell tests previously realized, only CHO, HEK-293 and fibroblasts cultures were studied. The breeding ground composition is discussed further in Appendix A. Figure 5.5 shows a pool of raw data from multiple immortalized CHO cell cultures. “CHO#+DMEM” labels the response from petri dishes hosting still both cells and the full quantity of breeding ground, “CHO# washed” labels the petri dishes from which the breeding ground was nearly completely removed, leaving just a thin film of that fluid over the cells to keep them lively (and thus monitor their emanations at different plating concentrations, different and proliferation times, without the background from the markers trapped and slowly freed from the DMEM itself), and “DMEM from CHO#” labels the measurements from the breeding ground washed away from the original hosting petri dishes into new ones, which exhales markers previously emanated from the cells but still trapped in the fluid. As previously stated, this last application brought to the idea of studying emanations from blood samples as well. The reason behind it is that the blood stream could carry tumor markers far away from the original neoplasia, if the tumor already reached the malignant state, and host them (even if in lower quantity due to their reactive nature) so that a screening device could exploit them once emanated from a normal sample taken from a donor.

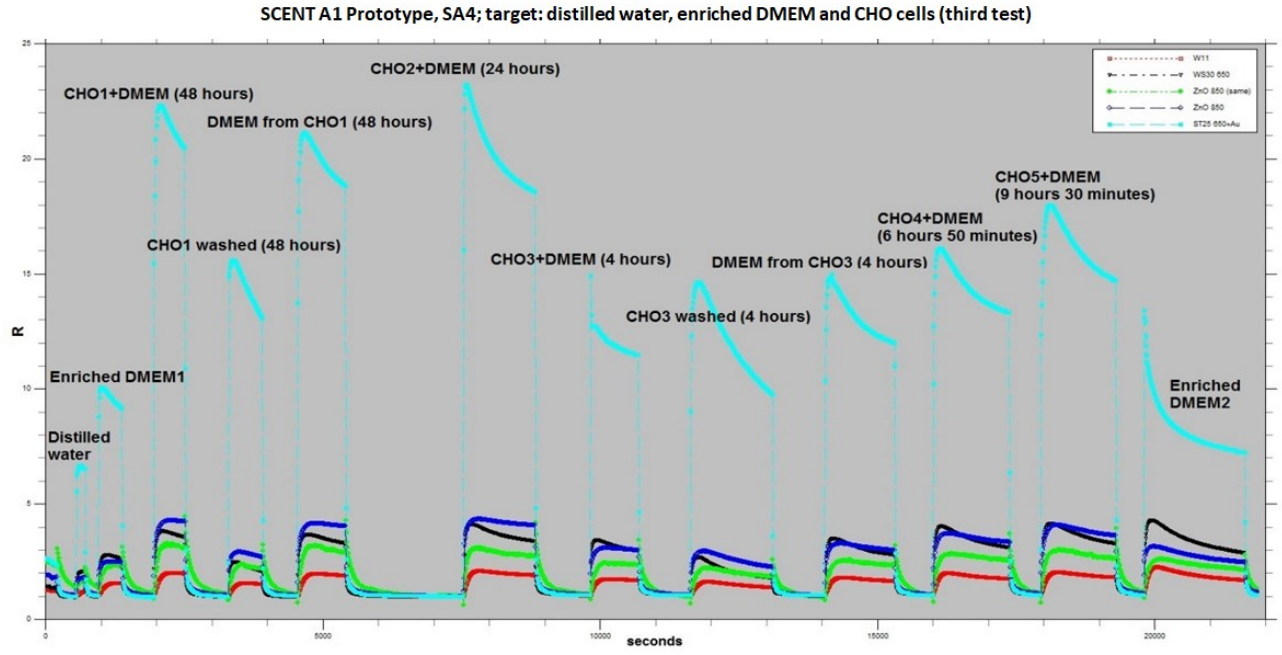

Figure 5.5: Various measures on CHO immortalized cell cultures samples, plated at different times (4 hours, 7 hours, 9 hours and 30 minutes,24 hours and 48 hours).

Figure 5.6 shows the responses from the 5 sensors to the CHO#+DMEM group of measures, present also in figure 5.5. Cell proliferation, verified with the optical microscope as shown in Figure 4.13, was observed also from the increase in the amplitude of those sensors outputs as time goes by.

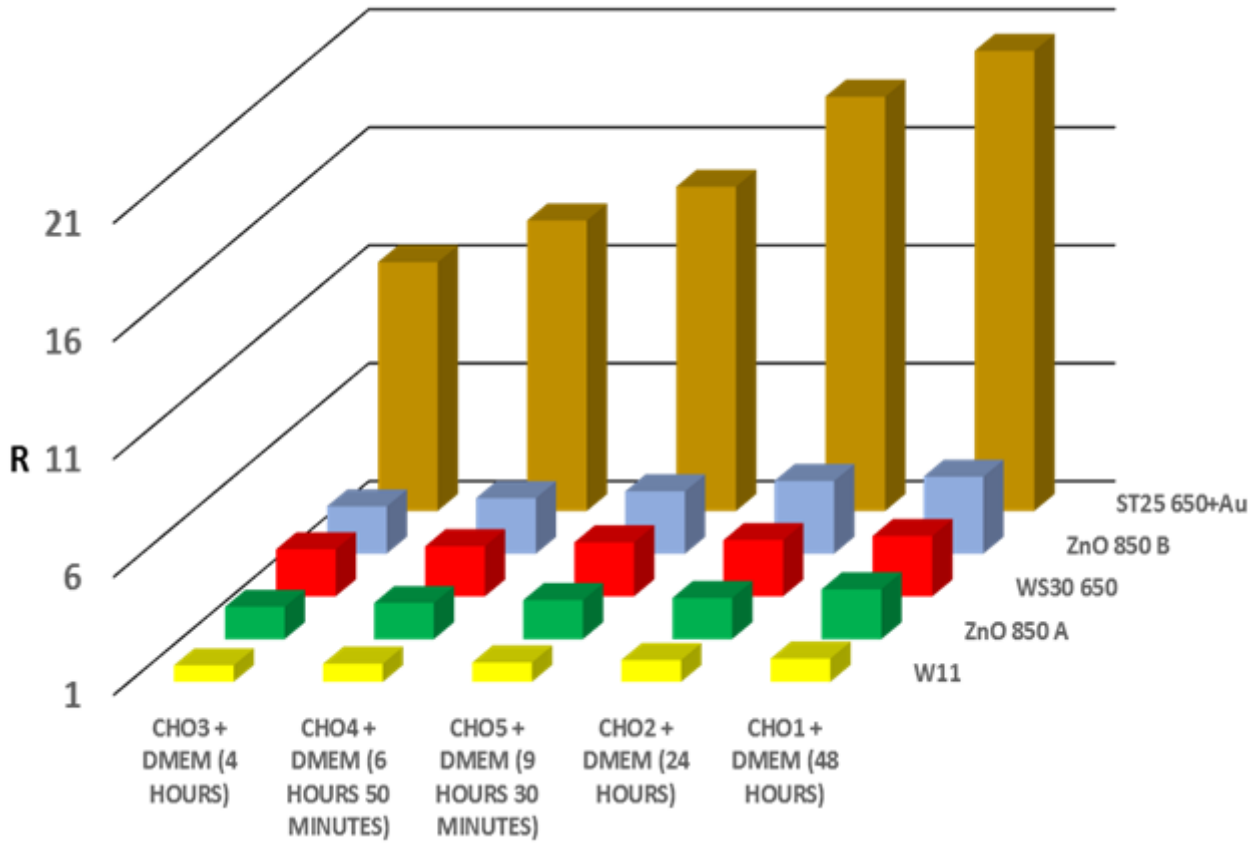

Figure 5.6: Resulting responses from the tests in Figure 5.5, ordered by plating time before the test [150].

Finally, in Figure 5.7, the comparison between the responses from standard breeding ground in which all cell cultures are kept, fibroblasts (which are from a primary line culture, still keeping their biological memory and healthy) and HEK-293, after 48 hours of incubation before the test. As obvious from the figure, amplitude of the responses differs heavily between the three samples, and thus all sensors, even if with different size of responses between them, could discriminate empty breeding ground fluids (for ST 25 650+Au, $R{\sim}2$), healthy cells (for ST 25 650+Au, $R{\sim}4.5$) and immortalized cells (for ST 25 650+Au on HEK-293, $R{\sim}9$) between them, and even between different types of tumor cells if tests at the same incubator time are compared (Figure 5.6 and 5.7 – ST 25 650+Au on HEK-293, $R{\sim}9$; ST 25 650+Au on CHO, $R{\sim}20$).

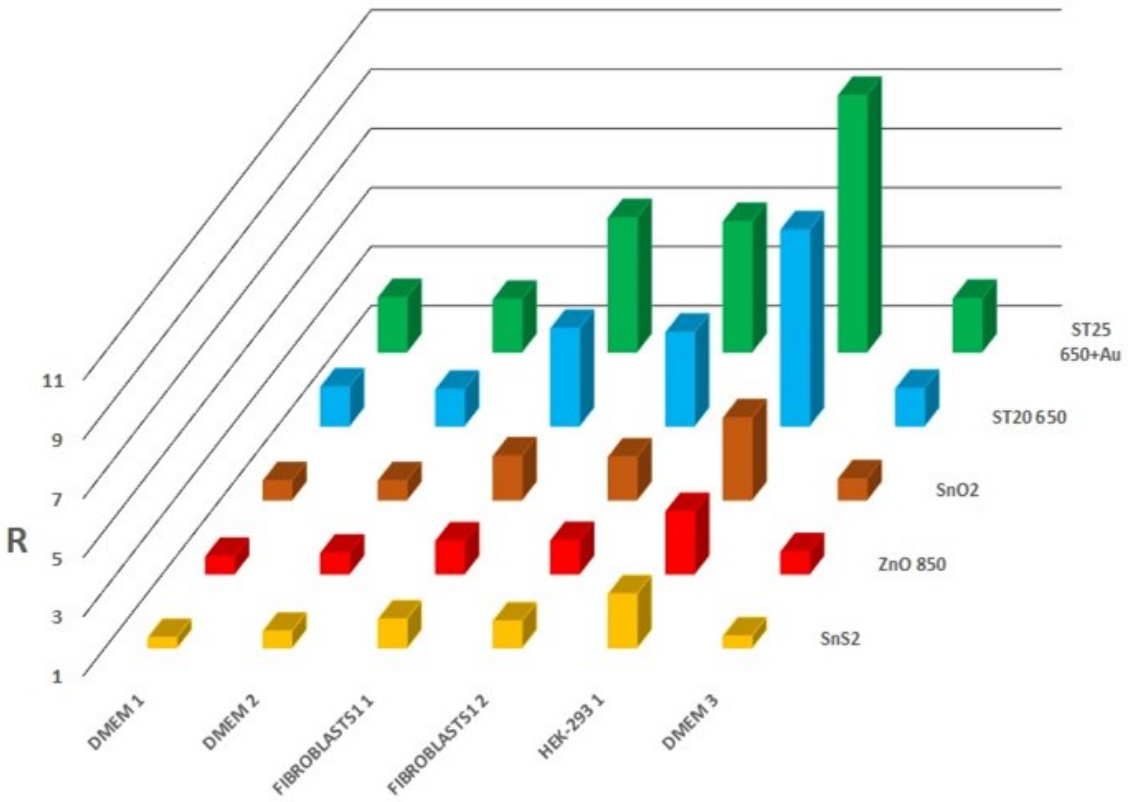

Figure 5.7: Results from the previous thesis, after 48 hours of incubation: comparison between breeding ground, fibroblasts and HEK-293 samples [150].

Chapter 6 – Cell Cultures Tests

Cell cultures tests idea came up to mind from the Master's Degree thesis that hosted the birth of the three branches of research discussed in this and in the next two chapters. It was necessary to observe, after simulations with the known markers on laboratory setup and on the temporary carrier of the tumor metabolites (feces), if cells could really emanate volatile tumor markers as a tissue, as reflection of the real phenomenon in the human body. The aim was to follow with SCENT B1 the progressive increase of the metabolite emanations, due to cellular metabolism, by testing the samples with different starting plating concentration (the number of cells present in the petri dish at the moment of the incubation, after placing them in the breeding ground) and monitoring them after different times of incubation. As introduced in Paragraph 4.6, four immortalized cell lines have been studied in this work:

- A549 cells, derived from the human lung cancer
- HEK 293 cells, derived from aborted human fetal cells and a virus
- HCT 116 cells, derived from human colorectal cancer
- CHO, Chinese hamster ovary cells

The reason behind the use of multiple cells kind was to test if the device could distinguish different types between them, and not just healthy from immortalized ones. To follow the evolution among time of the cell cultures, a visible ruse was taken as advantage. Figure 6.1 shows, in fact, how the color of the breeding ground changes depending on the incubation time (the longer, the more it turns from pinkish to yellow because of acidification of the pH), proving the growth and the consumption of nutrients and the increasing concentration of wastes from cellular metabolites.

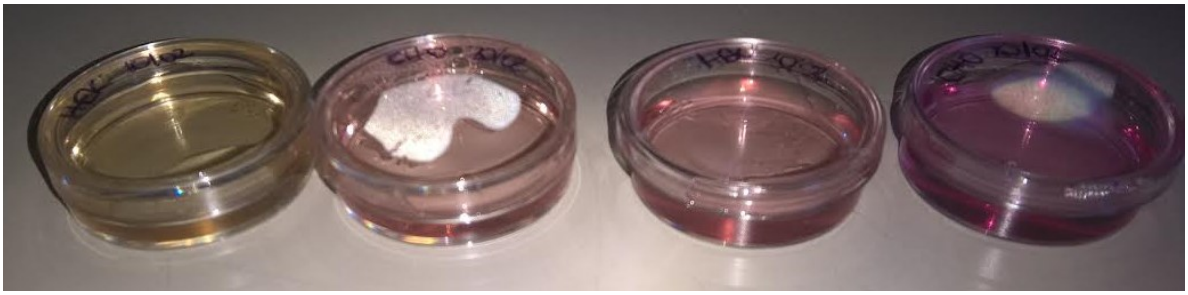

Figure 6.1: Petri dishes containing cell cultures (CHO and HEK-293).

6.1 – Cell Cultures Tests: Sampling

Each test has been realized with three petri dishes, in order to increase the emanation surface, hosted in a tripod as shown in Figure 8.2. The preparation for the samples has been carried out as it follows:

- Each petri dish ($diameter = 3.5cm$) has been filled with $1.5ml$ Dulbecco's Modified Eagle's Medium (High Glucose) without Fetal Bovine Serum, with various antibiotics added (penicillin, streptomycin and glutamine) to prevent contaminations from microorganisms that could harm the cells
- Fetal Bovine Serum was added, in quantity to reach the 10% of the total volume of the finished breeding ground
- Cells have been plated in the petri dishes with different concentrations (which can be guessed by using a gridded glass and the optical microscope): 80,000, 240,000, 350.000, 500,000 and 1,000,000. From these initial concentrations, the cells have been left in groups of three petri dishes each in the incubator at the same time, and then tested after different hours and days, so that the incubation time would have been for each group from 4 to 72 hours. For all samples, these two parameters are critical to define both their chances and state of proliferation during the test

---

6.2 – Cell Cultures Tests: Data and Results

Given the intrinsic complexity of the measures (type of cells tested, plating concentration and incubation time have to be taken in account), and the lower number of possible tests, cell cultures tests underwent only single sensors approaches, for all the arrays. One of the main successes in this study was the observation of contact inhibition phenomenon in the cultures, as expected from living organisms with limited space and nutrients to survive (being the surface of the petri dishes limited, as well as the nutrients in the breeding ground). Contact inhibition manifests itself as a lowering in the proliferation rate and in the metabolism of the cells once that they are close to confluency (when the whole bottom surface of the hosting container is covered, or when clusters of cells are too many to sustain more cellular proliferation), or when they lose space to reproduce or nutrients to sustain themselves in their surroundings. This final statement presents another problem with the preparation of the cell cultures: heterogeneous distribution of the initial

concentration of cells will end always in less prolific cell cultures over time, because 2D clusters rather than uniform covering will appear, starving the cells in the middle of the agglomerate and slowing or even blocking their metabolism. This means literally that the “hand” of the operator plating and preparing the cell cultures must be the most diligent as possible, not only in keeping the organisms safe from contamination, but also to spread the cells on the petri dishes during the plating process in the most homogenous way, to avoid contact inhibition before the total coverage of the surface. From an analytical point of view, the vital processes (like metabolism, reproduction and similar) of the organisms tend to increase when the environment allows it (space and nutrients), and instead slow and saturate as the population increases while the means of sustain lower (showing a logarithm behavior). This trend was observed by associating the optical microscope images (like in Figures 4.13, 6.9–17, 6.19 and 6.20) with the increase of the responses of the sensors (as shown in Figure 6.5–8), up to a saturation once the population of cells in the hosting container was too high and the nutrients too low to sustain their survival without the lowering of their metabolism. In Figure 6.2, the results from some of the cell tests done with SCENT A1 (the ones shown in Figure 5.6) are shown, together with logarithm trend and their $R^2 = determination\ coefficient = correlation\ coefficient^2$, which shows us how close the variability of the data is to that statistical trend (the closer R^2 to 1, the better). This correlation to the trend expected for contact inhibition, together with the optical proof from Figure 4.13, give us the confidence to asses that what is measured are markers strictly connected to the cell metabolism: the volatile metabolites, that in this study are used tumor markers.

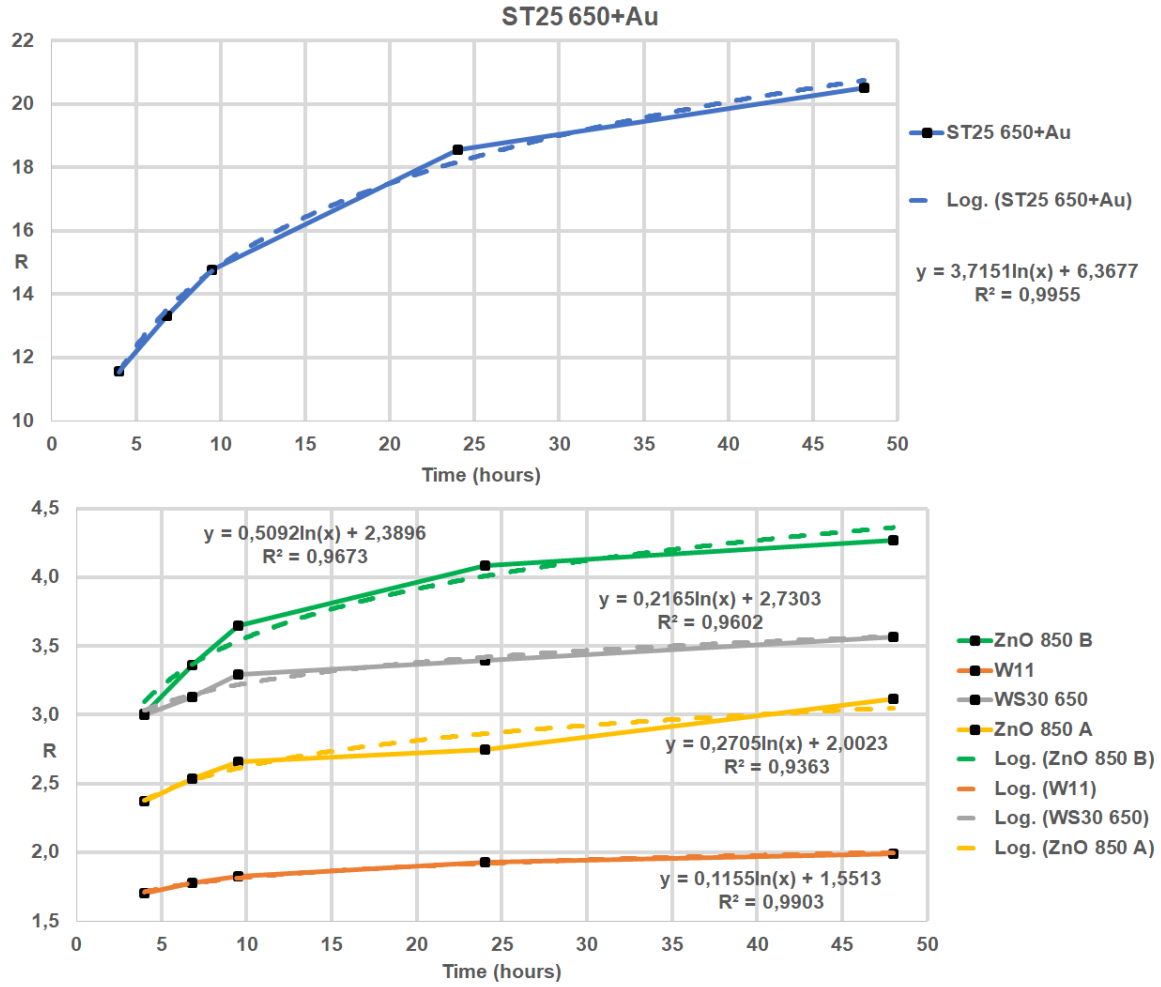

Figure 6.2: Responses from Figure 5.6, confronted with a logarithm trend.

Table 6.1 and Figure 6.3 shows the results from more CHO cell cultures analyzed with the first sensors array. In Figure 6.4, these results are plotted together with more logarithm trends, and again three of them show good resemblance with the statistical model proposed (especially ST25 650+Au sensor), strengthening the reliability of the hypothesis proposed. The coverage in % represents how densely covered from the cells is the bottom surface of the petri dish; the greater it is, the higher the number of cells and their density in the hosting container. This value obviously increases with time, since population of the cells logically increases with time due to their proliferation.

SENSOR	ENRICHED DMEM	CHO 48hr (coverage = 95%)	CHO 25hr (coverage = 60%)	CHO 6hr (coverage = 15%)	CHO 29hr (coverage = 30%)	CHO 53hr (coverage = 100%)	CHO 9hr (coverage = 20%)
ST25 650+Au	2.50	7.55	7.07	4.44	7.13	7.64	5.46
ZnO 850	1.21	1.93	1.90	1.57	1.98	1.98	1.75
SmFeO3	-2.15	-4.17	-4.17	-3.18	-4.45	-4.45	-3.71
CdS2	1.30	1.54	1.63	1.51	1.57	1.63	1.48

Table 6.1: Responses to which the graphic in Figure 6.3 is referred.

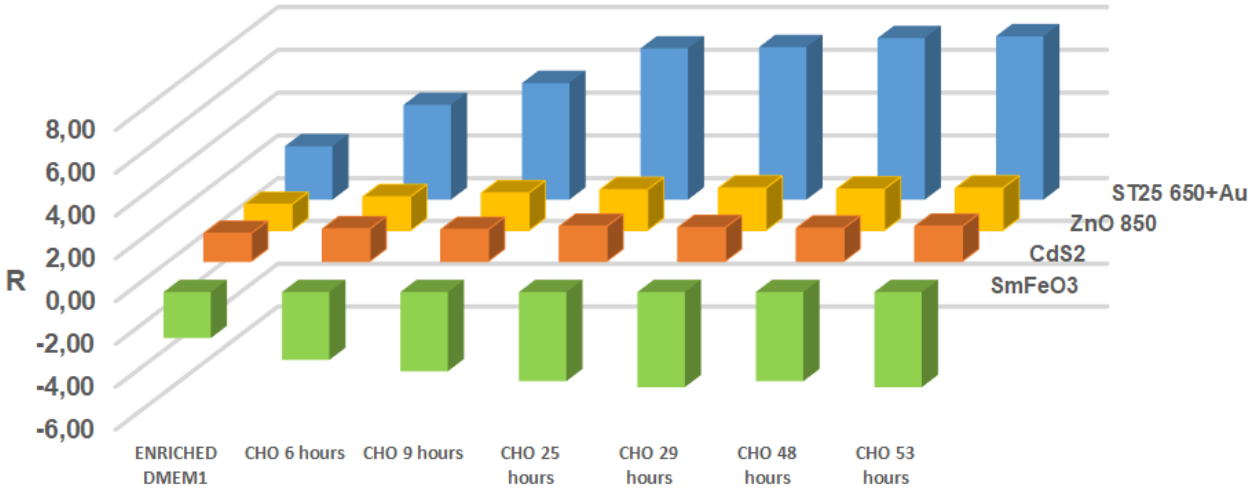

Figure 6.3: CHO cells responses on first sensors array.

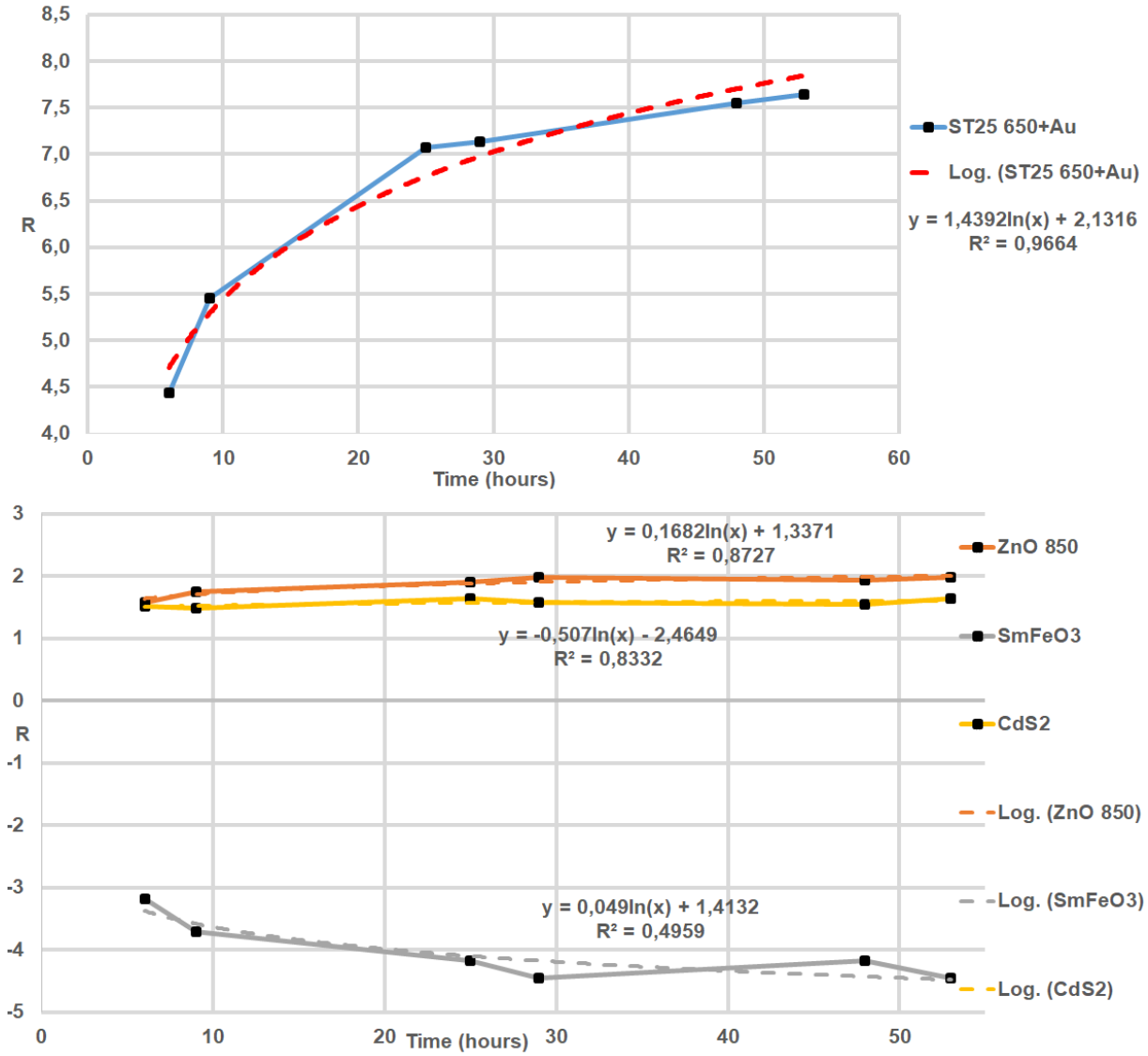

Figure 6.4: Responses from Figure 6.3, confronted with a logarithm trend.

Tables 6.2–4 and Figures 6.5–8 show a cross testing between HEK-293 and CHO, on the fourth sensors array. Figures 6.9 – 17, 6.19 and 6.20 show the optical microscope plating for some of these cases. Also in this case, the progressive increase of the responses with the increase of the cellular population, is observed, proving the capability of chemoresistive sensors to follow the enhancing tumor marker emanation from cell cultures. This time, the difference between the cell lines is not as strong as in the previous study, but the reason resides on the fact that the CHO cultures, this time, were not plated homogeneously as the previous times, as it is visible by confronting Figures 6.9–11, where CHO cells with 80k (48 hours of incubation) and 240k (24 and 72 hours of incubation) plating numbers were observed being suffering and not creating a vital tissue like in Figure 4.13, and also by comparison with the healthy state of the HEK-293 at the same times of incubation (Figure 6.12 for 80k and Figure 6.13 for 240k). In fact, it must be considered that these cells are living beings under stress condition (outside of the incubator, which is kept at $36°C$, they are tested at a temperature spanning between $22.4°C$ and $22.7°C$), thus their metabolism might slower for this reason, too. Instead, if the preparation is properly realized, they act like in Figure 6.14 (HEK-293, 1m plating number, 48 hours), reaching confluency with a homogenous, uniform tissue-like structure (and even starting to grow in 3D if left there for one more day, free to grow more, as in Figure 6.15). An important observation can be made on the measure “DMEM1 A 72H”: from comparison (using the optical microscope images in Figures 6.16 before and 6.17 after contamination) between it and another sample incubated for the same time, in the same set of measures, that sample of DMEM showed to be heavily contaminated from foreign microorganisms (and it was even visible at naked eye, Figure 6.18), while the other was not. These microorganisms were probably staphylococci, as they were found contaminating another set, a culture of CHO, shown in Figure 6.19; in this case, by leaving that petri dish not sterilized in a safe spot of the laboratory, it was possible to verify that the bacteria contamination was real and able to grow and proliferate, like Figure 6.20 proves. Bacteria activity was observed in that case, which reproduce way faster compared to immortalized cells, and the responses was clearly higher than the ones from cells themselves. This led to the idea, for a future application, of testing also bacteria cultures and the effect of drugs on them in real time, with the same device. It is important to notice that, by observing directly with the optical microscope, it was possible to know which petri dishes were contaminated, and thus prevent spreading of the pathogens to the rest of the experiment.

DMEM, CHO, HEK-293 24 HOURS, T = 22.5°C												
SENSOR	DMEM1 24H	CHO 80K 24H	CHO 240K 24H	CHO 500K 24H	DMEM 2 24H	HEK -293 80K 24H	HEK-293 240K 24H	HEK-293 500K 24H	HEK-293 1M 24H	DMEM 3 24H	CHO 80K OUT 24H	CHO 240K OUT 24H
ST25 650+Au	5.07	4.83	5.70	5.22	5.13	5.43	5.52	5.58	7.14	6.48	5.10	4.11
W11	1.59	1.56	1.53	1.44	1.29	1.35	1.32	1.38	1.44	1.47	1.68	1.56
ST20 650	7.87	7.44	8.93	7.92	8.52	8.04	8.28	9.98	8.87	8.70	7.08	5.60
ST25 650+Au B	7.32	7.14	8.67	7.65	7.74	7.89	7.98	8.13	11.13	9.15	7.50	5.88

Table 6.2: Cross test on HEK-293 and CHO, plating time = 24 hours.

DMEM, CHO, HEK-293 48 HOURS, TEMPERATURE = 22.4°C											
SENSORS	DMEM 1 48H	CHO 80K 48H	CHO 240K 48H	CHO 500K 48H	DMEM2 48H	HEK-293 80K 48H	HEK-293 240K 48H	HEK-293 500K 48H	HEK-293 1M 48H	DMEM3 A 48H	DMEM3 B 48H
ST25 650+Au	5.94	6.39	7.29	7.17	6.96	7.14	7.32	8.04	8.31	7.05	6.75
W11	1.19	1.21	1.38	1.32	1.28	1.25	1.30	1.30	1.29	1.39	1.51
ST20 650	9.48	9.36	10.50	10.68	9.33	10.26	10.50	11.76	11.97	9.63	8.88
ST25 650+Au B	10.23	10.53	11.70	11.43	10.65	11.22	11.43	12.93	13.32	10.29	10.02

Table 6.3: Cross test on HEK-293 and CHO, plating time = 48 hours.

DMEM, CHO, HEK-293 72 HOURS, TEMPERATURE = 22.7°C											
SENSOR	DMEM1 A 72H	CHO 80K 72H	CHO 240K 72H	CHO 500K 72H	DMEM2 72H	HEK-293 80K 72H	HEK-293 240K 72H	HEK-293 500K 72H	HEK-293 1M 72H	DMEM3 72H	DMEM1 B 72H
ST25 650+Au	11.16	7.48	7.52	7.52	7.20	7.60	7.84	8.32	7.40	7.52	8.36
W11	1.36	1.32	1.32	1.28	1.28	1.28	1.32	1.24	1.20	1.24	1.48
ST20 650	15.72	11.76	11.96	11.52	11.16	12.76	13.20	12.60	11.20	10.64	12.12
ST25 650+Au B	18.92	12.16	12.00	11.96	11.48	12.20	12.52	12.92	11.08	10.92	12.12

Table 6.4: Cross test on HEK-293 and CHO, plating time = 72 hours.

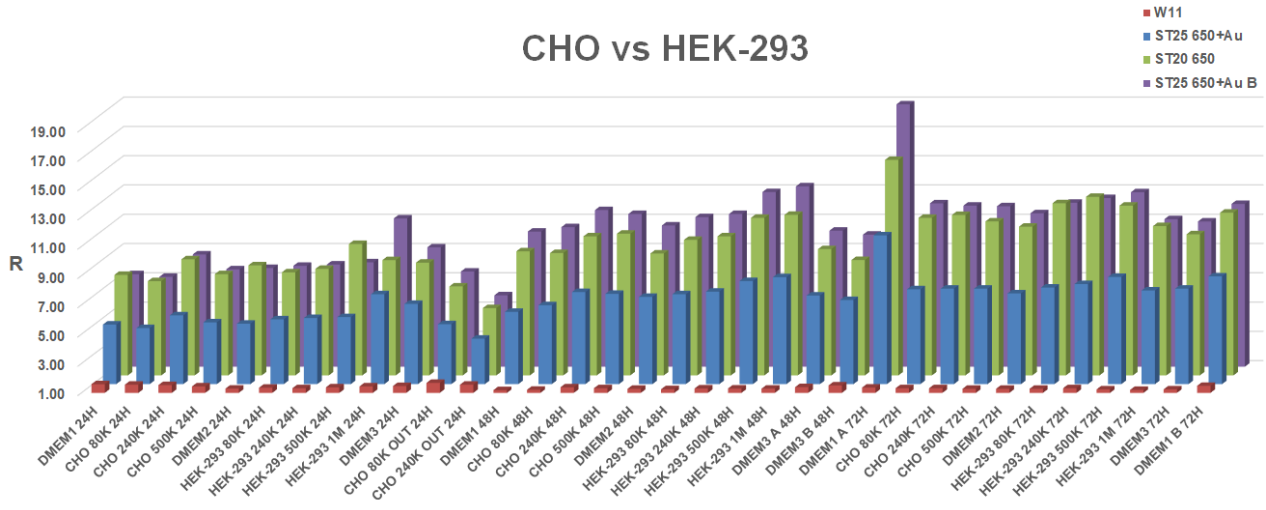

Figure 6.5: Crossed test between CHO and HEK-293.

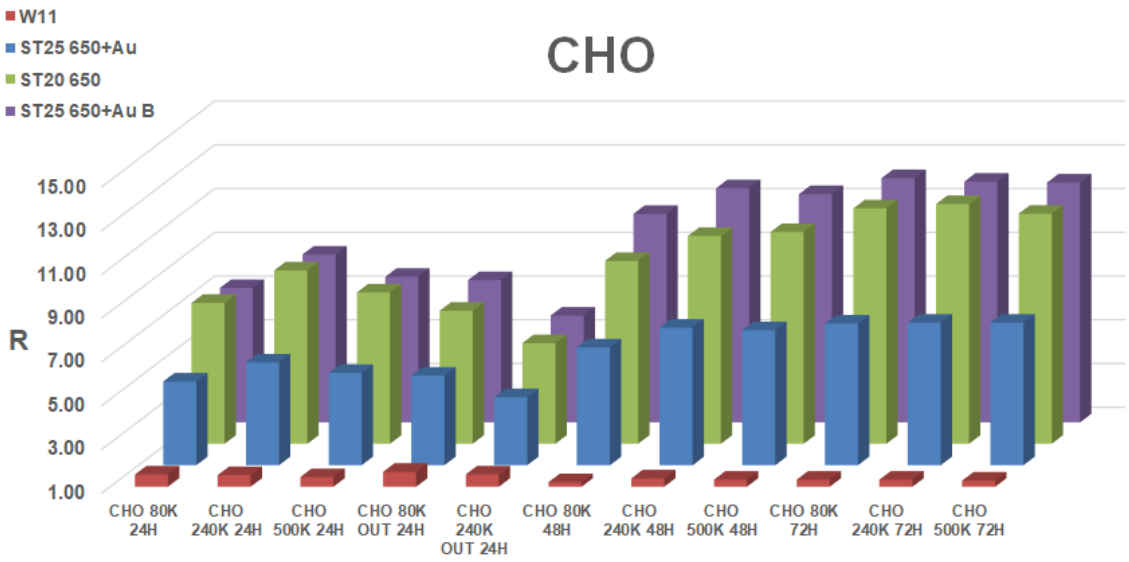

Figure 6.6: CHO results from the previous test, in chronological order.

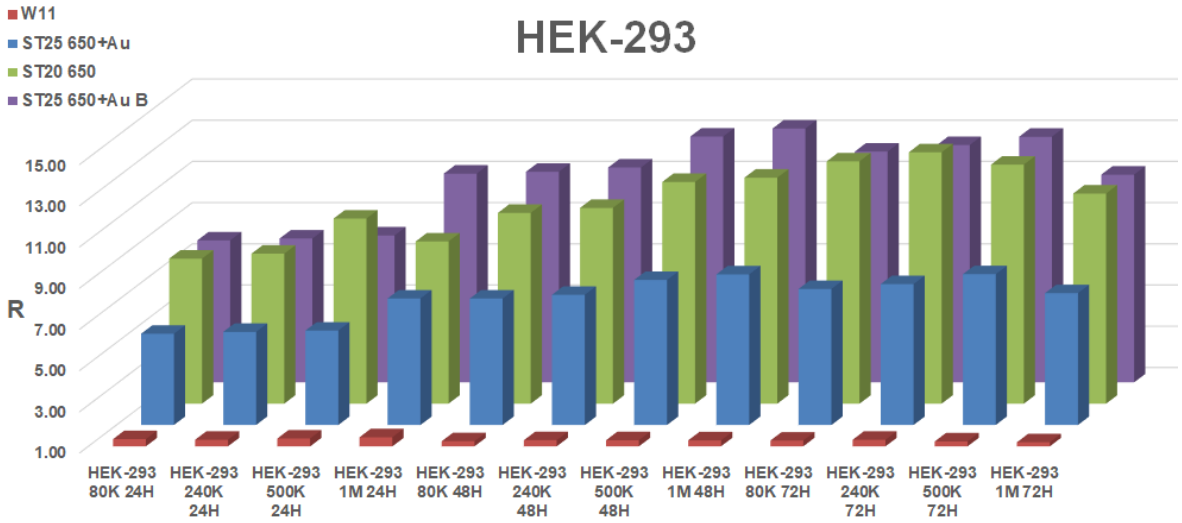

Figure 6.7: HEK-293 results from the previous test, in chronological order.

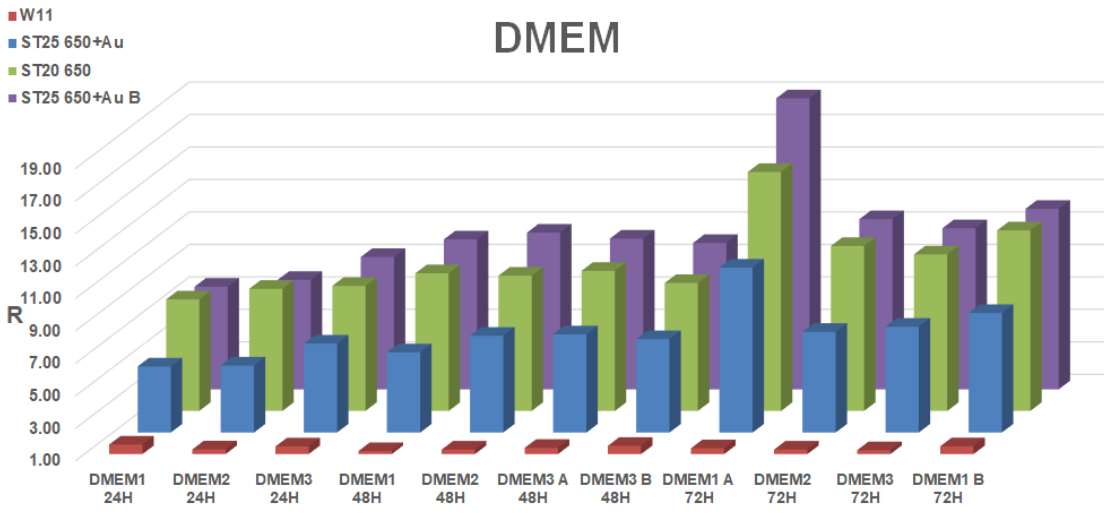

Figure 6.8: DMEM results from the previous test, in chronological order.

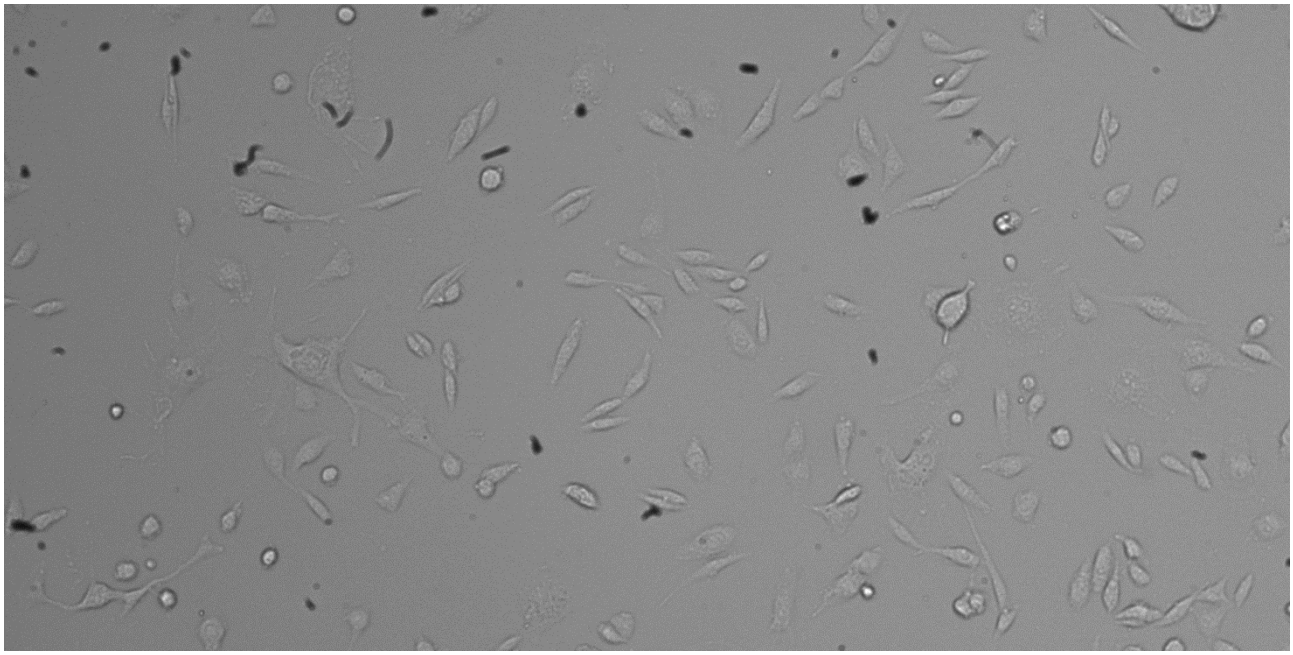

Figure 6.9: CHO cells 240k, 24 hours. Cells are poorly attached between them and to the petri dish bottom.

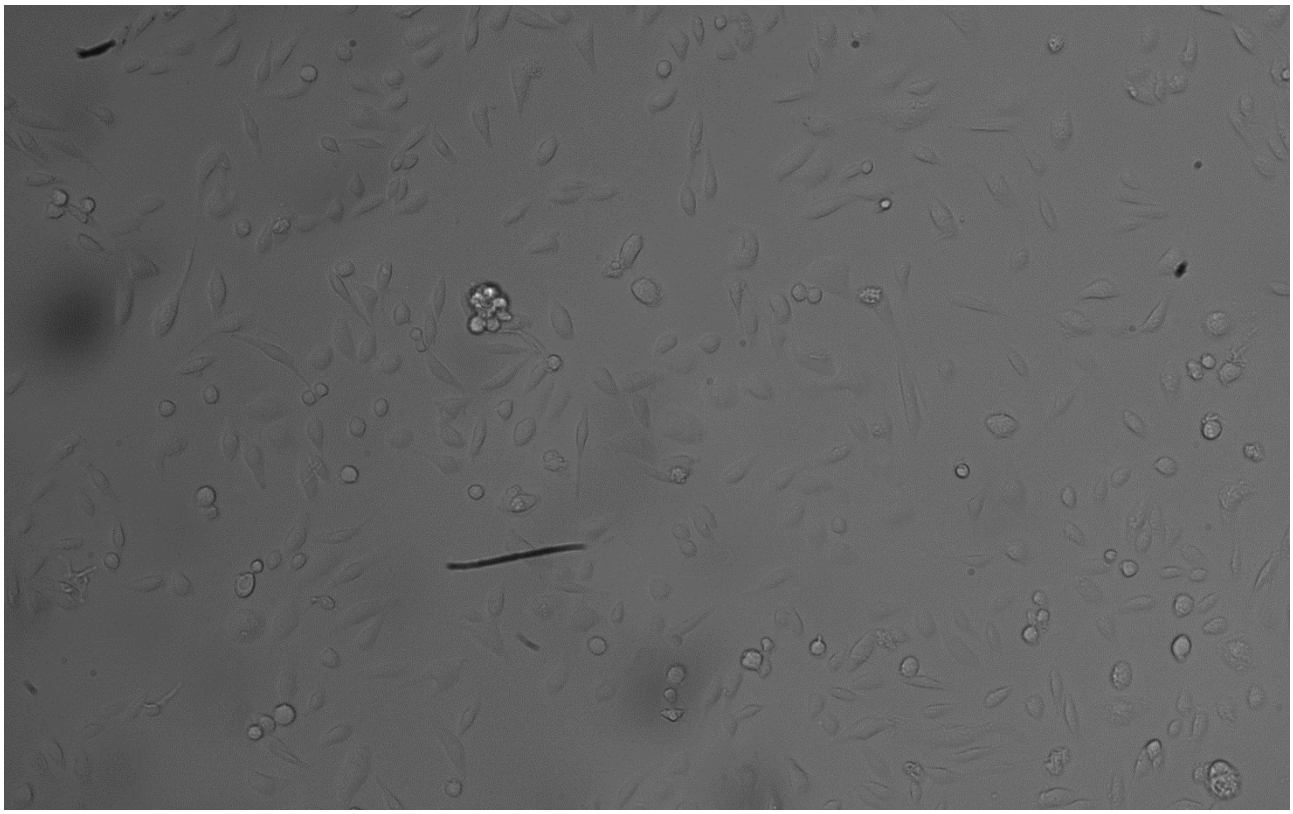

Figure 6.10: CHO cells 80k, 48 hours. Cells are poorly attached between them and to the petri dish bottom.

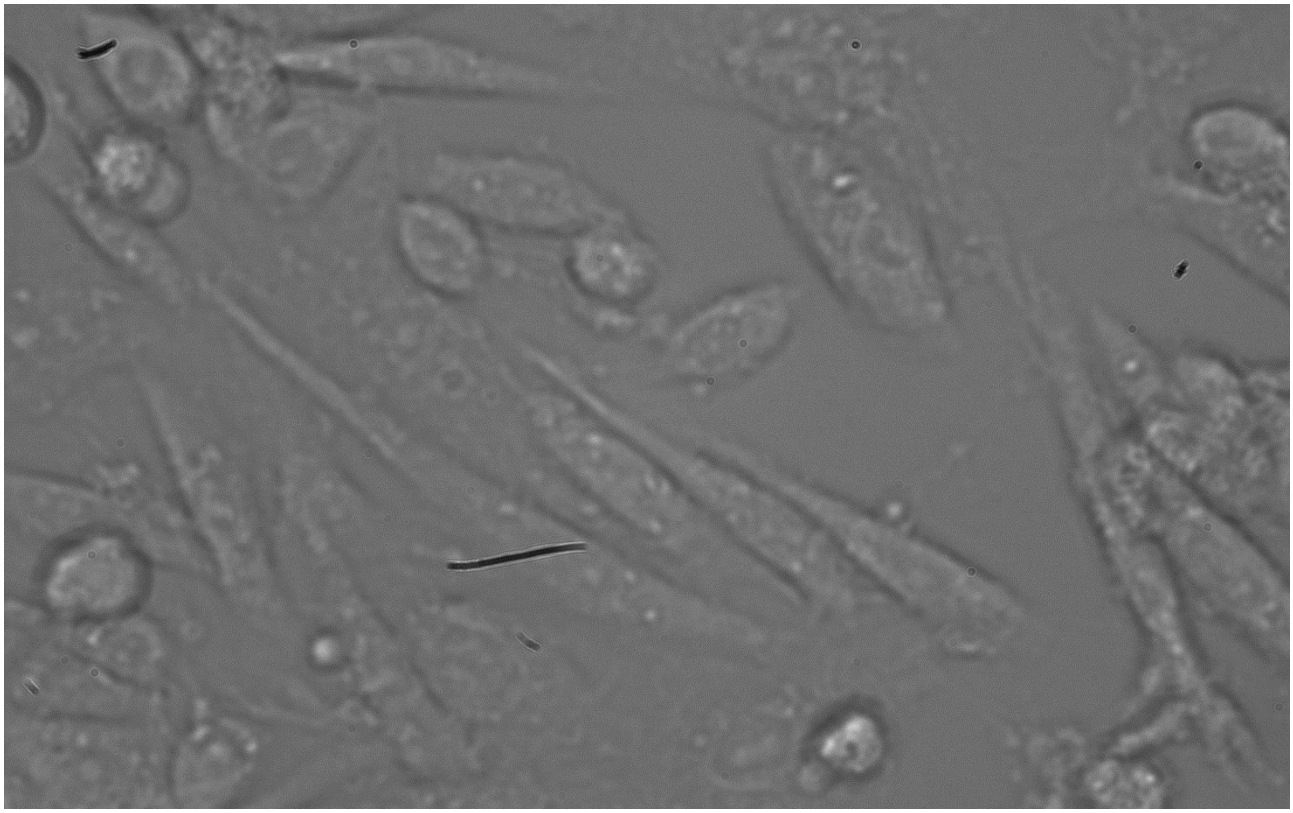

Figure 6.11: CHO cells 240k, 72 hours, greater magnification compared to the previous observation. Again, cells are poorly attached between them and to the petri dish bottom.

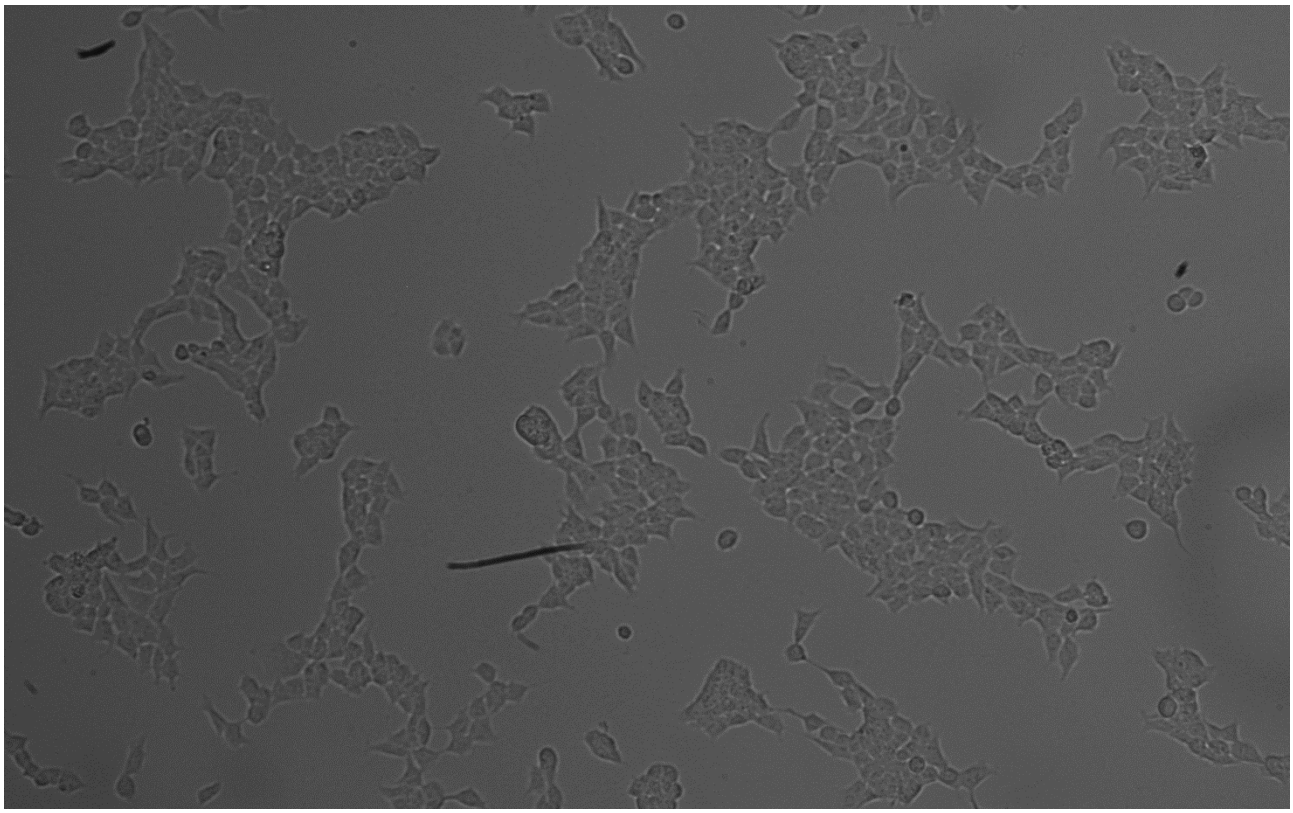

Figure 6.12: HEK-293 cells 80k, 48 hours. Cells are starting to form tissue-like conglomerates.

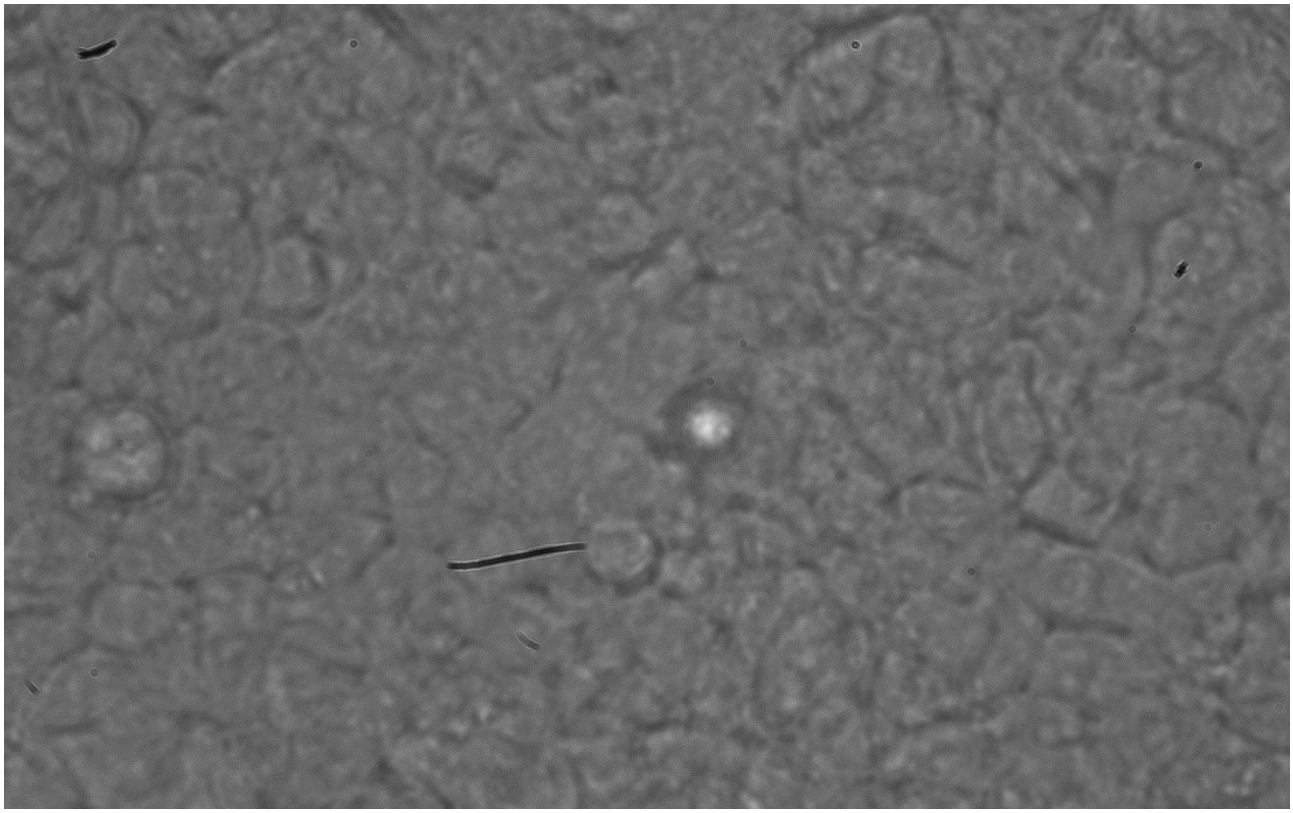

Figure 6.13: HEK-293 cells 240k, 72 hours. Cells have formed a steady tissue and have reached confluency.

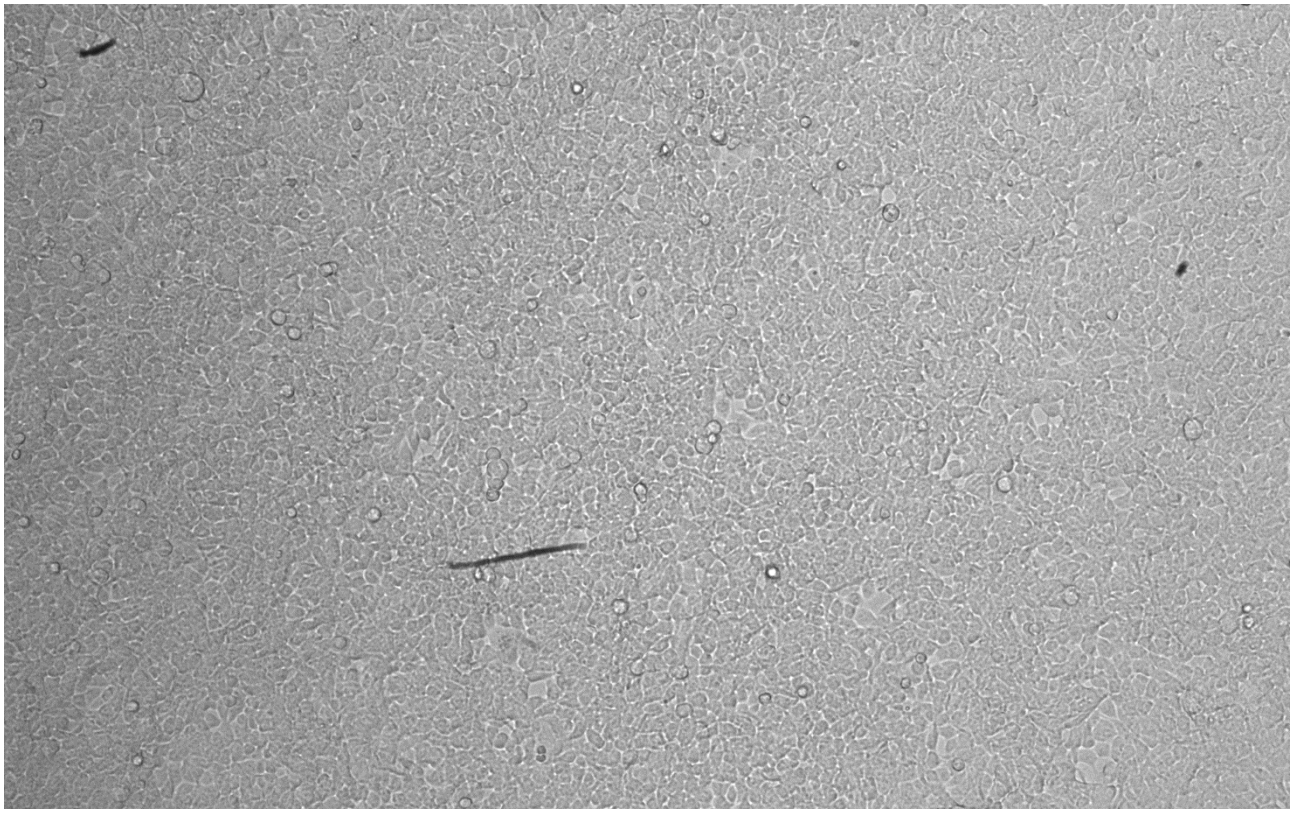

Figure 6.14: HEK-293 cells 1m, 48 hours. Cells have formed a steady tissue and have reached confluency.

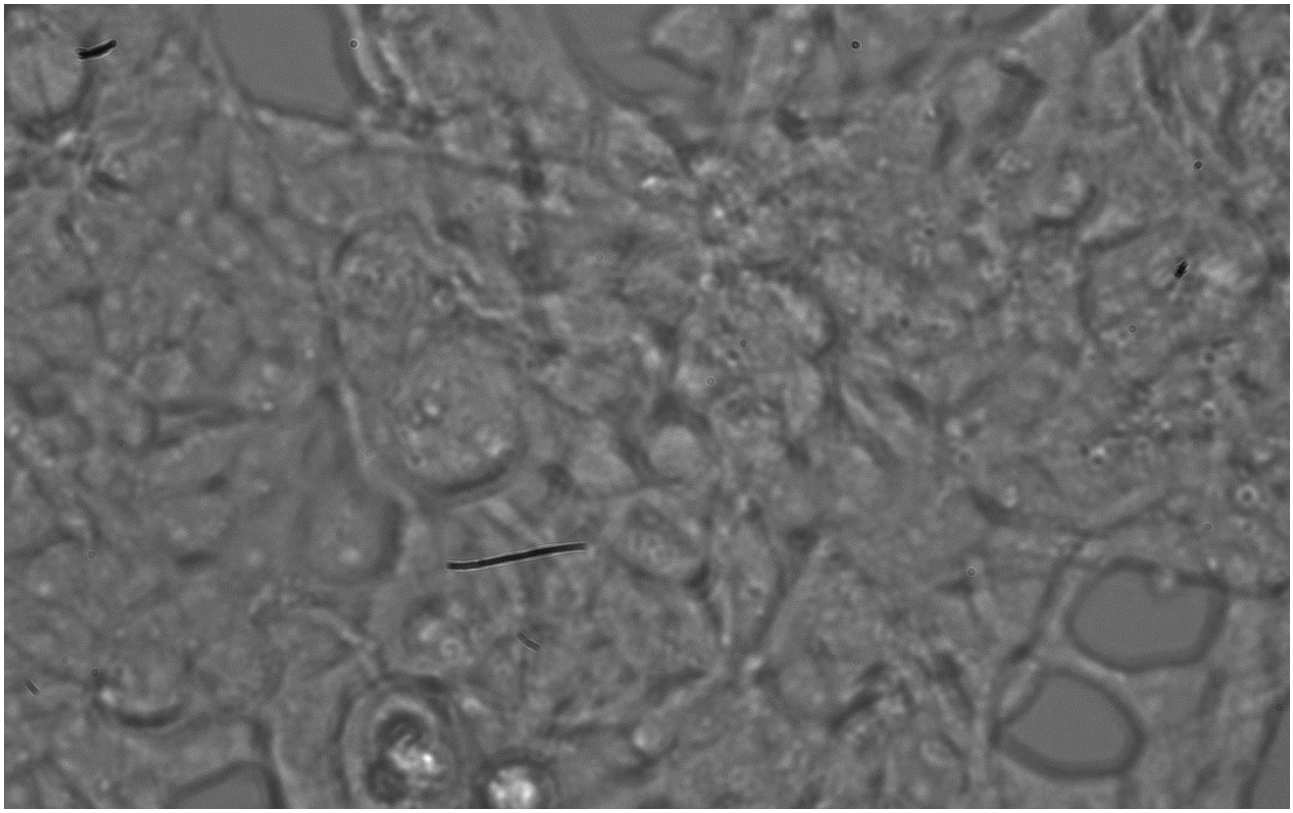

Figure 6.15: HEK-293 cells 1m, 72 hours. Cells have formed a steady tissue, reached confluency, and with this greater magnification compared to the previous figure, have even started to stack on 3D conglomerates due to their high vitality.

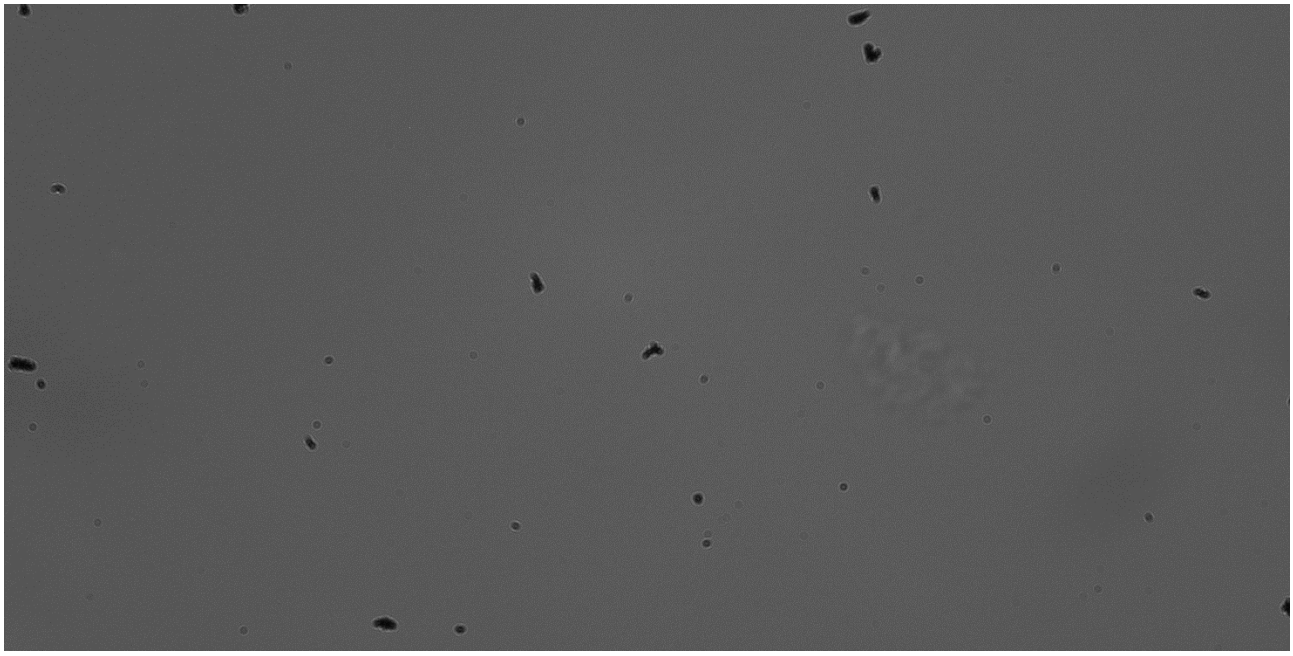

Figure 6.16: DMEM breeding ground without contaminations, after 24 hours of incubation.

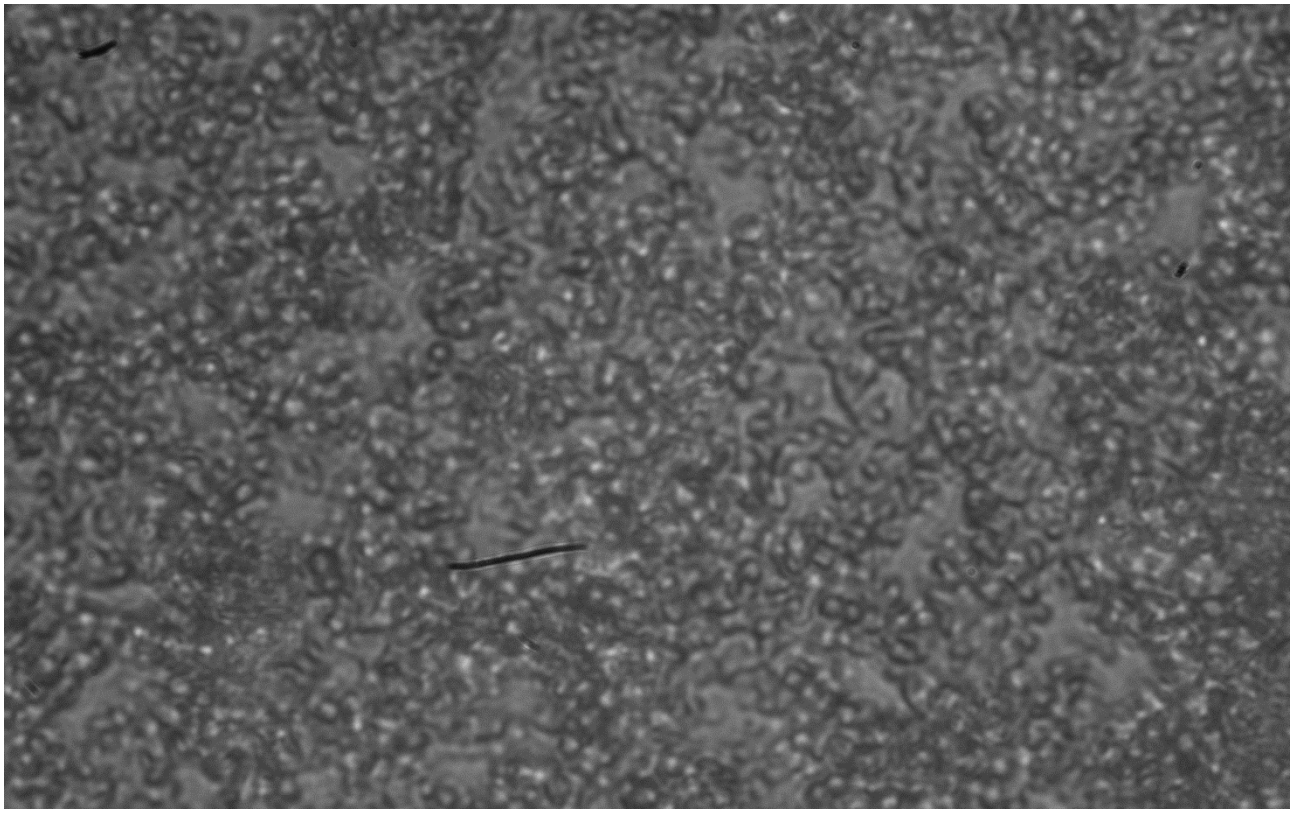

Figure 6.17: DMEM breeding ground after 72 hours of incubation, contaminated by staphylococci.

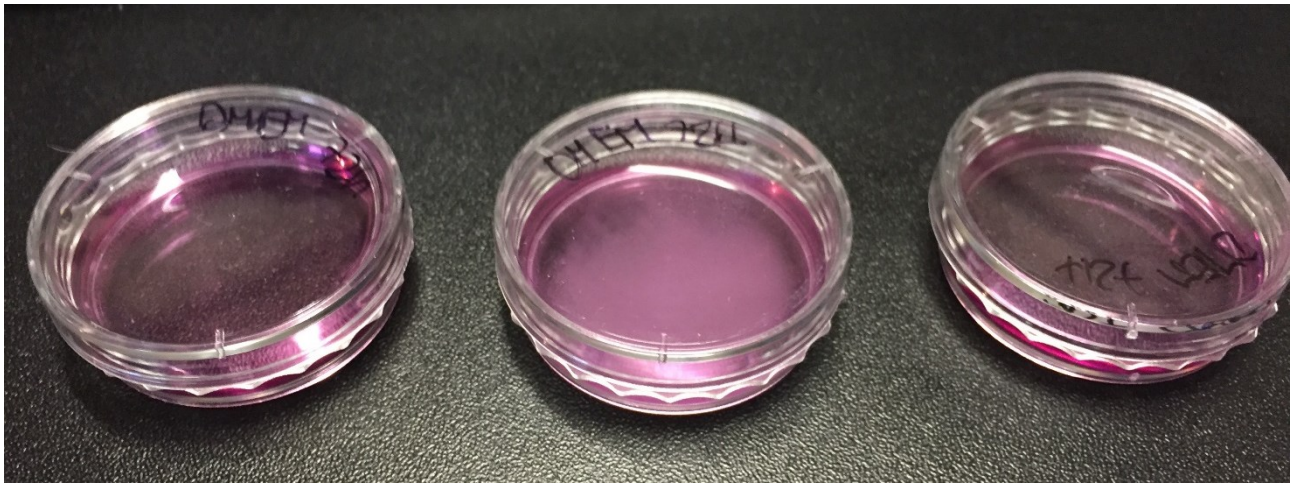

Figure 6.18: Petri dishes hosting DMEM 72 with hours of incubation. The middle one has a cloudy appearance due to the heavy bacteria contamination.

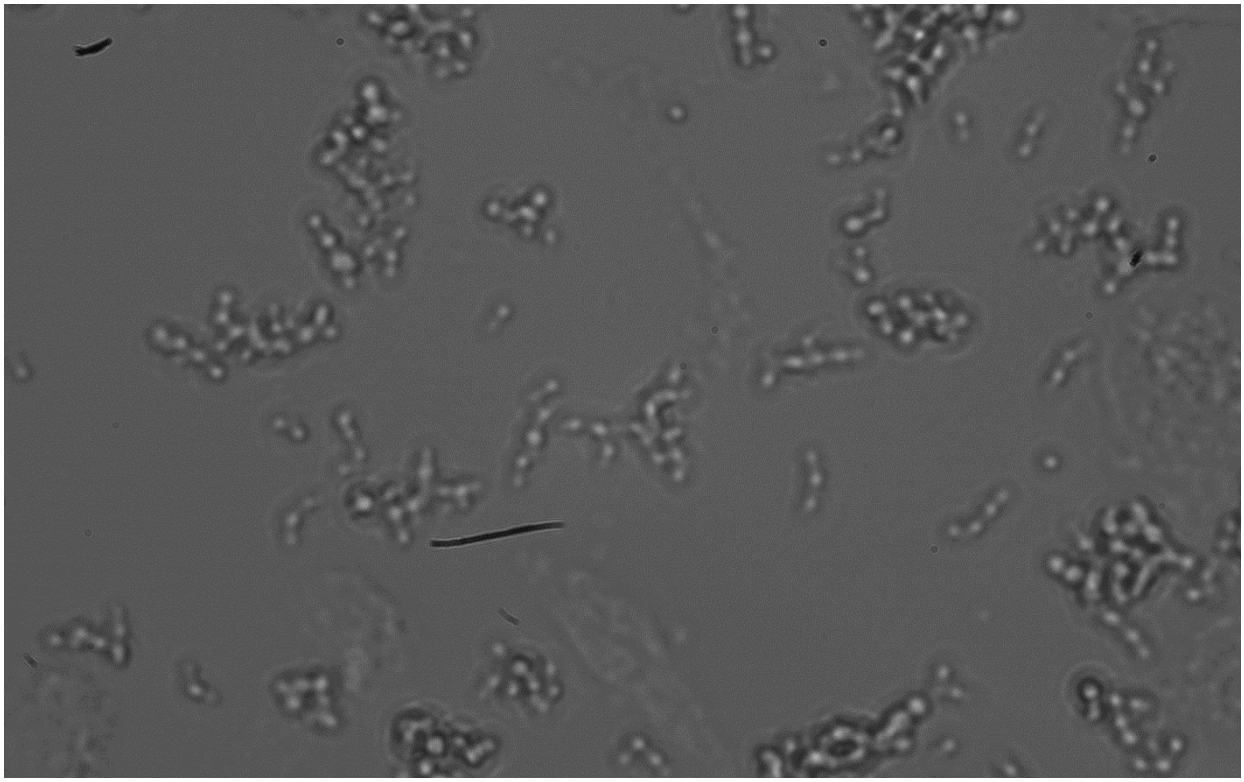

Figure 6.19: Petri dish hosting CHO 240k, after 48 hours of incubation, contaminated by staphylococci.

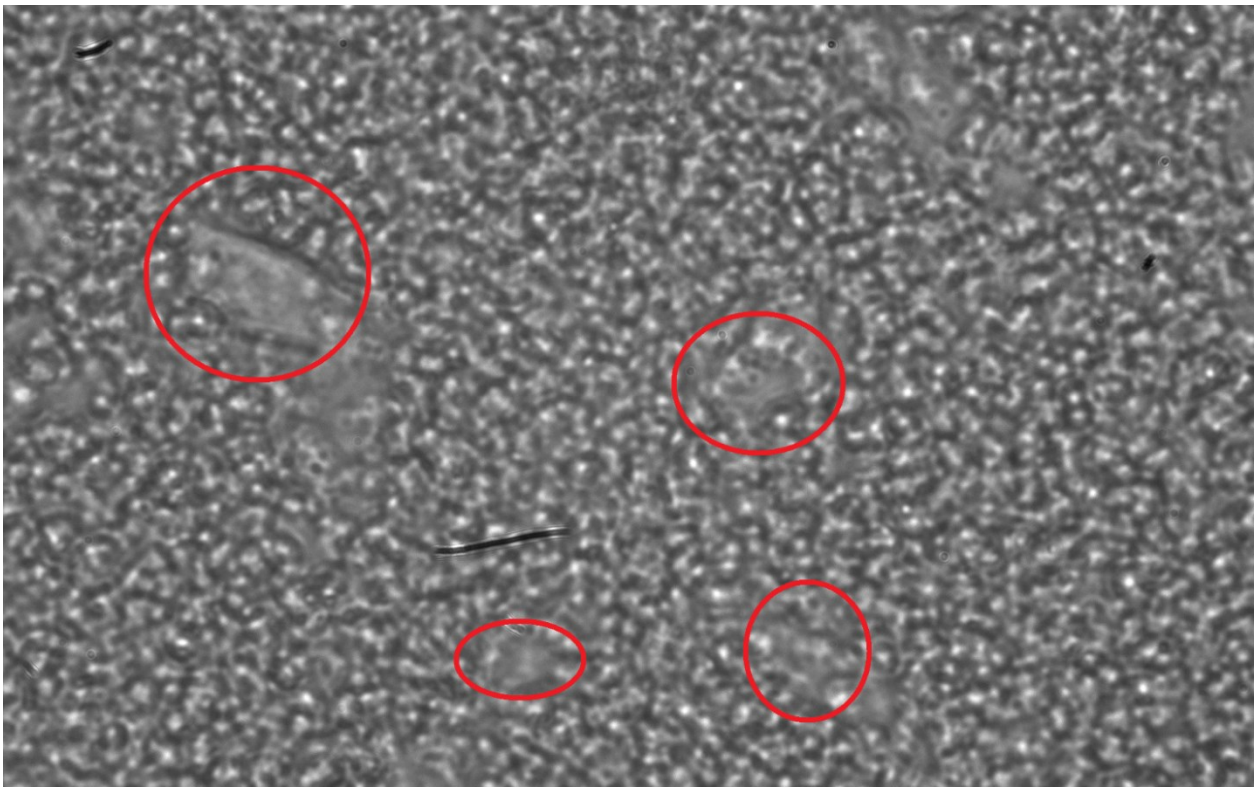

Figure 6.20: Petri dish hosting CHO 240k, after 48 hours of incubation and 24 hours outside of incubator. The container is completely contaminated, and only vestiges of the original cells remain (inside the red areas).

Tests were made on A549 and HCT 116 cells too, using the third sensors array (W11 and SmFeO3 data were negligible and not useful to the end of single sensors approach in this case, and for this reason have been omitted). While measures on lung cancer immortalized cells kept the trend expected, as saw from other ICL (Figure 6.21, Tables 6.5), this was not true for HCT 116. In Figure 6.22 (Tables 6.6), is in fact possible to see how responses decrease with the increase of the cell population, and rises again when they reach confluency. This might depend either, or by a combination of, the following phenomena:

- While the breeding ground emanates reducing gases, the HCT 116 cells might produce oxidizing and reducing volatile chemicals, and for this reason the response might lower with the increasing of the population
- Most of the tumor markers produced from the HCT 116 might not be volatile
- HCT 116, differently from the cells previously tested, do form 3D masses since the first moments of aggregation, rather than attaching to the bottom of the petri dish and form 2D tissues. This might mechanically and/or biologically alter the process with which markers are exhaled (since the surface of emission and the GAP junction network between cells change)

Sadly, there were not enough samples to test further this cell line, for example by letting them die and see if the response would rise again, or by stressing mechanically the agglomerates to make them spread into more 2-dimensional-like structures. These are ideas for the next works, since this type of cells, even if not exactly the ones studied on part the “real thing”, they are the closest cells as type to the ones to the ones contained, with all the rest, in the colorectal biopsies measured in Chapter 8.

A549								
SENSOR	**DMEM 1**	**A549 80K 24H**	**A549 240K 24H**	**A549 1M 24H**	**A549 80K 48H**	**A549 240K 48H**	**A549 80K 72H**	**A549 240K 72H**
ST25 650+Au	**2.09**	**2.43**	**2.71**	**3.02**	**4.78**	**4.7**	**4.42**	**4.58**
ST25 650+Au B	**2.44**	**2.84**	**3.23**	**3.61**	**5.8**	**5.76**	**5.63**	**5.80**

Table 6.5: Results from the two ST25 650+Au sensors on A549 tests.

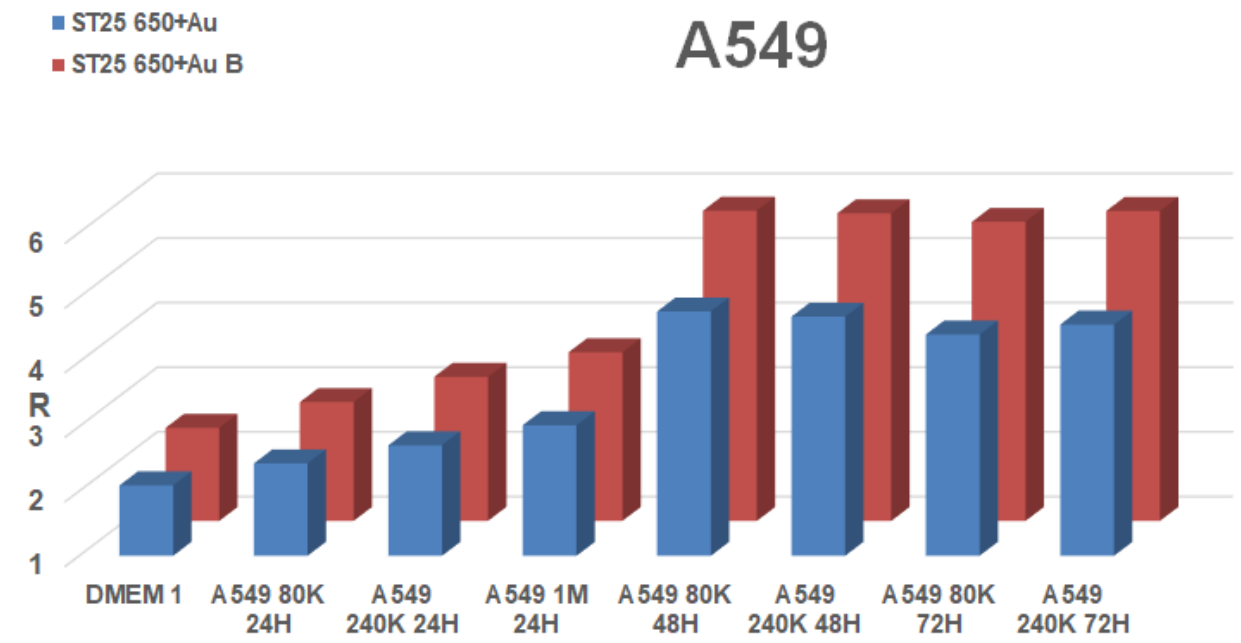

Figure 6.21: A549 test, with different plating concentrations and incubation times.

HCT 116							
SENSOR	**DMEM 1**	**HCT 116 80K 24H**	**HCT 116 350K 24H**	**HCT 116 80K 48H**	**HCT 116 350K 48H**	**HCT 116 80K 72H**	**HCT 116 350K 72H**
ST25 650+Au	**5.46**	**5.26**	**5.52**	**4.66**	**4.44**	**5.32**	**5.06**
ST25 650+Au B	**7.26**	**6.38**	**6.48**	**6.16**	**5.86**	**7.02**	**6.78**

Table 6.6: Results from the two ST25 650+Au sensors on HCT 116 tests.

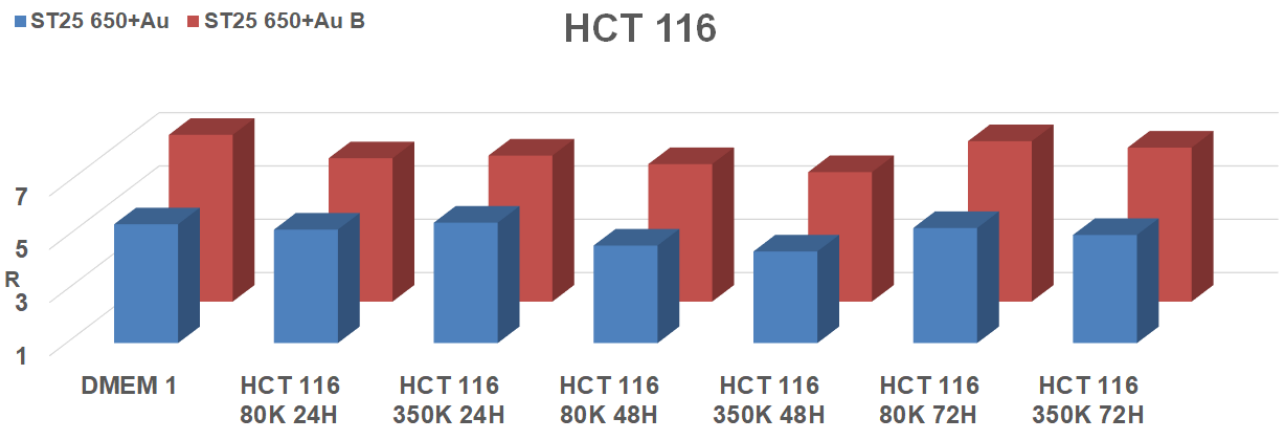

Figure 6.22: HCT 116 test, with different plating concentrations and incubation times.

In the end, immortalized cells tests, even if problematic with the preparation and the many variables involved, gave good results, like recognition respect of the behavior saw in the previous thesis, and observation of the bacteria contamination and contact inhibition phenomena when present, certifying the biological nature of the emanations monitored and their connection with the vitality of the cell lines.

Chapter 7 – Human Blood Tests

Figure 7.1: Samples of blood used during the tests. K_3-EDTA was the anticoagulant used for all the blood samples.

While cell cultures tests were carried on, a new application idea for the device came up to mind: if the breeding ground washed away from the cell cultures could still emanate tumor markers trapped as saturated vapors in it, so also other fluids in contact with the neoplasms could, too. Since malignant tumor dump their wastes (between which also the tumor markers discussed in Paragraph 4.5 are included) in the blood stream, and the chemicals here are mixed to the blood as saturated vapors, like in the previous measures, the idea of sampling and testing blood samples in order to detect tumor markers, came to hand. The reason behind it would be the development of a post-screening device, handy for the medical world, able to promptly verify the outcome of surgeries, chemotheraphy and radiotheraphy, on neoplasms with a single, standard sampling of blood from the donor. This would greatly improve the capability for oncologists and surgeons, in the direct proximity of the medical cures given to the patient, to monitor the actual state of metastatization of the tumor, the effectiveness of the operation brought for the medical team to remove the pathology, and also over time to monitor the appearance of possible relapses.

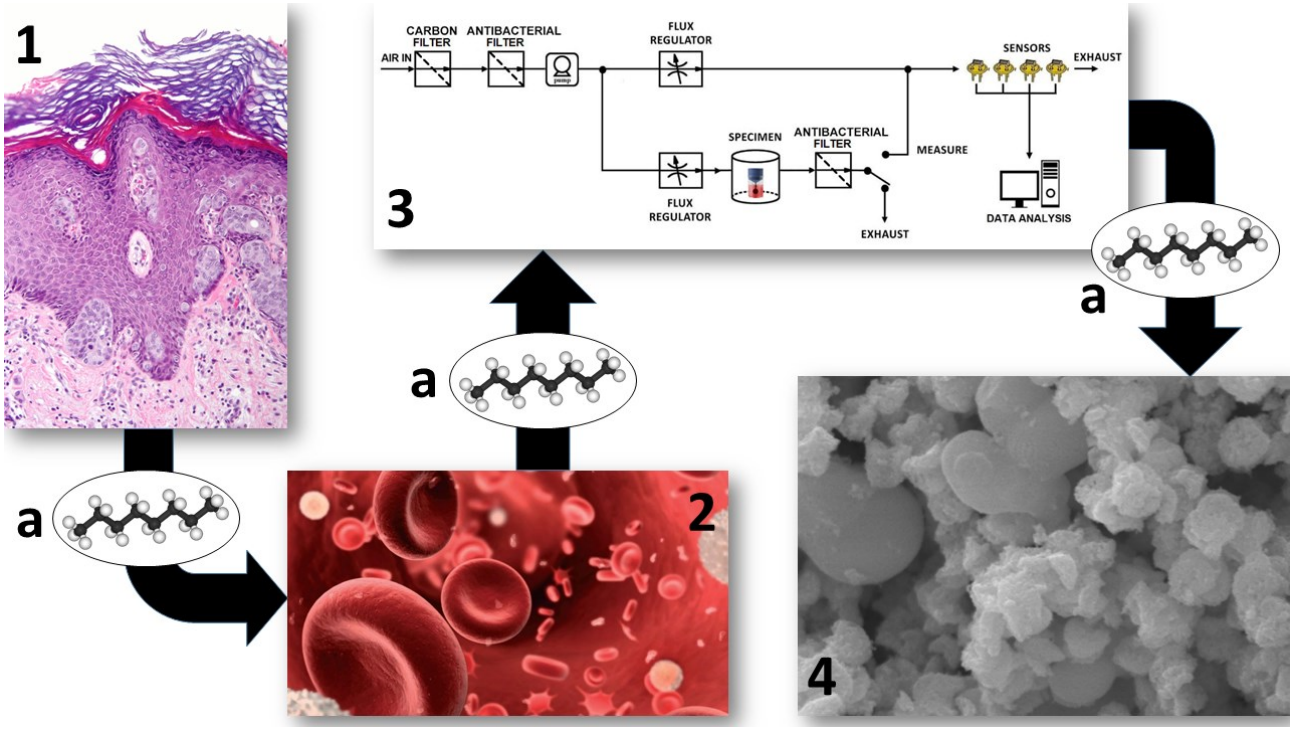

Figure 7.2: Schematization of the full travel of the tumor marker, from the tumor to the sensing nanostructures [47].

Figure 7.2 shows the path token from the tumor markers, in order to be detected from the device: colorectal and gastric malignant neoplasms (1) produce tumor markers of various

nature (a) and, being those tumors vascularized, pollute the blood stream with those chemicals (2). These markers are detected with SCENT B1 (3), which hosts nanostructured chemoresistive sensors (4), by sampling blood specimens from human donors and putting them into the device specimen chamber. A filtered airflow brings the markers exhaled to the sensitive chambers, where sensors reacts to their presence. Two different data set have been produced from the blood tests. The reason behind the choice was simply connected to the availability of new donors; being some time passed between the last donor from the first data set, and being the sensors in the array changed, the choice of starting a new data set, instead of integrating it with the previous, looked the more logical. This branch of the research gave the best results over the whole work of thesis, and the first data set has been published in a scientific journal recently [47].

7.1 – Human Blood Tests: Sampling

The collection of blood specimens has been realized in the Hospital of Cona, Ferrara, Italy. The trial protocol and the informed consent form were presented, accepted and retrospectively registered from the to the Ethical Committee of the District of Ferrara, with trial number 170484, on 13 July 2017. Blood was collected with standard medical sampling technique, by drawing it from the arm veins of the individuals, and classified between four different donor groups:

- Tumor affected individuals, more specifically patients with colorectal cancer and stomach cancer. Colorectal and gastric cancers have a high incidence compared to other tumor types, and previous works have proven the capability of sensors to detect its tumor markers (e.g. gases and on feces samples) [35,47,148–152]
- Metastasis affected individuals, who underwent surgeries or chemio- and radio-therapy to remove the cancer. The samples from patients treated with drugs due to the two therapies abovementioned were taken after at least one month and a half after the end of the treatment, to avoid that the drugs or their metabolites accumulated in their bodies and thus contaminate the sample
- Individuals with tumors not vascularized by blood vessels
- Healthy individuals (control group)

All blood samples were kept in blood collection tubes (7 ml, purple cap) containing anticoagulant agent K3-EDTA, in order to prevent the coagulation of the specimens. Blood have been collected by leaving $1cm$ of headspace as standard in every collection tubes. K3-EDTA (Tripotassium Ethylenediaminetetraacetic acid) is a standard (2004, European Standard EN 14820; and German Standard DIN ISO 6710 [154,155]) anticoagulant added to the test tubes, in order to inhibit the natural coagulation of blood samples, by strongly and irreversibly chelating (binding) calcium ions, thus preventing blood from clotting. Its effects on blood samples have been widely studied for the concentrations standardly added to the test tubes, showing no substantial variations in the biological and chemical nature of the specimens, nor of the volatile chemicals exhaled from it. [156–158]. It is important to notice that these test tubes are under vacuum, and for this reason there is no head space air contaminating the sample before its opening inside the controlled thermostated chamber. Instead, the saturated vapors, which compose the great part of the VOCs measured from the device are in equilibrium with blood in liquid phase. When a test is performed, the test tubes are quickly opened and the blood sample is rapidly poured in the single use containers as the one in Figure 7.3, placed inside the specimen chamber.

Figure 7.3: Example of the container used to host the blood samples in the specimen chamber.

There has not been further dilution nor alteration of the specimens collected. Serum and plasma have not been separated, and they have been kept mixed through the whole transportation and the measure itself. Tests have been carried out at room temperature in a thermostated chamber. Multiple specimens from every control and most of the patients (given their state of health and stress, to avoid aggravation of their clinical state) have been sampled, in order to verify the steadiness of the responses from the particular donors over the months, as shown for two of the healthy participants to the tests in Figure 7.4.

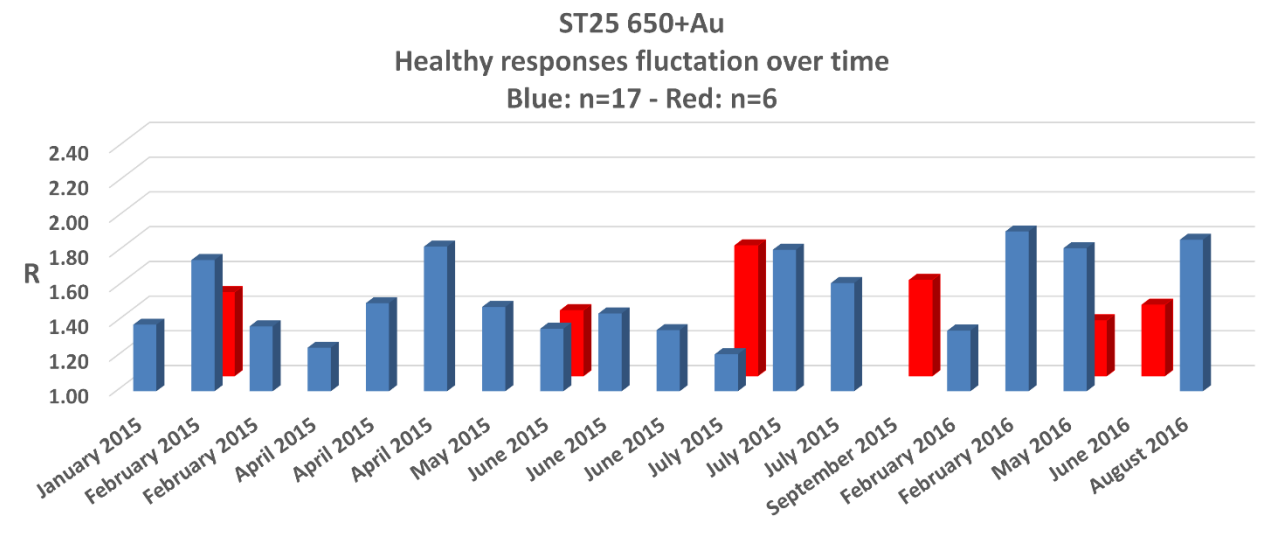

Figure 7.4: Fluctuation over time of R for ST25 650+Au sensor in 2 of the 42 healthy individuals that volunteered for the experiment. Sampling was repeated respectively $n = 17$ and $n = 6$ times over the lapse of time shown on the X-axis (20 months); average R±S.E.M.: $n = 17 \rightarrow 1.55 \pm 0.06$; $n = 6 \rightarrow 1.48 \pm 0.06$ [47].

Two data set were formed during the study, and analyzed with the aid of the sensors arrays presented in Paragraph 2.4. In the first data set, a total of 89 samples has been collected and accepted for the study (healthy samples: 42, ill samples: 47, total samples: 89), with wide anagraphical distribution between females (healthy: 13, tumor affected: 11, metastasis affected: 7, not vascularized: 2; total female ill: 20, total female samples: 33) and males (healthy: 29, tumor affected: 15; metastasis affected: 10; not vascularized: 2; total male ill: 27, total male: 56) donors, between the ages of 21 and 91 years old. The protocol followed for this set is shown in Figure 7.5. The threshold value refers to ST 25 650+Au upper value at which 95.45% (2σ, shown in Figure 7.7) of the healthy donors responses lay as distribution, in the single sensor approach for that sensor, and was obtained from the values calculated for healthy samples in Table 7.1.

	ST 25 650+Au SINGLE SENSOR APPROACH VALUES				
	HEALTHY SAMPLES (42)	ILL SAMPLES (47)	TUMOR AFFECTED (26)	ALL METASTATIC (METASTASIS AFFECTED+ NOT VASCULARIZED) (21)	METASTASIS AFFECTED (17)
AVERAGE VALUE	1.62	2.98	2.89	3.08	3.51
STANDARD DEVIATION	0.25	1.29	0.96	1.77	1.79

Table 7.1: Average values and their standard deviations for ST 25 650+Au responses on first data set.

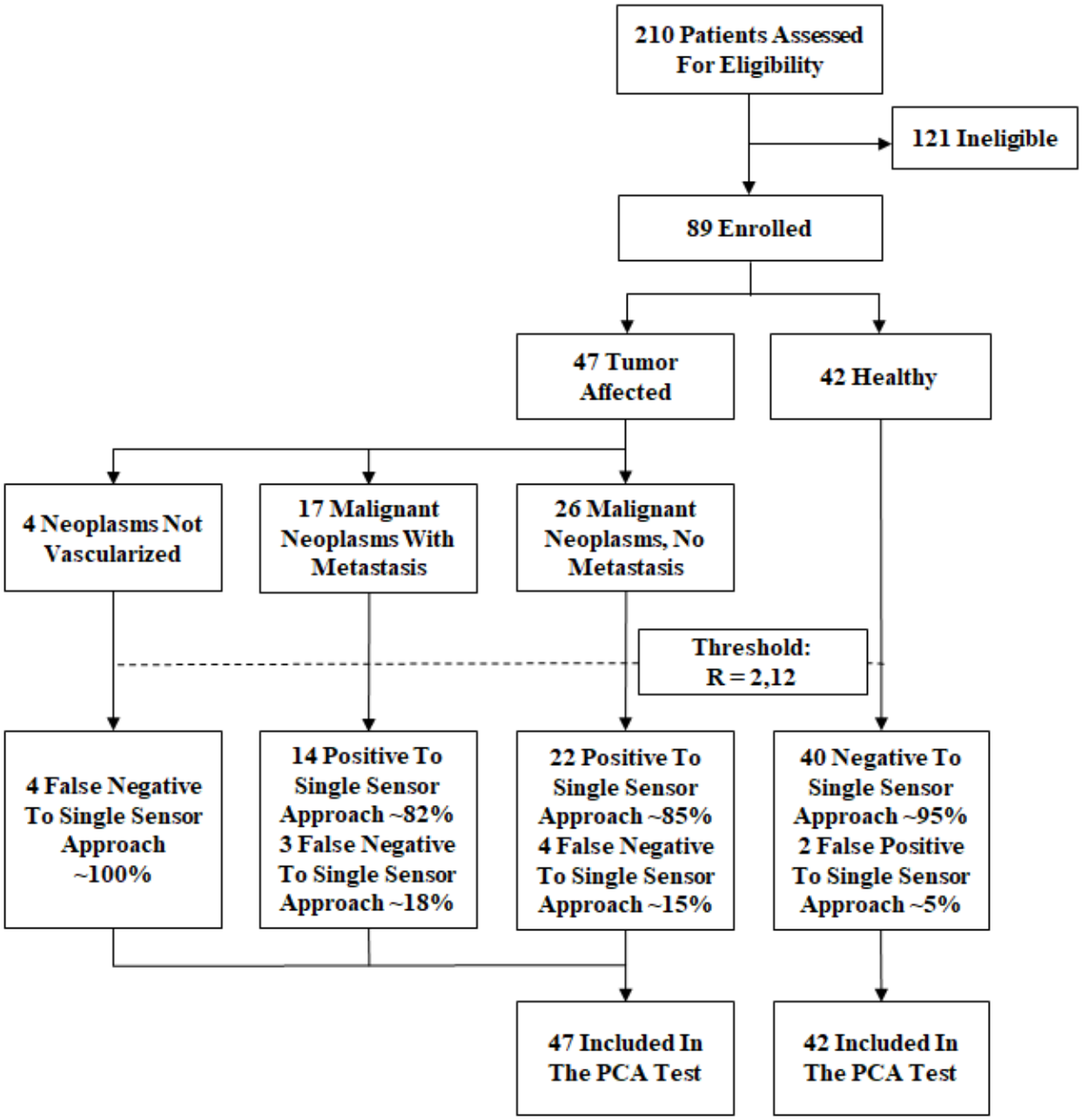

Figure 7.5: Protocol followed to build the first data set [47].

In the second data set, a total of 15 samples has been collected (healthy samples: 8, ill samples: 7, total samples: 15), with wide anagraphical distribution between females (healthy: 1, tumor affected: 2, metastasis affected: 1, total female ill: 3, total female samples: 4) and males (healthy: 7, tumor affected: 1; metastasis affected: 3; total male ill: 4, total male: 11) donors, between the ages of 21 and 87 years old. The protocol followed for this set is shown in Figure 7.6.

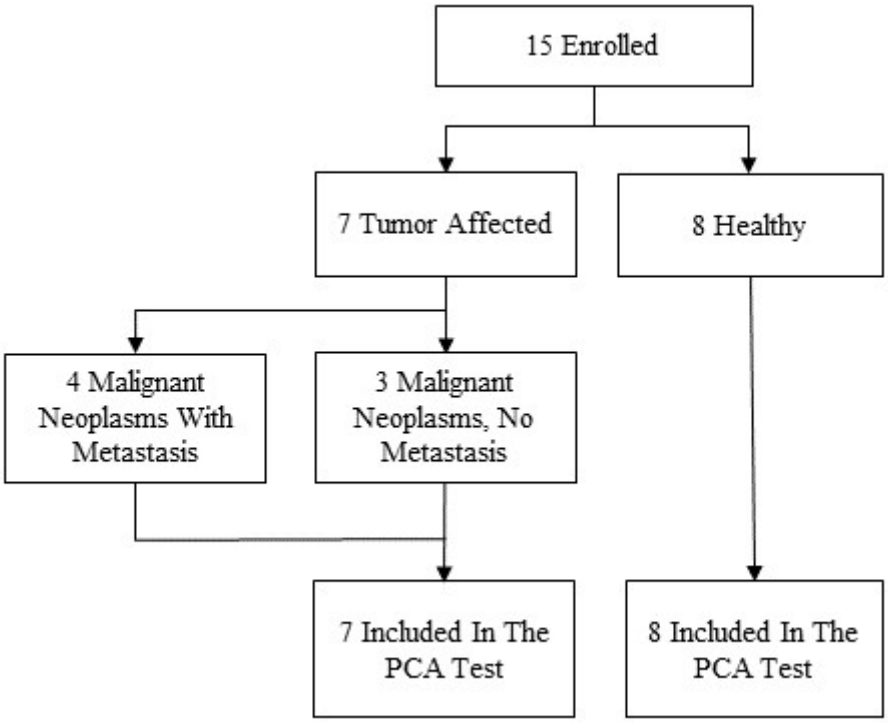

Figure 7.6: Protocol followed to build the first data set.

7.2 – Human Blood Tests: Data and Results

For the first data set, among the sensors tested, ST25 650+Au proved to be the most effective one for tumor markers detection, giving a progressively increasing response with the increase of size and vascularization of the tumor mass and of its metastasis, as shown in Figure 7.7. Specificity and selectivity of the test for the best responding single sensor approach (ST25 650+Au) are shown in Figure 7.6. It is important to notice how tumors not vascularized, and thus not in contact with the blood stream, do not get detected, enhancing as proof the connection between tumor markers emanated from the specimens, tumor vascularization and sensor responses.

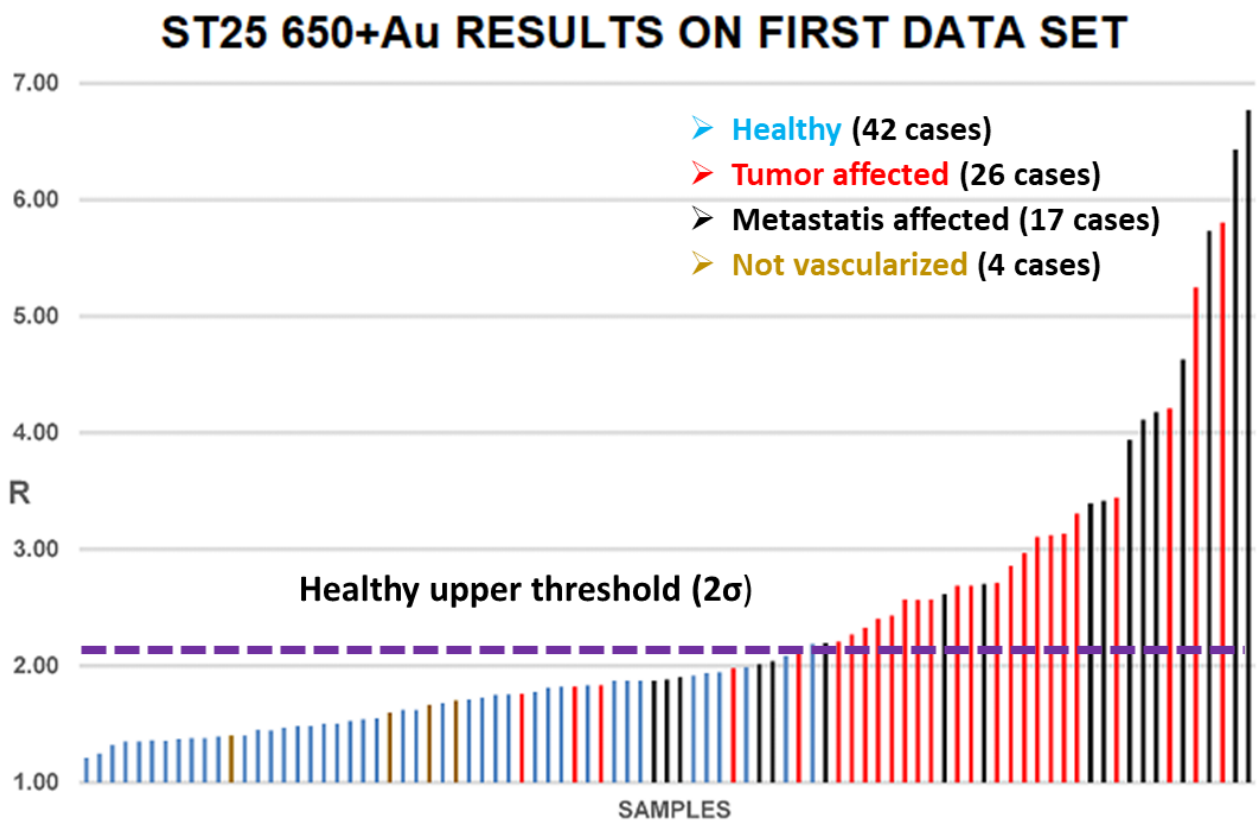

Figure 7.7: ST25 650+Au single sensor approach on first data set (total = 89 samples) [47].

ZnO 850 sensor showed instead to be ineffective for this purpose, both as single sensing unit and as a component of an array of four sensors (see PCAs on first data set, Figure 7.9 and Figure 7.10). SmFeO3 and CdS gave too small responses to selectively distinguish between the samples from healthy and tumor affected patients, but when their responses (in the form of normalized response R) were analyzed together with the responses of the ST25 650+Au and the SnO2 sensors (forming the second sensors array) with Principal Component Analysis (PCA; Figure 7.10, PCA C1 and C2), a significant difference emerged between the two patient groups. The ability to distinguish even the grade of tumor invasiveness of the ST25 650+Au sensor was also reinforced by the data of Figure 7.8A (red bars) where the responses to four samples from four patients having progressively smaller cancer formation were progressively smaller. In particular, “CANCER BIGSTO1” refers to the largest cancer mass confined to the stomach, the “META STO1” and the “CANCER STO1” ones have smaller masses (but the “META STO1” patient also had metastasis) while “CANCER LITRA1” refers to one of the smallest neoplasms considered in this study, a little malignant mass in the transverse colon. These differences were statistical significant, given the relatively large differences and small errors of

responses to all the subjects examined (Figure 7.7), distributed in five representative populations (Figure 7.8B). This statistical significance was also reinforced by the stability of the responses of healthy patients over time, as shown in Figure 7.4. Preliminary results indicate that the ST25 650+Au can be also used to track the progression (or regression) of a tumor following an anticancer therapy. Indeed, the responses of this sensor were progressively smaller in respect to the control in an individual with a large colon cancer and with liver metastasis that underwent surgery (Figure 7.8A, black bars), and in another individual that was subjected to surgery and a cycle of chemotherapy (Figure 7.8A, purple bars). To summarize, Figure 7.8 more statistic from single sensor approach on ST25 650+Au sensor:

A. Responses to a blood sample from a patient with a large colon cancer and with liver metastasis (large black bar) and to a sample from the same patient took three days after the surgical removal of the colon cancer (small black bar); a second patient with colon cancer (larger purple bar), three days after surgery (smaller purple bar) and one cycle of chemotherapy following surgery (smallest purple bar); four individual with cancers having different size and vascularization grade (red bars, from left to right: largest cancer mass confined to the stomach, smaller stomach cancer mass with metastasis, smaller colon cancer mass lacking metastasis, very small malignant mass in the transverse colon)
B. Average values and standard errors of ST25 650+Au responses to all the subjects examined, distributed in five representative populations, described in the legend at the top of each bar

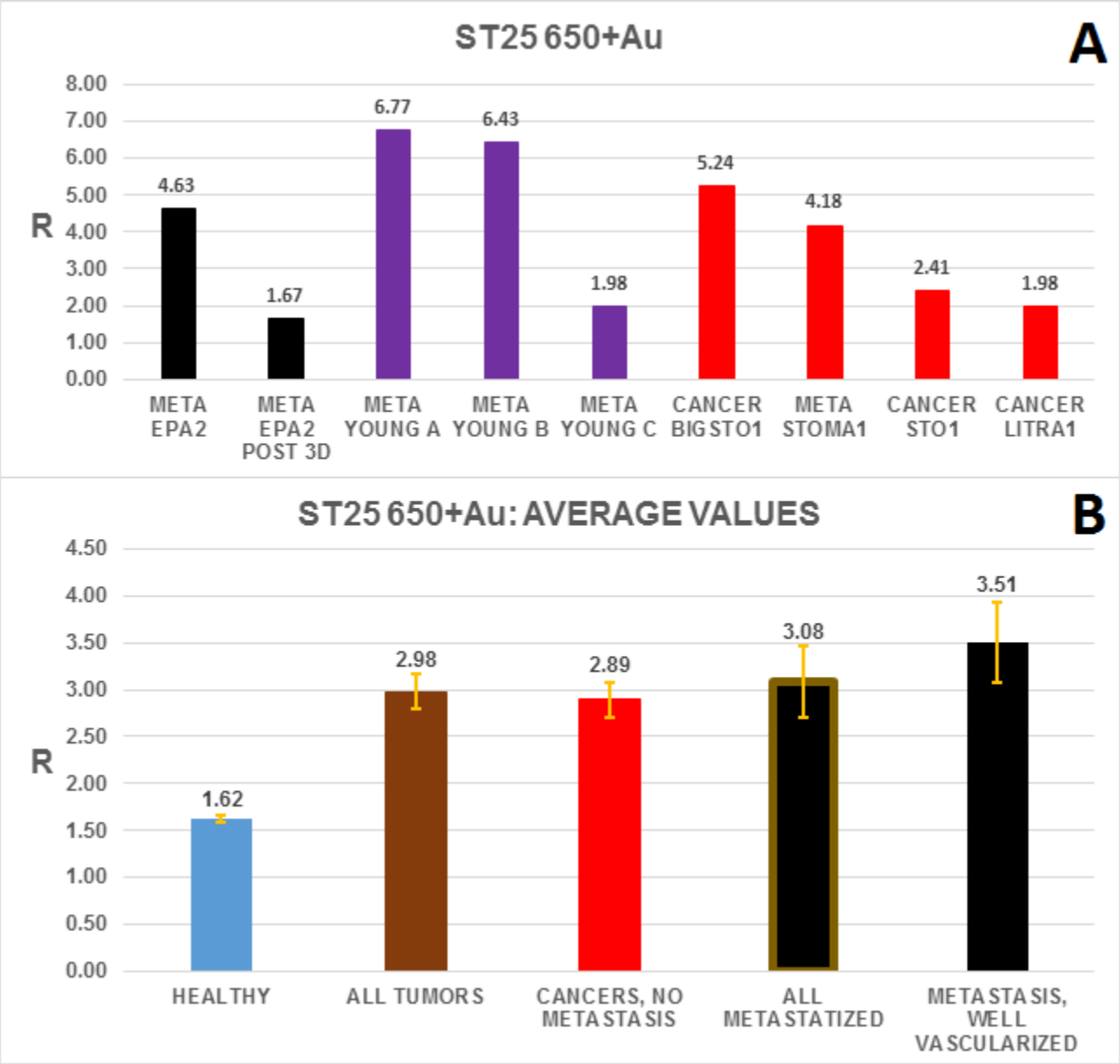

Figure 7.8: Performance of the ST25 650+Au sensor. A – Black: responses from the same patient before and after surgery. Purple: responses from the same patient before and after surgery, and after a cycle of chemotherapy. Red: responses to different tumor types. B – Average values (shown) of the donors groups, with their standard error [47].

After these brilliant results, PCA approach was carried out on the first data set. Full data sheet from all the arrays responses, normalized to be used with PCA approach, and their analytical reports with score and loading values, are shown in Tables C.1–12.

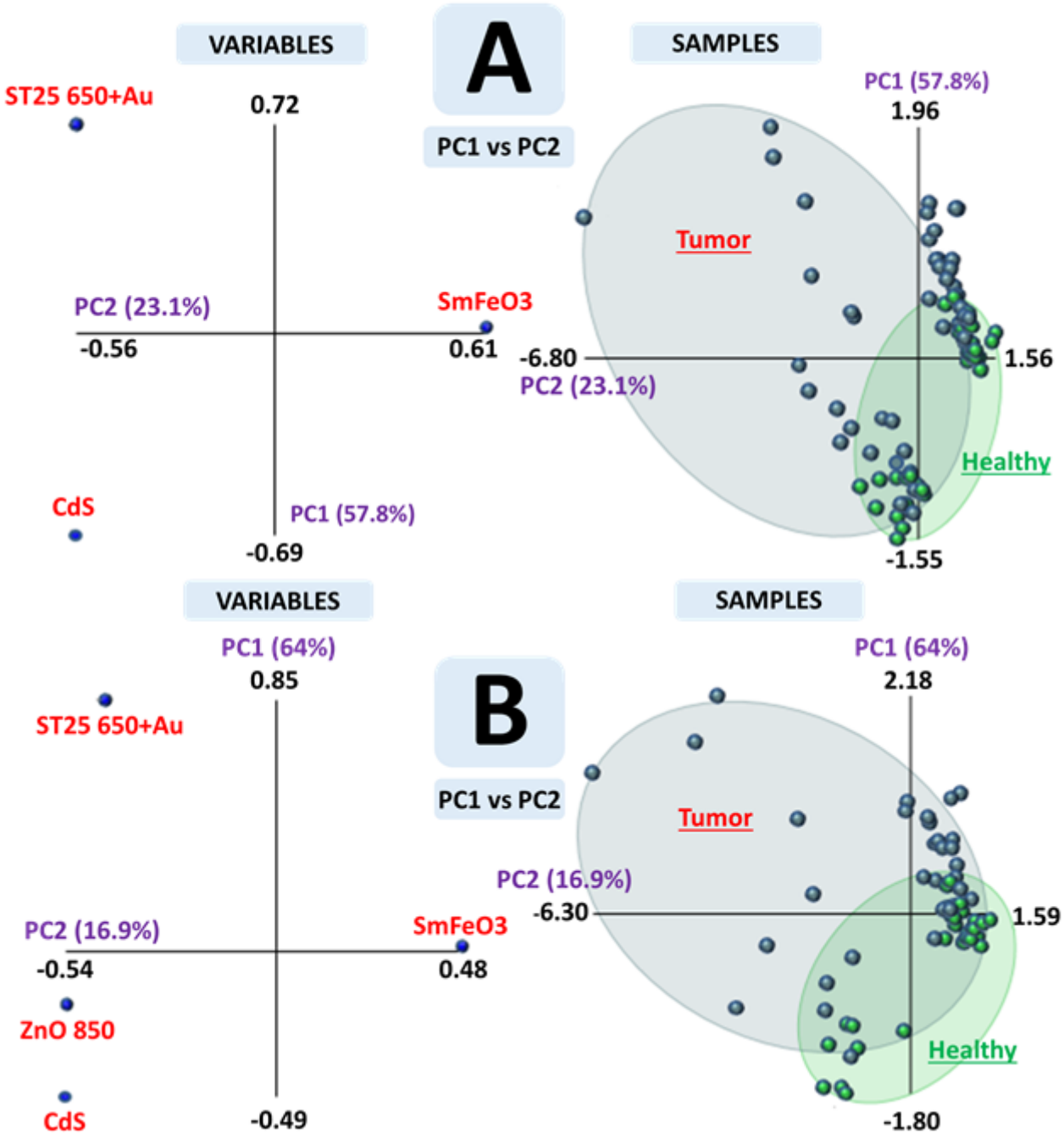

Figure 7.9: PCA (Principal Component Analysis) statistics of the responses from the three sensors (ST25 650+Au, SmFeO3, and CdS) used in both first and second sensors array (A), and of the responses of the first sensors array (B) [47].

In figure 7.10, VARIABLES graphic shows the loadings plot, related to the contribution of the sensors to the principal components obtained from the analysis, while SCORES graphic shows the R outputs from the tests in the new coordinates obtained from the PCA. It is possible to see how the first array, and the three sensors kept on both the arrays

alone, do not provide good results in order to separate healthy patients from tumor affected, being the two areas enclosing the results from the groups of patients and healthy donors greatly overlapped.

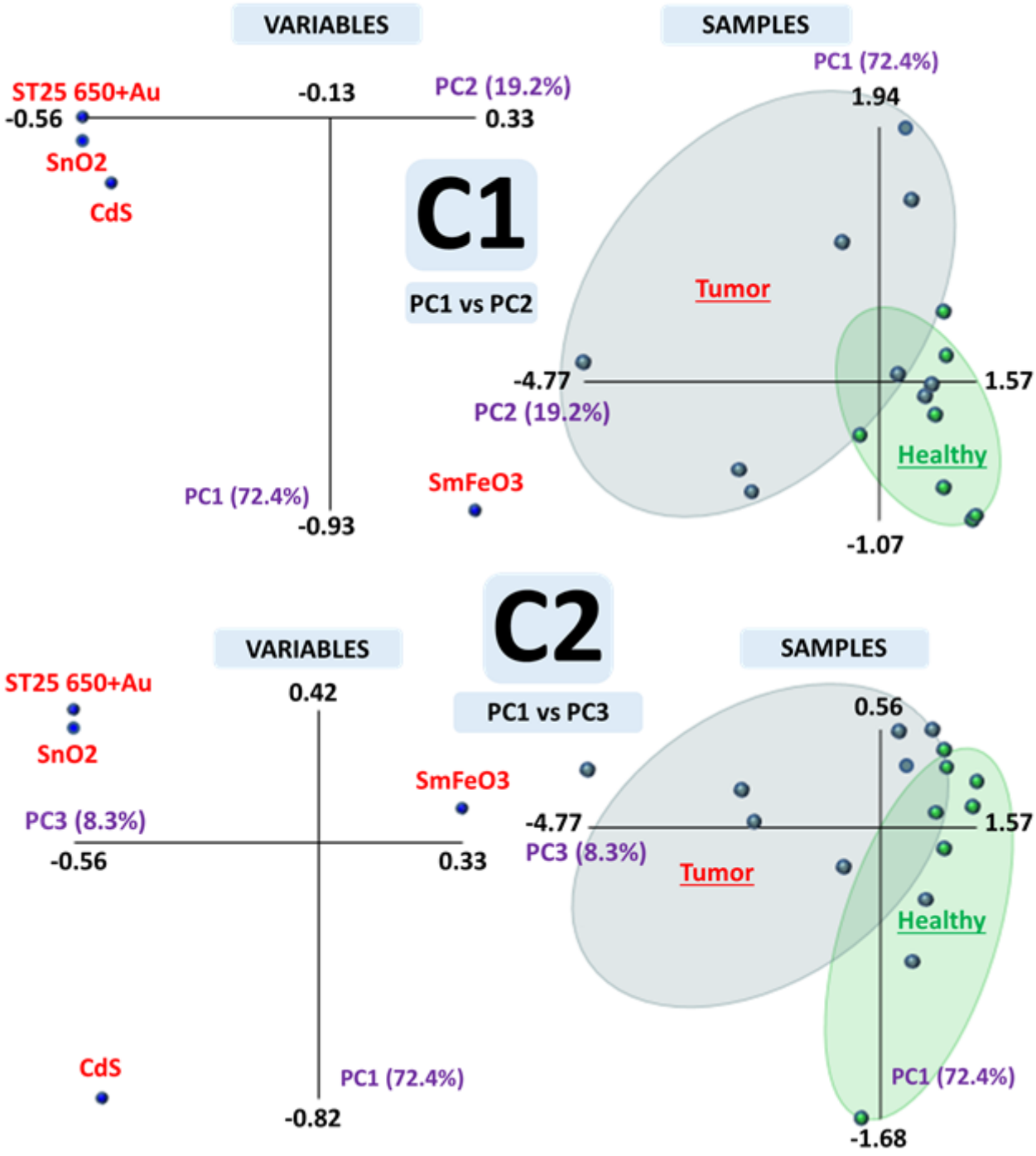

Figure 7.10: PCA statistics of the responses of the second sensors array (C1: PC1 vs PC2; C2: PC1 vs PC3) [47].

With this array, both the approaches with PC1 vs. PC2 ($72.4\% + 19.2\% = 91.6\%$ explained variance) and PC1 vs. PC3 ($72.4\% + 8.3\% = 80.7\%$ explained variance)

showed good capability of the sensors combination to discriminate the two macro groups (having green dots = healthy samples, and blue dots = tumor affected samples), healthy and tumor affected individuals, since the two areas enclosing the results show small overlaps. The second sensors array proved to be able to discriminate the two populations of healthy and tumor affected individuals, as shown by the little overlap between the "healthy individual responses" and the cancer affected ones (false-negative/false-positive area; FIGURE 7.10, PCA C1 and C2). ZnO 850 sensor was instead discarded in this work because it proved to be ineffective at discriminating between healthy and tumor affected samples, both as single unit or as part of an array. Indeed, the PCA statistics of the first sensors array responses (that include this sensor; Figure 7.9, PCA B) and the PCA statistics of the combined responses of the three sensors present in both arrays (Figure 7.9, PCA A), showed that the "healthy area" overlaps heavily with the "tumor area" in both cases. On the basis of the "VARIABLES" plot, the sensor SnO2 is close to the "good performer" ST25 650+Au, therefore the ZnO 850 sensor was substituted with the SnO2. As expected, this turned out to be a good strategy: the two areas (tumor and healthy) were now well discriminated and with little overlap between them, on both the combination PC1 vs PC2 (Figure 7.10, PCA C1) and PC1 vs PC3 (Figure 7.10, PCA C2). Therefore, even if SnO2 did not prove to be as good sensor as the tin and gold doped counterparts for single sensing unit purposes, it proved to be a good choice to form a functional set of sensors, able to discriminate healthy from tumor affected samples of blood. For what concerns the second data set, which have been studied only with the fifth sensors array, data for all the four single sensors approaches from the array are shown in Figure 7.11. For simplification, this time tumor affected and metastasis affected donors were united into the "Cancer" population.

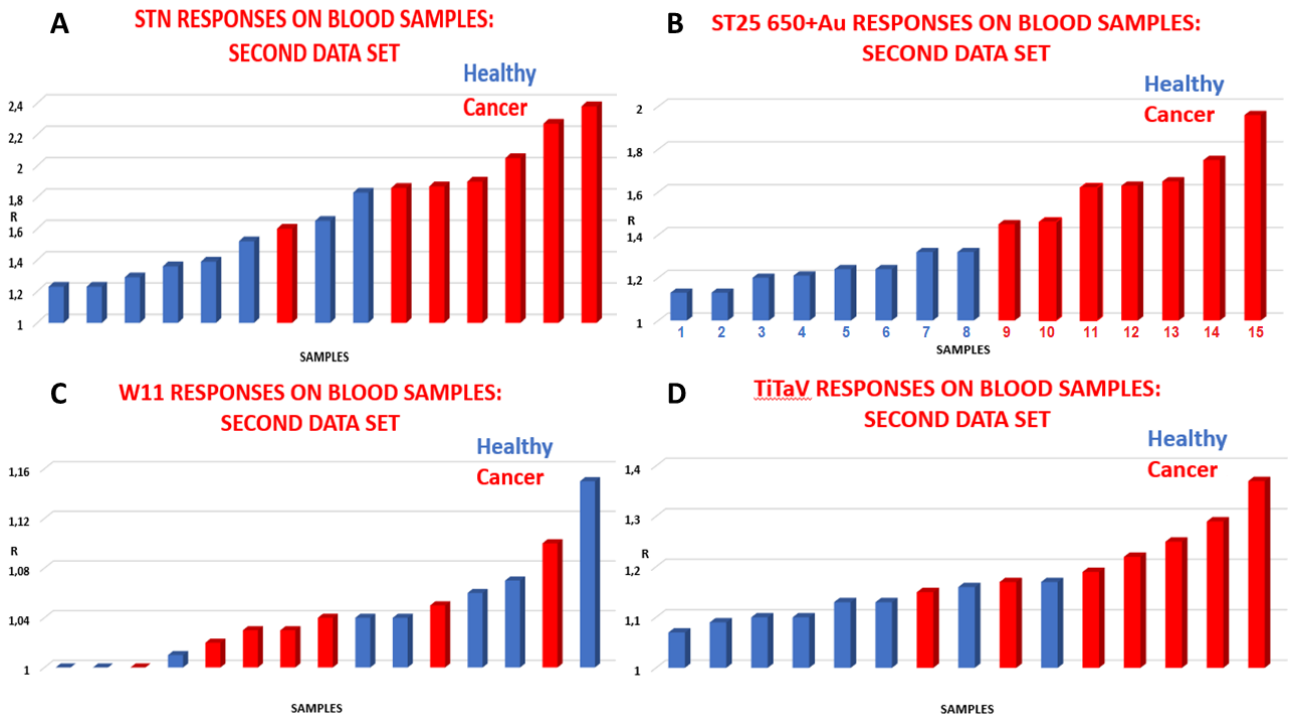

Figure 7.11: Second data set, all single sensors approaches.

This time, three sensors showed good capability to distinguish between healthy and tumor affected donors just from the amplitude of their responses, as visible from histograms A, B and D in Figure 7.11. This was a huge result, because showed that the choices of sensing materials made from the observations on the “SAMPLE” graphic from the first data set PCA approach followed a correct decisional path. Given the fact that the W11 unit, compared to the other sensors, showed really bad capability to distinguish blood samples populations (Figure 7.9C), it was not involved in the PCA approach for the second data set. Full data sheet from all the arrays responses, normalized to be used with PCA approach, and their analytical reports with score and loading values, are shown in Tables C.13 and C.14. For statistic interest, we decided to name the samples from this second set like number from 1 to 15, ordered like the results for the ST25 650+Au sensor (see Figure 7.11B).

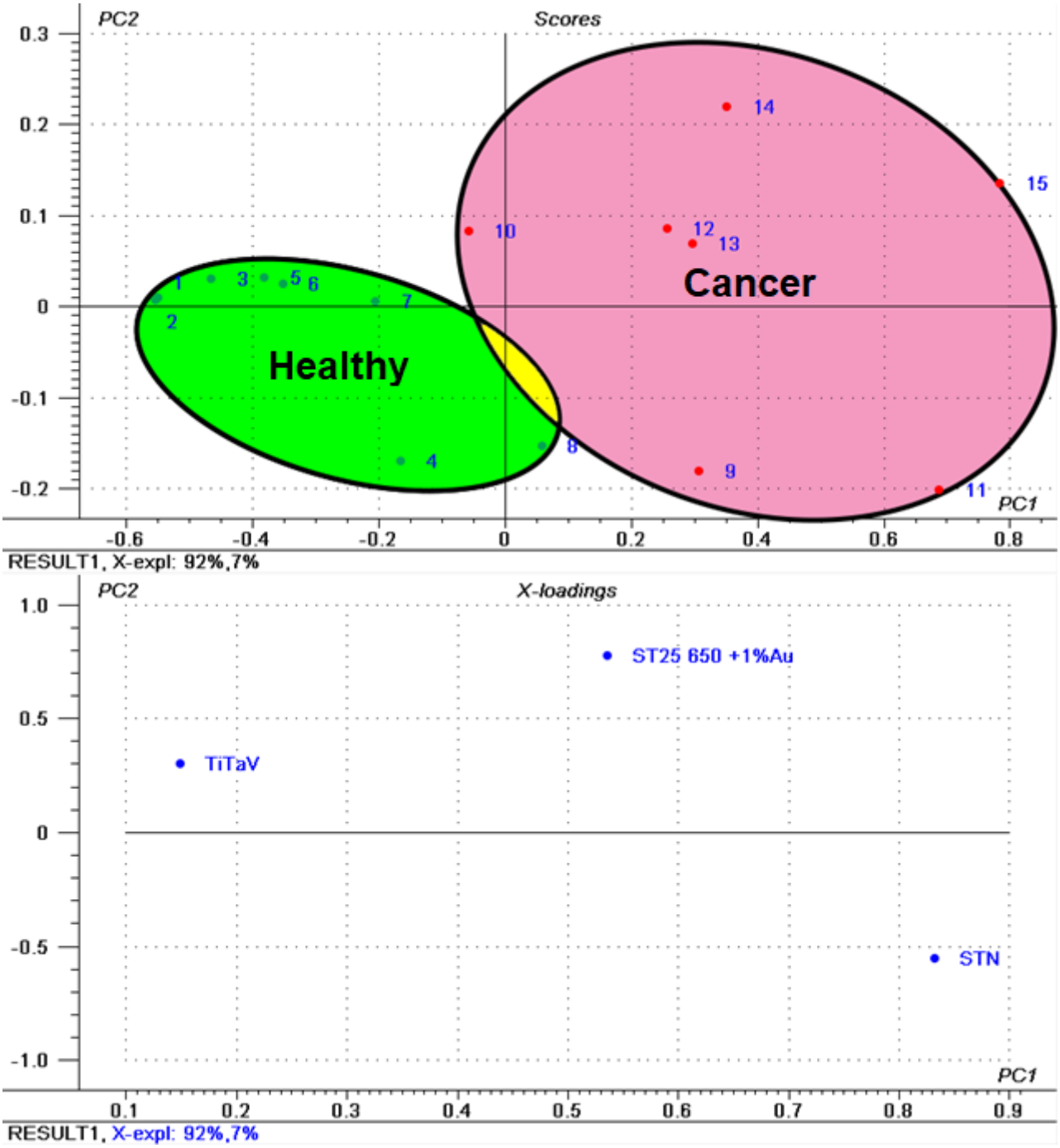

Figure 7.12: PCA statistics of the responses of the fifth sensors array on the second data set (PC1 vs PC2; $92.0\% + 7.0\% = 99.0\%$ explained variance).

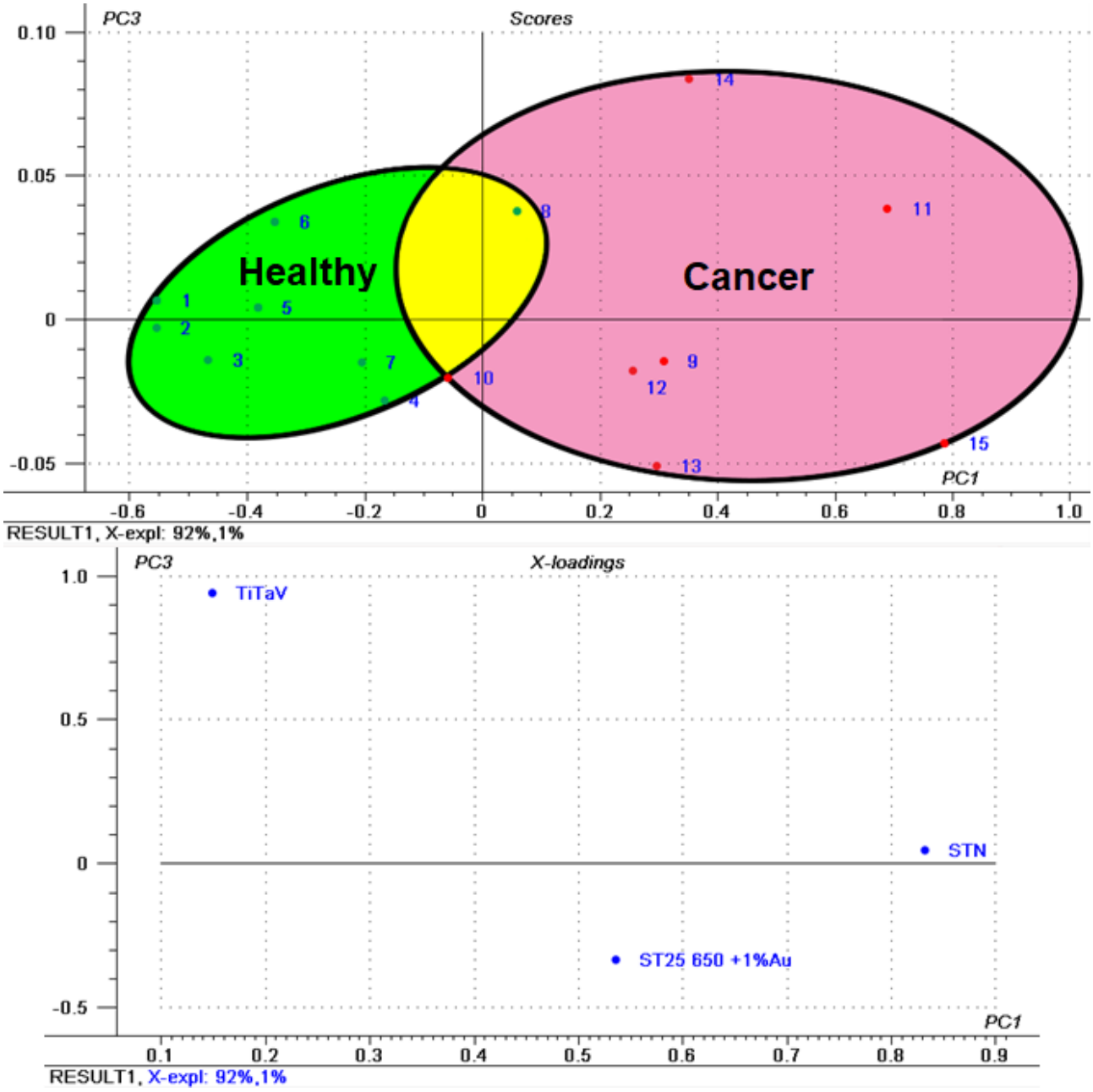

Figure 7.13: PCA statistics of the responses of the fifth sensors array on the second data set (PC1 vs PC3; $92.0\% + 1.0\% = 93.0\%$ explained variance).

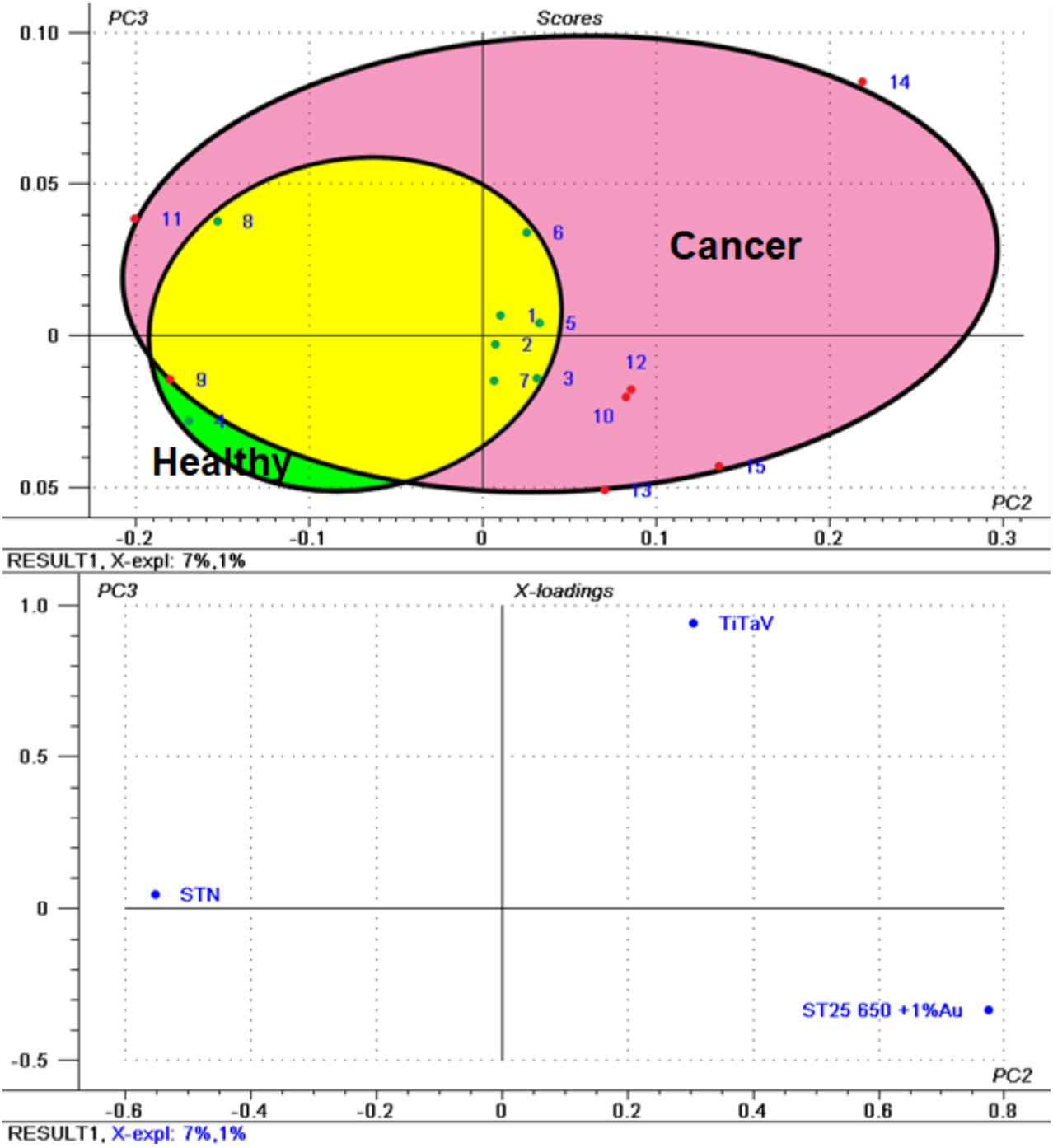

Figure 7.14: PCA statistics of the responses of the fifth sensors array on the second data set (PC2 vs PC3; $7.0\% + 1.0\% = 8.0\%$ explained variance).

Following the same logic used for the first data set, Figures 7.12–7.14 (having green dots = healthy samples, and red dots = cancer affected samples) show that, even with just three sensors, the two combinations having the highest explained variance (which, even for PCA approach, is amazingly high in those two cases, 99% and 93%) can greatly discriminate the two populations, and thus the sensors hosted in this array are good

choices for future implementation in the final device. In particular, the nearly negligible overlap shown in Figure 7.12, with the highest possible explained variance, is exactly the kind of pattern needed for a self-training machine learning setup, which will be developed in future. Chemoresistive sensors proved to efficiently distinguish between blood samples from healthy and tumor affected subjects, at least in the cases of gastric and colorectal cancers. These tumors are in highly vascularized regions of the human body, therefore they discharge in the blood stream large amounts of the metabolites, that can be therefore detected in the blood more easily, in respect to the metabolites produced by other tumor types, by the sensors employed here. Indeed, the sensor responses to the samples from patients with bigger and more vascularized tumors and metastasis were larger than the ones from less spread out neoplasms. Among all the sensors tested, the ST25 650+Au, STN and TiTaV proved to be the most sensitive ones in this discrimination, and they were even able, to some extent, to evaluate the effectiveness of the treatments aimed to remove a tumor mass. This suggests the possibility to follow the progression (or regression) of a tumor by following the concentration of the chemicals released from a blood sample with chemoresistive sensors. This would allow in the future the monitoring and the efficacy evaluation of surgeries and therapies aimed to tumor removal or containment. The major drawback of the single sensor approach concerns the metastasis, because they give a less reproducible amount of metabolites in the blood stream, being at different locations and at different levels of vascularization. Indeed, the sensor responses in individuals with metastatic cancers had a larger standard deviation in respect to the responses from individuals with a localized cancer. In any case, the average value of the response labeled “METASTASIS, WELL VASCULARIZED” (3.51 ± 0.43; Figure 7.8B), was significantly larger than the one “CANCERS, NO METASTASIS” (2.89 ± 0.19), and both were significantly larger than the one “HEALTHY” (1.62 ± 0.04), indicating that even in these unfavorable cases the three best sensors, and in particular ST25 650+Au, were able to some extent to discriminate among these pathological states. The discriminating power of a single sensor can be enhanced when used in combination with other ones and their collective responses are statistically processed by Principal Component Analysis. This statistical procedure turned out to be useful in selecting the most appropriate sensor to be included in a multisensor device, and it resulted that tin and tin doped materials have been the best choices so far. Therefore, tin- and titan-based sensors with different doping will be explored in the future, as well as other type of semiconductor materials, in order to find the

best sensors combination able to distinguish with high sensitivity and selectivity blood samples of healthy subjects from the ones of subjects with a cancerous pathology, and to assess its grade of invasiveness. Nonetheless, further studies on single sensors will proceed, with the aim to develop also single sensing unit devices whose analysis software would be simpler than the one implementing the PCA statistics. In conclusion, the ultimate goal of this work to develop new devices able to detect the presence of neoplasms as a pre-screening protocol, and as post-surgery/post-therapy simplified screening, in order to confirm the removal of the tumors and the absence of metastasis or relapses, looks like it has been reached.

Chapter 8 – Human Tissues Tests

After analyzing, between SCENT A1 and SCENT B1, chemical markers in laboratory setups, feces samples, immortalized cells and blood samples, it is time to effectively test the device on the “real thing”, the origin of the markers monitored on biological samples for pre- and post-screening purposes: human tissues from neoplastic masses. The goals here are to finally demonstrate if tumors, compared to healthy tissues, exhale recognizable volatile markers, and to develop in the future devices able to discriminate between the two populations (healthy and tumor affected) to hasten the histological exams and give to physicians and surgeons supplementary information after few hours from a oncological treatment.

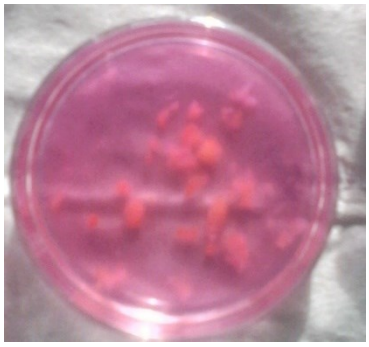

Figure 8.1: Petri dish hosting colorectal cancer tissues, prepared for the test.

Figure 8.2: Tripod used to host three petri dishes each test, to increase the exhalation surface of the samples.

8.1 – Human Tissues Tests: Sampling

The collection of colorectal and gastric tissues samples has been realized in the Hospital of Cona, Ferrara, Italy. The trial protocol and the informed consent form were presented, accepted and retrospectively registered from the Ethical Committee of the District of Ferrara, with trial number 170484, on 13 July 2017. Donors age spanned between 41 and 91 years old, from both sexes. Each test has been realized with three petri dishes, hosted in a tripod as shown in Figure 8.2. The preparation for the samples has been carried out as it follows:

- Tumor mass was weighted, with mg accuracy
- Healthy tissue mass was weighted, and an amount equal to the one of the tumor mass was selected
- The two masses were washed 2 times by using PBS (Phosphate-buffered saline) with penicillin, streptomycin, amphotericin added, to sterilize from a wide gamma of bacteria
- A teflon support with two holes was put under a fume tube. $1.8ml$ of DMEM was poured in each hole
- The tumor and healthy masses were inserted in the two holes, one type of specimen in each
- A sterilized scalpel and a pair of tweezers were used for the mechanical dissection, and trituration, of the two masses
- A pipette with $1000ml$ capacity is cut obliquely to simplify the management of bigger biological pieces, while the operator keeps on triturate the mass, to homogenize the specimen
- 3 petri dishes for specimen type (which means 3 for the healthy tissue and 3 more for the tumoral tissue) are prepared with $0.9ml$ of DMEM inside each of them. The mixtures prepared in the fume hood is divided equally in 3 parts (being $1.8ml$ total, it will be $0.6ml$ for each specimen kind), which are added to the prepared petri dishes, so to have, like for cell tests, a $1.5ml$ volume of breeding ground and biological material each petri dish, as shown in Figure 8.1

8.2 – Human Tissues Tests: Data and Results

Before passing to the results, it is important to consider the following features, correlated to the biological material tested:

- Human tissues samples are highly heterogeneous (see Figure 8.3): connective tissue of various kind, fat, red and white blood cells, various kind of healthy cells depending on the tissue, pathogenic elements, and neoplastic cells possibly in different development stages compose a greatly complicated mixture, in which most of the mass extracted after the surgery (given the limits scheduled from the Ethical Committee) is not composed from the tumor cells themselves (and for this reason, the sterilization and mechanical dissection are required to remove the most useless or contaminating components from the weight that will finally set the quantity tested for both neoplastic and healthy masses)
- The tumoral and healthy masses are devascularized for long time before the test (usually, 45 minutes elapse between devascularization and extraction, and then 2 more hours and a half are needed for the transport and preparation of the samples). Many cells in the two masses are harmed or even die due to the deprivation of nutrients and the stress caused by the transport inside the cooler to the laboratories before they can even be tested
- Since the material comes mostly from colorectal tissues, the floral bacteria added to the foreign microorganisms reaching the pieces extracted guarantee high contamination of the sample before the sterilization, harming some of the cells useful for the study
- While healthy mass around the tumor usually abound, neoplastic mass often limits the test outcome simply because of its scarcity
- All the masses are tested in couples: healthy and tumor affected tissues. Those masses always come from the same donor for surgical and scientific reasons, and thus are extracted from the same organ. The only difference between them is that one of the two tissues was affected from the neoplasia, the other was not
- All tumors tested were malignant, and some metastasized already

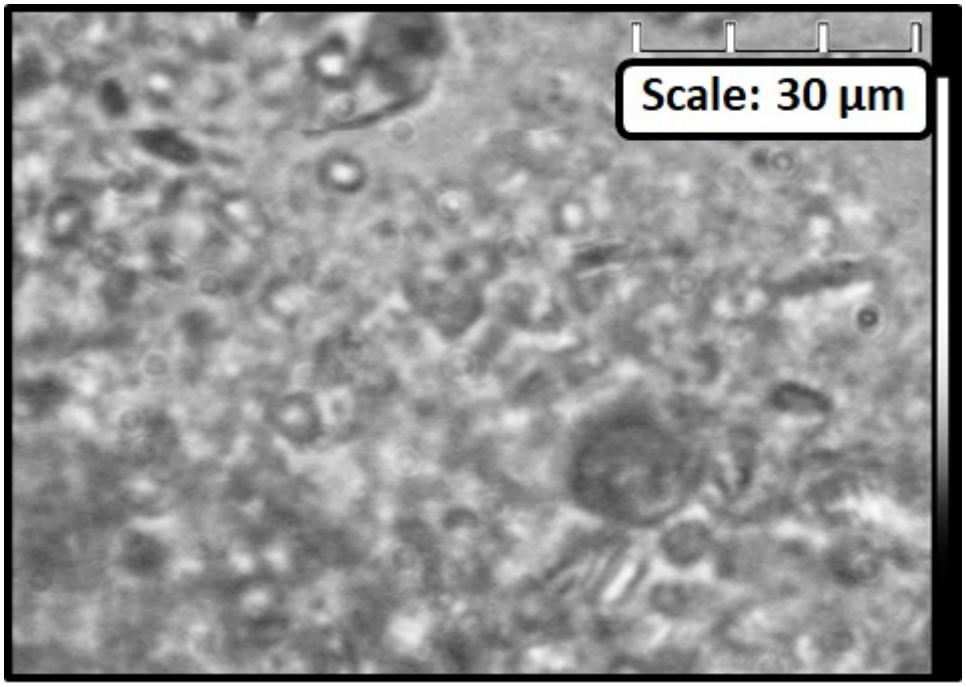

Figure 8.3: Optical microscope image from colorectal tumor tissue. Opalescent bubbles are composed by fat, while concave cells are red blood cells, mixed with the tissue and the neoplastic cells.

After taking into account these concerns, together with the difficulties linked to the preparation of the sample (and discussed in Paragraph 8.1), we can move forward to the measurements. While the PCA approach is, again, not possible due to the low amount of data coherent from all the sensors in the array, single sensors approach was still possible and consistent in the results, especially for ST25 650+Au and fourth and fifth sensors array. The first tests were carried on both gastric and colorectal tissues, while the next from year 2018 were carried on only the second type of tissues, because of lack of material from the first. Figures 8.4 and 8.5 refer to the first wave of tests, which gave encouraging results only for ST25 650+Au sensor. It was possible to observe that, after 2 hours and a half from the extraction from the donor (and so, after nearly 3 hours and 15 minutes from their devascularization), the tumor cells were still growing and reproducing, while most of the healthy cells started to suffer their detachment from the original organism, if not dying. After 2 more hours, tumors were still lively and emanating markers, while healthy cells were not so healthy anymore, and mostly dead.

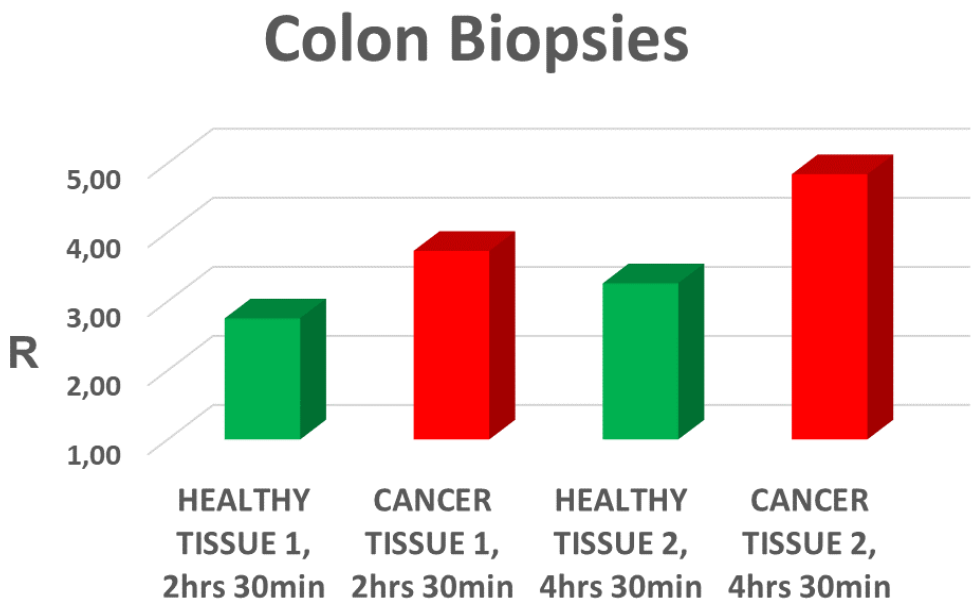

Figure 8.4: ST25 650+Au sensor responses to emanations of healthy and tumor affected human colorectal tissues. While healthy tissue response feebly increased (probably due to contamination, since cells looked mostly dead), after 4 hours and a half from the extraction from the human body, the cancer tissue was still lively and growing.

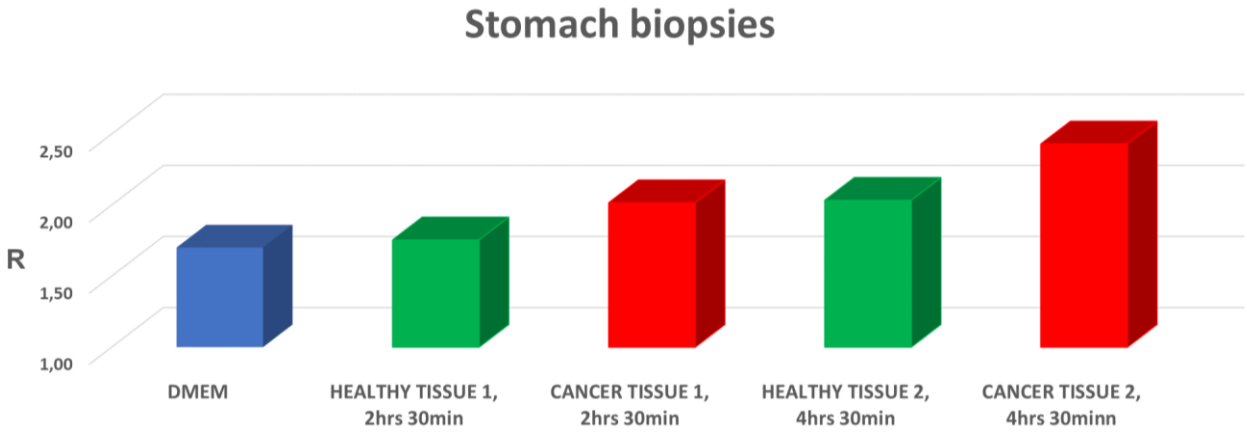

Figure 8.5: ST25 650+Au sensor responses to emanations of healthy and tumor affected human gastric tissues. Even if the responses are lower here, they share the same trend of the previous responses on colorectal tissues.

Figure 8.6 shows the results (listed in Table 8.1) from a first set of data gathered between January and March 2018, again only on ST25 650+Au sensor. Here, the approach used for cells tests were proposed again, with each round of measures having tested one breeding ground, one control samples, and one tumor affected sample. The samples here are not in chronological order, but following the greatness of mass weighted and tested, with the bigger quantity to the left and the lower to the right.

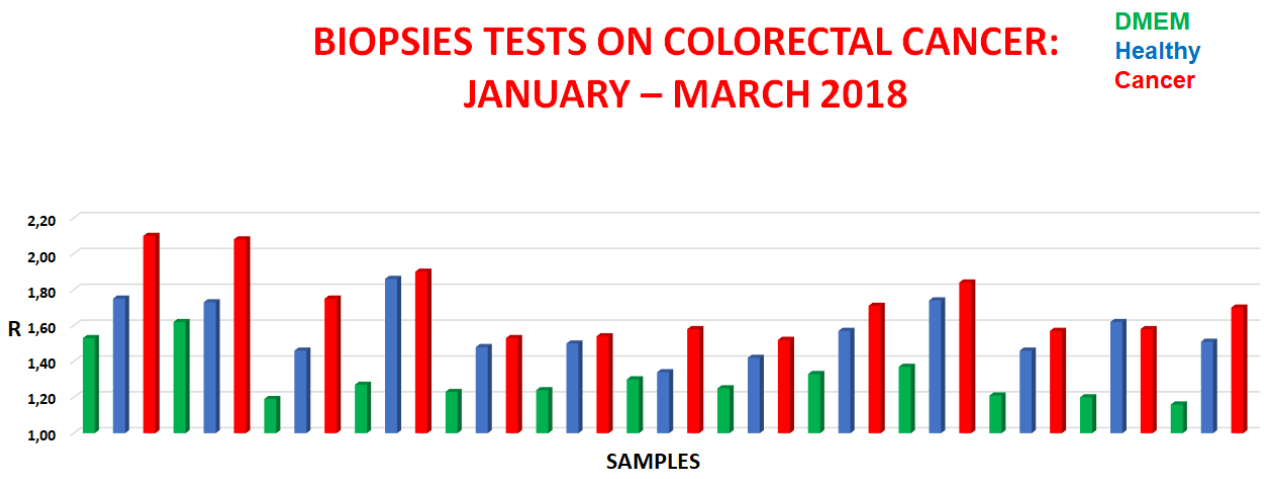

Figure 8.6: ST25 650+Au responses to 13 rounds of measurements over colorectal tissues, ordered to have the bigger masses to the left and the lower to the right. As it is visible, discrimination between healthy and cancer samples is strictly and directly correlated to the amount of material tested.

SAMPLE	ST25 650+Au
0.52g	
DMEM	1.53
Healthy	1.75
CANCER	2.10
0.49g	
DMEM	1.62
Healthy	1.73
CANCER	2.08
0.43g	
DMEM	1.19
Healthy	1.46
Cancer	1.75
0.42g	
DMEM	1.27
Healthy	1.86
Cancer	1.9
0.32g	
DMEM	1.23
Healthy	1.48
Cancer	1.53
0.30g	
DMEM	1.24
Healthy	1.5
Cancer	1.54
0.30g	
DMEM	1.3
Healthy	1.34
Cancer	1.58
0.27g	
DMEM	1.25
Healthy	1.42
Cancer	1.52
0.26g	
DMEM	1.33
Healthy	1.57
Cancer	1.71

SAMPLE	ST25 650+Au
0.26g	
DMEM	1.37
Healthy	1.74
Cancer	1.84
0.23g	
DMEM	1.21
Healthy	1.46
Cancer	1.57
0.21g	
DMEM	1.2
Healthy	1.62
Cancer	1.58
0.19g	
DMEM	1.16
Healthy	1.51
Cancer	1.7

Table 8.1: Results from human tissues tests realized between January and March 2018.

For what concerns the tests from March to the end of the thesis, in Figures 8.7–13 (and Table 8.2) is visible how finally the fifth sensors array gave good results with all the sensing units, even with low quantities of material. Still, before performing deeper and more refined statistical analysis, like PCA or machine learning models, higher amount of data (and thus more measurements) will be required.

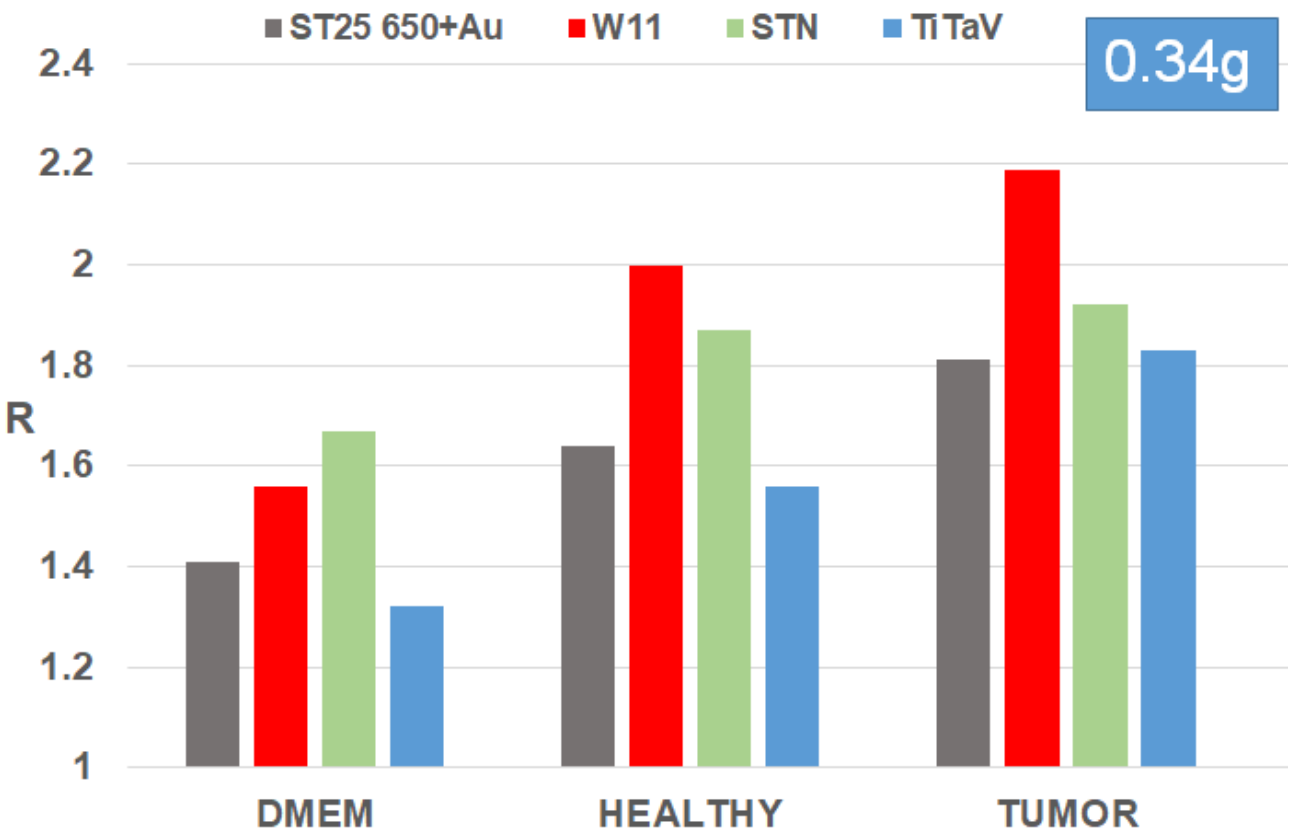

Figure 8.7: Fifth sensors array responses to DMEM, 0.34g of healthy colorectal tissue, and 0.34g of tumor affected colorectal tissue.

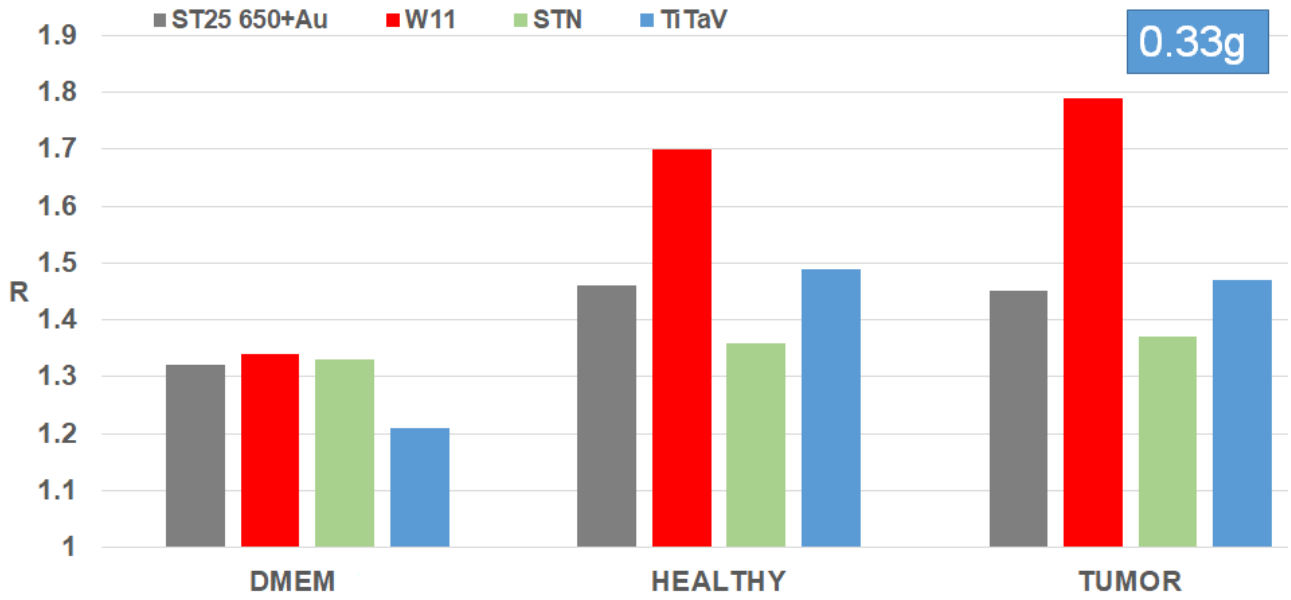

Figure 8.8: Fifth sensors array responses to DMEM, 0.33g of healthy colorectal tissue, and 0.33g of tumor affected colorectal tissue.

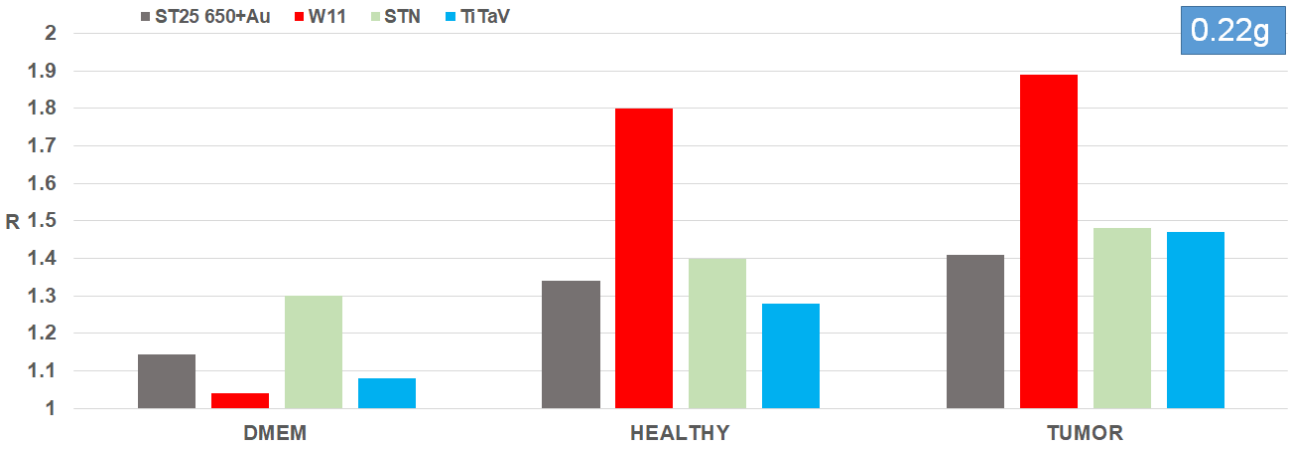

Figure 8.9: Fifth sensors array responses to DMEM, 0.22g of healthy colorectal tissue, and 0.22g of tumor affected colorectal tissue.

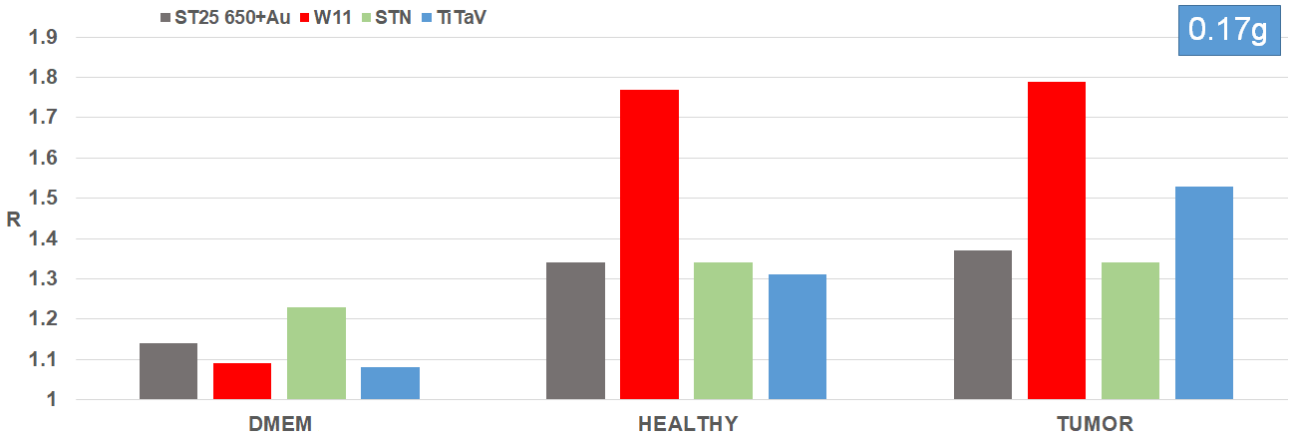

Figure 8.10: Fifth sensors array responses to DMEM, 0.17g of healthy colorectal tissue, and 0.17g of tumor affected colorectal tissue.

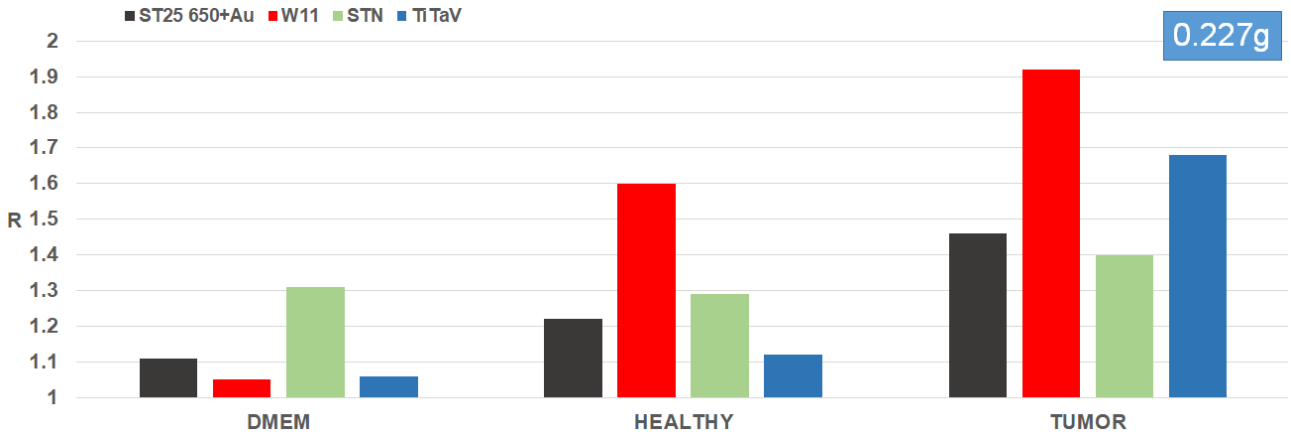

Figure 8.11: Fifth sensors array responses to DMEM, 0.227g of healthy colorectal tissue, and 0.227g of tumor affected colorectal tissue.

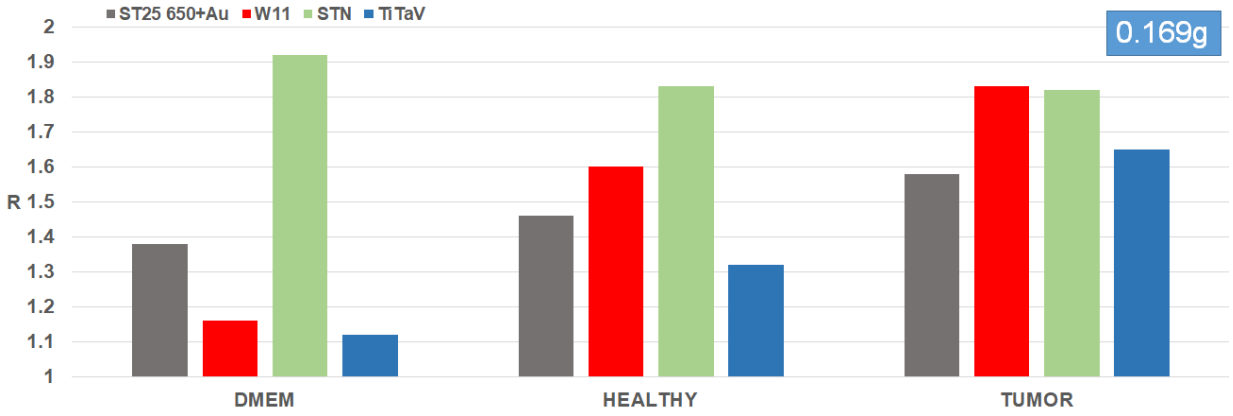

Figure 8.12: Fifth sensors array responses to DMEM, 0.169g of healthy colorectal tissue, and 0.169g of tumor affected colorectal tissue.

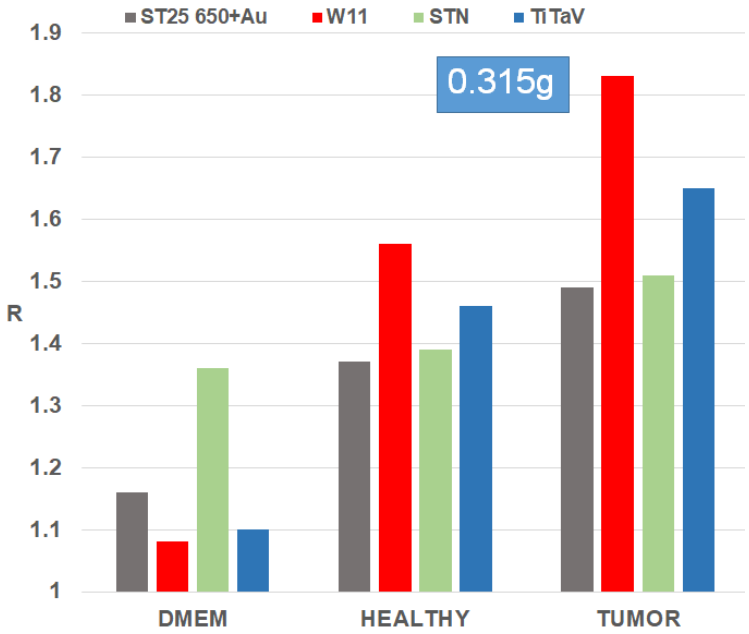

Figure 8.13: Fifth sensors array responses to DMEM, 0.315g of healthy colorectal tissue, and 0.315g of tumor affected colorectal tissue.

SENSOR	ST25 650+Au	W11	STN	TiTaV
0.34g				
DMEM	1.41	1.56	1.67	1.32
HEALTHY	1.64	2	1.87	1.56
TUMOR	1.81	2.19	1.92	1.83
0.33g				
DMEM	1.32	1.34	1.33	1.21
HEALTHY	1.46	1.7	1.36	1.49
TUMOR	1.45	1.79	1.37	1.47
0.22g				
DMEM	1.145	1.04	1.3	1.08
HEALTHY	1.34	1.8	1.4	1.28
TUMOR	1.41	1.89	1.48	1.47
0.17g				
DMEM	1.14	1.09	1.23	1.08
HEALTHY	1.34	1.77	1.34	1.31
TUMOR	1.37	1.79	1.34	1.53
0.227g				
DMEM	1.11	1.05	1.31	1.06
HEALTHY	1.22	1.6	1.29	1.12
TUMOR	1.46	1.92	1.4	1.68
0.169g				
DMEM	1.38	1.16	1.92	1.12
HEALTHY	1.46	1.6	1.83	1.32
TUMOR	1.58	1.83	1.82	1.65
0.315g				
DMEM	1.16	1.08	1.36	1.1
HEALTHY	1.37	1.56	1.39	1.46
TUMOR	1.49	1.83	1.51	1.65

Table 8.2: Last results, from March onward, of the fifth array on biopsies.

In particular, from the data shown above, we saw that W11, ST25 650+Au and TiTaV sensors proved to give the best discrimination between the populations, and also STN with minor extent gave some promising result. In conclusion, even if human tissues tests heavily depended on the actual amount of tumor cells successfully harvested from the neoplastic mass extracted, we could observe the capability of the sensors to discriminate healthy and tumor affected population when enough oncologic material was at hand for the test. In these cases, the difference from the control group was enormous, often with the latter giving half the response of the correlated neoplastic mass, which it is important to remember, came from the same organ of the same donor, having only the degeneration into tumor as difference. In the future, the idea to develop a post-screening device for fast histological pre-exams, especially for tissues close to the malignant mass, does not look so far anymore.

Chapter 9 – Conclusions

All the branches of research gave coherent and interesting results:

- Immortalized cell growth, concentration, health status and type was successfully observed from the sensors, for three out of four cell lines studied (HEK-293, A549, CHO). HCT 116 did not show the same visible trends as the previous ones, but some hypotheses have been made about their different behavior, and studies in the future will be realized in order to verify their veracity. The goal of the prosecution of this research will be the building of the odor fingerprint database for most of the human cell lines, to help researchers, physicians and oncologists to better understand tumor and cellular metabolites. This will enhance both pharmacological and biological research fields in order to detect and monitor neoplasms activity, also by combining the continuous observation of cultures with the addition of drugs, to see their effect on the cells metabolism in real time. Bacteria contamination has been observed too, and well distinguished by the metabolites emanation from aseptic cell cultures; this led to idea to try in future to cultivate bacteria, too, and test the effect of drugs on them, for enhancing and medical purposes, as previously proposed for tumor cells.
- Chemoresistive sensors, able to convey the results in few minutes, have successfully detected the contamination of blood stream by tumor markers. Successful results were already obtained employing a single sensor as ST25 650+Au on first data set, and with STN, ST25 650+Au and TiTaV on the second data set, which showed increasingly responses with the worsening of the cancer degeneration. Preliminary data indicated that this sensor allowed also tracking the progression or the regression of a neoplasia with time by taking blood samples from the patient before, during and after the surgery and/or the application of specific oncological therapies. The Principal Component Analysis of the sensor responses (possible due to the high amount of data obtained) allowed not only to visualize the patterns able to show the difference between healthy and tumor affected samples just from the analysis, but also helped in the selection of the most appropriate sensing units to build a multisensor instrument with enhanced performances. Tin and titanium oxide materials appeared the best choice to create arrays capable of discriminating samples from healthy and tumor affected individuals from their blood

sample emanations, as the second sensors array employed in the patented instrument SCENT B1. Given the encouraging results obtained in this preliminary step, the idea is now aiming to develop a machine learning software, to be implemented in a prototype instrument for a new set of double blind experiments, before the development of the true post-screening, fast responding instrument.

- Human tissues tests gave preliminary, yet solid, results, showing how some sensors (in particular tin and titan oxide family) can distinguish between healthy and tumor affected portions of surgical removed material with single sensors approach. Even if more statistic is required before being able to use more refined analysis methods, yet this study opened the way to more tests, also on different kind of tumors, in order to develop fast responding post-screening devices, aimed to hasten histologic analysis and biopsies research.

Overall, in these three years of tests, nanostructured chemoresistive sensors proved to be the right choice for a multitude of applications connected to the three different kind of samples analyzed, successfully detecting tumor markers under the most variable conditions, and allowing to either distinguish control groups from diseased samples, or even detect the degeneration or proliferation grade of the samples itself.

APPENDIX A – Breeding Grounds: DMEM High Glucose Composition

In order to ensure the reliability of the results given from the device during human tissues and cell cultures tests, the breeding ground used was the same for both the branches of research. The chosen one was Dulbecco's Modified Eagle's Medium (DMEM), with high glucose concentration, and its components and their concentration are listed below in the Table A.1 [162].

Components	Molecular Weight	Concentration (mg/L)	mM
Amino Acids			
Glycine	75.0	30.0	0.4
L-Arginine hydrochloride	211.0	84.0	0.40
L-Cystine 2HCl	313.0	63.0	0.20
L-Glutamine	146.0	580.0	3.97
L-Histidine hydrochloride-H2O	210.0	42.0	0.2
L-Isoleucine	131.0	105.0	0.80
L-Leucine	131.0	105.0	0.80
L-Lysine hydrochloride	183.0	146.0	0.80
L-Methionine	149.0	30.0	0.20
L-Phenylalanine	165.0	66.0	0.4
L-Serine	105.0	42.0	0.4
L-Threonine	119.0	95.0	0.80
L-Tryptophan	204.0	16.0	0.08
L-Tyrosine	181.0	72.0	0.40
L-Valine	117.0	94.0	0.80
Vitamins			
Choline chloride	140.0	4.0	0.03
D-Calcium pantothenate	477.0	4.0	0.01
Folic Acid	441.0	4.0	0.01
Niacinamide	122.0	4.0	0.03
Pyridoxine hydrochloride	206.0	4.0	0.02
Riboflavin	376.0	0.4	0.001
Thiamine hydrochloride	337.0	4.0	0.01
i-Inositol	180.0	7.2	0.04
Inorganic Salts			
Calcium Chloride (CaCl2-2H2O)	147.0	264.0	1.80
Ferric Nitrate (Fe(NO3)3"9H2O)	404.0	0.1	$2.48 \cdot 10^{-4}$
Magnesium Sulfate (MgSO4-7H2O)	246.0	200.0	0.81
Potassium Chloride (KCl)	75.0	400.0	5.33
Sodium Bicarbonate (NaHCO3)	84.0	3700.0	44.05
Sodium Chloride (NaCl)	58.0	6400.0	110.34
Sodium Phosphate monobasic (NaH2PO4-2H2O)	154.0	141.0	0.92
Other Components			
D-Glucose (Dextrose)	180.0	4500.0	25.0
Phenol Red	376.4	15.0	0.04

Table A.1: Composition of DMEM breeding ground.

APPENDIX B – Human Blood Composition

Blood is a non-Newtonian fluid and a connective tissue of animals body, with the main function of bringing oxygen, nutrients of various kind, defensive cells and corpuscles for the organism self-repair (white blood cells and platelets) around the body, together with the wastes directed to the waste system, through the blood vessels. It has a viscosity, at $37°C$, normally between $3 \cdot 10^{-3} Pa\,s$ to $4 \cdot 10^{-3} Pa\,s$ (pascal-seconds), and a specific weight around $1.041 - 1.062 g/cm^3$. It constitutes 7.7% of the human body weight and its pH spans, in the arteries, around $7.38 - 7.42$. While for men the liquid part, called plasma, composes the 55% of the whole blood, and the corpuscular part 45%, for women those quantities change to 60% and 40% respectively. The percentage relative to the corpuscular part is called hematocrit.

The composition of a blood sample for an adult, healthy male human, is:

- **PLASMA** ($\sim 55\%$ of the whole blood):
  - Water ($\sim 90 - 92\%$ of the plasma) – Solvent which carries other substances, absorbs heat, and hydrates other tissues
  - Proteins ($\sim 8 - 10\%$ of the plasma) – Albumin ($\sim 60\%$ of all the proteins in blood) keeps the osmotic balance. Globulins ($\sim 35\%$ of all the proteins in blood) which are a wide family that includes between them globulins β, which have ionic transport function of hormones and lipids, and immunoglobulins, also known as antibodies, which constitute part of the immune defense system. Fibrinogen ($\sim 5\%$ of all the proteins in blood), which are the inactive version of fibrin, and are responsible for the clotting of blood; when the plasma is free from this protein, is called serum. Prothrombin (traces), which is another clotting factor
  - Salts (traces) – Sodium, potassium, calcium, magnesium, chloride, bicarbonate, aside for the use made from organs to which some of them are carried for other specific purposes, they serve as electrolytes, thus guaranteeing osmotic balance, pH buffering and regulation of membrane permeability

    - Nutrients of various kind (traces) – Glucose, fatty acids, lipids (both phospholipids and triglycerides), amino acids, lipoprotein particles, vitamins, carried around the cardiovascular system to nourish the organism
    - Respiratory gases (traces) – Oxygen and carbon dioxide can be carried both from hemoglobin in red blood cells and plasma around the body, the first gas to energize it, the second to be expelled.
    - Waste products from the metabolism (traces) – Urea, uric acid and acetate are the most common, and are carried to the waste system for the final expulsion from the body
    - Hormones (traces) – There are a wide gamma of them, with different rules and targets, but mostly all play important roles in the regulation of the various physiological processes and behaviors in the human body
    - Other chemicals and markers (traces) – Anything that is expelled or drawn in the blood stream, on purpose or accidentally, circulates with it. Vascular regulators and tumor markers are just two of these chemicals group.
- **CORPUSCULAR ELEMENTS** (also known as formed element, composed from cells and parts of them, $\sim 45\%$ of the whole blood):
    - Erythrocytes (red blood cells, $\sim 98\%$ of the corpuscular part, $\sim 44\%$ of the whole blood) – These cells have the principal function to carry oxygen around the body for nourishment, and carbon dioxide from the body to the lungs for expulsion
    - Leukocytes (white blood cells, traces) – Basophil, eosinophil, neutrophil, monocyte, natural killer cells and lymphocyte are all cells part of the immune system, and all of them have the role to defend and safeguard the organism by attacking and containing external hazardous elements and microorganisms, like virus, bacteria or parasites. Some of them also destroy and remove old cells, or even aberrant ones, like tumor cells
    - Thrombocytes (platelets, $\sim 2\%$ of the corpuscolar part, 1% of the whole blood) – Their function is linked to the blood clotting, by forming platelet plugs

The two major components (plasma and corpuscular part) of the whole blood are usually mixed between them, but leaving the blood at room temperature to rest for some time, or

by centrifuging the test tube, separates them as shown in Figure B1B, with the plasma on top, the erythrocytes to the bottom, and the thin layer of leukocytes and thrombocytes separating them.

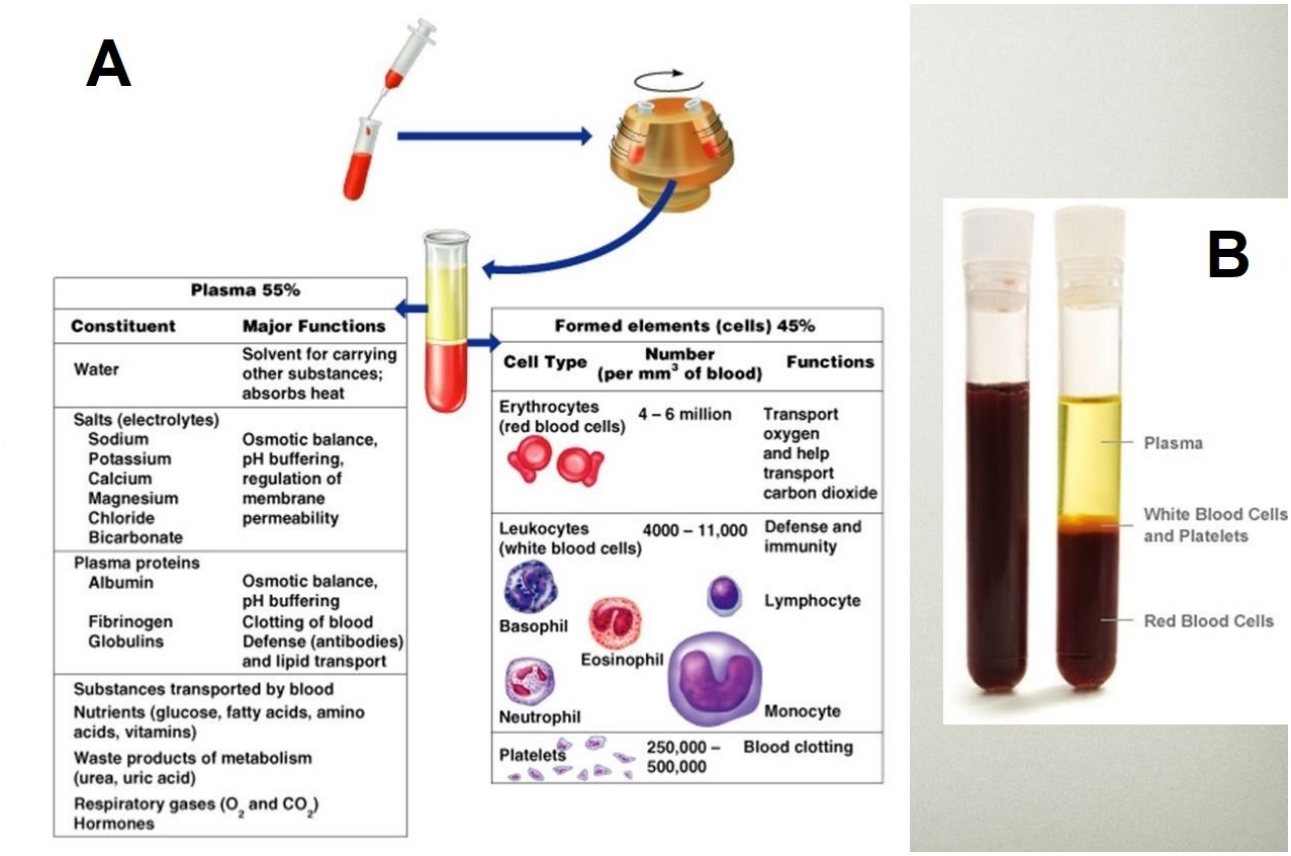

Figure B1: A – Average composition of a healthy human blood sample, with some components schematized. B – Blood specimens, the left just sampled and with its components mixed, the right centrifuged and with the components separated [169,170].

APPENDIX C – PCA Data

3 Sensors Array Data				
SAMPLE	HEALTH STATUS	ST25 650+Au (X)	SmFeO3 (X)	CdS2 (X)
HEALTHY G1	HEALTHY	-0.72	-0.27	1.21
HEALTHY NA 1	HEALTHY	-0.82	-0.14	1.26
PATIENT 46 1	TUMOR	0.48	-1.26	1.10
PATIENT 47 1	TUMOR	0.95	-1.54	1.36
HEALTHY BN 1	HEALTHY	-0.93	-0.38	1.27
PATIENT 53 1	TUMOR	0.11	-1.51	1.12
HEALTHY CP 1	HEALTHY	-0.70	-1.06	1.10
HEALTHY AR 1	HEALTHY	-0.42	-1.30	1.12
PATIENT 54 A 1	TUMOR	-0.04	-0.59	1.12
PATIENT 55 1	TUMOR	0.23	-1.06	1.08
HEALTHY GO 1	HEALTHY	-0.72	-0.11	1.06
PATIENT 59 1	TUMOR	-0.16	-0.65	-0.90
HEALTHY RA 1	HEALTHY	-0.83	0.10	-0.82
HEALTHY C1 1	HEALTHY	-0.80	0.09	-0.87
HEALTHY F1 1	HEALTHY	-0.68	0.13	-0.86
PATIENT 62 1	TUMOR	-0.48	-0.41	-0.86
HEALTHY NE 1	HEALTHY	-0.75	0.21	-0.84
PATIENT 63 1	TUMOR	0.02	0.43	-0.83
HEALTHY OP 1	HEALTHY	-0.84	0.24	-0.85
PATIENT 66 1	TUMOR	-0.42	0.17	-0.84
PATIENT 67 1	TUMOR	3.06	-7.22	1.26
PATIENT 68 1	TUMOR	0.58	0.12	-0.84
HEALTHY ANT1 1	HEALTHY	-0.81	0.25	-0.85
HEALTHY C1b 1	HEALTHY	-0.83	0.47	-0.84
HEALTHY AND1 1	HEALTHY	-0.19	-0.11	-0.85
HEALTHY IN 1	HEALTHY	-0.96	0.39	-0.83
PATIENT 69A 1	TUMOR	0.35	0.20	-0.84
PATIENT 72 1	TUMOR	-0.09	0.45	-0.84
HEALTHY LA 1	HEALTHY	-0.43	0.39	-0.84
HEALTHY FI 1	HEALTHY	-0.60	0.19	-0.83
PATIENT 73 1	TUMOR	0.99	-2.10	1.08
HEALTHY SAMA1 1	HEALTHY	-0.52	0.10	-0.84
HEALTHY EDO1 1	HEALTHY	-0.11	0.32	-0.84
HEALTHY LOR1 1	HEALTHY	-0.49	0.23	-0.83
PATIENT 71A 1	TUMOR	0.70	0.41	-0.82
PATIENT 74 1	TUMOR	0.33	0.12	-0.84
HEALTHY RUG1 1	HEALTHY	-0.84	0.29	-0.86
PATIENT 76A 1	TUMOR	0.23	0.10	-0.87

3 Sensors Array Data				
SAMPLE	HEALTH STATUS	ST25 650+Au (X)	SmFeO3 (X)	CdS2 (X)
HEALTHY CAT1 1	HEALTHY	-0.66	0.41	-0.83
PATIENT 87 1	TUMOR	0.33	0.66	-0.83
HEALTHY FLOR1 1	HEALTHY	-0.67	0.38	-0.85
HEALTHY PAOL1 1	HEALTHY	-0.75	0.38	-0.86
PATIENT 88 1	TUMOR	0.23	0.48	-0.84
PATIENT 89 1	TUMOR	0.71	0.96	-1.06
HEALTHY ENRI1 1	HEALTHY	-0.73	0.93	-1.04
PATIENT 92 1	TUMOR	0.72	0.93	-1.06
HEALTHY ANS1	HEALTHY	-0.70	0.97	-0.90
PATIENT MB11	TUMOR	-0.37	0.42	-0.84
PATIENT MB24	TUMOR	-0.26	0.37	-0.86
PATIENT noF1A	TUMOR	-0.42	0.48	-0.84
HEALTHY GIUCHI1	HEALTHY	-0.38	0.53	-0.87
PATIENT ME1	TUMOR	-0.62	0.17	-0.86
PATIENT STO1	TUMOR	0.08	0.20	-0.87
PATIENT X	TUMOR	0.97	0.42	-0.88
HEALTHY C1c 1	HEALTHY	-0.51	0.49	-0.89
HEALTHY GIAN1	HEALTHY	-0.34	0.55	-0.87
PATIENT 105	TUMOR	0.87	0.28	-0.87
PATIENT MX1	TUMOR	-0.36	0.40	-0.86
PATIENT VINCEN1	TUMOR	-0.38	0.53	-0.86
PATIENT METAEPA2	TUMOR	2.03	-0.72	1.08
HEALTHY ROC1	HEALTHY	-0.42	-0.75	1.04
HEALTHY LU1	HEALTHY	-0.28	0.11	1.20
PATIENT METAEPA2 3DAYS	TUMOR	-0.56	0.01	1.23
PATIENT METAYOUNG1 SHORT	TUMOR	3.90	-0.25	1.21
PATIENT METAYOUNG1 LONG	TUMOR	3.61	-0.35	1.26
HEALTHY STUDXVIC	HEALTHY	-0.32	0.35	1.16
PATIENT METAEPAENDO1	TUMOR	1.58	0.35	1.15
PATIENT METAENDO1	TUMOR	2.99	0.03	1.18
HEALTHY GIULIO1	HEALTHY	-0.60	0.60	1.08
HEALTHY ANNACAMP1	HEALTHY	-0.47	0.53	1.09
PATIENT METASTOMA1	TUMOR	1.63	0.32	1.14
PATIENT SPLESX1	TUMOR	-0.53	0.39	1.10
HEALTHY IRENE1	HEALTHY	-0.33	0.43	1.09
PATIENT METAEPA3	TUMOR	-0.80	0.12	1.10
PATIENT METALINFO1	TUMOR	0.34	0.12	1.11
HEALTHY BEA1	HEALTHY	-0.55	0.60	1.08
PATIENT DXMALMETA1	TUMOR	-0.10	0.40	1.07

3 Sensors Array Data				
SAMPLE	HEALTH STATUS	ST25 650+Au (X)	SmFeO3 (X)	CdS2 (X)
PATIENT DXMALMETA2	TUMOR	0.27	0.35	1.08
HEALTHY NKI 1	HEALTHY	-0.38	0.32	1.07
HEALTHY SERA1	HEALTHY	-0.38	0.37	1.07
PATIENT METAEPA4	TUMOR	-0.24	0.04	1.07
Basic Statistical Information	Maximum	6.77	-1.04	1.35
	Max Sample	PATIENT METAYOUNG1 SHORT	HEALTHY ANS1	PATIENT 47 1
	Minimum	1.21	-3.82	-1.27
	Min Sample	HEALTHY IN 1	PATIENT 67 1	PATIENT 89 1
	Average	2.31	-1.37	-0.12
	Standard Deviaton	1.14	0.34	1.08
	CV	0.49	-0.25	-8.89

Table C.1: First data set, 3 sensors array normalized data and basic statistical information.

	Analytical Report 3 Sensors Array	
	Comp 1	Comp 2
R2	58%	23%
R2(cum)	58%	81%
Eigenvalue	46.83	18.68
Q2	58%	55%
Q2(cum)	58%	81%

Table C.2: First data set, 3 sensors array data, analytical report.

Scores				
Samples	Groups	Comp 1	Comp 2	DmodX
HEALTHY G1	HEALTHY	-0.44	-1.37	0.03
HEALTHY NA	HEALTHY	-0.33	-1.47	0.15
PATIENT 46 1	TUMOR	-1.66	-0.44	0.42
PATIENT 47 1	TUMOR	-2.23	-0.29	0.30
HEALTHY BN	HEALTHY	-0.42	-1.55	0.16
PATIENT 53 1	TUMOR	-1.60	-0.73	0.88
HEALTHY CP 1	HEALTHY	-0.87	-1.29	0.86
HEALTHY AR 1	HEALTHY	-1.19	-1.10	0.94
PATIENT 54 A 1	TUMOR	-0.96	-0.81	0.02
PATIENT 55 1	TUMOR	-1.38	-0.61	0.36
HEALTHY GO 1	HEALTHY	-0.26	-1.26	0.12
PATIENT 59 1	TUMOR	0.20	0.50	1.30

Scores				
Samples	Groups	Comp 1	Comp 2	DmodX
HEALTHY RA 1	HEALTHY	0.99	-0.03	0.83
HEALTHY C1 1	HEALTHY	0.99	0.03	0.86
HEALTHY F1 1	HEALTHY	0.95	0.11	0.75
PATIENT 62 1	TUMOR	0.50	0.25	1.21
HEALTHY NE 1	HEALTHY	1.02	0.05	0.69
PATIENT 63 1	TUMOR	0.72	0.60	0.03
HEALTHY OP 1	HEALTHY	1.09	-0.01	0.70
PATIENT 66 1	TUMOR	0.81	0.29	0.54
PATIENT 67 1	TUMOR	-6.80	1.19	5.21
PATIENT 68 1	TUMOR	0.22	1.00	0.06
HEALTHY ANT1 1	HEALTHY	1.09	0.01	0.68
HEALTHY C1b 1	HEALTHY	1.22	0.00	0.46
HEALTHY AND1 1	HEALTHY	0.52	0.45	0.72
HEALTHY IN 1	HEALTHY	1.25	-0.10	0.60
PATIENT 69A 1	TUMOR	0.40	0.84	0.09
PATIENT 72 1	TUMOR	0.80	0.53	0.07
HEALTHY LA 1	HEALTHY	0.95	0.28	0.32
HEALTHY FI 1	HEALTHY	0.92	0.15	0.62
PATIENT 73 1	TUMOR	-2.44	-0.07	1.04
HEALTHY SAMA1 1	HEALTHY	0.83	0.21	0.67
HEALTHY EDO1 1	HEALTHY	0.73	0.51	0.22
HEALTHY LOR1 1	HEALTHY	0.88	0.23	0.52
PATIENT 71A 1	TUMOR	0.32	1.08	0.32
PATIENT 74 1	TUMOR	0.36	0.83	0.19
HEALTHY RUG1 1	HEALTHY	1.14	0.00	0.66
PATIENT 76A 1	TUMOR	0.42	0.77	0.29
HEALTHY CAT1 1	HEALTHY	1.08	0.11	0.42
PATIENT 87 1	TUMOR	0.68	0.83	0.38
HEALTHY FLOR1 1	HEALTHY	1.09	0.12	0.47
HEALTHY PAOL1 1	HEALTHY	1.14	0.06	0.51
PATIENT 88 1	TUMOR	0.63	0.76	0.14
PATIENT 89 1	TUMOR	0.78	1.27	0.78
HEALTHY ENRI1 1	HEALTHY	1.56	0.21	0.04
PATIENT 92 1	TUMOR	0.75	1.27	0.75
HEALTHY ANS1	HEALTHY	1.49	0.14	0.10
PATIENT MB11	TUMOR	0.94	0.33	0.25
PATIENT MB24	TUMOR	0.85	0.42	0.26
PATIENT noF1A	TUMOR	1.00	0.29	0.23
HEALTHY GIUCHI1	HEALTHY	1.02	0.34	0.16
PATIENT ME1	TUMOR	0.94	0.16	0.67
PATIENT STO1	TUMOR	0.56	0.67	0.26

Scores				
Samples	Groups	Comp 1	Comp 2	DmodX
PATIENT X	TUMOR	0.21	1.32	0.46
HEALTHY C1c 1	HEALTHY	1.09	0.26	0.28
HEALTHY GIAN1	HEALTHY	1.02	0.37	0.12
PATIENT 105	TUMOR	0.17	1.23	0.26
PATIENT MX1	TUMOR	0.93	0.35	0.28
PATIENT VINCEN1	TUMOR	1.02	0.33	0.16
PATIENT METAEPA2	TUMOR	-2.18	0.69	0.99
HEALTHY ROC1	HEALTHY	-0.80	-1.04	0.40
HEALTHY LU1	HEALTHY	-0.46	-1.03	0.67
PATIENT METAEPA2 3DAYS	TUMOR	-0.37	-1.26	0.43
PATIENT METAYOUNG1 SHORT	TUMOR	-3.02	1.96	2.59
PATIENT METAYOUNG1 LONG	TUMOR	-2.95	1.70	2.35
HEALTHY STUDXVIC	HEALTHY	-0.26	-1.03	0.88
PATIENT METAEPAENDO1	TUMOR	-1.32	0.34	1.91
PATIENT METAENDO1	TUMOR	-2.32	1.33	2.37
HEALTHY GIULIO1	HEALTHY	0.09	-1.18	0.94
HEALTHY ANNACAMP1	HEALTHY	-0.04	-1.09	0.95
PATIENT METASTOMA1	TUMOR	-1.37	0.38	1.90
PATIENT SPLESX1	TUMOR	-0.09	-1.14	0.77
HEALTHY IRENE1	HEALTHY	-0.17	-0.98	0.92
PATIENT METAEPA3	TUMOR	-0.10	-1.34	0.34
PATIENT METALINFO1	TUMOR	-0.75	-0.52	0.97
HEALTHY BEA1	HEALTHY	0.07	-1.13	0.97
PATIENT DXMALMETA1	TUMOR	-0.31	-0.81	1.00
PATIENT DXMALMETA2	TUMOR	-0.55	-0.55	1.16
HEALTHY NKI 1	HEALTHY	-0.19	-1.01	0.75
HEALTHY SERA1	HEALTHY	-0.16	-1.01	0.82
PATIENT METAEPA4	TUMOR	-0.44	-0.91	0.55

Table C.3: First data set, 3 sensors array data, scores (samples) data.

Loadings			
Variables	Type	Comp 1	Comp 2
ST25 650+Au	X	-0.56	0.72
SmFeO3	X	0.61	0.02
CdS2	X	-0.56	-0.70

Table C.4: First data set, 3 sensors array data, loadings (variables) data.

Array 1 Data					
SAMPLE	HEALTH STATUS	ST25 650+Au (X)	ZnO 850 (X)	SmFeO3 (X)	CdS2 (X)
HEALTHY G1	HEALTHY	-0.69	2.02	-0.17	1.59
HEALTHY NA	HEALTHY	-0.79	1.49	-0.05	1.64
PATIENT 46 1	TUMOR	0.52	3.58	-1.08	1.47

Array 1 Data					
SAMPLE	HEALTH STATUS	ST25 650+Au (X)	ZnO 850 (X)	SmFeO3 (X)	CdS2 (X)
PATIENT 47 1	TUMOR	0.99	1.55	-1.32	1.75
HEALTHY BN	HEALTHY	-0.90	1.23	-0.27	1.65
PATIENT 53 1	TUMOR	0.14	0.33	-1.30	1.49
HEALTHY CP 1	HEALTHY	-0.67	0.23	-0.89	1.47
HEALTHY AR 1	HEALTHY	-0.39	0.17	-1.11	1.50
PATIENT 54 A 1	TUMOR	0.00	1.23	-0.46	1.49
PATIENT 55 1	TUMOR	0.26	-0.36	-0.89	1.45
HEALTHY GO 1	HEALTHY	-0.69	-0.67	-0.02	1.43
PATIENT 59 1	TUMOR	-0.13	-0.62	-0.51	-0.67
HEALTHY RA 1	HEALTHY	-0.80	-0.57	0.17	-0.58
HEALTHY C1 1	HEALTHY	-0.77	-0.73	0.16	-0.64
HEALTHY F1 1	HEALTHY	-0.65	0.07	0.19	-0.63
PATIENT 62 1	TUMOR	-0.45	-0.73	-0.30	-0.63
HEALTHY NE 1	HEALTHY	-0.73	-0.86	0.26	-0.61
PATIENT 63 1	TUMOR	0.05	-0.78	0.47	-0.60
HEALTHY OP 1	HEALTHY	-0.81	-0.46	0.29	-0.62
PATIENT 66 1	TUMOR	-0.39	-0.57	0.23	-0.61
PATIENT 67 1	TUMOR	3.11	1.76	-6.50	1.64
PATIENT 68 1	TUMOR	0.61	-0.46	0.18	-0.61
HEALTHY ANT1 1	HEALTHY	-0.79	-0.57	0.31	-0.62
HEALTHY C1b 1	HEALTHY	-0.80	-0.78	0.50	-0.61
HEALTHY AND1 1	HEALTHY	-0.16	-0.62	-0.02	-0.62
HEALTHY IN 1	HEALTHY	-0.93	-0.88	0.43	-0.60
PATIENT 69A 1	TUMOR	0.38	-0.38	0.26	-0.61
PATIENT 72 1	TUMOR	-0.06	-0.60	0.49	-0.61
HEALTHY LA 1	HEALTHY	-0.40	-0.46	0.43	-0.61
HEALTHY FI 1	HEALTHY	-0.57	-0.38	0.25	-0.60
PATIENT 73 1	TUMOR	1.03	-0.34	-1.84	1.44
HEALTHY SAMA1 1	HEALTHY	-0.49	-0.78	0.17	-0.61
HEALTHY EDO1 1	HEALTHY	-0.08	-0.46	0.37	-0.61
HEALTHY LOR1 1	HEALTHY	-0.46	-0.30	0.28	-0.60
PATIENT 71A 1	TUMOR	0.73	-0.25	0.44	-0.59
PATIENT 74 1	TUMOR	0.37	-0.57	0.18	-0.61
HEALTHY RUG1 1	HEALTHY	-0.81	-0.62	0.34	-0.63
PATIENT 76A 1	TUMOR	0.26	-0.62	0.16	-0.65
HEALTHY CAT1 1	HEALTHY	-0.63	-0.88	0.44	-0.60
PATIENT 87 1	TUMOR	0.37	-0.67	0.67	-0.60
HEALTHY FLOR1 1	HEALTHY	-0.64	-0.88	0.42	-0.62
HEALTHY PAOL1 1	HEALTHY	-0.72	-0.78	0.42	-0.63
PATIENT 88 1	TUMOR	0.26	-0.67	0.51	-0.61

Array 1 Data					
SAMPLE	HEALTH STATUS	ST25 650+Au (X)	ZnO 850 (X)	SmFeO3 (X)	CdS2 (X)
PATIENT 89 1	TUMOR	0.75	-0.78	0.95	-0.85
HEALTHY ENRI1 1	HEALTHY	-0.70	-0.46	0.92	-0.82
PATIENT 92 1	TUMOR	0.76	-0.46	0.92	-0.84
HEALTHY ANS1	HEALTHY	-0.68	-0.89	0.95	-0.67
PATIENT MB11	TUMOR	-0.34	-0.31	0.46	-0.61
PATIENT MB24	TUMOR	-0.23	-0.66	0.41	-0.63
PATIENT noF1A	TUMOR	-0.39	-0.89	0.51	-0.61
HEALTHY GIUCHI1	HEALTHY	-0.35	-0.42	0.55	-0.64
PATIENT ME1	TUMOR	-0.59	0.39	0.23	-0.63
PATIENT STO1	TUMOR	0.12	0.28	0.26	-0.64
PATIENT X	TUMOR	1.01	0.35	0.46	-0.65
HEALTHY C1c 1	HEALTHY	-0.48	-0.11	0.52	-0.66
HEALTHY GIAN1	HEALTHY	-0.31	0.04	0.58	-0.65
PATIENT 105	TUMOR	0.91	0.35	0.33	-0.64
PATIENT MX1	TUMOR	-0.33	0.04	0.44	-0.63
PATIENT VINCEN1	TUMOR	-0.35	-0.07	0.55	-0.63
PATIENT METAEPA2	TUMOR	2.08	0.51	-0.58	1.45
HEALTHY ROC1	HEALTHY	-0.39	0.51	-0.61	1.41
HEALTHY LU1	HEALTHY	-0.25	1.79	0.17	1.58
PATIENT METAEPA2 3DAYS	TUMOR	-0.53	1.09	0.08	1.61
PATIENT METAYOUNG1 SHORT	TUMOR	3.96	2.21	-0.15	1.58
PATIENT METAYOUNG1 LONG	TUMOR	3.66	3.15	-0.24	1.65

Basic Statistical Information					
	Maximum	6.77	1.24	-1.04	1.35
	Max Sample	PATIENT METAYOUNG1 SHORT	PATIENT 46 1	HEALTHY ANS1	PATIENT 47 1
	Minimum	1.21	1.01	-3.82	-1.27
	Min Sample	HEALTHY IN 1	PATIENT noF1A	PATIENT 67 1	PATIENT 89 1
	Average	2.27	1.05	-1.40	-0.42
	Standard Deviaton	1.14	0.05	0.37	1.01
	CV	0.50	0.05	-0.27	-2.43

Table C.5: First data set, first sensors array normalized data and basic statistical information.

	Analytical Report Array 1 Data		
	Comp 1	Comp 2	Comp 3
R2	64%	17%	14%
R2(cum)	64%	81%	95%
Eigenvalue	41.62	10.96	9.40
Q2	64%	47%	76%
Q2(cum)	64%	81%	95%

Table C.6: First data set, first sensors array data, analytical report.

Scores					
Samples	Groups	Comp 1	Comp 2	Comp 3	DmodX
HEALTHY G1	HEALTHY	-1.72	-1.75	-0.98	0.95
HEALTHY NA	HEALTHY	-1.36	-1.75	-0.78	0.08
PATIENT 46 1	TUMOR	-3.45	-0.95	-1.25	3.31
PATIENT 47 1	TUMOR	-2.84	-0.32	-0.03	0.18
HEALTHY BN	HEALTHY	-1.29	-1.80	-0.44	0.10
PATIENT 53 1	TUMOR	-1.66	-0.69	0.76	1.04
HEALTHY CP 1	HEALTHY	-1.05	-1.35	0.60	0.96
HEALTHY AR 1	HEALTHY	-1.27	-1.12	0.76	1.10
PATIENT 54 A 1	TUMOR	-1.68	-0.97	-0.40	0.25
PATIENT 55 1	TUMOR	-1.13	-0.44	0.78	2.32
HEALTHY GO 1	HEALTHY	-0.12	-1.17	0.38	2.81
PATIENT 59 1	TUMOR	0.50	0.33	0.83	0.61
HEALTHY RA 1	HEALTHY	1.05	-0.29	0.33	0.46
HEALTHY C1 1	HEALTHY	1.15	-0.20	0.43	0.31
HEALTHY F1 1	HEALTHY	0.69	-0.25	-0.05	1.35
PATIENT 62 1	TUMOR	0.78	0.06	0.76	0.44
HEALTHY NE 1	HEALTHY	1.24	-0.15	0.41	0.03
PATIENT 63 1	TUMOR	0.94	0.49	0.08	0.54
HEALTHY OP 1	HEALTHY	1.08	-0.30	0.17	0.58
PATIENT 66 1	TUMOR	0.91	0.08	0.22	0.21
PATIENT 67 1	TUMOR	-6.31	1.41	3.82	2.69
PATIENT 68 1	TUMOR	0.40	0.91	0.06	0.19
HEALTHY ANT1 1	HEALTHY	1.13	-0.26	0.22	0.41
HEALTHY C1b 1	HEALTHY	1.33	-0.23	0.18	0.04
HEALTHY AND1 1	HEALTHY	0.73	0.28	0.43	0.20
HEALTHY IN 1	HEALTHY	1.41	-0.33	0.31	0.08
PATIENT 69A 1	TUMOR	0.49	0.70	-0.01	0.00
PATIENT 72 1	TUMOR	0.91	0.37	-0.02	0.21
HEALTHY LA 1	HEALTHY	0.96	0.05	0.00	0.23
HEALTHY FI 1	HEALTHY	0.89	-0.12	0.13	0.57
PATIENT 73 1	TUMOR	-1.93	0.20	1.44	2.09
HEALTHY SAMA1 1	HEALTHY	1.04	0.03	0.40	0.01
HEALTHY EDO1 1	HEALTHY	0.78	0.32	0.01	0.08

Scores					
Samples	Groups	Comp 1	Comp 2	Comp 3	DmodX
HEALTHY LOR1 1	HEALTHY	0.82	-0.03	0.04	0.59
PATIENT 71A 1	TUMOR	0.35	0.97	-0.29	0.18
PATIENT 74 1	TUMOR	0.56	0.72	0.15	0.21
HEALTHY RUG1 1	HEALTHY	1.19	-0.26	0.22	0.35
PATIENT 76A 1	TUMOR	0.64	0.66	0.21	0.15
HEALTHY CAT1 1	HEALTHY	1.29	-0.08	0.25	0.27
PATIENT 87 1	TUMOR	0.85	0.74	-0.19	0.72
HEALTHY FLOR1 1	HEALTHY	1.29	-0.07	0.27	0.21
HEALTHY PAOL1 1	HEALTHY	1.27	-0.16	0.23	0.00
PATIENT 88 1	TUMOR	0.82	0.65	-0.05	0.53
PATIENT 89 1	TUMOR	1.01	1.21	-0.40	0.91
HEALTHY ENRI1 1	HEALTHY	1.44	-0.09	-0.34	0.40
PATIENT 92 1	TUMOR	0.81	1.16	-0.55	0.44
HEALTHY ANS1	HEALTHY	1.59	-0.07	-0.15	0.49
PATIENT MB11	TUMOR	0.87	0.07	-0.12	0.40
PATIENT MB24	TUMOR	0.99	0.25	0.10	0.10
PATIENT noF1A	TUMOR	1.22	0.14	0.17	0.44
HEALTHY GIUCHI1	HEALTHY	0.99	0.10	-0.13	0.22
PATIENT ME1	TUMOR	0.50	-0.26	-0.27	1.76
PATIENT STO1	TUMOR	0.27	0.37	-0.33	1.16
PATIENT X	TUMOR	-0.05	1.12	-0.67	0.62
HEALTHY C1c 1	HEALTHY	0.88	-0.05	-0.25	0.80
HEALTHY GIAN1	HEALTHY	0.74	0.06	-0.41	0.86
PATIENT 105	TUMOR	-0.09	1.03	-0.54	0.74
PATIENT MX1	TUMOR	0.67	0.03	-0.29	0.95
PATIENT VINCEN1	TUMOR	0.80	0.03	-0.32	0.71
PATIENT METAEPA2	TUMOR	-2.24	0.95	-0.21	2.39
HEALTHY ROC1	HEALTHY	-1.15	-1.13	0.17	0.83
HEALTHY LU1	HEALTHY	-1.62	-1.31	-1.20	0.11
PATIENT METAEPA2 3DAYS	TUMOR	-1.18	-1.44	-0.71	0.71
PATIENT METAYOUNG1 SHORT	TUMOR	-3.84	2.18	-1.77	1.56
PATIENT METAYOUNG1 LONG	TUMOR	-4.29	1.73	-2.17	0.07

Table C.7: First data set, 3 sensors array data, scores (samples) data.

Loadings				
Variables	Type	Comp 1	Comp 2	Comp 3
ST25 650+Au	X	-0.44	0.85	-0.14
ZnO 850	X	-0.54	-0.18	-0.54
SmFeO3	X	0.48	0.02	-0.82
CdS2	X	-0.54	-0.49	-0.07

Table C.8: First data set, first sensors array, loadings (variables) data.

Array 2 Data					
SAMPLE	HEALTH STATUS	ST25 650+Au (X)	SmFeO3 (X)	CdS2 (X)	SnO2 (X)
HEALTHY STUDXVIC	HEALTHY	-0.43	0.11	1.66	-0.41
PATIENT METAEPAENDO1	TUMOR	1.38	0.11	1.24	1.24
PATIENT METAENDO1	TUMOR	2.74	-1.70	2.07	2.88
HEALTHY GIULIO1	HEALTHY	-0.70	1.52	-0.56	-0.58
HEALTHY ANNACAMP1	HEALTHY	-0.57	1.10	-0.20	-0.46
PATIENT METASTOMA1	TUMOR	1.44	-0.10	1.14	1.51
PATIENT SPLESX1	TUMOR	-0.63	0.32	0.01	-0.50
HEALTHY IRENE1	HEALTHY	-0.44	0.56	-0.45	-0.44
PATIENT METAEPA3	TUMOR	-0.89	-1.21	0.01	-0.74
PATIENT METALINFO1	TUMOR	0.20	-1.21	0.21	-0.04
HEALTHY BEA1	HEALTHY	-0.65	1.52	-0.72	-0.59
PATIENT DXMALMETA1	TUMOR	-0.22	0.37	-0.87	-0.29
PATIENT DXMALMETA2	TUMOR	0.13	0.11	-0.61	-0.07
HEALTHY NKI 1	HEALTHY	-0.49	-0.10	-1.03	-0.51
HEALTHY SERA1	HEALTHY	-0.49	0.22	-0.87	-0.53
PATIENT METAEPA4	TUMOR	-0.35	-1.63	-1.03	-0.47
Basic Statistical Information	Maximum	5.73	-1.17	1.15	6.91
	Max Sample	PATIENT METAENDO1	HEALTHY BEA1	PATIENT METAENDO1	PATIENT METAENDO1
	Minimum	1.4	-1.36	1.03	1.41
	Min Sample	PATIENT METAEPA3	PATIENT METAENDO1	PATIENT METAEPA4	PATIENT METAEPA3
	Average	2.46	-1.26	1.07	2.54
	Standard Deviaton	1.19	0.06	0.04	1.52
	CV	0.49	-0.05	0.04	0.60

Table C.9: First data set, second sensors array normalized data and basic statistical information.

	Analytical Report Array 2		
	Comp 1	Comp 2	Comp 3
R2	72%	19%	8%
R2(cum)	72%	92%	100%
Eigenvalue	11,58	3,07	1,32
Q2	72%	69%	98%
Q2(cum)	72%	92%	100%

Table C.10: First data set, second sensors array, analytical report.

Score					
Samples	Groups	Comp 1	Comp 2	Comp 3	DmodX
HEALTHY STUDXVIC	HEALTHY	-0,31	-0,42	-1,68	0,84
PATIENT METAEPAENDO1	TUMOR	-2,06	-0,85	0,02	1,70
PATIENT METAENDO1	TUMOR	-4,78	0,14	0,33	1,50
HEALTHY GIULIO1	HEALTHY	1,51	-1,07	0,11	0,77
HEALTHY ANNACAMP1	HEALTHY	1,05	-0,82	-0,13	0,67
PATIENT METASTOMA1	TUMOR	-2,26	-0,68	0,21	0,42
PATIENT SPLESX1	TUMOR	0,75	-0,12	-0,42	0,93
HEALTHY IRENE1	HEALTHY	0,91	-0,26	0,08	0,07
PATIENT METAEPA3	TUMOR	0,51	1,39	-0,78	1,49
PATIENT METALINFO1	TUMOR	-0,60	1,06	-0,23	1,85
HEALTHY BEA1	HEALTHY	1,57	-1,03	0,26	0,26
PATIENT DXMALMETA1	TUMOR	0,85	-0,03	0,56	0,32
PATIENT DXMALMETA2	TUMOR	0,31	0,05	0,55	1,46
HEALTHY NKI 1	HEALTHY	1,05	0,53	0,44	0,33
HEALTHY SERA1	HEALTHY	1,08	0,19	0,34	0,03
PATIENT METAEPA4	TUMOR	0,43	1,94	0,35	0,10

Table C.11: First data set, 3 sensors array data, scores (samples) data.

Loading				
Variables	Type	Comp 1	Comp 2	Comp 3
ST25 650+Au	X	-0,56	-0,13	0,42
SmFeO3	X	0,33	-0,94	0,10
CdS2	X	-0,50	-0,27	-0,82
SnO2	X	-0,57	-0,18	0,37

Table C.12: First data set, first sensors array, loadings (variables) data.

Second Data Set					
SAMPLE	#of Missing	Min	Max	Mean	SDev
1	0	1.10	1.23	1.15	$6.81 \cdot 10^{-4}$
2	0	1.09	1.23	1.15	$7.21 \cdot 10^{-2}$
3	0	1.10	1.29	1.20	$9.50 \cdot 10^{-2}$
4	0	1.07	1.65	1.31	0.30
5	0	1.13	1.36	1.24	0.12
6	0	1.16	1.39	1.26	0.12
7	0	1.13	1.52	1.32	0.20
8	0	1.17	1.83	1.44	0.35
9	0	1.15	2.05	1.55	0.46
10	0	1.17	1.60	1.41	0.22
11	0	1.25	2.38	1.75	0.58
12	0	1.22	1.86	1.57	0.32
13	0	1.19	1.90	1.58	0.36
14	0	1.37	1.87	1.66	0.26
15	0	1.29	2.27	1.84	0.50

Table C.13: Second data set, second sensors array data, normalized.

	Second Data Set		
	ST25 650 +1%Au	STN	TiTaV
#of Missing	0	0	0
Min	1.13	1.23	1.07
Max	1.96	2.38	1.37
Mean	1.42	1.70	1.17
SDev	0.25	0.37	$8.17 \cdot 10^{-2}$
Skewness	0.58	0.32	0.89

Table C.14: First data set, second sensors array, analytical report.

Bibliography

[1]. C. Kittel, Introduction to Solid State Physics, Wiley, 7th edition, 1996, pp. 232.

[2]. C. Kittel, Introduction to Solid State Physics, Wiley, 7th edition, 1996, pp. 164.

[3]. J.P. Colinge, C.A. Colinge, Physics of Semiconductor Devices, Kluwer Academic Publishers, 2000, pp. 15.

[4]. C. Kittel, Introduction to Solid State Physics, Wiley, 7th edition, 1996, pp. 181.

[5]. C. Kittel, Introduction to Solid State Physics, Wiley, 7th edition, 1996, pp. 187.

[6]. J.P. Colinge, C.A. Colinge, Physics of Semiconductor Devices, Kluwer Academic Publishers, 2000, pp. 17.

[7]. J.P. Colinge, C.A. Colinge, Physics of Semiconductor Devices, Kluwer Academic Publishers, 2000, pp. 18–20.

[8]. J.P. Colinge, C.A. Colinge, Physics of Semiconductor Devices, Kluwer Academic Publishers, 2000, pp. 20–21.

[9]. J.P. Colinge, C.A. Colinge, Physics of Semiconductor Devices, Kluwer Academic Publishers, 2000, pp. 21–25.

[10]. J.P. Colinge, C.A. Colinge, Physics of Semiconductor Devices, Kluwer Academic Publishers, 2000, pp. 25–29.

[11]. J.P. Colinge, C.A. Colinge, Physics of Semiconductor Devices, Kluwer Academic Publishers, 2000, pp. 29–30.

[12]. J.P. Colinge, C.A. Colinge, Physics of Semiconductor Devices, Kluwer Academic Publishers, 2000, pp. 31–40.

[13]. J.P. Colinge, C.A. Colinge, Physics of Semiconductor Devices, Kluwer Academic Publishers, 2000, pp. 40–42.

[14]. J.P. Colinge, C.A. Colinge, Physics of Semiconductor Devices, Kluwer Academic Publishers, 2000, pp. 51–54.

[15]. J.P. Colinge, C.A. Colinge, Physics of Semiconductor Devices, Kluwer Academic Publishers, 2000, pp. 59–61.

[16]. J.P. Colinge, C.A. Colinge, Physics of Semiconductor Devices, Kluwer Academic Publishers, 2000, pp. 65–67.

[17]. J.P. Colinge, C.A. Colinge, Physics of Semiconductor Devices, Kluwer Academic Publishers, 2000, pp. 95–106.

[18]. J.P. Colinge, C.A. Colinge, Physics of Semiconductor Devices, Kluwer Academic Publishers, 2000, pp. 139–142.

[19]. J.P. Colinge, C.A. Colinge, Physics of Semiconductor Devices, Kluwer Academic Publishers, 2000, pp. 145–146.

[20]. D. Puzzovio, Surface Interaction Mechanisms In Metal-Oxide Semiconductors For Alkane Detection, PhD thesis, 2006/2008, pp. 10–14.

[21]. D. Puzzovio, Surface Interaction Mechanisms In Metal-Oxide Semiconductors For Alkane Detection, PhD thesis, 2006/2008, pp. 15–21.

[22]. N. Zettili, Quantum Mechanics Concepts and Applications, Jacksonville State University USA, Wiley, 2009, pp. 528.

[23]. J.P. Colinge, C.A. Colinge, Physics of Semiconductor Devices, Kluwer Academic Publishers, 2000, chapter 10.

[24]. M. Shur, Physics of Semiconductor Devices, Prentice-Hall, 1990, pp. 194–200.

[25]. D. Puzzovio, Surface Interaction Mechanisms In Metal-Oxide Semiconductors For Alkane Detection, PhD thesis, 2006/2008, pp. 39–48.

[26]. D. Puzzovio, Surface Interaction Mechanisms In Metal-Oxide Semiconductors For Alkane Detection, PhD thesis 2006/2008, pp. 21–25.

[27]. A. Ponzoni, E. Comini, I. Concina, M. Ferroni, M. Falasconi, E. Gobbi, V. Sberveglieri, G. Sberveglieri, Nanostructured Metal Oxide Gas Sensors, a Survey of Applications Carried out at SENSOR Lab, Brescia (Italy) in the Security and Food Quality Fields; 2012, pp. 25–27.

[28]. C.M. Aldao, D.A. Mirabella, M.A. Ponce, A. Giberti, C. Malagù, Role of intragrain oxygen diffusion in polycrystalline tin oxide conductivity, J. Appl. Phys. 109(6) (2011) pp. 063723.

[29]. C.M. Aldao, C. Malagù, Non-parabolic intergranular barriers in tin oxide and gas sensing, J. Appl. Phys. 112 (2012) pp. 024518–024521.

[30]. P. Romppainen, V. Lantto, J. Appl. Phys. 63 (1988) pp. 5159.

[31]. J. Maier, W. Gopel, J. Sol. Stat. Chem. 72 (1998) pp. 293.

[32]. N. Barsan, M. Hübner, U. Weimar, Sens. Actuators B: Chem. 157 (2011) pp. 510.

[33]. C. Malagù, M. Benetti, M.C. Carotta, A. Giberti, V. Guidi, L. Milano, G. Martinelli, Investigation of the humidity effects on SNO2-based sensors in CO detection, Mater. Res. Soc. Symp. Proc. 915 (2006).

[34]. N. Landini, G. Zonta, C. Malagù, Detection of tumor markers on feces with nanostructured sensors. Scholar's Press., 2015.

[35]. C. Malagù, N. Landini, Simulation of Intestinal Gaseous Environment in Order to Verify the Capability of Nanostructured Chemoresistive Sensors to Detect Colorectal Tumor Markers (Benzene, 1-Iodo-Nonane, Decanal), J. Mol. Biomark. Diagn. S:2 (2015). http://dx.doi.org/10.4172/2155-9929.S2–012.

[36]. M. Sacerdoti, M.C. Dalconi, M.C. Carotta, B. Cavicchi, M. Ferroni, S. Colonna, M.L. Di Vona, XAS investigation of tantalum and niobium in nanostructured TiO_2anatase, J. Solid State Chem. 177 (2004) pp. 1781–1788.

[37]. M.C. Carotta, M. Ferroni, S. Gherardi, V. Guidi, C. Malagù, G. Martinelli, M. Sacerdoti, M.L. Di Vona, S. Licoccia, E. Traversa, Thick-film gas sensors based on vanadium titanium oxide powders prepared by sol-gel synthesis, J. Eur. Ceram. Soc. 24 (2004) pp. 1409–1413.

[38]. M.C. Carotta, V. Guidi, C. Malagù, B. Vendemiati, A. Zanni, G. Martinelli, M. Sacerdoti, S. Licoccia, M.L. Di Vona E. Traversa, Vanadium and tantalum-doped titanium oxide (TiTaV): a novel material for gas sensing, Sens. Actuators B: Chem. 108 (2005) pp. 89–96.

[39]. T. Seiyama, A. Kato, K. Fulishi, M. Nagatani, A new detector for gaseous components using semiconductive thin films, Anal. Chem. 34 (1962) pp. 1502–1503.

[40]. L. Schmidt-Mende, J.L. MacManus-Driscoll, ZnO-nanostructures, defects, and devices, Matter Today 10 (5) (2007) pp. 40–48.

[41]. Z.L. Wang, Zinc oxide nanostructures: growth, properties and applications, J. Phys.: Condens. Matter 16 (2004) pp. 829–858.

[42]. M.C. Carotta, S. Gherardi, V. Guidi, C. Malagù, G. Martinelli, B. Vendemiati, M. Sacerdoti, G. Ghiotti, S. Morandi, A. Bismuto, P. Maddalena, A. Setaro, (Ti, Sn)O2 binary solid solutions for gas sensing: Spectroscopic, optical and transport properties, Sens. Actuators B: Chem. 130(1) (2008) pp. 38–45.

[43]. W. Erbs, J. Desilvestro, E. Borgarello, M. Gratzel, Visible-light-induced O2 generation from aqueous dispersions of WO, J. Phys. Chem. 88 (1984) pp. 4001–4006.

[44]. A. Chiorino, F. Prinetto, M.C. Carotta, C. Malagù, Preparation and characterization of SnO2 and WOx-SnO2 nano-sized powders and thick-films for gas sensing, Sens. Actuators B: Chem. 78 (2001) pp. 89–97.

[45]. A. Gaiardo, B. Fabbri, V. Guidi, P. Bellutti, A. Giberti, S. Gherardi, L. Vanzetti, C. Malagù, G. Zonta, Metal Sulfides as Sensing Materials for Chemoresistive Gas Sensors, Sens. 16(3) (2016) pp. 296.

[46]. M.C. Carotta, G. Martinelli, Y. Sadaoka, P. Nunziante, E. Traversa, Gas-sensitive electrical properties of perovskite-type SmFeO3 thick-films, Sens. Actuators B: Chem. 48(1–3) (1998) pp. 270–276.

[47]. N. Landini, G. Anania, B. Fabbri, A. Gaiardo, Sandro Gherardi, V. Guidi, G. Rispoli, L. Scagliarini, G. Zonta, C. Malagù, Neoplasms and metastasis detection in human blood exhalations with a device composed by nanostructured sensors, Sens. Actuators B: Chem. 271 (2018) pp. 203–214. https://doi.org/10.1016/j.snb.2018.05.102.

[48]. E.J. Taylor, Dorland's Illustrated medical dictionary, Saunders, 29th edition, Philadelphia, 2000, pp. 1184.

[49]. Stedman's medical dictionary, Lippincott Williams & Wilkins, 28th edition, Philadelphia, 2006, pp. Neoplasm.

[50]. G. Abrams, Neoplasia I, 2012.

[51]. D. Ambrosi, F. Mollica, On the mechanics of a growing tumor, Int. J. Eng. Sci. 40(12) (2002) pp. 1297–1316.

[52]. K.Y. Volokh, Stresses in growing soft tissues, Acta Biomater. 2(5) (2006) pp. 493–504.

[53]. C. Bernstein, A.R. Prasad, V. Nfonsam, H. Bernstei, DNA Damage, DNA Repair and Cancer, New Research Directions in DNA Repair, IntechOpen, edited by Clark Chen, 2013, pp.413–465.

[54]. C. Bernstein, DNA Damage and Cancer, SciTopics, 2009.

[55]. F.H. Cunningham, S. Fiebelkorn, M. Johnson, C. Meredith, A novel application of the Margin of Exposure approach: segregation of tobacco smoke toxicants, Food Chem. Toxicol. 49(11) (2011) pp. 2921–2933.

[56]. H.E. Kanavy, M.R. Gerstenblith, Ultraviolet radiation and melanoma, Semin. Cutan. Med. Surg. 30 (4) (2011) pp. 222–228.

[57]. O. Handa, Y. Naito, T. Yoshikawa, Redox biology and gastric carcinogenesis: the role of Helicobacter pylori, Redox Rep., 16(1) (2011) pp. 1–7.

[58]. C. Bernstein, H. Holubec, A.K. Bhattacharyya, H. Nguyen, C.M. Payne, B. Zaitlin, H. Bernstein, Carcinogenicity of deoxycholate, a secondary bile acid, Arch. Toxicol. 85(8) (2011) pp. 863–871.

[59]. M. Katsurano, T. Niwa, Y. Yasui, Y. Shigematsu, S. Yamashita, H. Takeshima, M.S. Lee, Y.J. Kim, T. Tanaka, T. Ushijima, Early-stage formation of an epigenetic field defect in a mouse colitis model, and non-essential roles of T- and B-cells in DNA methylation induction, Oncog. 31(3) (2011) pp. 342–351.

[60]. C. Bernstein, H. Bernstein, C.M. Payne, K. Dvorak, H. Garewal, Field defects in progression to gastrointestinal tract cancers, Cancer Lett. 260(1–2) (2008) pp. 1–10.

[61]. H. Nguyen, C. Loustaunau, A. Facista, L. Ramsey, N. Hassounah, H. Taylor, R. Krouse, C.M. Payne, V.L. Tsikitis, S. Goldschmid, B. Banerjee, R.F. Perini, C. Bernstein, Deficient Pms2, ERCC1, Ku86, CcOI in field defects during progression to colon cancer, J. Vis. Exp. 41 (2010) pp. 1931.

[62]. M.W. Schmitt, M.J. Prindle, L.A. Loeb, Implications of genetic heterogeneity in cancer, Ann. N. Y. Acad. Sci. 1267 (2012) pp. 110–116.

[63]. International Human Genome Sequencing Consortium (E.S. Lander, L.M. Linton, B. Birren, C. Nusbaum, M.C. Zody, J. Baldwin, K. Devon, K. Dewar, M. Doyle, W. FitzHugh, et al.), Initial sequencing and analysis of the human genome, Nat. 409(6822) (2001) pp. 860–921.

[64]. B. Vogelstein, N. Papadopoulos, V.E. Velculescu, S. Zhou, L.A. Diaz, K.W. Kinzler, Cancer genome landscapes, Sci. 339(6127) (2013) pp. 1546–1558.

[65]. A. Facista, H. Nguyen, C. Lewis, A.R. Prasad, L. Ramsey, B. Zaitlin, V. Nfonsam, R.S. Krouse, H. Bernstein, C.M. Payne, S. Stern, N. Oatman, B. Banerjee, C. Bernstein, Deficient expression of DNA repair enzymes in early progression to sporadic colon cancer, Genome Integr 3(1) (2012) pp. 3.

[66]. L. Narayanan, J.A. Fritzell, S.M. Baker, R.M. Liskay, P.M. Glazer, Elevated levels of mutation in multiple tissues of mice deficient in the DNA mismatch repair gene Pms2, Proc. Natl. Acad. Sci. U.S.A. 94(7) (1997) pp. 3122–3127.

[67]. D.C. Hegan, L. Narayanan, F.R. Jirik, W. Edelmann, R.M. Liskay, P.M. Glazer, Differing patterns of genetic instability in mice deficient in the mismatch repair genes Pms2, Mlh1, Msh2, Msh3 and Msh6, Carcinog. 27(12) (2006) pp. 2402–2408.

[68]. A.N. Butt, C.T. van Oostrom, G.M. Ross, H. van Steeg, A. Ashworth, Disruption of Brca2 increases the spontaneous mutation rate in vivo: synergism with ionizing radiation, EMBO Rep. 3(3) (2002) pp. 255–260.

[69]. K.A. Wilson, A. Waugh, G. Chambers, A. Grant, J. Ross, Ross and Wilson anatomy and physiology in health and illness, Churchill Livingstone, Edinburgh, 2006, pp. 53–54.

[70]. N.L. Silverstein, A. Silverstein, V.B. Silverstein, Cancer, Brookfield, Conn: Twenty-First Century Books, 2006, pp. 11–12.

[71]. D.L. Strayer; R. Rubin; E. Rubin, Rubin's pathology: clinicopathologic foundations of medicine, Wolters Kluwer/Lippincott Williams & Wilkins, Philadelphia, 2008, pp. 138–139.

[72]. W.B. Ober, F. Martini, Fundamentals of anatomy & physiology. San Francisco: Pearson Benjamin Cummings, San Francisco, 2006.

[73]. W.H. Clark, Tumour progression and the nature of cancer, Br. J. Cancer 64(4) (1991) pp. 631–644.

[74]. J. Reece, N. Campbell, L. Urry, Biology, Pearson Benjamin Cummings, San Francisco, 2005, pp. 232.

[75]. A. Chang, Oncology: An Evidence-Based Approach, Springer, 2007, pp.162.

[76]. J.A. Ridge, B.S. Glisson, M.N. Lango, T. Galloway, Head and Neck Tumors, Cancer Management: A Multidisciplinary Approach, 11th edition, 2008.

[77]. G.P. Gupta, J. Massagué, Cancer metastasis: building a framework, Cell 127(4) (2006) pp. 679–695.

[78]. E. Racila, D. Euhus, A.J. Weiss, C. Rao, J. McConnell, L.W. Terstappen, J.W. Uhr, Detection and characterization of carcinoma cells in the blood, Proc. Natl. Acad. Sci. 95(8) (1998) pp. 4589–4594.

[79]. D. Marrinucci, K. Bethel, A. Kolatkar, M. Luttgen, M. Malchiodi, F. Baehring, K. Voigt, D. Lazar, J. Nieva, L. Bazhenova, A. Ko, W.M. Korn, E. Schram, M. Coward, X. Yang, T. Metzner, R. Lamy, M. Honnatti, C. Yoshioka, J. Kunken, Y.

Petrova, D. Sok, D. Nelson, P. Kuhn, Fluid Biopsy in Patients with Metastatic Prostate, Pancreatic and Breast Cancers, Phys. Biol. 9(1) (2012) pp. 016003.

[80]. N. Aceto, A. Bardia, D. Miyamoto, M. Donaldson, B. Wittner, J. Spencer, M. Yu, A. Pely, A. Engstrom, H. Zhu, B. Brannigan, R. Kapur, S. Stott, T. Shioda, S. Ramaswamy, D. Ting, C. Lin, M. Toner, D. Haber, S. Maheswaran, Circulating Tumor Cell Clusters Are Oligoclonal Precursors of Breast Cancer Metastasis, Cell. 158(5) (2014) pp. 1110.

[81]. G. Wilkes, K. Hartshorn, Colon, Rectal, and Anal Cancers, Semin. Oncol. Nurs., Nat. Rev. Clin. Oncol. 25(1) (2009) pp 32–47.

[82]. http://www.emedicinehealth.com.

[83]. R. Hompes, C. Cunningham, Colorectal cancer: management (2011).

[84]. J.W. Berlin, R.M. Gore, V. Yaghmai, G.M. Newmark, F.H. Miller, Staging of colorectal cancer, Semin. Roentgenol. 35(4) (2000) pp. 370–384.

[85]. World Cancer Report 2014, World Health Organization, 2014, Chapter 1.1. ISBN 978-9283204299.

[86]. D.M. Parkin, F. Bray, J. Ferlay, P. Pisani, Global Cancer Statistics, 2002, CA: Cancer J. Clin. 55(2) (2005) pp. 74–108. doi:10.3322/canjclin.55.2.74.

[87]. Are the number of cancer cases increasing or decreasing in the world?, WHO Online Q&A. WHO, 2008.

[88]. World Cancer Report 2014. International Agency for Research on Cancer, World Health Organization. 2014. ISBN 978-92-832-0432-9.

[89]. R. Lozano, M. Naghavi, K. Foreman, S. Lim, K. Shibuya, V. Aboyans, J. Abraham, T. Adair, R. Aggarwal, S.Y. Ahn, M. Alvarado, H.R: Anderson, L.M. Anderson, K.G. Andrews, C. Atkinson, L.M. Baddour, S. Barker-Collo, D.H. Bartels, M.L. Bell, E.J. Benjamin, D. Bennett, K. Bhalla, B. Bikbov, A. Bin Abdulhak, G. Birbeck, F. Blyth, I. Bolliger, S. Boufous, C. Bucello, et al. Global and regional mortality from 235 causes of death for 20 age groups in 1990 and 2010: a systematic analysis for the Global Burden of Disease Study 2010, Lancet 380(9859) (2012) pp. 2095–2128. doi:10.1016/S0140-6736(12)61728-0.

[90]. Global battle against cancer won't be won with treatment alone: Effective prevention measures urgently needed to prevent cancer crisis, WHO, Press Release 224, 2014.

[91]. Gastric Cancer in Young Adults, Rev. Bras. Cancerol. 46(3) (2000).

[92]. Health profile: United States, Le Duc Media, 2016.

[93]. Health profile: China, Le Duc Media, 2016.

[94]. Stomach cancer statistics, Cancer Res. UK, 2014.

[95]. Statistics and outlook for stomach cancer, Cancer Res. UK, 2014.

[96]. Guidance on Commissioning Cancer Services Improving Outcomes in Upper Gastro-intestinal Cancers, NHS, 2001.

[97]. R. Wadhwa, T. Taketa, K. Sudo, M.A. Blum, J.A. Ajani, Modern Oncological Approaches to Gastric Adenocarcinoma, Gastroenterol. Clin. N. Am. 42(2) (2013) pp. 359–369. doi:10.1016/j.gtc.2013.01.011. PMID 23639645.

[98]. K. Chen, X.W. Xu, R.C. Zhang, Y. Pan, D. Wu, Y.P. Mou, Systematic review and meta-analysis of laparoscopy-assisted and open total gastrectomy for gastric cancer, World J. Gastroenterol. 19(32) (2013) pp. 5365–5376. doi:10.3748/wjg.v19.i32.5365. PMC 3752573. PMID 23983442.

[99]. A.D. Wagner, N.L.X. Syn, M. Moehler, W. Grothe, W.P. Yong, B.C. Tai, J. Ho, S. Unverzagt, Cochrane Database of Systematic Reviews, Cochrane Database Syst. Rev. 8 (2017). doi:10.1002/14651858.cd004064.pub4. PMID 28850174.

[100]. J.L. Pretz, J.Y. Wo, H.J. Mamon, L.A. Kachnic, T.S. Hong, Chemoradiation Therapy: Localized Esophageal, Gastric, and Pancreatic Cancer, Surg. Oncol. Clin. N. Am. 22(3) (2011) pp. 511–524. doi:10.1016/j.soc.2013.02.005. PMID 23622077.

[101]. J. Meza-Junco, H.-J. Au, M.B. Sawyer, Critical appraisal of trastuzumab in treatment of advanced stomach cancer, Cancer Manag. Res. 3 (2011) pp. 57–64. doi:10.2147/CMAR.S12698. PMC 3085240. PMID 21556317.

[102]. M. Orditura, G. Galizia, V. Sforza, V. Gambardella, A. Fabozzi, M.M. Laterza, F. Andreozzi, J. Ventriglia, B. Savastano, A. Mabilia, E. Lieto, F. Ciardiello, F. De Vita, Treatment of gastric cancer, World J. Gastroentero. 20(7) (2014) pp. 1635–1649. doi:10.3748/wjg.v20.i7.1635. PMC 3930964. PMID 24587643.

[103]. L.M. Best, M. Mughal, K.S. Gurusamy, Laparoscopic versus open gastrectomy for gastric cancer, Cochrane Database Syst. Rev. 3 (2016).

[104]. N.L. Syn, I. Wee, A. Shabbir, G. Kim, J.B.Y. So, Pouch Versus No Pouch Following Total gastrectomy, Ann. Surg. (2018). doi:10.1097/sla.0000000000003082. ISSN 0003–4932.

[105]. J. Sun, Y. Song, Z. Wang, X. Chen, P. Gao, Y. Xu, B. Zhou, H. Xu, Clinical significance of palliative gastrectomy on the survival of patients with incurable

advanced gastric cancer: a systematic review and meta-analysis, BMC Cancer 13(1) (2013) pp. 577. doi:10.1186/1471-2407-13-577.

[106]. M. Scartozzi, E. Galizia, L. Verdecchia, R. Berardi, S. Antognoli, S. Chiorrini, S. Cascinu, Chemotherapy for advanced gastric cancer: across the years for a standard of care, Expert Opin. Pharmaco. 8(6) (2007) pp. 797–808. doi:10.1517/14656566.8.6.797.

[107]. N. Fusco, E.G. Rocco, C. Del Conte, C. Pellegrini, G. Bulfamante, F. Di Nuovo, S. Romagnoli, S. Bosari, HER2 in gastric cancer: a digital image analysis in pre-neoplastic, primary and metastatic lesions, Mod. Pathol. 26(6) (2013) pp. 816–824.

[108]. R.A. Cairns, I.S. Harris, T.W. Mak, Regulation of cancer cell metabolism, Nat. Rev. Cancer. 11 (2011) pp. 85–95.

[109]. Y. Qiu, G. Cai, M. Su, T. Chen, X. Zheng, Y. Xu, Y. Ni, A. Zhao, L.X. Xu, S. Cai, W. Jia, Serum Metabolite Profiling of Human Colorectal Cancer Using GC−TOFMS and UPLC−QTOFMS, J. Proteome Res. 8(10) (2009) pp. 4844–4850.

[110]. E.C.Y. Chan, P.K. Koh, M. Mal, P.Y. Cheah, K.W. Eu, A. Backshall, R. Cavill, J.K. Nicholson, H.C. Keun, Metabolic Profiling of Human Colorectal Cancer Using High-Resolution Magic Angle Spinning Nuclear Magnetic Resonance (HR-MAS NMR) Spectroscopy and Gas Chromatography Mass Spectrometry (GC/MS), J. Proteome Res. 8(1) (2009) pp. 352–361.

[111]. M. Phillips, K. Gleeson, J.M.B. Hughes, J. Greenberg, R.N. Cataneo, L. Baker, W.P. McVay, Volatile organic compounds in breath as markers of lung cancer: a cross-sectional study, Lancet 353(9168) (1999) pp. 1930–1933.

[112]. C.S.J. Probert, I. Ahmed, T. Khalid, E. Johnson, S. Smith, N. Ratcliffe, Volatile Organic Compounds as Diagnostic Biomarkers in Gastrointestinal and Liver Diseases, J. Gastrointestin. Liver Dis.18(3) (2009) pp. 337–343.

[113]. D.F. Altomare, M. Di Lena, F. Porcelli, L. Trizio, E. Travaglio, M. Tutino, S. Dragonieri, V. Memeo, G. de Gennaro, Exhaled volatile organic compounds identify patients with colorectal cancer, Br. J. Surg. 100(1) (2013) pp. 144–150.

[114]. S. Takano, Y. Yoshii, S. Kondo, H. Suzuki, T. Maruno, S. Shirai, T. Nose, Concentration of Vascular Endothelial Growth Factor in the Serum and Tumor Tissue of Brain Tumor Patients, Cancer Res. 56(9) (1996) pp. 2185–2190.

[115]. M. Tamura, Y. Ohta, T. Kajita, K. Kimura, T. Go, M. Oda, H. Nakamura, G. Watanabe, Plasma VEGF concentration can predict the tumor angiogenic capacity in non-small cell lung cancer, Oncol. Rep. 8(5) (2001) pp. 1097–1102.

[116]. K. Werther, I.J. Christensen, N. Brünner, H.J. Nielsen, The Danish RANX05 Colorectal Cancer Study Group Soluble vascular endothelial growth factor levels in patients with primary colorectal carcinoma, Eur. J. Surg. Oncol. 26(7) (2000) pp. 657–662.

[117]. L.M. Ellis, Y. Takahashi, W. Liu, R.M. Shaheen, Vascular endothelial growth factor in human colon cancer: biology and therapeutic implications, Oncologist. 5(1) (2000) pp. 11–15.

[118]. S.J. Cohen, C.J. Punt, N. Iannotti, B.H. Saidman, K.D. Sabbath, N.Y. Gabrail, J. Picus, M. Morse, E. Mitchell, M.C. Miller, G.V. Doyle, H. Tissing, L.W. Terstappen, N.J. Meropol, Relationship of Circulating Tumor Cells to Tumor Response, Progression-Free Survival, and Overall Survival in Patients With Metastatic Colorectal Cancer, J. Clin. Oncol. 26(19) (2008) pp. 3213–3221.

[119]. S. Riethdorf, H. Fritsche, V. Müller, T. Rau, C. Schindlbeck, B. Rack, F. Jänicke, S. Jackson, T. Gornet, M. Cristofanilli, K. Pantel, Detection of Circulating Tumor Cells in Peripheral Blood of Patients with Metastatic Breast Cancer: A Validation Study of the CellSearch System, Clin. Cancer Res. 13(3) (2007) pp. 920–928.

[120]. W.J. Allard, J. Matera, M.C. Miller, M. Repollet, M.C. Connelly, C. Rao, A.G. Tibbe, J.W. Uhr, L.W. Terstappen, Tumor Cells Circulate in the Peripheral Blood of All Major Carcinomas but not in Healthy Subjects or Patients With Nonmalignant Diseases, Clin. Cancer Res. 10(20) (2004) pp. 6897–6904.

[121]. N. Udilova, D. Jurek, B. Marian, L. Gille, R. Schulte-Hermann, H. Nohl, Induction of lipid peroxidation in biomembrane by dietary oil components, Food Chem. Toxicol. 41(2003) pp. 1481–1489.

[122]. M. Repetto, J. Semprine, A. Boveris Lipid Peroxidation: Chemical Mechanism, Biological Implications and Analytical Determination, IntechOpen, 2012.

[123]. A. Amann, P. Spanel, D. Smith, Breath analysis: the approach towards clinical applications, Mini-Rev. Med. Chem. 7 (2007) pp. 115–129.

[124]. P.J. Mazzone, Analysis of volatile organic compounds in the exhaled breath for the diagnosis of lung cancer, J. Thorac. Oncol. 3 (2008) pp. 774–780.

[125]. A. Bajaj, O.R. Miranda, I.B. Kim, R.L. Phillips, D.J. Jerry, U.H.F. Bunz, V.M. Rotello, Detection and differentiation of normal, cancerous, and metastatic cells using nanoparticle-polymer sensor arrays, Proc. Natl. Acad. Sci. USA 106 (2009) 10912–10916.

[126]. O. Barash, N. Peled, F.R. Hirsh, H. Haick, Sniffing the unique 'odor print' of non-small-cell lung cancer with gold nanoparticles, Small 5 (2009) pp. 2618–2624.

[127]. W. Filipiak, A. Sponring, A. Filipiak, C. Ager, J. Shubert, W. Miekisch, A. Amann, J. Troppmair, TD-GC-MS analysis of volatile metabolites of human lung cancer and normal cells in-vitro, Cancer Epidiemiol. Biomarkers Prev. 19 (2010) pp. 182–195 (2010).

[128]. T. Ligor, M. Ligor, A. Amann, C.B. Ager, M. Pienz, A. Dzien, B. Buszewski, The analysis of healthy volunteers' exhaled breath by the use of solid-phase microextraction and GC-MS, J. Breath. Res. 2 (2008) pp. 046006/1-046006/8.

[129]. A. Bajtarevich, C. Ager, M. Pienz, M. Klieber, K. Schwarx, M. Ligor, T. Ligor, W. Filipiak, H. Denz, W. Hilbe, W. Weiss, P. Lukas, H. Jamnig, M. Hackl, A. Haidenberger, B. Buzewski, W. Miekisch, J. Schubert, A. Amann, Noninvasive detection of lung cancer by analysis of exhaled breath, BMC Cancer 9 (2009) pp. 348.

[130]. L. Horvath, Z. Lazar, N. Gyulai, M. Kollai, G. Losonczy, Exhaled biomarkers in lung cancer, Eur. Respir. J. 34 (2009) pp. 261–275.

[131]. M. Ligor, T. Ligor, A. Bajtarevic, C. Ager, M. Pienz, M. Klieberm H. Denz, M. Fiegl, W. Hilbe, W. Weiss, P. Lukas, H. Jamnig, M. Hackl, W. Miekish, J. Schubert, A. Amann, Determination of volatile organic compounds in exhaled breath of patients with lung cancer using solid phase microextraction and gas chromatography mass spectrometry, Clin. Chem. Lab. Med. 47 (2009) pp. 550–560.

[132]. G. Peng, M. Hakim, Y.Y. Broza, S. Billan, R. Abdah-Bortnyak, A. Kuten, U. Tish, H. Haick, Detection of lung, breast, colorectal, and prostate cancers from exhaled breath using a single array of nanosensors, Brit. J. Cancer 103 (2010) pp. 542–551.

[133]. C.M.F. Kneepkens, G. Lepage, C.C. Roy, The potential of the hydrocarbon breath test as a measure of lipid peroxidation, Free Radical Bio. Med. 17 (1994) pp. 127–160.

[134]. J.I. Baubach, V. Vautz, V. Ruzsanyi, Metabolites in Human Breath: Ion Mobility Spectrometers as Diagnostic Tools for Lung Diseases. Breath Analysis for Clinical Diagnosis and Therapeutic Monitoring, World Scientific Publishing Co. Pte. Ltd: Toh Tuck Link, Singapore, 2005.

[135]. D.F. Altomare, M. Di Lena, F. Porcelli, L. Trizio, E. Travaglio, M. Tutino, S. Dragonieri, V. Memeo, G. de Gennaro, Exhaled volatile organic compounds identify patients with colorectal cancer, Wiley Online Library.

[136]. http://www.medicinenet.com/ca_125/article.htm.

[137]. http://www.clontech.com/US/Products/Cell_Biology_and_Epigenetics/Cancer_and_.Inflammation/CEA.

[138]. I. Ivanov, J. Stojcic, A. Stanimirovic, E. Sargent, R.K. Nam, S.O. Kelley, Chip-Based Nanostructured Sensors Enable Accurate Identification and Classification of Circulating Tumor Cells in Prostate Cancer Patient Blood Samples, Anal. Chem. 85(1) (2013) pp. 398–403.

[139]. A.A. Adams, P.I. Okagbare, J. Feng, M.L. Hupert, D. Patterson, J. Göttert, R.L. McCarley, D. Nikitopoulos, M.C. Murphy, S.A. Soper, Highly Efficient Circulating Tumor Cell Isolation from Whole Blood and Label-Free Enumeration Using Polymer-Based Microfluidics with an Integrated Conductivity Sensor, J. Am. Chem. Soc. 130(27) (2008) pp. 8633–8641.

[140]. S. Wang, K. Liu, J. Liu, Z.T.F. Yu, X. Xu, L. Zhao, T. Lee, E.K. Lee, J. Reiss, Y.K. Lee, L.W.K. Chung, J. Huang, M. Rettig, D. Seligson, K.N. Duraiswamy, C.K.F. Shen, H.R. Tseng, Highly Efficient Capture of Circulating Tumor Cells by Using Nanostructured Silicon Substrates with Integrated Chaotic Micromixers, Angew. Chem. Int. Ed. Engl. 50(13) (2011) pp. 3084–3088.

[141]. I.E. Tothill, Biosensors for cancer markers diagnosis, Semin. Cell. Dev. Biol. 20(1) (2009) pp. 55–62.

[142]. G. Zheng, F. Patolsky, Y. Cui, W.U. Wang, C.M. Lieber, Multiplexed electrical detection of cancer markers with nanowire sensor arrays, Nat. Biotechnol. 23 (2005) pp. 1294–1301.

[143]. M.S. Wilson, Electrochemical Immunosensors for the Simultaneous Detection of Two Tumor Markers, Anal. Chem. 77(5) (2005) pp. 1496–1502.

[144]. J. Wang, Electrochemical biosensors: Towards point-of-care cancer diagnostics, Biosens. Bioelectron. 21(10) (2006) pp. 1887–1892.

[145]. Y.E. Choi, J.W. Kwak, J.W. Park, Nanotechnology for Early Cancer Detection, Sens. 10(1) (2010) pp. 428–455.

[146]. R.M. Penner, Chemical Sensing with Nanowires, Annu. Rev. Anal. Chem. 5 (2012) pp. 461–485.

[147]. S. Krishnamoorthy, Nanostructured sensors for biomedical applications — a current perspective, Curr. Opin. Biotechnol. 34 (2015) pp. 118–124.

[148]. C. Malagù, B. Fabbri, S. Gherardi, A. Giberti, V. Guidi, N. Landini, G. Zonta, Chemoresistive Gas Sensors for the Detection of Colorectal Cancer Biomarkers, Sens. 14(10) (2014) pp. 18982–18992.

[149]. G. Zonta, G. Anania, B. Fabbri, A. Gaiardo, S. Gherardi, A. Giberti, V. Guidi, N. Landini, C. Malagù, Detection of colorectal cancer biomarkers in the presence of interfering gases, Sens. Actuators B: Chem. 218 (2015) pp. 289–295.

[150]. N. Landini, B. Fabbri, A. Gaiardo, S. Gherardi, V. Guidi, G. Rispoli, M. Valt, G. Zonta, C. Malagù, Detection of tumor markers and cell metabolites in cell cultures, using nanostructured chemoresistive sensors, Sens. Microsystems – Proc. 19th AISEM 2017 Natl. Conf. (2017) pp. 51–58.

[151]. G. Zonta, G. Anania, B. Fabbri, A. Gaiardo, S. Gherardi, A. Giberti, N. Landini, C. Malagù, L. Scagliarini, V. Guidi, Preventive screening of colorectal cancer with a device based on chemoresistive sensors, Sens. Actuators B: Chem. 238 (2016) pp. 1098–1101.

[152]. G. Zonta, G. Anania, C. Feo, A. Gaiardo, S. Gherardi, A. Giberti, V. Guidi, N. Landini, C. Palmonari, L. Ricci, A. de Togni, C. Malagù, Use of gas sensors and FOBT for the early detection of colorectal cancer, Sens. Actuators B: Chem. 262 (2018) pp. 884–891.

[153]. M.I. Maqsood, M.M. Matin, A.R. Bahrami, M.M. Ghasroldasht, Immortality of cell lines: Challenges and advantages of establishment, Cell Biol. Int. 37 (10) (2013) pp. 1038–1045.

[154]. https://www.en-standard.eu/csn-en-14820-single-use-containers-for-human-venous-blood-specimen-

collection/?gclid=EAIaIQobChMIsr2dx5HS1wIVbSjTCh0kAQuPEAAYASAAEgKL4fD_BwE.

[155]. https://www.beuth.de/de/norm-entwurf/din-en-iso-6710/261188601.

[156]. W. Goossens, R.L. Van Duppen, R.L. Verwilghen, K2-or K3-EDTA: the anticoagulant of choice in routine haematology? Int. J. Lab. Hematol. (1991).

[157]. E.M. Van Cott, K.B. Lewandrowski, S. Patel, D.Y. Grzybek, H.S. Patel, S.R. Fletcher, A. Kratz, Comparison of glass K3EDTA versus plastic K2EDTA blood-drawing tubes for complete blood counts, reticulocyte counts, and white blood cell differentials, Lab Hematol. 9(1) (2003) pp. 10–14.

[158]. https://www.researchgate.net/file.PostFileLoader.html?id=55d494855cd9e392178b45dd&assetKey=AS%3A273835104899073%401442298784205.

[159]. https://www.sparkfun.com/datasheets/Sensors/SHT1x_datasheet.pdf.

[160]. C. Mencuccini, V. Silvestrini, Fisica I Meccanica - Termodinamica, Liguori Editors, 2004, ISBN 88-207-1493-0.

[161]. A. Giberti, M. Benetti, M.C. Carotta, V. Guidi, C. Malagu', G. Martinelli, Heat exchange and temperature calculation in thick-film semiconductor gas sensor systems, Sens. Actuators B: Chem. 130 (2008) pp. 277–280.

[162]. R. Dulbecco, G. Freeman, Virology 8 (1959) pp. 396.

[163]. M.J. Madou, S.R. Morrison, Chemical Sensing with Solid State Devices, Chapter 2, Academic Press Inc.

[164]. K. Ellmer, A. Klein, B. Rech, Transparent Conductive Zinc Oxide, Springer Series in Materials Science 104, Springer, Chapter 1, pp. 15.

[165]. http://www.cs.otago.ac.nz/cosc453/student_tutorials/principal_components.pdf.

[166]. https://www.sciencesource.com/archive/Fibrolipoma-in-the-larynx--endoscope-view-SS221231.html.

[167]. https://www.researchgate.net/figure/External-photograph-of-carcinoma-in-situ-showing-typical-leukoplakic-appearance-of_fig1_230602867.

[168]. K.A. Vermeersch, M.P. Styczynski, Applications of metabolomics in cancer research., J Carcinog. 12(9) (2013). doi: 10.4103/1477-3163.113622.

[169]. https://www.slideshare.net/raghuveer12327/composition-og-blood.

[170]. http://givingblood.org/about-blood/blood-components.aspx.

Ringraziamenti

Ringrazio mio padre e mia madre, i miei nonni, mio zio, Marina, la piccola Marta, Iggy e Birba. La mia famiglia, che fino ad oggi mi ha supportato, voluto bene e spronato lungo la mia strada. Un altro traguardo è stato raggiunto.

Ringrazio Cesare Malagù, mio relatore di tesi, tutore di dottorato e mentore, per avermi seguito e guidato lungo tutti questi anni accademici, e per la fiducia dimostratami nel permettermi di gestire tanto filoni di ricerca quanto mansioni amministrative. Ad maiora.

Ringrazio Vincenzo Guidi, tanto come professore ordinario di fisica generale quanto come coordinatore del corso di dottorato, per il supporto ed i consigli forniti sia per ciò che concerne le pubblicazioni scientifiche sottomesse in questi anni ed accettate per la pubblicazione, sia per il sostegno nella parte burocratica relativa al percorso di dottorato.

Ringrazio i miei colleghi Giulia, Sandro, Michele, Alessio, Barbara, Andrea e Matteo, e con loro tutti i dottorandi e ricercatori conosciuti in questi anni nel dipartimento, per tutto ciò che abbiam vissuto, e per tutto il lavoro, il divertimento e le situazioni assurde in cui solo tra fisici ci si poteva ficcare.

Ringrazio Giorgio Rispoli e Gabriele Anania, con i loro team al completo e collaboratori (Mascia, Beppe, Serafino, Veronica, Marta e tutti gli altri) per il prezioso aiuto e le mille iniziative, esperimenti, idee e successi condivisi con voi.

Ringrazio i miei soci di SCENT, per l'avventura che abbiamo creato e ad oggi continua a crescere e evolversi.

Ringrazio tutti i miei amici, diurni e notturni, tra San Venanzio, Padova, Bologna, Ferrara, Como, Torino, Montecarlo di Lucca e oltre. Siete tanti e sparsi ovunque, e siete stati voi spesso a sciacquarmi dal cervello stress e pensieri negativi, a farmi ricaricare le batterie e soprattutto a ridarmi il sorriso e la spensieratezza, col vostro calore e la vostra allegria. Un pensiero lo lascio per ognuno di voi, qui.

Ringrazio chiunque io abbia incontrato, nel bene e nel male. La personalità e la mente di un individuo si sviluppano attraverso l'esperienza e gli stimoli ricevuti dall'ambiente circostante, come dimostrato ormai solidamente da plurime scoperte e pubblicazioni in campo biofisico e sociologico. Per questo ho un debito di esistenza, in ogni frammento che mi compone, nei confronti di tutte le persone che ho incontrato sinora.

Infine, e consequenzialmente a tutto ciò che è stato precedentemente asserito, ringrazio la mia rabbia, la mia sete di conoscenza, la mia testardaggine e la mia volontà. Non fossero sempre state con me non sarei qui, ora, e queste righe non sarebbero state scritte.